Onshore-offshore post-seismic data analysis of the Mw=7.8 2016 Pedernales earthquake (Ecuador) : key to understanding earthquake supercycles

Caroline Chalumeau

UNIVERSITÉ CÔTE D'AZUR

ÉCOLE DOCTORALE
SCIENCES FONDAMENTALES ET APPLIQUÉES

THÈSE DE DOCTORAT

Analyse des données post-sismiques terre-mer du séisme de Pedernales 2016 Mw=7.8 (Équateur)

Une clef pour comprendre les supercycles sismiques

Caroline CHALUMEAU

Géoazur UMR 7329

Présentée en vue de l'obtention du grade de docteur en Sciences de la Terre et de l'Univers **d'**Université Côte d'Azur
Dirigée par Philippe Charvis
Co-encadrée par : Hans Agurto-Detzel et Louis De Barros
Soutenue le : 13/07/2022

Devant le jury, composé de :
Kate Huihsuan Chen, Professeure, Department of Earth Sciences - National Taiwan Normal University
Françoise Courboulex, Directrice de recherche CNRS, Géoazur
David Marsan, Professeur, Université de Savoie Mont-Blanc - ISTerre
Mathilde Radiguet, Physicienne-Adjointe CNAP, Observatoire des Sciences de l'Univers de Grenoble - ISTerre
Andreas Rietbrock, Professeur, Institute of Geophysics - Karlsruhe Institute of Technology

Analyse des données post-sismiques terre-mer du séisme de Pedernales 2016 Mw=7.8 (Équateur)

Une clef pour comprendre les supercycles sismiques

Jury :

Présidente du jury

Françoise Courboulex, Directrice de recherche CNRS, Géoazur

Rapporteur.se.s

David Marsan, Professeur, Université de Savoie Mont-Blanc - ISTerre

Kate Huihsuan Chen, Professeure, Department of Earth Sciences - National Taiwan Normal University

Examinateur.ice.s

Mathilde Radiguet, Physicienne-Adjointe CNAP, Observatoire des Sciences de l'Univers de Grenoble - ISTerre

Andreas Rietbrock, Professeur, Institute of Geophysics - Karlsruhe Institute of Technology

Onshore-offshore post-seismic data analysis of the Mw=7.8 2016 Pedernales earthquake (Ecuador)

Key to understanding earthquake supercycles

Jury :

Head of the jury

Françoise Courboulex, CNRS researcher, Géoazur

Reporters

David Marsan, Professor, Université de Savoie Mont-Blanc - ISTerre

Kate Huihsuan Chen, Professor, Department of Earth Sciences - National Taiwan Normal University

Examiners

Mathilde Radiguet, CNAP Physicist, Observatoire des Sciences de l'Univers de Grenoble - ISTerre

Andreas Rietbrock, Professor, Institute of Geophysics - Karlsruhe Institute of Technology

Abstract

The Ecuador-Colombian subduction zone has hosted a series of large subduction earthquakes over the course of the 20th century. This earthquake sequence started in 1906 with a Mw 8.4-8.8 earthquake, which ruptured a 200-500 km long segment of the megathrust. It was followed by three large earthquakes that broke, from south to north, portions already contained in the 1906 rupture. These earthquakes occurred in 1942 (Mw=7.8), 1958 (Mw=7.6) and 1979 (Mw=8.2), respectively. In 2016, the Pedernales earthquake re-ruptured the 1942 coseismic region, possibly starting a new cascade of large events.

The Pedernales earthquake and its aftershocks, recorded thanks to the international deployment of seismic stations in the months following the mainshock, provide an opportunity to better understand the seismotectonic processes that occur in the region. This thesis will focus primarily on the interactions between seismicity and aseismic slip, and on the influence of the structure of the megathrust on the seismic activity.

For this purpose, a catalogue of repeating earthquakes was created by correlating the existing aftershock catalogue. The families of repeating earthquakes were then completed using template-matching to find missing events. Repeating earthquakes were then relocated in a 1D model, first using manual picks and then using differential times from correlations. Finally, source properties were determined for a portion of the aftershock catalogue.

Repeating earthquakes in Ecuador occur primarily within larger aftershock clusters situated at the edge of the main afterslip regions. Additionally, the slip associated with individual repeating earthquake families seems to have an indirect link to the slip modelled using GPS data. Indeed, family slip appears heterogeneous, suggesting perhaps a more complex link between afterslip and repeating earthquakes, and likely reflecting the complexity of the megathrust structure.

Additionally, the study of source properties of Pedernales aftershocks reveals a segmentation of the subduction zone with distance to the trench. Stress drops near the trench are low, and decrease with time during the postseismic period, as observed within families of repeating earthquakes. This is probably due to a variation in pore fluid pressure, which is likely very high near the trench, and which plays a crucial role in seismogenesis in the region.

Keywords: Seismology; Repeating earthquakes; Postseismic processes; Afterslip; Subduction; South America

Résumé

La zone de subduction qui s'étend du nord de l'Equateur au sud de la Colombie a subi une séquence de grands séismes au cours du XXe siècle. Cette séquence débute en 1906 avec un séisme de magnitude 8.4-8.8, qui rompt une portion du chevauchement d'interplaque d'environ 200-500 km de long. S'ensuit ensuite trois grand séismes de magnitudes 7.6 à 8.2, qui rompent à nouveau cette zone du sud au nord en 1942, 1958 et 1979. Cette séquence est à nouveau amorcée en 2016 lorsque le séisme de Pedernales casse la zone de rupture du séisme de 1942, marquant ainsi peut-être le début d'une nouvelle cascade sismique.

Le séisme de Pedernales et ses répliques, enregistrées grâce au déploiement de stations sismiques dans les mois suivant le séisme, permettent de mieux comprendre la zone. Cette thèse s'intéresse tout particulièrement aux interactions entre sismicité et glissement asismique dans la région, ainsi qu'au lien entre la sismicité et la structure de la zone de subduction.

Pour ce faire, un catalogue de séismes répétitifs est élaboré par corrélation à partir du catalogue de répliques existant. Les données sont également scannées par template-matching afin de compléter les familles de séismes répétitifs. Ceux-ci sont ensuite relocalisés dans un modèle de vitesse 1D grâce à des pointés manuels et à des temps relatifs d'arrivée. Enfin, nous déterminons les propriétés de sources d'une partie des répliques de Pedernales.

Les séismes répétitifs en Equateur ont lieu principalement au sein de clusters de sismicité, en marge des zones de glissement post-sismique. Par ailleurs, le glissement associé aux familles individuelles de séismes répétés ne semble pas avoir de lien direct avec le glissement modélisé à l'aide de données GNSS. Il semble au contraire être bien plus hétérogène, laissant penser à un lien plus complexe entre glissement asismique et séismes répétitifs, et reflétant probablement une géométrie complexe de la zone de subduction.

Par ailleurs, l'étude des propriétés de sources des répliques de Pedernales met en évidence une segmentation de la zone de subduction basée sur la distance à la fosse. Les chutes de contrainte des séismes près de la fosse sont basses, et diminuent au cours du temps durant la période postsismique, comme le montre l'étude des séismes répétitifs. Cela est probablement dû à une variation de pression des fluides, qui sont très abondants au niveau de la fosse, et qui jouent un rôle crucial dans le comportement sismogène de la zone.

Mots clés: Sismologie ; Séismes répétés ; Processus postsismiques ; Afterslip ; Subduction ; Amérique du Sud

"The beginning of a story is a sudden event;
The start, a happy accident,
The end, the fate for which it's meant.
A story that never ends is a sad fate"

From: Princess Tutu

"If it cannot hatch from its shell, the chick will die without ever truly being born. We are the chick; the world is our egg. If we don't break the world's shell, we will die without truly being born."

From: Revolutionary Girl Utena

Acknowledgements

I once heard someone say that aknowledgements were one of the hardest part to write in a dissertation. Having now gone through the process myself, I have to say I disagree on that front. Nevertheless, I hope you'll forgive me for being forgetful or self-indulgent, as I attempt to map the last four years of my life with the people that filled it. I will do my best.

Une thèse ne se faisant jamais seule, je veux commencer par remercier mon directeur de thèse, Philippe Charvis, qui a cru en moi dès mon premier stage ici et qui a toujours su trouver une place entre deux réunions pour me voir lorsque j'en avais besoin. Merci aussi à Louis De Barros, dont les discussions scientifiques toujours passionnantes ont grandement enrichi ce manuscrit. And of course, many thanks to Hans Agurto-Detzel, whose constant presence throughout the first three years of my thesis helped me immeasurably.

Similarly, a special thank you should go to Diane Rivet and Andreas Rietbrock for their involvement in my thesis committee and all of their helpful advice throughout my thesis. More broadly, I want to thank everyone who took the time to talk science with me or to review my work, including (but limited to) Audrey Galve, Mireille Laigle, Yvonne Font, Frédérique Rolandone and Jean-Mathieu Nocquet.

I also want to thank my jury for their helpful comments and questions, namely Françoise Courboulex, David Marsan, Kate Huihsuan Chen, Mathilde Radiguet and Andreas Rietbrock. Special thanks to my two reporters, Kate Huihsuan Chen and David Marsan, who both took the time to evaluate my dissertation in full.

Thank you also to everyone who collected, managed or picked any of the data used in this study. There may be too many of you to thank, but I particularly want to highlight the contribution of the people of the Instituto Geofisico in Quito, without whom none of this work would have been possible.

Merci à Jean-Xavier Dessa, qui m'a permis de participer à la campagne SEFASILS alors que j'étais alors nouvelle au laboratoire. Merci aussi à ma partenaire de cabine, Marie-Odile Beslier, ainsi qu'à mes partenaires de quart Laure Combe et Laure Schenini, qui m'ont accompagnée avec patience et bienveillance lors de ces dix jours de campagne.

Il me semble également important de souligner que l'environnement de travail, au sens plus large, a grandement contribué au bon déroulement de ma thèse. Aussi j'aimerais remercier tout d'abord l'équipe Marge de m'avoir accueillie, depuis mes stages volontaires de license jusqu'à ma thèse. Je tiens aussi à remercier toutes celles et ceux travaillant au service

informatique (Lionel, Caroline, David, Jean-Baptiste et Thuy) pour leur patience et leur soutien constant. De même, je remercie aussi l'intégralité du service administratif de Géoazur (Valérie, Myriam, Emilie, Candice, Véronique, Stéphanie, Magali, Fabienne, Martine et bien sûr Sandrine), autant pour leur efficacité que pour leur gentillesse. Merci par ailleurs à Jenny Trévisan, sans qui le laboratoire peinerait à bien fonctionner, et Arnaud Berry, dont les efforts constants depuis son arrivée ont amélioré le quotidien de tous. Merci également à l'équipe coordinatrice des séminaires, et des Mardis Séismes, pour avoir élargi mes connaissances (special thanks to Martijn, without whom machine learning would be a mystery to me). Enfin, je tiens à remercier Corinne Nicolas-Cabane pour m'avoir accueillie dès mon arrivée, et Jelena Giannetti pour son aide (et pour m'avoir laissée garder les livres dont j'avais besoin lors de cette dernière année de thèse).

Mon souvenir le plus fort de Géoazur restera probablement celui de sa convivialité. J'ai fait la connaissance de nombreuses personnes devenues amies, et je tiens à remercier tous ceux qui ont fait partie de ma vie ces dernières années.

Tout d'abord, je tiens à remercier mes co-bureaux successifs, Manue, Sara, Zoé, Josselin, Lise et Bastien. Merci pour les discussions, les commentaires, les blagues, et le soutien, particulièrement en fin de thèse (merci aussi d'avoir égayé le bureau avec de nombreuses plantes, moi-même j'aurais pas pu). De même, aux doctorants/postdocs du bâtiment 1 (en particulier Alexita, Albane, Alexito, Andréa, Pierre et Mathilde), merci pour toutes les discussions scientifiques (ou non) du matin.

Merci à tous les amateurs de jeux de société et JDR (ils sont nombreux), pour les soirées chez les uns et les autres. En particulier, merci à Pierre, Zoé, Flo, Nico, Ophélie, Lionel, Serge, Marion et plus occasionnellement Daniel, Philippe, Alexito, Marie, Aurélie et Andréa. Je tiens particulièrement à remercier Zoé, instigatrice du groupe Géomusic qui a été essentiel à ma santé mentale pendant le confinement. Merci à Zoé, Serge et Nico pour toutes les soirées trivia et les photomontages bancals (champions !), et merci à Marion, Lise, Daniel, Laurie, Hector et Alexita de nous avoir occasionnellement rejoins.

De même, merci à Laure et Nico, mes partenaires de danse (pas littéralement dans le cas de Laure), qui m'ont introduite au Lindy dès ma première semaine à Géoazur, alors que je ne connaissais pas encore grand monde.

J'aimerais maintenant prendre un moment pour remercier tout particulièrement mes amis et camarades rencontrés tout au long de cette thèse (attention liste non exhaustive) : Albane pour ton sourire et ton soutien (et ta patience face à la prolifération d'avocatier dans ta proximité) ; Alexita, camarade de congrès et surtout d'aventure en Equateur, pour ta bonne humeur et les discussions éthiques ; Théa pour tes bons conseils et pour m'avoir aidée à m'intégrer dès le début de ma thèse ; Lise pour ton soutien, surtout à la fin (et pour l'entraide de fin de thèse) ; Andréa (travaillant aussi sur l'Equateur, même si Guayaquil, c'est loin !) pour

ta convivialité et ton franc-parler ; Pierre pour ton humour (malgré tous tes problèmes de santé !) ; Alexito, aussi membre de la team Equateur, pour ton soutien discret et les nombreuses discussions sismo ; Maria José (véritable Equatorienne cette fois-ci), pour ton sourire toujours chaleureux ; Marion, partenaire de congrès, pour ton enthousiasme effusif et sans failles ; Chao, my car mate, for your friendliness ; Laeticia pour ton affection, et pour m'avoir fait découvrir les cultures des îles ; Marie, de même, ainsi que pour toutes les discussions geeks, partagées aussi par Bougha ; Daniel pour tes chansons et ton expressivité ; Philippe pour tes blagues douteuses et ton amour inconditionnel pour ton chat qui est très chou ; Ophélie, camarade de début de thèse (et de fête de la science), pour ton amour de la raclette et des jeux ; Lionel pour ta gentillesse et tes pâtisseries vachement bonnes (dédicace aussi à Laurie pour les crêpes et les cookies) ; Hector pour toutes tes histoires incroyables et tes discussions géopolitiques ; Sara pour ta force de caractère et ta franchise (et tes bons conseils administratifs) ; Zoé pour ta convivialité, surtout en période de confinement ; Serge, franc, brillant et toujours prêt à aider malgré tout ; Manue pour ta sérénité ; Mathilde pour tes conseils (en particulier lors des demandes de poste) et pour ta gentillesse.

Je tiens tout particulièrement à remercier Flo, camarade de début et de fin de thèse. Merci pour les cours de sabre, pour les soirées jeux, pour ta bonne humeur, pour ta gentillesse, et même (et je ne l'écrirai qu'une seule fois) pour toutes tes blagues nulles qu'on aime secrètement bien.

Je remercie aussi Nico pour ta générosité sans faille, pour ton calme et ta sérénité, pour ton intelligence et ta perceptivité. Merci pour toutes les après-midi (/week-ends) à jouer, à discuter animé, à prodiguer des conseils, à parler de tout ou de rien, à faire la cuisine, à regarder des films, et même à jardiner et à bricoler (à l'encontre de mon plein gré évidemment). Et je ne parle même pas des deux mois passés à covoiturer lorsque j'étais infirme, ni du flot continu de cookies ces dernières années. Tu as été mon premier ami de Géoazur et mon soutien durant toute ma thèse.

Merci enfin à mes parents, ma sœur et toute ma famille, ainsi qu'à tous mes amis hors-thèse (dédicace spéciale à Cécile et Jean-Noël pour les soirées jeux hebdomadaires), qui m'aiment et me soutiennent depuis le début de cette aventure.

Table of Contents :

Introduction

Earthquakes in subduction zones can be some of the most destructive events on Earth. Not only are the seismic waves they generate potentially devastating, but they can additionally trigger fires, landslides and tsunamis, greatly impacting populations living on the coast. Over the last 20 years, two great subduction earthquakes have had a particularly large impact: The Mw 9.1 Sumatra-Andaman earthquake in 2004 and the Mw 9.0 Tohoku-Oki earthquake in 2011. Combined, they have caused the deaths of several hundreds of thousands of people and the displacement of many others, along with widespread damage and economic devastation. Yet they have also undeniably improved our understanding of these phenomena, from the nucleation and rupture process to the postseismic period, all the while revealing our blind spots (Avouac, 2011; Kanamori, 2006). Thus large subduction earthquakes can also be an opportunity to learn more about them, and to better prepare ourselves to withstand future catastrophes.

This was also the case with the Pedernales earthquake, a Mw 7.8 subduction earthquake that occurred on the 16th of April 2016 off the coast of Ecuador. The earthquake killed 670 people, injured at least 7000 more, and caused about 30000 people to lose housing. It also triggered several thousands of aftershocks, including two Mw 6.7 and Mw 6.9 earthquake, which caused further damage.

Notably, this earthquake is the latest in a sequence of large earthquakes that have occurred offshore Colombia and Ecuador over the past century. This sequence started in 1906 with a Mw 8.4-8.8 earthquake rupturing a 200-500 km long segment of the megathrust (Kanamori and McNally, 1982; Kelleher, 1972). Three other Mw 7.6-8.2 earthquakes occurred in a south-to-north cascade 1942, 1958 and 1979, each rupturing a portion of the 1906 coseismic region. The 2016 Pedernales earthquake seemingly ruptured the same area as the 1942 earthquake, possibly starting a new cascade and thus a time of increased seismic hazard in the north of Ecuador and south of Colombia (Nocquet et al., 2017). To better face this challenge, it is necessary to learn about the Ecuadorian subduction zone and the factors controlling seismicity in the region.

The Pedernales aftershock sequence offers valuable insight into the friction and structure at the plate interface. While the mainshock and early aftershocks were recorded only by the local seismic network (Alvarado et al., 2018), international efforts in collaboration with the Instituto Geofísico at the Escuela Politécnica Nacional led to the temporary deployment of 65 seismometers, which significantly improved the detection of aftershocks (Meltzer et al., 2019). Meanwhile, the GNSS network in place allowed for the detection and modelling of slow postseismic deformation, particularly in three regions near the trench (Rolandone et al., 2018).

This improved our understanding of the driving mechanisms for aftershocks, as well as the structure of the subduction zone (Agurto-Detzel et al., 2019).

This thesis will concern itself more specifically with the interplay between seismic and aseismic slip in Ecuador, and the way this relates to the structure of the megathrust. In the following chapter, I will provide some background regarding subduction zones, seismic and aseismic slip, and repeating earthquakes. I will then summarize our knowledge of the Ecuadorian subduction zone and its seismicity. This will be followed by a chapter in which I will describe the work I did during my thesis, that is to say the elaboration of a catalogue of repeating seismicity for the years 2015 to 2017 and the calculation of source properties for a number of Pedernales aftershocks. The results from these two points will be presented separately in the next two chapters. Finally, I will discuss outstanding points and offer perspectives for future work.

Chapter 1: Structure and slip in subduction zones

Before diving into my work, it is first important to establish a baseline understanding of important seismological and tectonic concepts that will be discussed in the rest of this work. Thus this first chapter will give a brief overview of processes occurring at subduction zones, in order to understand the large-scale tectonic context of the work. I will then introduce major concepts relating to friction on a fault, before bringing these two threads together to discuss seismic and aseismic slip in subduction zones. Finally, I will focus specifically on repeating earthquakes, as they represent a specific kind of seismicity that interacts with aseismic slip, and they are the main tools used in this work.

1.1 Subduction zone architecture

Subduction zones are regions on earth where two lithospheric plates converge, leading the denser one, called the slab, to sink under the overriding plate, along a plane of contact called the megathrust fault. This can induce hydrothermal circulation, intraplate deformation, volcanism and seismicity, all of which are influenced directly by the shape and processes occurring at the subduction zone. In this section, I will introduce the basic anatomy of a typical subduction zone, as well as the main processes at work, particularly those that influence seismogenesis (Figure 1). Although subduction can occur between two oceanic plates, an oceanic plate and a continental plate, or two continental plates, I will focus on cases when an oceanic plate is subducted under a continental one, as this is the configuration in South America.

After its creation at a mid-ocean ridge, the oceanic lithosphere gradually thickens as its temperature decreases. This is accompanied by hydrothermal circulation, both at the mid-ocean ridge and off the ridge axis, which contributes to the geochemical alteration and hydration of the oceanic crust (Stein and Stein, 1994). Gradually, sediments, first from the marine environment and then eventually from the continent, are deposited on the plate, reducing the interaction between the crust and seawater. As the plate nears the subduction zone, it is forced to bend to enter subduction. Because the plate behaves elastically on a large scale, this leads to a bulge about 50-100 km away from the trench. This bulge, or outer trench high, causes extensional faulting to occur at the top of the lithosphere, potentially reaching the mantle, which promotes fluid circulation deep within the plate (Grevemeyer et al., 2018; Ranero et al., 2003).

This circulation plays a critical role in the seismic and volcanic activity of the subduction zone, as fluids are dragged into the subduction itself.

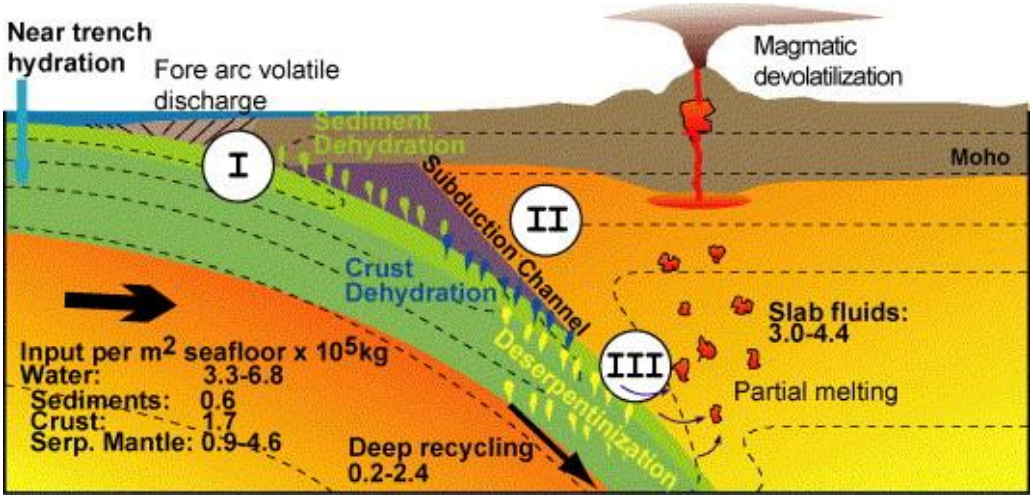

Figure 1 : Schematic cross section of a subduction zone and its water cycle by Rüpke et al. (2004). Numbers represent the main stages of water release within a subduction. I: shallow (< 20 km) fluid release from the subduction of sediments. II: Intermediate-depth (20-100 km) fluid release from the sediments and oceanic crust, which may lead to cold upwelling along the subduction channel. III: Deep (> 100 km) fluid release from the oceanic crust and serpentinized oceanic lithosphere, triggering melting in the overlying mantle. Black dashed lines are schematic temperature contours.

The plate often enter subduction along with some of its sediments. The meters to kilometers thick layer separating the slab from the upper plate is known as the subduction channel, and contains sheared, often fluid-saturated sediments mixed with fragments of oceanic crust, and sometimes of the overlying plate (Fagereng and Sibson, 2010). An important property of the subduction relates to the amount and fate of the sediments entering subduction. Convergent margins can be categorized as accretionary, intermediate or erosional margins (Figure 2). Accretionary margins grow following the addition and imbrication along the trench of sediments scraped off the slab by the subduction, which form an accretionary prism (Stern, 2002). Sediments can also enter the subduction channel, and possibly thicken the forearc by underplating (Stern, 2002). At erosional margins, the upper plate itself is eroded either at the front of the forearc by slumping of material into the trench, or at its base by tectonic forces, leading to subsidence or normal faulting (Saffer and Tobin, 2011; Stern, 2002). Both the amount of sediments in the subduction channel and the presence of an accretionary prism affect the friction, and thus the seismic behavior of the subduction zone.

Once the plate enters subduction, it experiences a gradual increase in pressure and temperature. As depth increases the slab dehydrates, first releasing water from sediments, then from the oceanic crust, and finally from the oceanic mantle (Rüpke et al., 2004), as is illustrated in Figure 1. These fluids affect the subduction's frictional properties and move heat around

through convection, making the trench hotter while making deeper parts of the subduction colder. In the first few kilometers, water is released through the compaction of sediments, particularly within the first ~3–7 km of burial as porosity decreases (Saffer and Tobin, 2011). This can sometimes be linked to mud volcanism in the forearc region (Hensen et al., 2004). Later, as temperature and pressure increase, the main source of fluids becomes dehydration rather than compaction (Saffer and Tobin, 2011). Clay dehydration, particularly the transition between smectite and illite, is the largest source of dehydration-derived fluids (Saffer and Tobin, 2011). It also controls the updip limit of the seismogenic zone, as smectite clays promote stable sliding while illite material promotes stick-slip behavior (Hyndman et al., 1997). While sediments are initially the main fluid source, at 20-30 km depth, the igneous crust starts to release fluids through dehydration and pore collapse, as hydrous basalts and gabbros start to metamorphose to blueschist (Stern, 2002). The water released at these depths either migrates along the plate interface or into the overlying plate (Saffer and Tobin, 2011). Then, usually at around 100 km depth, the mineral-bound water from the mantle and the crust enters the mantle and cause partial melting, which leads to volcanism in the overriding plate (Zheng et al., 2016). Some water stored in serpentinized mantle may however be transferred even further into the deeper mantle by the subduction process, as the slab sinks sometimes down to the core-mantle boundary (Rüpke et al., 2004).

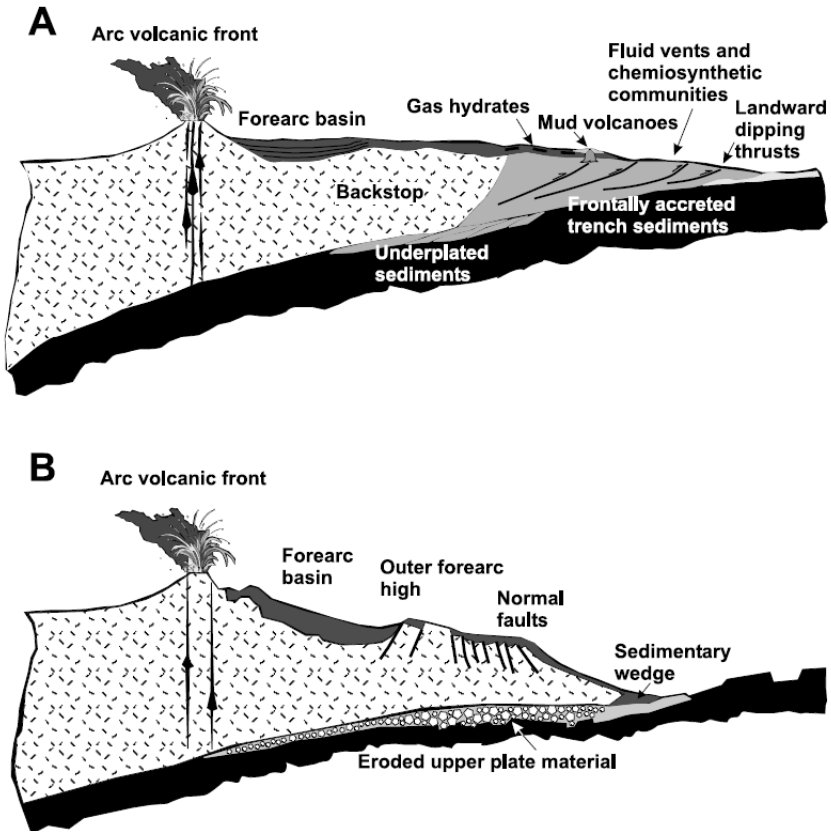

Figure 2 : Schematic drawings of an accretionary (A) and erosional (B) subduction margin, by Clift and Vannucchi (2004).

The oceanic plate meets the overriding plate at the trench, a long bathymetric low that can be several kilometers deeper than the abyssal plain. Although in this work I will focus primarily on seismicity occurring at the plate interface, a broader understanding of the structure of the subduction zone, including the upper plate, is still necessary. The overriding plate can be separated into three main domains: the fore-arc, the volcanic arc and the back arc. The fore-arc is the region between the trench and the volcanic arc, and can experience deformation or seismic activity due to the tectonic forces acting on the margin. One component of subduction that can affect the deformation of the fore-arc is the obliquity of the subduction relative to the trench axis. The most common result of subduction obliquity is the partial decoupling between the trench-parallel and trench-perpendicular components of motion (Demets, 1995; Fitch, 1972). The strain is partitioned into a compressional component, that is in large part accommodated by seismic slip at the megathrust interface, and a shear component, that is mostly accommodated by slip on trench-parallel strike-slip faults in the overriding plate. Such a partitioning requires the presence of a weak zone in the overriding plate, as well as the mechanical coupling of the two plates (Chemenda et al., 2000). When the two plates cannot slip past each other freely, the subducting plate drags the forearc in the direction of convergence (Chemenda et al., 2000). This trench-parallel motion can lead to the creation and lateral displacement of a forearc sliver independent of the upper plate. These two models are illustrated in Figure 3.

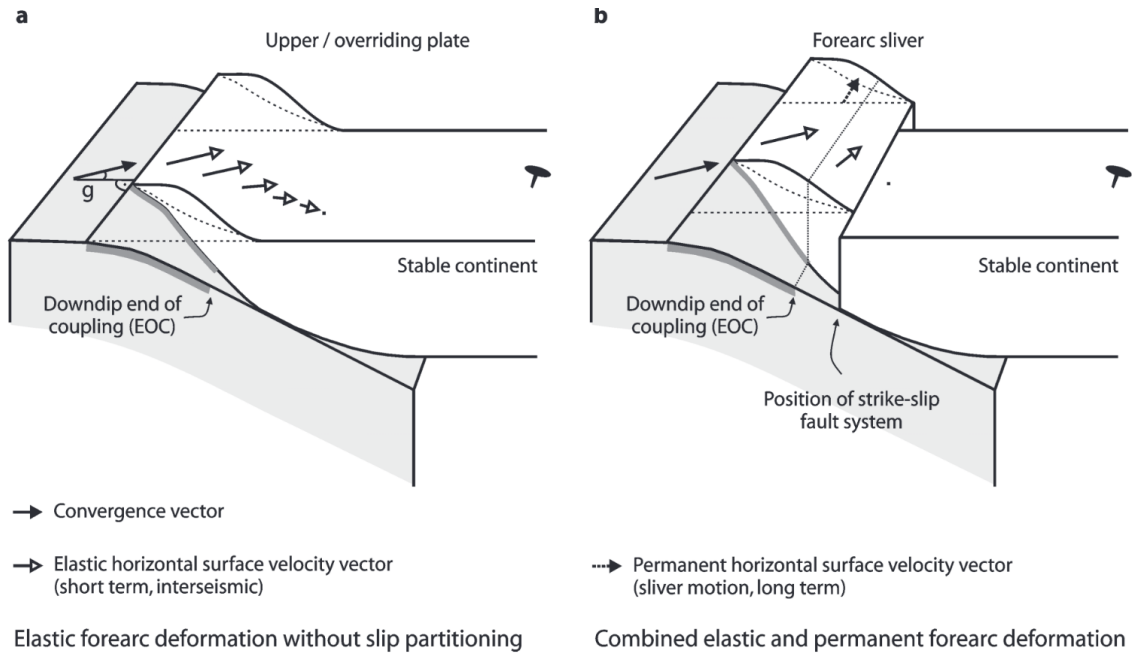

Figure 3 : Cartoon showing the expected horizontal deformation of the forearc in an oblique subduction context by Hoffmann-Rothe et al. (2006). A: No strain partitioning occurs as the leading edge of the overriding plate is dragged along

its coupled portion in the direction of the subduction. B: Strain partitioning occurs as a forearc sliver moves parallel to the trench independently from the rest of the overriding plate.

The rest of the upper plate is composed of the volcanic arc and, beyond it, the back-arc. The volcanic arc corresponds to a topographic high, due to the erupted material and sometimes to the formation of mountains due to compressive forces, and a crustal thickening associated to magma underplating. Behind the volcanic arc is the back-arc region, which can experience extension or compression, depending on the geometry of the slab, its dip angle and its possible forward or backward migration (Heuret, 2005). Extension in the back-arc may result in rifting and seafloor spreading, while compression will result in folding and thrusting.

I have given a general description of the subduction process, but in reality it varies between subduction zones depending on properties of the incoming slab and the upper plate. One important property is the slab geometry, which itself depends on the density of the incoming plate and on the geometry of the plate boundary. As such, the slab dip is affected by the age and thermal state of the oceanic lithosphere, and can also be flattened by the subduction of buoyant material like ridges. The angle of the slab controls not only the position of the volcanic arc in the overriding plate (Jarrard, 1986), but the very presence of volcanism and seismicity. A shallow slab, otherwise known as a flat slab, can cause a decrease in seismic activity and even an end to volcanic activity.

Having given a brief overview of the subduction process, I will now proceed to introduce concepts related to friction and slip, which are essential to better understand what occurs at the plate interface.

1.2 Friction and modes of slip

Faults are planes of weakness within a rock body where slip can occur. In this section, I will explain how friction works on a fault, and introduce the various kinds of slip that can result from it.

Our understanding of friction is guided in large part by analog experiments and modelling. In the lab, a fault is typically modelled as a sliding block pulled by a spring of known stiffness (Figure 4). As shear stress is gradually applied to the block, it begins to slide when the ratio of shear stress to normal stress reaches the static friction coefficient. Then, while moving, the sliding resistance changes to the dynamic friction coefficient. This behavior is often modelled using the rate and state friction law, which describes both the static and dynamic friction. Static friction is defined as the friction coefficient while the block remains unmoving (Marone, 1998).

It increases slowly with the logarithm of the contact time, as the surface contact creeps slightly, helping the two sides of the fault to adjust to each other and thus increasing the contact area (Scholz, 1998). Meanwhile, dynamic friction is defined as the friction coefficient while the block is sliding at a steady state, and is dependent on the sliding velocity (Marone, 1998).

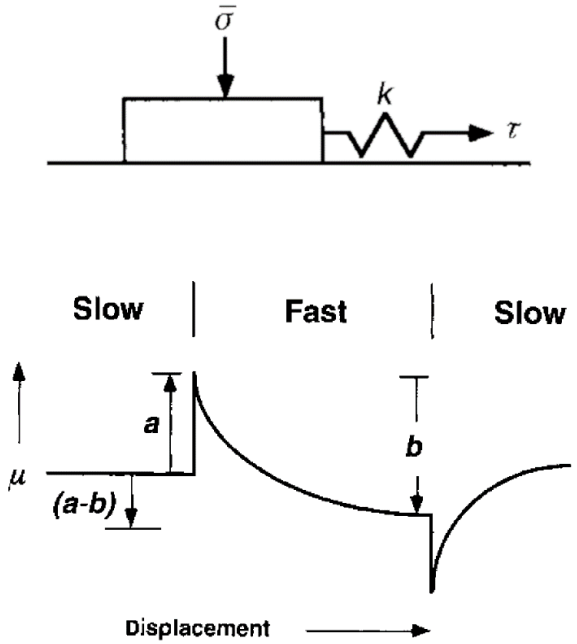

Figure 4 :Block-slider model and slip behavior from Scholz (1998). The top panel is a diagram of a sliding block, pulled by a string of stiffness k. The shear and normal stresses acting on the block are expressed as τ and $\bar{\sigma}$. The bottom panel shows a schematic diagram of the evolution of friction as a function of the displacement of the block.

The law used to describe friction is the Dietrich-Ruina law, expressed as:

$$\tau = \left[\mu_0 + a \ln\left(\frac{V}{V_0}\right) + b \ln\left(\frac{V_0\theta}{L}\right)\right]\bar{\sigma}$$

Where τ is the shear stress and $\bar{\sigma}$ is the effective normal stress. V is the slip velocity while V_0 is the reference velocity, and μ_0 is the steady state friction coefficient when $V = V_0$. L is the critical slip distance, often interpreted as the sliding distance required to renew contacts, or the friction breakdown distance, and a and b are material properties (Marone, 1998). The state variable θ evolves as:

$$\frac{d\theta}{dt} = 1 - \frac{\theta V}{L}$$

This means that at a steady state when $d\theta/dt = 0$, then:

$$\tau = \left[\mu_0 + (a-b)\ln\left(\frac{V}{V_0}\right)\right]\bar{\sigma}$$

Since the dynamic coefficient of friction μ_d is defined as the steady-state friction at velocity V, then $d\mu_d/d\ln(\mathrm{V}) = a - b$. Meanwhile, the coefficient of friction μ_s is the starting friction after a time t of stationary contact, and so for a long t, $d\mu_s/d\ln(\mathrm{t}) = b$. The significance of these different parameters is illustrated in Figure 4.

The sliding is governed by the friction rate parameter a-b, as well as by the critical slip L (Marone, 1998). L controls the size of the rupture nucleation, the scale over which precursory changes in physical properties is expected, the magnitude of pre and postseismic slip and the length scale over which dynamic stress is concentrated at the front of the propagating rupture (Marone, 1998). Meanwhile, a-b determines the stability of the sliding. If a-b <0, the fault is called velocity-weakening and exhibits unstable sliding, meaning that earthquakes can nucleate in the region (Scholz, 1998). If a-b is negative but close to 0, the slip will instead be conditionally stable, and earthquakes will not be able to nucleate in the region, but may be able to propagate inside it (Scholz, 1998). Finally, if a-b >0, the fault is velocity-strengthening and therefore stable. Stable regions are able to stop earthquake rupture propagation, as they cannot accumulate stress (Scholz, 1998). Whether a-b is positive or negative depends on temperature, rock type, the presence of fault gouge, and the geometry of the fault among other parameters.

In reality, faults are complex and heterogeneous, and therefore do not have a uniform a-b. Instead, the fault surface is divided into barriers and asperities. Asperities are defined as areas of nearly full locking comprised of clustered rate-weakening patches where large slip occurs during earthquakes, and on the opposite end, barriers are areas that prevent the propagation of rupture (Avouac, 2015). Barriers are not necessarily fixed in the seismic cycle, as while they can be regions without accumulated stress, barriers can also be regions with higher friction, unable to break in small or medium-sized earthquakes.

Due to these variations in frictional properties, three main types of slip can occur on a fault: stick-slip, creep and transient slow slip. The first type of slip is stick-slip, as happens during an earthquake. This is a sudden and fast slip that releases the accumulated strain in large part as seismic energy. The name, stick-slip, comes from the dual behavior of the fault. Between earthquakes, movement on a fault is partially or fully blocked, leading to an accumulation of stress. Once the strength threshold of the material is reached, the fault breaks into an earthquake. This forms a cycle called the seismic cycle, which describes the behavior of the fault between successive earthquakes. The seismic cycle comprises four stages. The first stage is the interseismic period, during which the fault is loaded by tectonic forces. Then comes the preseismic period, during which the slip accelerates until the instability results in coseismic motion in a process known as earthquake nucleation. Often, nucleation occurs at the edge of a velocity-weakening patch (Avouac, 2015). This leads to the coseismic period, during which

rupture propagates. While rupture occurs primarily in velocity-weakening patches, it can sometimes propagate briefly into stable regions between asperities, possibly leading to the rupture of several different asperities (Avouac, 2015). The final extent of the rupture is dependent on the stress distribution on the fault, and on the amount of energy spent propagating through rate-strengthening areas (Avouac, 2015). Finally, after the earthquake, we enter the postseismic period, during which the stress is relaxed through aftershocks and afterslip. Long recurrence times tend to lead to a larger amount of energy stored during the interseismic period, and therefore to large earthquakes

The size of an earthquake is quantified by its magnitude, which can be measured in several ways. Local magnitude scales have been used since the early 20th century to describe an earthquake, with the most famous being the Richter magnitude scale. This non-dimensional scale uses the amplitude of displacement on a seismogram to describe the earthquake itself, but has no direct physical link to the source process. To remedy this, the moment magnitude scale was introduced, based on the seismic moment of the earthquake (Hanks and Kanamori, 1979). Seismic moment is a physical quantity, calculated as $M_0 = \mu DA$ with μ the shear modulus of the medium, D the mean displacement during the earthquake and A the total area of the rupture, and measured using the low-frequency energy of the earthquake's displacement spectrum. From this, Hanks and Kanamori (1979) derived the moment magnitude $M_w = \frac{2}{3}(\log_{10}(M_0) - 9.1)$.

Earthquakes are not the only type of intermittent slip to occur on a fault. Over the last few decades, the existence of slow slip events (SSEs) has become well-documented. Slow slip events differ from regular earthquakes in a few important ways. The first is that they do not themselves radiate seismic energy (i.e. seismic waves), although they can be associated with low-frequency signals or tremor signatures (Peng and Gomberg, 2010). They can also trigger swarms of microseismic events by activating asperities embedded within or at the edge of the slow slip region. The second characteristic of SSEs is that, while earthquakes last seconds to minutes, SSEs can last days to years (Peng and Gomberg, 2010). They also often have small displacements of up to 10s of centimeters, compared to their slip area. This leads to a broad separation between slow and fast earthquakes with regards to the relationship between the event duration and its moment (Ide et al., 2007). This separation is illustrated in Figure 5. These differences between earthquakes and SSEs are rooted in the different frictional properties of the fault portions that host them. SSEs typically occur in conditionally stable areas where a-b is close to 0, at the transition between areas that favor seismic slip and areas that favor aseismic creep (Saffer and Wallace, 2015). That said, the reasons these regions are conditionally stable, and the mechanisms triggering SSEs, are not all fully understood. This transitional state can be the result of rock frictional properties which promote transient aseismic slip (Den Hartog et al., 2012; Ikari et al., 2013) or of low effective stress linked to high fluid pressure (Saffer and

Wallace, 2015). The latter is supported by models and observations of near-lithostatic pore fluid pressure driving deep slow slip events (Audet et al., 2009; Liu and Rice, 2007; Shelly et al., 2006; Song et al., 2009). In fact, some authors have proposed that SSEs are part of a cycle of fluid circulation. In this model, pressure builds up as fluids are trapped in the slab and interface, until the fracturing of the interface releases them, triggering slow slip. After this, the plate boundary is sealed again by subsequent precipitation of minerals (Audet et al., 2009; Warren-Smith et al., 2019). This is however not the only way that slow slip events can be triggered. They can also occur as a result of earthquakes occurring nearby (Liu and Rice, 2007), as static stress changes have been found to hasten or delay periodic SSEs (Hirose et al., 2012). Dynamic stress changes from large earthquakes, even hundreds of kilometers away, can also trigger SSEs (Araki et al., 2017; Wallace et al., 2017). This is likely most effective for shallow SSEs due to surface wave amplitudes (which are the largest signal) decaying with depth, and due to the sedimentary wedge potentially trapping and amplifying seismic energy (Wallace et al., 2017). Finally, some authors have invoked climate- driven stress perturbations as a potential explanation of the periodicity of some SSEs (Lowry, 2006).

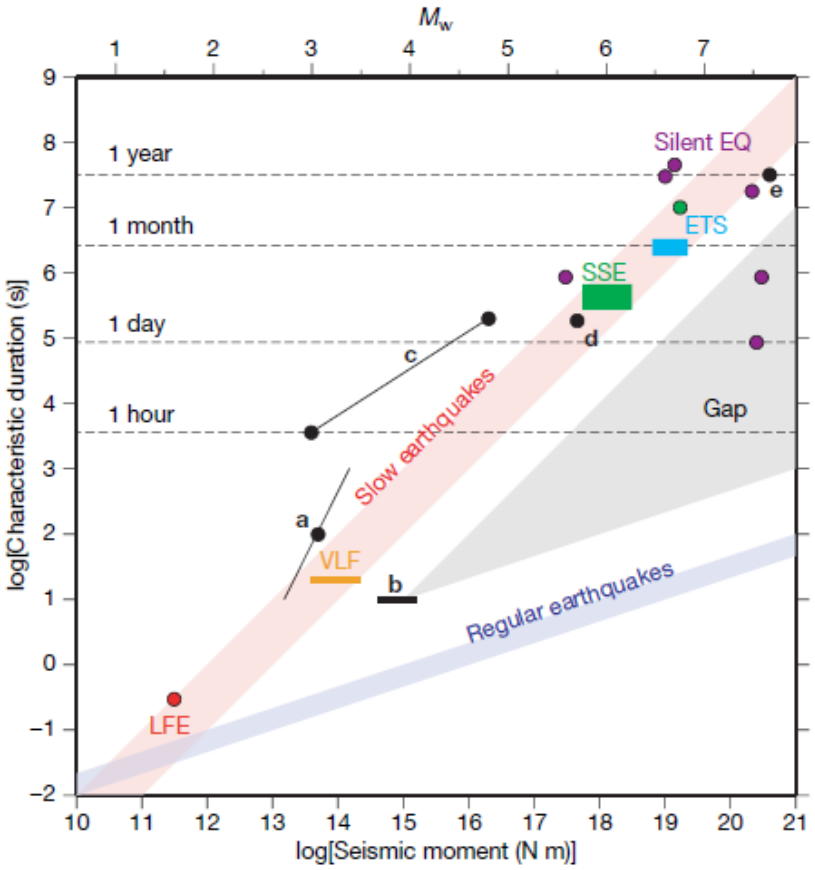

Figure 5 : Duration Vs seismic moment of different types of earthquakes and slip, by Ide et al. (2007). LFEs, VLFEs and SSEs shown in this figure occur in the Nankai trouh, while ETS occur in the Cascadia subduction zone.

The last type of slip is similar to SSEs in that it is slow and aseismic. Creep is defined as stable aseismic slip, which, unlike the previous two types of deformation, does not involve any accumulation of strain. It occurs in stable regions where a-b > 0, often at depth. Several explanations have been proposed for the existence of such aseismic slip (Avouac, 2015). One is the presence of minerals like serpentinite, talc or particular types of clay in the fault gouge, as those are easily deformable. Another is a stable supply of fluids, especially CO_2 of metamorphic or volcanic origin, as high pore pressures decrease the normal stress on a fault and thus promote creep (Avouac, 2015). Additionally, at large depths the high temperature prevents seismic slip at the plate interface

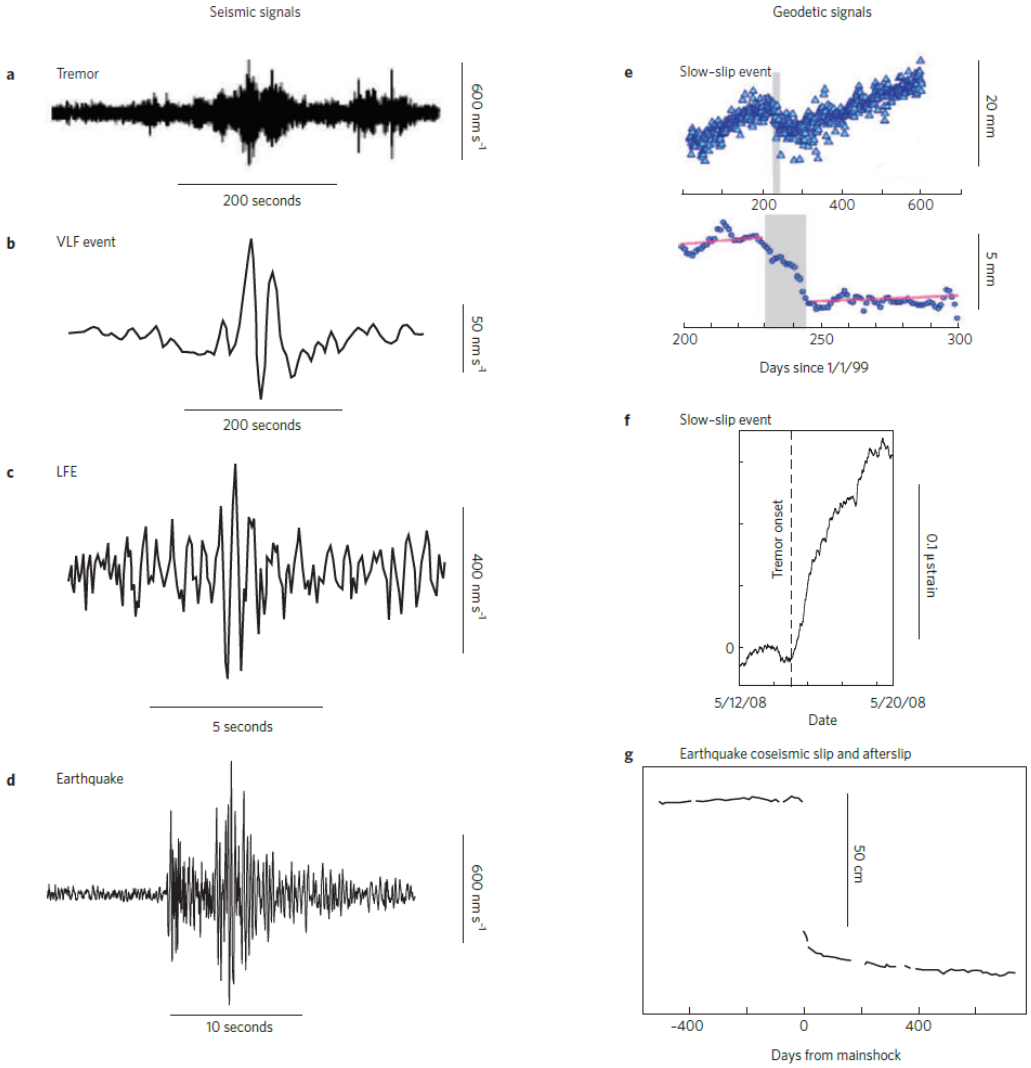

Figure 6 : Examples of seismic and geodetic signals by Peng and Gomberg (2010). A: Tremor seismic signal. B: Very Low Frequency Earthquake seismic signal. C: Low Frequency Earthquake seismic signal. D: Regular earthquake seismic signal. E and F: Slow Slip Event geodetic signal. G: Earthquake coseismic slip and afterslip geodetic signal.

While the three modes of slip introduced above involve different frictional properties, they are often adjacent and frequently interact through stress transfers. One example of these interactions is the range of seismic signals that occur concurrently with slow slip and creep (Peng and Gomberg, 2010). SSEs are often accompanied by low-frequency earthquakes (LFEs), which typically have source durations of under 1s, and very low-frequency earthquakes (VLFEs), which tend to have source durations of several tens of seconds (Figure 6) (Peng and Gomberg, 2010). Additionally, seismologists have identified non-volcanic tremors occurring around SSE regions, which are defined as weak continuous vibrations with no clear impulsive phase, and which themselves contain LFE and VLFE signals (Peng and Gomberg, 2010). Because tremors and deep SSEs very frequently occur together, the joint phenomenon has been given the name of episodic tremor and slip (ETS) (Peng and Gomberg, 2010; Rogers and Dragbert, 2003). Both tremors and VLFEs have durations that scale with seismic moment in a way that is similar to slow earthquakes, rather than regular events (Figure 5). Other types of seismicity have been found to accompany both SSEs and creep. This includes repeating earthquakes, defined as earthquakes that occur repeatedly on the same asperity. More broadly, slow slip is often linked to increased rate of microseismicity (Hirose et al., 2012). This seismicity can organize into clusters of earthquakes with no obvious mainshock known as seismic swarms (Hirose et al., 2012; Reyners and Bannister, 2007). However, when seismicity and slow slip occur together, the event is only considered an SSE if the moment released by the aseismic slip is larger than the moment released by the seismic slip. When the reverse occurs, the categorization of the slow slip becomes different. In particular, transient slow slip can occur after a large earthquake, in which case it is called afterslip. Afterslip is driven by coseismic deficit, meaning it occurs away from the rupture as a direct response to a large earthquake (Marone, 1998). It is the relaxation of the stress accumulated in velocity-strengthening regions as a result of the rupture's inability to propagate there (Marone, 1998). Afterslip has a different time evolution to SSEs as a result of the difference in trigger mechanisms. Instead of initiating slowly, afterslip instead has a fast slip rate at the start that decays with the logarithm of time over days to years (Avouac, 2015). The process can itself influence the aftershock sequence, controlling its spatial extent or the daily rate of aftershocks (Perfettini and Avouac, 2004). Although afterslip is the most commonly observed interaction between large earthquakes and aseismic slip, slow transients have also been observed before the mainshock, in particular for the 2011 Mw 9.0 Tohoku earthquake (Kato et al., 2012) and the 2014 Mw 8.1 Iquique earthquake (Kato and Nakagawa, 2014; Socquet et al., 2017). These aseismic transients are thought to be part of the nucleation process, unlocking a portion of the fault before the main rupture.

These different types of slip are all found within subduction zones, and I will now delve further into the way subduction is segmented with regards to seismicity and slip.

1.3 Slip and coupling in subduction zones

There are several contexts within a subduction zone where earthquakes and slow slip can occur. Intraplate earthquakes for example can occur in the slab due to the plate bending, or in the forearc and the accretionary wedge, especially when topographic features enter subduction. However, in my thesis, I will focus specifically on slip occurring at shallow depths and usually at the plate interface.

To understand the distribution of asperities on the plate interface, we can measure the coupling between the two plates. This refers to the large-scale strain accumulation occurring at the megathrust. Slightly different types of coupling exist, referring to the different ways of calculating it (Avouac, 2015). The seismic coupling is defined as the seismic slip / the total long-term slip occurring on a fault patch, or as the total seismic moment released / the total moment calculated based on the plate velocity. Accurately calculating seismic coupling requires observation of the fault over several seismic cycles, which is often impossible considering that the seismic instrumental period is only about a century old. Another type of coupling is aseismic coupling, and refers to the amount of slip released by aseismic transients (afterslip and SSEs) / the total long-term slip (Avouac, 2015). Added together, they are equal to the interseismic coupling, or the total deficit of slip during the interseismic period / the total long-term slip. This value is expressed between 0 and 1, with 0 corresponding to an entirely decoupled creeping fault with no strain accumulation and 1 to a completely locked fault only able to release energy through large earthquakes. Interseismic coupling can be obtained by geodesy and does not necessitate centuries of records, making it much less sensitive to catalogue completeness. Instead, it is modelled using the interseismic acceleration transmitted to the upper plate and detected at the surface. When a segment is coupled, the motion of the slab causes compression in the upper plate, which deforms elastically in both the horizontal and vertical directions. With an adequately dense GPS network, a good approximation of the plate interface geometry and accurate physical properties for the plate, the interseismic coupling can then be recovered. In subduction zones however, owing to the frequent absence of instrumentation at sea, the coupling is always less well resolved near the trench than it is under land.

Interseismic coupling at a subduction zone varies both laterally and with depth, as is schematically shown in Figure 7. All subduction zones are segmented with depth, usually in similar ways. Near the trench, the megathrust is usually velocity-strengthening or conditionally stable (Wang and Tréhu, 2016). However, so-called tsunami earthquakes can occur in this region, defined as earthquakes with a slow rupture but an anomalously large tsunamigenic effect relative to their magnitude, which are thought to rupture the interplate primarily in conditionally

stable regions at shallow depths (Bilek and Lay, 2002). Below this shallow portion of the megathrust sits the seismogenic zone, an area that exhibits stick-slip behavior and where earthquakes can therefore nucleate (Wang and Tréhu, 2016). The exact definition of the seismogenic zone differs between papers, and can be seen as the region where large earthquakes occur, the velocity-weakening region, the region where any earthquakes can nucleate, or the geodetically determined locked zone (Wang and Tréhu, 2016). In any case, viewing it as uniformly earthquake-prone is a mistake, as there is a lot of lateral variation in slip behavior within the seismogenic zone (Figure 7). The downdip edge of the seismogenic zone, meanwhile, is controlled by the thermally-regulated rheology of the rocks, although the exact temperature at which it occurs is difficult to determine as various materials could be responsible for earthquake nucleation (Wang and Tréhu, 2016). Below this point is another velocity-strengthening or conditionally stable region. This segmentation in depth is summarized in Figure 8.

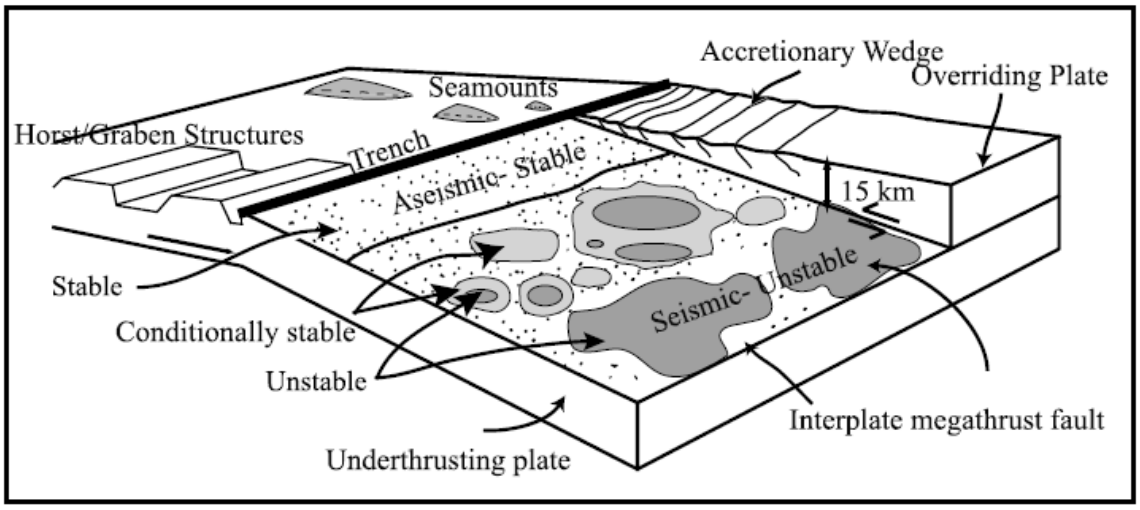

Figure 7 : Schematic cartoon of a subduction zone by Lay and Schwartz (2004).

Slow slip events can occur in both the shallow and deep portions of the megathrust. Deep SSEs are particularly well documented, especially in the Cascadia subduction zone in North America (Wang and Tréhu, 2016) and in southwest Japan (Obara et al., 2004). Deep SSEs are often instances of episodic tremor and slip (ETS), as they are usually accompanied by tremors, LFEs or VLFEs. ETS can occur at the boundary of seismogenic zone, or further downdip, with a gap between seismogenic zone and ETS zone (Wang and Tréhu, 2016). In this area, fluids are likely supplied by the dehydration of the oceanic crust, or episodes of metamorphic fluid release (Liu and Rice, 2007). It is still debated whether SSEs happen in contact with the mantle wedge, and if so, what role it plays (Wang and Tréhu, 2016). The serpentinized mantle and high fluid

pressures could help cause ETS, giving rise to a second conditionally stable region and explaining the gap sometimes present between the seismogenic zone and the deep SSE region. But in some regions, it seems that the ETS zone is landward (Japan) or seaward (Cascadia) of mantle wedge, making its role contested (Wang and Tréhu, 2016).

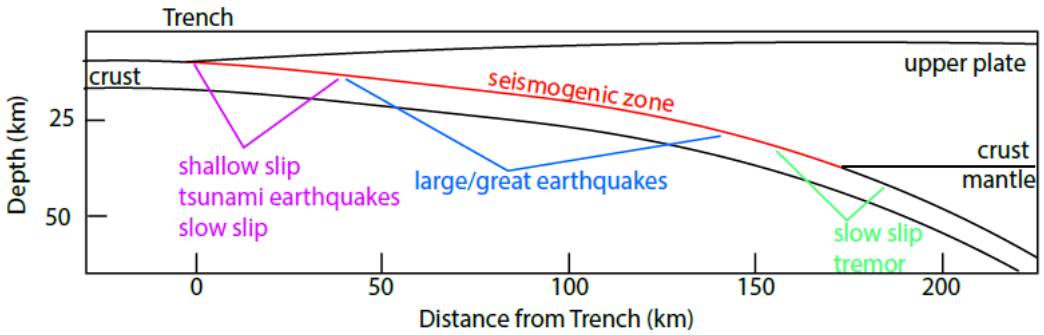

Figure 8 : Schematic segmentation of subduction zones in depth from Bilek and Lay (2018). It should be noted that in some cases large earthquakes can extend under the mantle wedge, below the Moho of the overriding plate (Dessa et al., 2009).

Shallow SSEs have also been observed in regions like the Hikurangi subduction in New Zealand (Wallace et al., 2016), the Costa Rican margin (Saffer and Wallace, 2015) or the Ecuadorian margin (Vaca et al., 2018). Compared to their deep counterparts, they tend to be of shorter duration and are more often accompanied by microseismicity and seismic swarms (Saffer and Wallace, 2015). Although their location is different, shallow SSEs, like deep ones, are often associated with fluids, here supplied by the compaction of marine sediments rather than metamorphism (Bürgmann, 2018; Saffer and Wallace, 2015). Some shallow SSEs lie within the seismogenic depth range, while others occur within regions dominated by interseismic creep. This variability is in part explained by the basement relief on the oncoming plate leading in some cases to heterogeneous frictional properties prone to seismic and aseismic slip (Saffer and Wallace, 2015). Due to this, some authors posit that SSEs may in fact be the result of brittle and ductile processes combining at the macroscopic level into slow slip (Saffer and Wallace, 2015; Wang and Bilek, 2014). In fact, some authors suggest that the frictional, rheological and geometrical complexity of the megathrust itself may be enough to generate large-scale slow slip (Barnes et al., 2020; Skarbek et al., 2012).

As mentioned, the structure of the subducting plate can significantly affect the frictional properties of the megathrust. Subducting bathymetric features can segment a subduction zone and therefore influence individual earthquake ruptures (Bilek, 2010). Similarly, sediments and fracture zones influence the subduction and the rupture type for a given portion of the megathrust (Bilek, 2010). Generally, the subduction of rugged seafloor tends to lead to creep rather than large subduction earthquakes (Wang and Bilek, 2014). This is because rugged

seafloor impedes shear localization and promotes a heterogeneous stress field. This causes creep from broad deformation, as well as transient slip and small to medium sized earthquakes (Wang and Bilek, 2014). On the other hand, large megathrust earthquakes like the Tohoku earthquake usually occur on smooth subducting plate (Wang and Bilek, 2014). This is not a hard rule however, as some examples of large earthquakes occurring in the vicinity of subducted seamounts exist (Abercrombie et al., 2001; Husen et al., 2002). It seems instead that depending on context a seamount could act as either an asperity or a barrier to rupture (Yang et al., 2012). This is because seamounts in particular affect the stress field significantly. At their leading edge, compression is enhanced, which increases the normal stress and yield strength, favors the development of faults in the upper plate, and induces a rotation in principal-stress orientation (Sun et al., 2020). This increases drainage through upper plate faults and leads to sediment overconsolidation and very low porosity (Sun et al., 2020). On the other hand, behind the seamount a stress shadow is formed, accompanied by high porosity and an underconsolidation of sediments. Thus the increased fault strength at the leading edge of the seamount encourages seismic slip, and the upper plate above the seamount tends to experience a lot of small earthquakes, while behind the seamount the low fault strength promotes stable sliding (Sun et al., 2020).

I have now introduced the main types of slip found in subduction zones, and the way they relate to each other. I will now focus specifically on repeating seismicity, its various uses, and its relationship to aseismic slip.

1.4 Repeating earthquakes

Repeating earthquakes or repeaters, are earthquakes with similar waveforms, identical locations and identical focal mechanisms that occur repeatedly at different times, as shown in Figure 9 (Nadeau et al., 1994; Nadeau and Johnson, 1998). They are interpreted as events that rupture the same asperity multiple times, with the same focal mechanism. During the interseismic period, repeating earthquake families can be separated into two categories: quasiperiodic families that occur at regular time intervals and burst-type families that occur very close together (Igarashi et al., 2003). The latter are often not real repeaters, but rather the result of neighboring asperities rupturing without overlap, later incorrectly classified as repeaters (K. H. Chen et al., 2016; Lengliné and Marsan, 2009). True repeaters are generally thought to occur on velocity-weakening asperities embedded within creeping or slowly slipping regions, and therefore being consistently loaded by the surrounding aseismic slip, as Figure 10 illustrates. This allows them to act as creep-meters and to illuminate the spatio-temporal

distribution of slow-slip. Additionally, repeating earthquakes are useful as tools to study other features of interest, like the velocity structure of the medium.

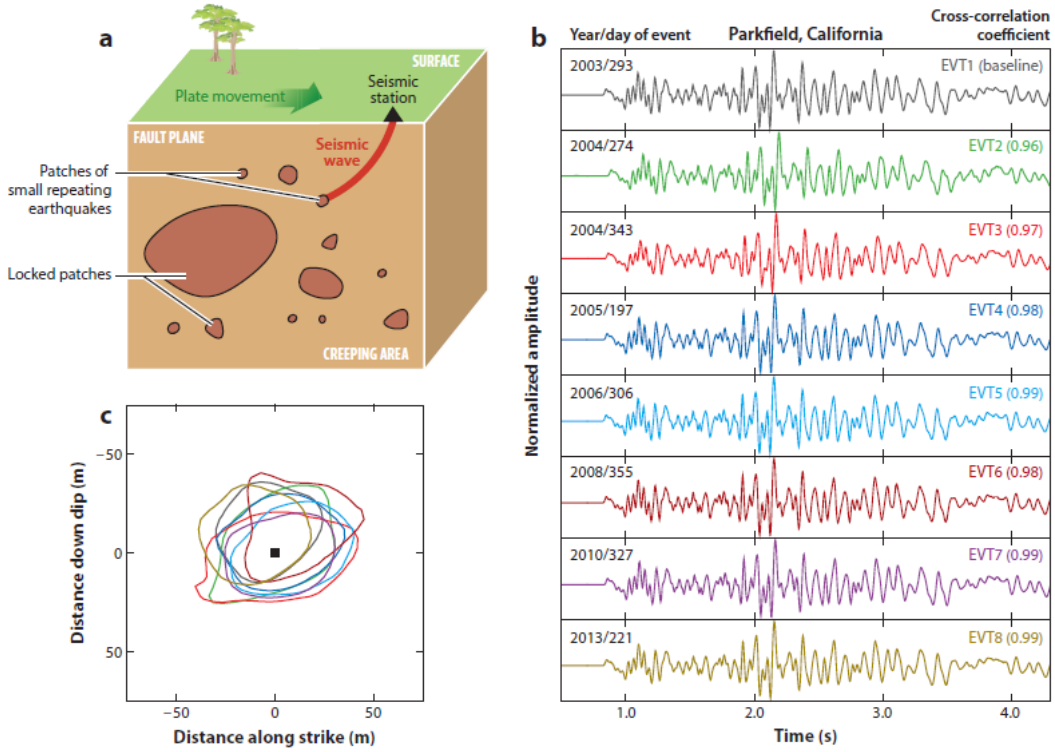

Figure 9 : Examples of repeating earthquakes in Parkfield, California, in the context of a strike-slip fault, by (Uchida and Bürgmann, 2019). A: schematic diagram of the fault surface, with creeping portions and asperities where repeaters occur. B: Waveforms of one family or repeating earthquakes. C: Overlapping peak slip areas of repeating earthquakes

Because repeaters are useful tools, care must be taken in detecting them, both to avoid misclassifying regular earthquakes, and to ensure that repeating earthquake families are complete. The identification of repeaters rests on two main parameters (Uchida, 2019). The first is the overlap between the earthquake sources, since repeaters occur on the same asperity. This method requires very accurate hypocenters and source size estimates, which themselves cannot be obtained without a very good station coverage. The second parameter used to classify repeating earthquakes is the waveform similarity, usually quantified by a correlation coefficient above 0.9 or a coherency above 0.95 (Uchida, 2019). The shape of the waveform is affected by the volume it traverses (the Fresnel zone along the ray path), itself dependent on wavelength, and so differences in travel path inevitably lead to a decrease in the waveform similarity. It is often assumed that if the propagation path differs by more than the wavelength/4, then the correlation coefficient decreases significantly (Uchida and Bürgmann, 2019). However, an inherent issue with the reliance on this parameter is that it is dependent on the frequency band

examined, as well as on the time window and the threshold coefficient used. This is why authors usually use both location and waveform similarity together when possible.

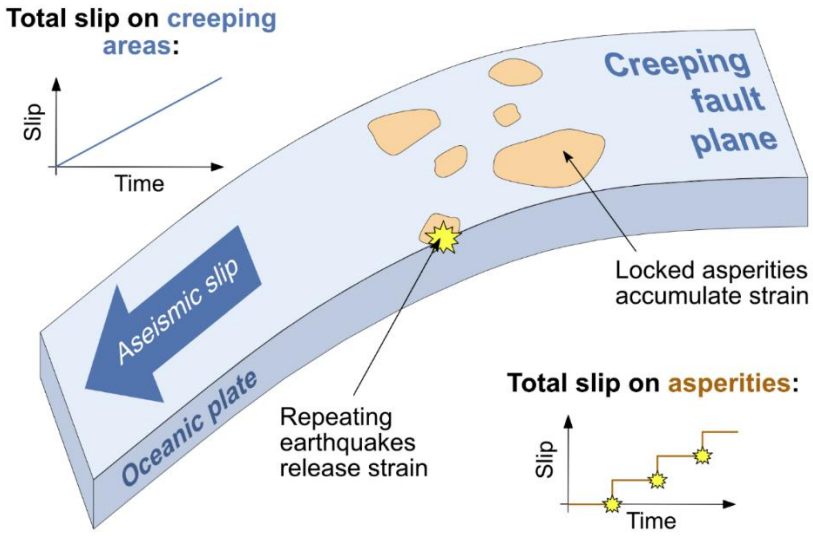

Figure 10 : Cartoon representation of the mechanism driving repeating earthquakes. Asperities are embedded in a creeping fault and accumulate strain with time. At regular intervals, the asperity fails and releases this strain. A relationship can be found between the creep of the fault, and the slip of repeating earthquakes embedded in it, allowing repeaters to act as creep-meters (Nadeau and Johnson, 1998).

Repeating earthquakes have been detected around the world in a variety of tectonic and non-tectonic settings (Uchida and Bürgmann, 2019). Usually, they occur where microseismicity is abundant (Kawamura and Chen, 2017) and are anticorrelated with large rupture zones (Meng et al., 2015). Often, creep, afterslip or SSEs are detected concurrently with repeating earthquakes. Throughout these different contexts, there still are similarities between repeaters around the world. Nadeau and Johnson (1998) found in California an unexpected scaling relationship between the moments and recurrence times of quasiperiodic repeating earthquake families, where $T_r \propto {M_0}^{1/6}$. This relationship was found to hold true in other regions around the globe, proving that there is a common mechanism controlling all repeaters (K. H. Chen et al., 2007). This went against expectations, as for a constant stress drop on an asperity releasing all its energy seismically, we would expect that $T_r \propto {M_0}^{1/3}$. The observed relationship instead indicates either that stress drops are larger for smaller repeaters, which is not supported by observation, or that the slip occurring on the asperity is in part aseismic (Beeler et al., 2001). In that case, asperities producing smaller-magnitude earthquakes experience more aseismic slip than asperities producing larger-magnitude earthquakes (Beeler et al., 2001).

Although repeaters are largely driven by aseismic slip, they are still affected by neighboring seismic activity (K. H. Chen et al., 2013; K. H. Chen, Bürgmann and Nadeau, 2010). Small repeating earthquakes can be triggered by neighboring Mw4-5 earthquakes (K. H. Chen, Bürgmann and Nadeau, 2010) or even by smaller earthquakes (K. H. Chen et al., 2013), with the triggering distance being largely dependent on magnitude (K. H. Chen, Bürgmann and Nadeau, 2010). Meanwhile, large earthquakes and their afterslip can significantly affect the recurrence times, seismic moments and stress drops of repeating earthquakes. After a big earthquake, recurrence times decrease, then gradually increase following Omori's law (Lengliné and Marsan, 2009; Schaff et al., 1998). The change in seismic moment is less consistent, as sometimes a large earthquake causes an increase and sometimes a decrease (K. H. Chen, Bürgmann, Nadeau, et al., 2010; Peng et al., 2005). This is because, on the one hand, some repeaters' slip area increases after a large earthquake as a result of the faster loading, in a process called transient embrittlement. However, the smaller recurrence times also reduce the static coefficient of friction of the locked portion of the patch, and the faster slip on the creeping portions of the velocity-weakening patch decreases the shear stress. This leads to a smaller stress drop and smaller coseismic displacement (K. H. Chen, Bürgmann, Nadeau, et al., 2010). The evolution of seismic moment after a mainshock depends on which of these two processes is dominant. For small repeaters occurring within a larger asperity, the velocity-weakening patch tends to experience mostly aseismic slip, with a small amount of seismic slip at the center where the stress concentrates (K. H. Chen, Bürgmann, Nadeau, et al., 2010). Under faster loading, the stress concentration at the center increases, leading to the rupture area increasing in size (K. H. Chen, Bürgmann, Nadeau, et al., 2010). However, for larger repeaters that span the entire velocity-weakening patch, the rupture size remains the same after the mainshock (K. H. Chen, Bürgmann, Nadeau, et al., 2010). Both of the processes described have been observed for repeating earthquake sequences (Abercrombie, 2014; Chaves et al., 2020; Uchida et al., 2015). It is worth noting that, sometimes, repeating earthquake sequences can also appear or disappear after the mainshock, which may be related to these processes (Hatakeyama et al., 2017; Lengliné and Marsan, 2009).

I have now introduced the different modes of slip present in subduction zones, and have explained the main characteristics and uses of repeating earthquakes. The latter will be the focus of my work in the Ecuador-Colombia subduction zone, which I will now introduce in more detail.

Chapter 2: The Ecuadorian subduction

Having given an overview of subduction as a general process, I will now introduce the specificities of the Ecuadorian subduction zone, and the way that they affect its seismic behavior. I will start on the larger scale by discussing the geodynamic setting of Ecuador. This will be followed by an overview of the main features of the upper and lower plate and the plate interface, in which I will discuss the way these structures potentially affect seismicity in the region. Finally, I will properly detail the history of seismic and aseismic slip in the region, focusing specifically on the megathrust.

2.1 Geodynamic setting

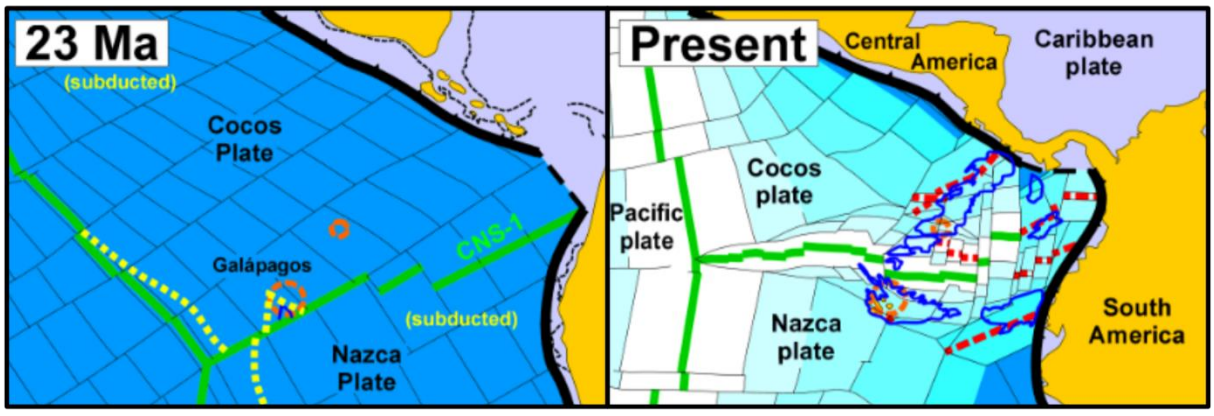

Figure 11 : Breakup of the Farallon plate into the Nazca, Cocos and Pacific plates, modified from Meschede and Barckhausen (2000). The dotted yellow line on the left is the outline of the present subduction zone. Green and dashed red lines are the active and abandoned mid-ocean ridges respectively. The outline of the Cocos, Malpelo and Carnegie ridges are shown in dark blue in the final figure, while the Galapagos hotspot is shown as an orange dotted circle.

To understand the dynamics of the subduction zone in Ecuador, it is useful to place it in the regional geodynamic context of the last 23 Ma. The Nazca oceanic plate is subducting under the South American plate in the N83E direction at a speed of 56 mm/year along the Ecuadorian margin (Nocquet et al., 2009). Along with the Cocos plate in the north, it is the result of the Farallon plate breakup in the early Miocene (Lonsdale and Klitgord, 1978), as shown in Figure 11. Nazca subduction started in the early Miocene and stabilized in the late Miocene once the Panama basin spreading center became extinct (Yepes et al., 2016). During that time, the basin

was home to active spreading ridges offset by transform faults, some of which are still visible today. As such, the Nazca plate is composed of both the old Farallon lithosphere, and the young Nazca lithosphere newly created at the Cocos-Nazca spreading center over the last 23 Ma (Lonsdale, 2005). The separation between these two crusts occurs at the Grijalva ridge in the South of Ecuador, outlined by a 500 m step in the bathymetry caused by the density contrast between the younger Nazca lithosphere in the North and the older Farallon lithosphere in the South.

Spreading at the Cocos-Nazca spreading center is affectated by the Galapagos hotspot, which generates the thickened oceanic crust of the Carnegie, Cocos and Malpelo Ridges (Sallarès et al., 2003, 2005; Sallarès and Charvis, 2003).

The Nazca plate meets the South American plate at a very long, convex subduction zone (Figure 12). In fact, in the Ecuadorian and Peruvian regions, the obliquity of the subduction changes by 60° between 2°N and 8°S (Yepes et al., 2016). In particular, convergence gradually increases from perpendicular to the trench at 5°S to a maximum obliquity of about 35° at 2°N (Yepes et al., 2016). The shape of the plate boundary impacts the geometry and stress field of the slab, bending the slab towards a focal point (Yepes et al., 2016). Additionally, the strain partitioning resulting from the subduction leads to the movement of two forearc slivers, the northbound North Andean Sliver in Ecuador and the southbound Inca Sliver in Peru (Nocquet et al., 2014).

The North Andean sliver (NAS) is the 300-400 km wide, 1500 km long forearc sliver that encompasses the Andes from Western Venezuela to Ecuador, moving with a velocity of 7.5 - 9.5 mm/year towards the Northeast relative to the South American plate (Nocquet et al., 2014). Its southern boundary is in the Gulf of Guayaquil, which sits almost at the point where convergence changes obliquity (Figure 12). The diverging motion between the North Andean and the Inca Sliver in the region causes extension, crustal thinning and the opening of the Gulf of Guayaquil (Witt et al., 2006) (Figure 12). The landward boundary of the NAS then cuts through the Andean Cordillera and stretches along the eastern front of the Eastern Cordillera (Nocquet et al., 2014). Although this boundary has migrated eastward over the last 15 years, the active continental deformation is currently localized along a major fault system known as the Chingual-Cosanga-Pallatanga-Puná fault system (CCPP), which experiences slip rates of ~ 8 to 10 mm/yr (Alvarado et al., 2016). Overall, the northward motion of the block is a result of the strain partitioning induced by the obliquity of convergence (Yepes et al., 2016), although the subduction of the Carnegie Ridge likely exacerbates it (Michaud et al., 2009).

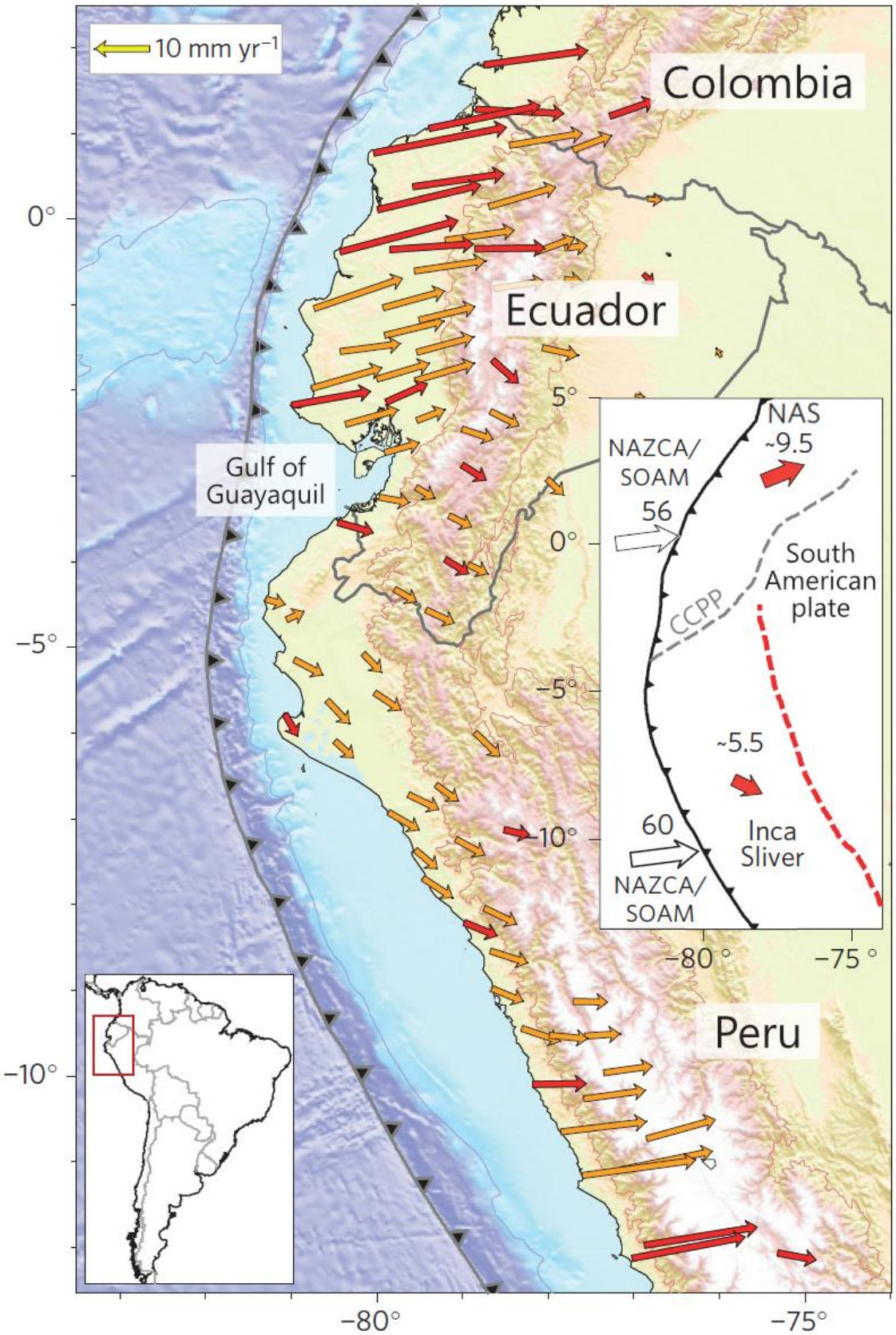

Figure 12 : Kinematic field in the Ecuador-Peruvian subduction zone from (Nocquet et al., 2014). NAS = North Andean Sliver; SOAM = South American plate; CCPP = Chingual-Cosanga-Pallatanga-Puná fault.

As a consequence of the subduction, the topography of Equador is complex. The overriding plate is divided into three main regions (Figure 13). First, the forearc is comprised of the coastal region, with a low coastal Cordillera reaching up to 850 m above sea level. Then the Andes correspond to the volcanic arc. North of 1.7°S, they are split into two distinct parallel ranges called the Western and Eastern Cordilleras (Figure 13). Between them is the Inter-Andean Depression, as wide as 30 km in places and home to the city of Quito. Finally, beyond the Andean range, the Amazonian basin forms the back-arc.

This wider context has implications for the structure of the subducting and upper plate, and impacts seismogenesis and interseismic coupling. I will now introduce these features in more detail.

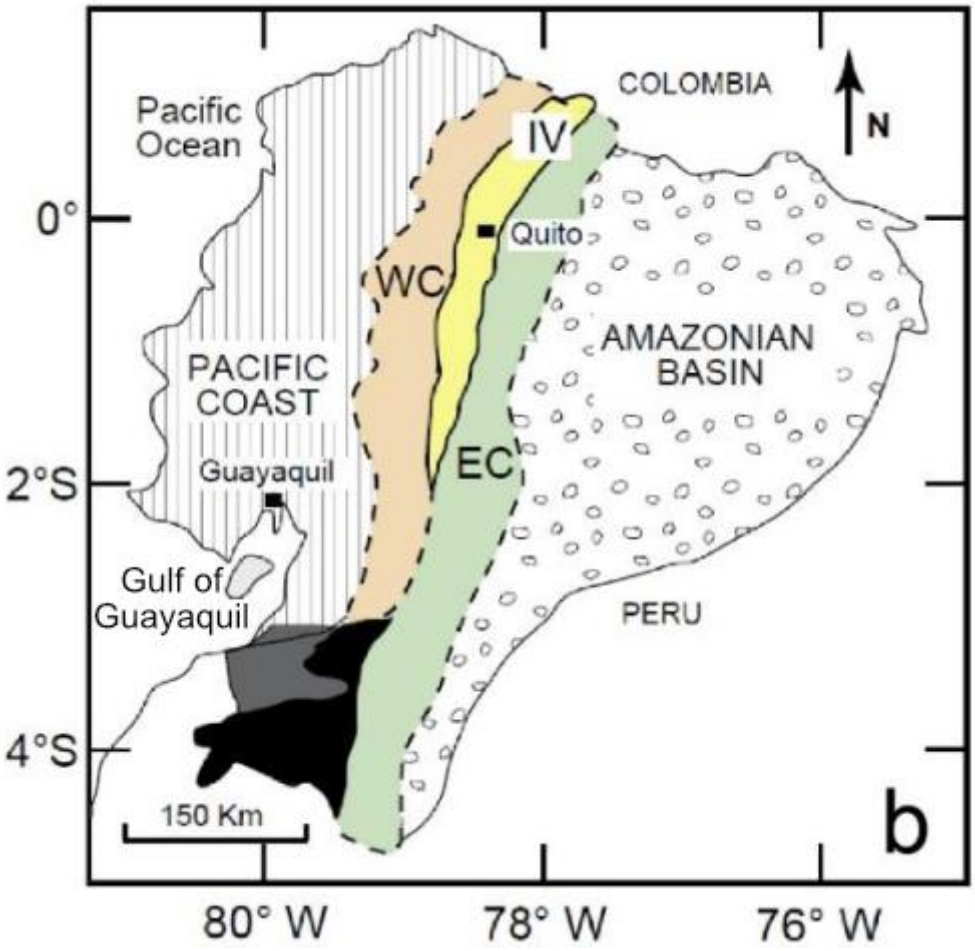

Figure 13 : Simplified map of the different regions of the upper plate, by Bablon (2018). The striped Pacific coast is part of the forearc, and contains a low coastal range. The orange Western Cordillera (WC), yellow Interandean Valley (IV) and green Eastern Cordillera (EC) correspond to the volcanic arc. The dotted Amazonian basin is part of the back-arc.

2.2 Possible influences on interseismic coupling and subduction geometry

2.2.1 Interseismic coupling at the plate interface

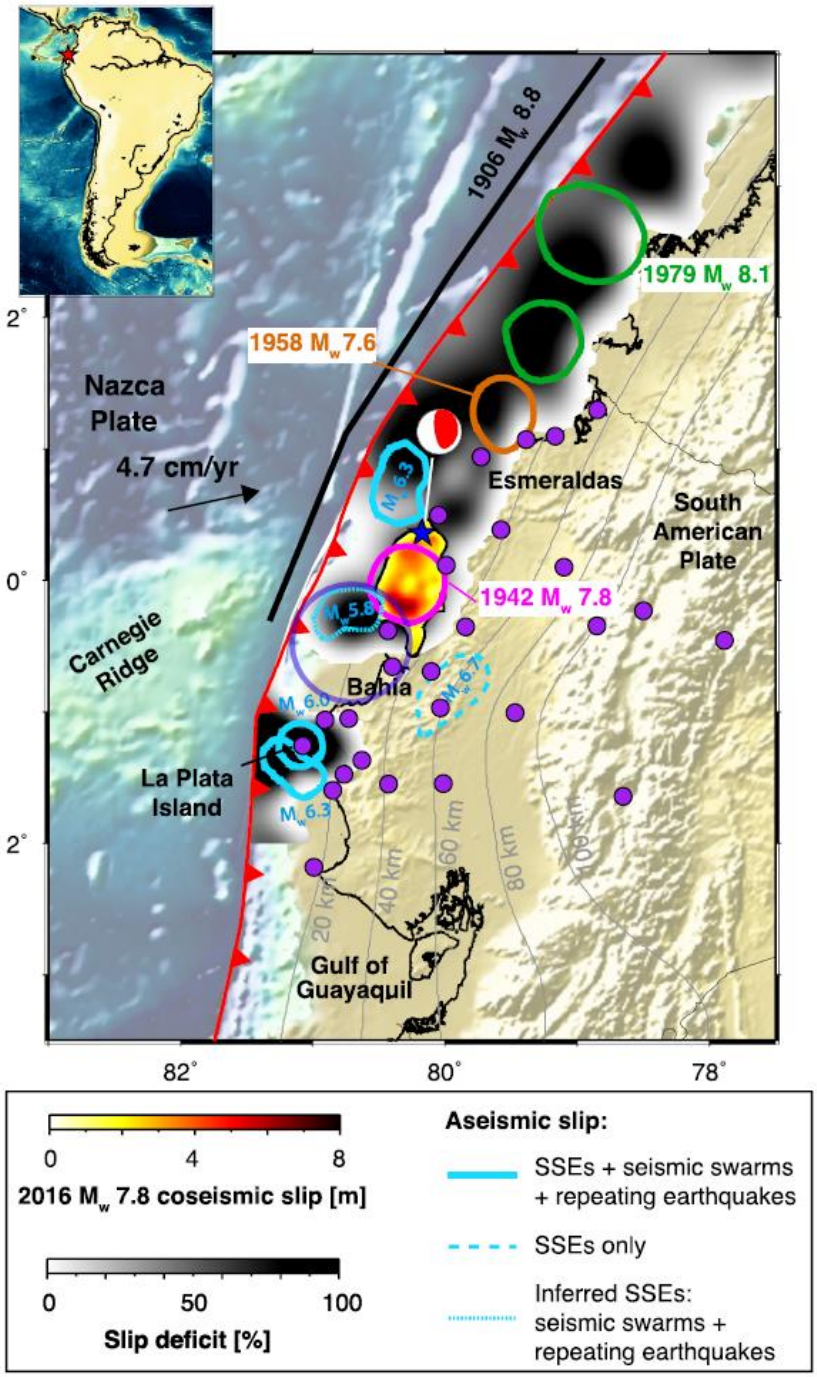

Figure 14 : Interseismic coupling (slip deficit) and modes of slip along the Ecuadorian margin, modified from Tsang et al. (2019). The blue star shows the epicenter of the 2016 Mw7.8 earthquake, and its coseismic slip distribution is shown in red (Nocquet et al., 2017). The distribution of the interseismic slip deficit is shown in grey (Nocquet et al., 2014). The Nazca/North Andean Sliver convergence rate is 4.7cm/yr (Nocquet et al., 2014). The rupture zones of the 1906, 1942, 1958, 1979 and 1998 earthquakes are shown in black, pink, brown, green and purple (Beck and Ruff, 1984; Kanamori and McNally, 1982; Segovia, 2001; Swenson and Beck, 1996). Swarm and slow slip areas are outlined in light blue (compiled by Rolandone et al., 2018), and magnitudes indicated correspond to the moments of SSEs or largest seismic swarm. Slab depth contours from Slab 1.0 are shown in grey (Hayes et al., 2012). Purple circles are GPS stations.

Interseismic coupling along the Ecuadorian margin is highly variable, as illustrated in Figure 14. In northern Peru and southern Ecuador, a 1000 km long stretch of the subduction interface with a very low interseismic coupling that likely creeps aseismically (Nocquet et al., 2014). In this portion of the megathrust, no Mw>8 earthquake has occurred since at least 1500 A.D., although two earthquakes with magnitudes 7.6 and 7.5 occurred in 1960 and 1996 respectively (Nocquet et al., 2014). In northern Ecuador however, the interseismic coupling is very high, reflecting the rupture zone of the 1906 earthquake (Nocquet et al., 2014). Based on the analysis of microseismicity, Manchuel et al. (2011)suggest that the seismogenic zone extends between 12 and 30 km in depth north of 1°S. This is in perfect agreement with the coupling map deduced from geodetic analysis (Figure 14) and means that the seismogenic zone extends 120 km from the trench (Beauval et al., 2013). The updip limit of the seismogenic zone is often associated with a temperature of 100-150° C, at which clays are dehydrated and become brittle (Hyndman et al., 1997). In Ecuador, temperature does not fully control the upper bound of the seismogenic zone, as around 1-2°N, the updip boundary corresponds to the 100°C isotherm, while around 2-3°N it corresponds to the 60°C isotherm (Marcaillou et al., 2008). Overall, the spatial variability of the interseismic coupling can be explained in part by properties of the lower and upper plate, including their structure and bathymetry.

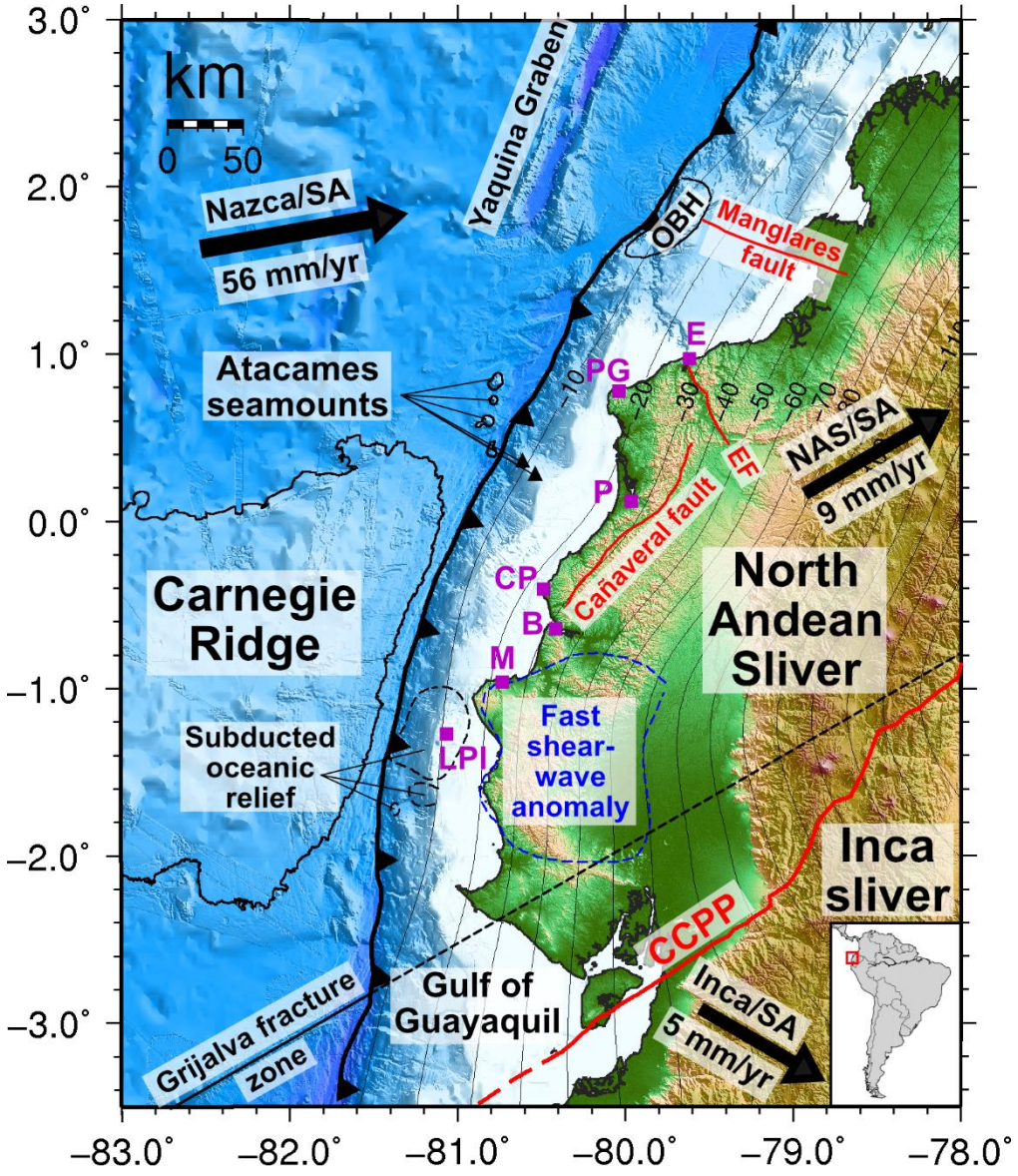

Figure 15 : Geodynamic setting and main structural features possibly affecting the seismic behavior of the Ecuadorian subduction zone. Plate convergence (black arrows) is from Nocquet et al. (2014). Fault traces (in red) are from Alvarado et al. (2016), J.-Y. Collot et al. (2004) and Eguez et al. (2003). The fast shear wave anomaly (in blue) was detected by Lynner et al. (2020). The subducted Atacames seamounts (black triangles) were detected by Marcaillou et al. (2016) using seismic imaging. The subducted oceanic relief beneath La Plata Island was outlined by J.-Y. Collot et al. (2017), also using seismic imaging. Depth contours from the slab 1 model are shown every 10 km (Hayes et al., 2012). Purple squares are geographic points of reference.

CCPP = Chingual-Cosanga-Pallatanga-Puná fault; EF = Esmeraldas fault; OBH = Outer basement high; E = Esmeraldas; PG = Punta Galera; P = Pedernales; CP = Cabo Pasado; B = Bahía; M = Manta; LPI = La Plata Island; NAS = North Andean Sliver; SA = South American plate.

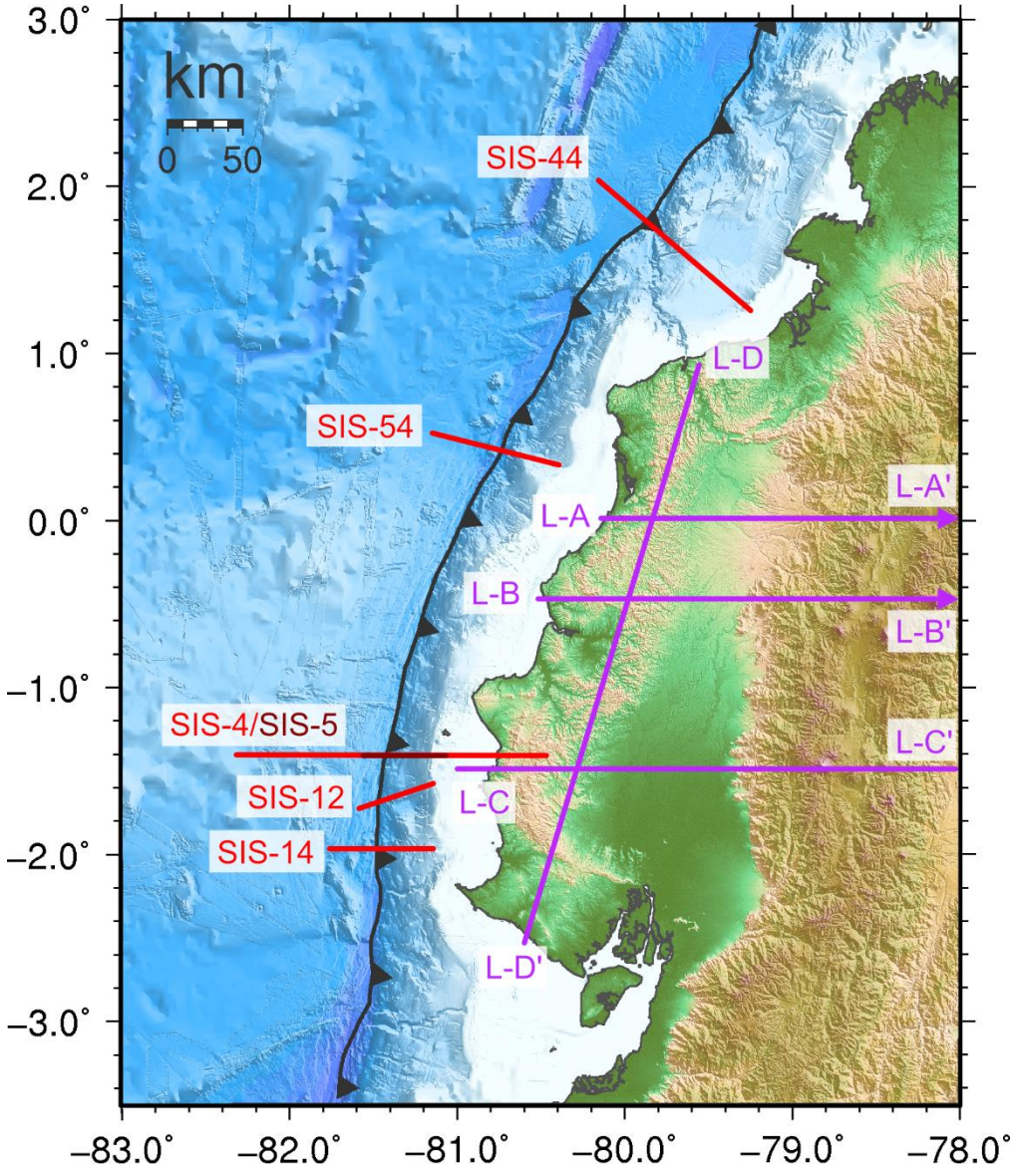

Figure 16 : Locations of all the seismic lines and cross sections shown in this chapter.

2.2.2 Lower plate features

Interseismic coupling is affected by the properties and roughness of the incoming plate. Some of these important features are shown in Figure 15, along with place names for geographical reference. Here I will present results from different studies, which are shown in map view in Figure 16. After entering subduction, the slab dips by 4 to 10 degrees from the trench down to 15 km at around 1°S (Graindorge et al., 2004), but has a steeper dip of around 10 degrees at around 1.5°N (Collot et al., 2008). Several of its bathymetric features influence the seismicity along the plate interface (Figure 15). In the South, the Grijalva fracture zone may act as a barrier to rupture, as its elongated shape makes it difficult to circumvent for any rupture (Yepes et al., 2016). Further north is the Carnegie Ridge, a 2 km high and 280 km wide volcanic

ridge that originates at the Galapagos hotspot and enters the subduction between 0° and 2.5°S, where it causes an indentation in the margin (Gailler et al., 2007; Michaud et al., 2009; Sallarès et al., 2005). Its 14 (Graindorge et al., 2004) to 19 (Sallarès et al., 2005) km thick crust is imaged in Figure 17. The ridge started subducting 3-8 My ago, which allowed it to penetrate 300-600 km into the subduction zone (Michaud et al., 2009). As such, its elevated bathymetry and elongated shape likely help to prevent the propagation of seismic rupture towards the south (Collot et al., 2004). The Carnegie Ridge seems to affect the coupling as well, which is moderate to high at its northern edge and along its southern half but very low along its axis (Chlieh et al., 2014; Nocquet et al., 2014). However, its effect on the overall geometry of the slab at depth is limited (Michaud et al., 2009). Despite the expected higher buoyancy of the Carnegie ridge, local microseismicity studies have shown that there is no flat slab in the region (Guillier et al., 2001; Manchuel et al., 2011). This confirms that the ridge subduction is likely younger than 10 Ma and thus does not significantly affect the slab dip (Guillier et al., 2001; Manchuel et al., 2011).

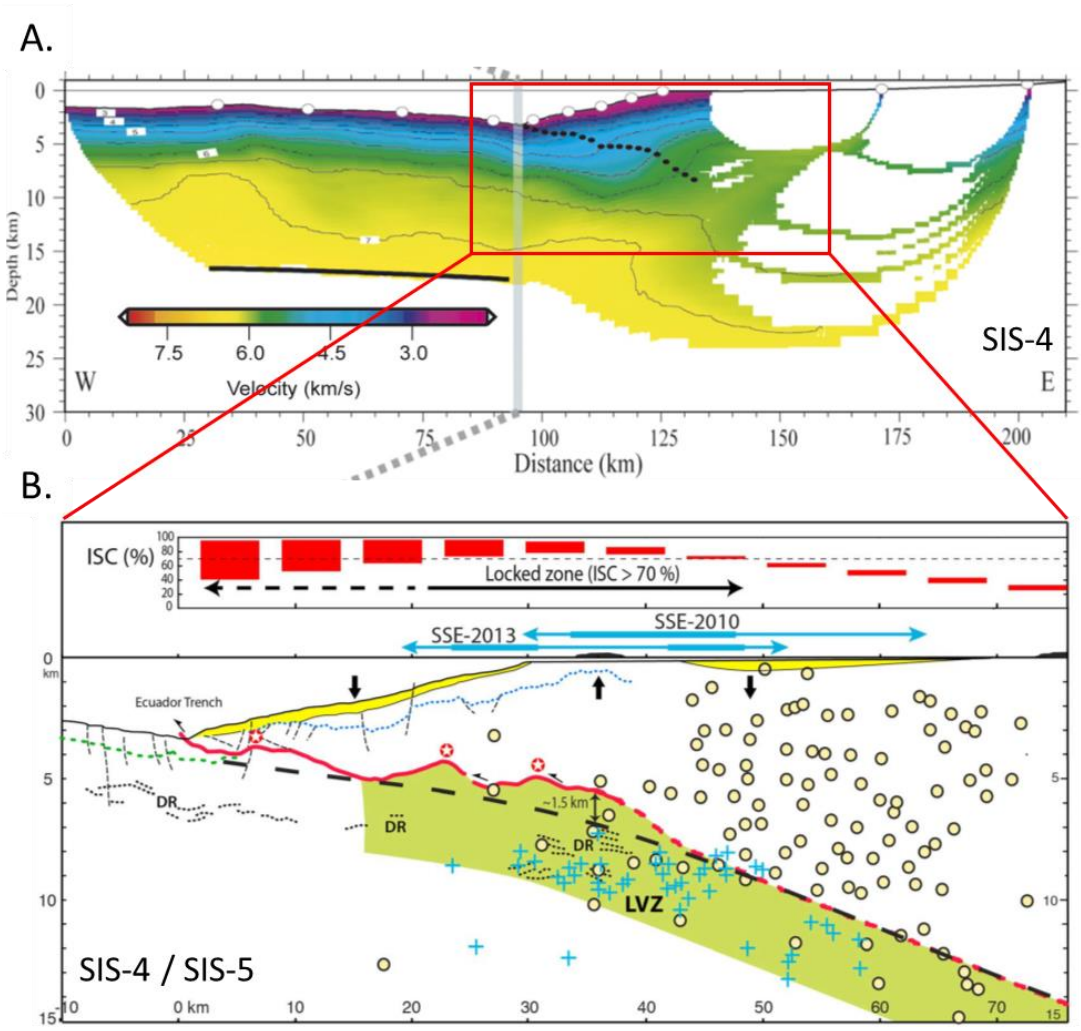

Figure 17 : A : Wide angle tomography velocity model by Gailler et al. (2007) along the SIS-4 seismic line on the southern flank of the Carnegie Ridge (Figure 16). The continuous black line is the Moho, determined by inverting PmP arrivals. The white circles are ocean bottom seismometers, and the black circles are the top of the oceanic crust derived from coincident Multi-Channel Seismic (MCS) data converted to depth. B: Interpretative cross-section of the margin from J.-Y. Collot et al. (2017) based on wide angle tomography data of the SIS-4 line and MCS data of the SIS-5 line. Red line shows the top of the oceanic crust. The interseismic coupling and its uncertainty (red bars) are shown at the top (Chlieh et al., 2014). The yellow layer shows sediments, and the vertical black arrows show the current subsidence and uplift of the margin as a result of the subduction of oceanic relief. The green LVZ is the downgoing plate low-velocity zone. Yellow circles show the relocated 1994-2007 seismicity within the inner wedge (Font et al., 2013), while blue crosses show the microseismicity triggered by the 2010 SSE (Vallée et al., 2013).

Other smaller bathymetric features influence the seismicity at the interface. Several seamount chains enter subduction. Under La Plata Island, 55x50 km wide, 1.5-2 km tall seamounts associated with the Carnegie Ridge cause an increase in the interseismic coupling of the margin (Collot et al., 2017; Nocquet et al., 2014). This is clearly visible in Figure 17, which also shows the impact of the oceanic relief subduction on the vertical motion of the margin basement. Meanwhile, the Atacames seamount chain, composed of 30x40 km wide and 1-2 km tall seamounts, enters subduction at around 0.3°N (Marcaillou et al., 2016). An interpreted cross-section of the margin in this region is shown in Figure 18. The compressive stress from seamount subduction, combined with the likely expulsion of overpressurized fluids, lead to the pervasive fracturing of the upper plate and to subduction erosion (Marcaillou et al., 2016). This weakens the margin, and likely explains the low interseismic coupling in the region (Marcaillou et al., 2016). The different effect that the La plata and the Atacames seamounts have on the interseismic coupling is notable, and may be explained by a difference in aspect ratio, as the steeper Atacames seamounts might more effectively damage the upper plate and reduce coupling than the flatter La Plata subducted relief (Collot et al., 2017).

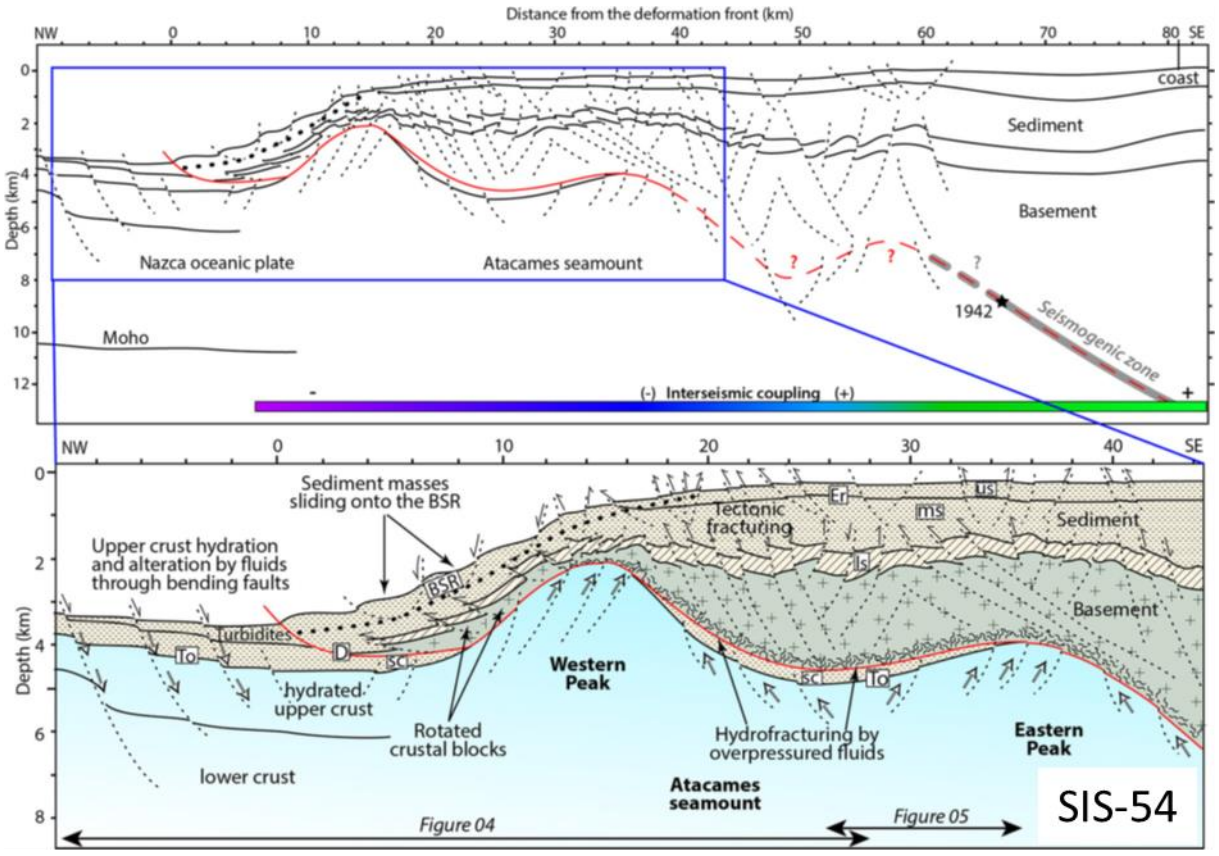

Figure 18 : Interpretative cross-section of the margin in the region where the Atacames seamounts enter subduction from Marcaillou et al. (2016), based on Multi-Channel Seismic (MCS) imaging. This section is based on two seismic lines, SIS-54, which images the oceanic plate up to the leading edge of the western peak (Figure 16), and SIS-55, which images the southern flank of the eastern peak. The likely epicenter of the 1942 earthquake is shown as a star (Swenson and Beck, 1996).

2.2.3 Sediment input into the subduction

The roughness of the plate interface is not only dependent on the bathymetric features of the incoming plate, but also on its sediment cover, and the amount of sediment entering the subduction zone. The Ecuadorian subduction zone is a primarily erosional margin, characterized by the small amount of sediment filling within the trench and the lack of accretionary prism (Collot et al., 2002). This is exacerbated on the Carnegie Ridge, where the trench is particularly shallow and narrow, while it widens away from it (Collot et al., 2004). On the Carnegie Ridge, the sediment cover and trench fill is therefore as low as 0.5-1 km, particularly since the ridge acts as a barrier for sedimentation (Gailler et al., 2007). However, the sediment cover thickness increases again to 7 km in the Gulf of Guayaquil (Gailler et al., 2007). In fact, in the Gulf of Guayaquil there is a small 8 km wide, 1 km thick accretionary prism (Calahorrano et al., 2008). The sediment cover is also larger towards the north. North of 1.5°N, the sediment over the oceanic plate is 1.5-2 km thick, while the sediment in the trench

is 2-3 km thick (Gailler et al., 2007). Even further north offshore Colombia, the accretionary prism is much larger, reaching a width of 35 km (Marcaillou et al., 2008).

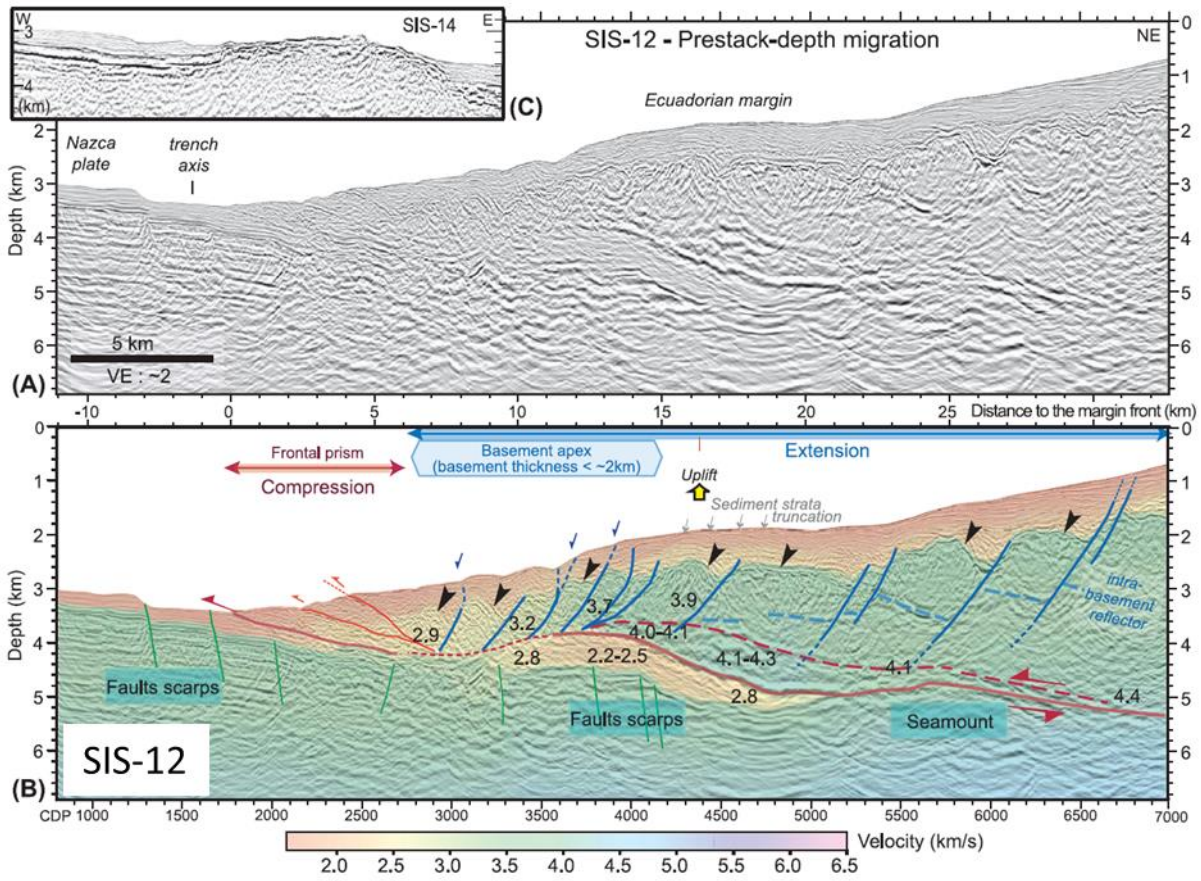

Figure 19 : Prestack depth migrated Multi-Channel Seismic (MCS) line SIS12, located at the southern edge of the Carnegie Ridge (Figure 16), from Sage et al. (2006). Black arrows indicate the top of the margin basement. The full red line indicates the base of the upper plate, while the dashed red line defines the top of a highly reflective zone likely affected by fluids.

These sediment thicknesses in front of the subduction zone, along with the presence of subducting features, affect the thickness of the subduction channel, which is in turn linked to the fluid circulation and frictional properties of the megathrust. The margin undergoes severe tectonic erosion from the Gulf of Guayaquil to the Carnegie Ridge, and between 1 and 2.5°N, where most of the incoming sediments are consumed by the subduction channel (Collot et al., 2002). Seismic imaging shows a 400-800 m thick reflective zone above the interplate between La Plata Island and the Gulf of Guayaquil, which extends 20-25 km landward (Sage et al., 2006). This may correspond to fluids circulating across the base of the basement (Sage et al., 2006). As is seen in Figure 19, the subduction channel in the region does not have a regular shape, instead forming fluid-rich sediment lenses between subducting basement highs and seamounts (Sage et al., 2006). This likely causes spatial variations in interseismic coupling at a

local scale, especially in the deeper part of the subduction (Sage et al., 2006). At the Carnegie ridge, a 3-4 km thick low-velocity zone is observed, but it is primarily due to the low velocity of the Carnegie Ridge layer 2 (Graindorge et al., 2004). The subduction channel thickness is very variable, as several-kilometers-wide fluid-rich sediment lenses are found along with stretches of thin subduction channel (Sage et al., 2006). This patchiness is caused primarily by the roughness of the incoming plate, and contributes to subduction erosion, as well as to the highly heterogeneous plate coupling. It is also observed by other seismic studies. For example, Marcaillou et al. (2016) found that around 0°N, the subduction channel is thin, but locally thicker on the flank of the subducted Atacames seamount. Meanwhile, the subduction channel becomes thicker further north, reaching a 2.2 km thickness at 5 km depth near the Esmeraldas canyon, due to higher sedimentation rates in the region (Marcaillou et al., 2008). However, the upper part of the subduction channel (around 6-8 km depth) likely has a low fluid content, as evidenced from its poor reflectivity (Collot et al., 2008). As can be seen in Figure 20, the subduction channel in the region is large at the trench and thins to a non-resolvable value below 90 m at around 15 km depth (Collot et al., 2008). J. Collot et al. (2008) found evidence of both basal erosion and transient underplating of sediments in the region.

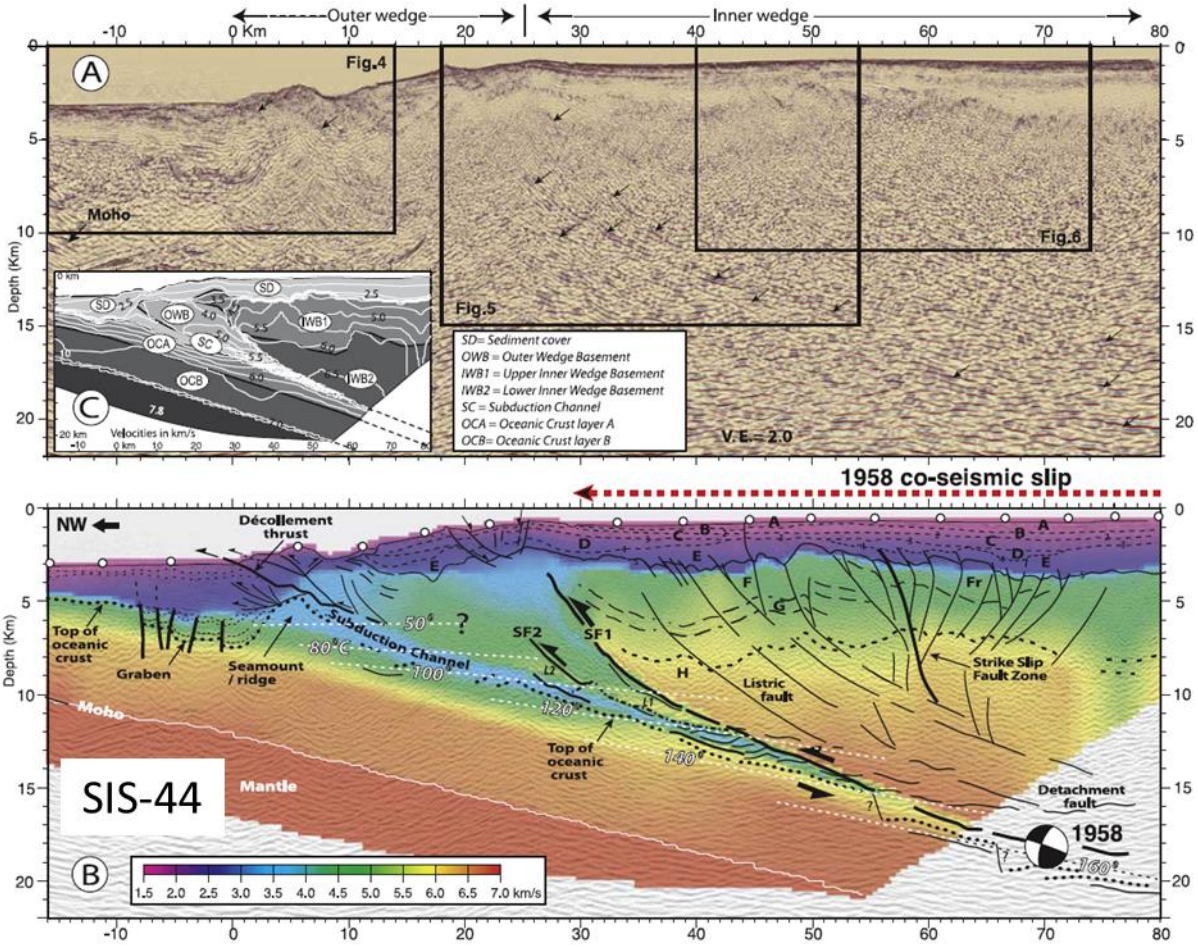

Figure 20 : Seismic imaging along the Multi-Channel Seismic (MCS) SIS-44 line in the north of Ecuador from J. Collot et al. (2008) (Figure 16). The top panel (A) shows the prestack depth-migrated (PSDM) line. The bottom panel (B) shows the velocity model and line drawing overlain over the PSDM image. SF1 and SF2 are splay faults. The focal mechanism shown is for the 1958 megathrust event (Swenson and Beck, 1996). The white dashed lines are isotherms projected from the thermal model calculated by Marcaillou et al. (2006) on the neighboring line SIS-42. The white circles along the seafloor are ocean bottom seismometers.

2.2.4 Upper plate structures

The role played by upper plate structures in seismogenesis should also not be neglected. The composition and density of the forearc is one such important parameter. Western Ecuador is made up of accreted island arc and oceanic plateau terranes. Three main terranes exist in Ecuador (Figure 21). The first, the San Juan terrane, is incorporated into the Western Cordillera. It was formed ~150 My ago and accreted 75 My ago (Jaillard et al., 2009). To the west is the ~90 My old Guaranda terrane, accreted 68 My ago, which forms the Eastern part of the western Cordillera (Jaillard et al., 2009). Finally, spanning the forearc is the Piñon-Naranjal terrane, of a similar age of ~90 My but accreted 58 My ago (Jaillard et al., 2009). The Guaranda and Piñon terranes are both thought to originate from the Caribbean-Colombian oceanic plateau (CCOP), which later fragmented before it collided with the South American plate (Jaillard et al., 2009; Luzieux et al., 2006). The lithologies of the Piñon terrane are largely covered by sediments in the coastal region, but outcrop in a few specific areas in the north and south of the forearc. The unit comprised of ultramafic, mafic and intermediate magmatic rocks is commonly referred to as the Piñon formation, and is thought to underlay most of the Ecuadorian forearc (Luzieux et al., 2006). Above it, several sedimentary basins lie on top of the forearc, most importantly the Manabi basin, the Borbon basin and the Progreso basin (Figure 21).

Overall, the thickness of the forearc is poorly constrained. North of Bahia, it appears to be around 20-25 km thick (Koch et al., 2020). Above the crest of the Carnegie Ridge, under the southern part of the Manabi basin, sits a portion of seemingly thinned and slow lithosphere, possibly due to the fracturing and alteration from fluid circulation caused by the subduction of oceanic relief (Koch et al., 2020; Lynner et al., 2020). This thinning can be seen in Figure 22, along with the slowness of the lithosphere. South of Bahia, the forearc lithosphere appears thicker, closer to 30 km (Koch et al., 2020). Lynner et al. (2020) used ambient noise tomography to find a fast shear wave anomaly in the forearc at around 20 km depth, around 80°W and 1-2°S, which can be observed in Figure 22. This anomaly was also observed in the shear wave velocity model of Koch et al. (2020) derived by jointly inverting receiver functions and surface wave dispersion data obtained through ambient noise cross-correlations. This region on the southern flank of the Carnegie Ridge corresponds to a significant positive gravity anomaly, and was interpreted as accreted mantle lithosphere (Koch et al., 2020; Lynner et al., 2020). This

was corroborated by gravity and magnetic modelling, which support the presence of a hydrated mantle wedge or of magnetic underplated material (Aizprua et al., 2020). Lynner et al. (2020) and Koch et al. (2020) suggest that it may play an important role in the margin segmentation, acting as a barrier to rupture propagation. Gailler et al. (2007) also suggested that the differences in the density structure of the forearc, evidenced through wide-angle tomography, could explain the variation in coupling between the north and the south of Ecuador.

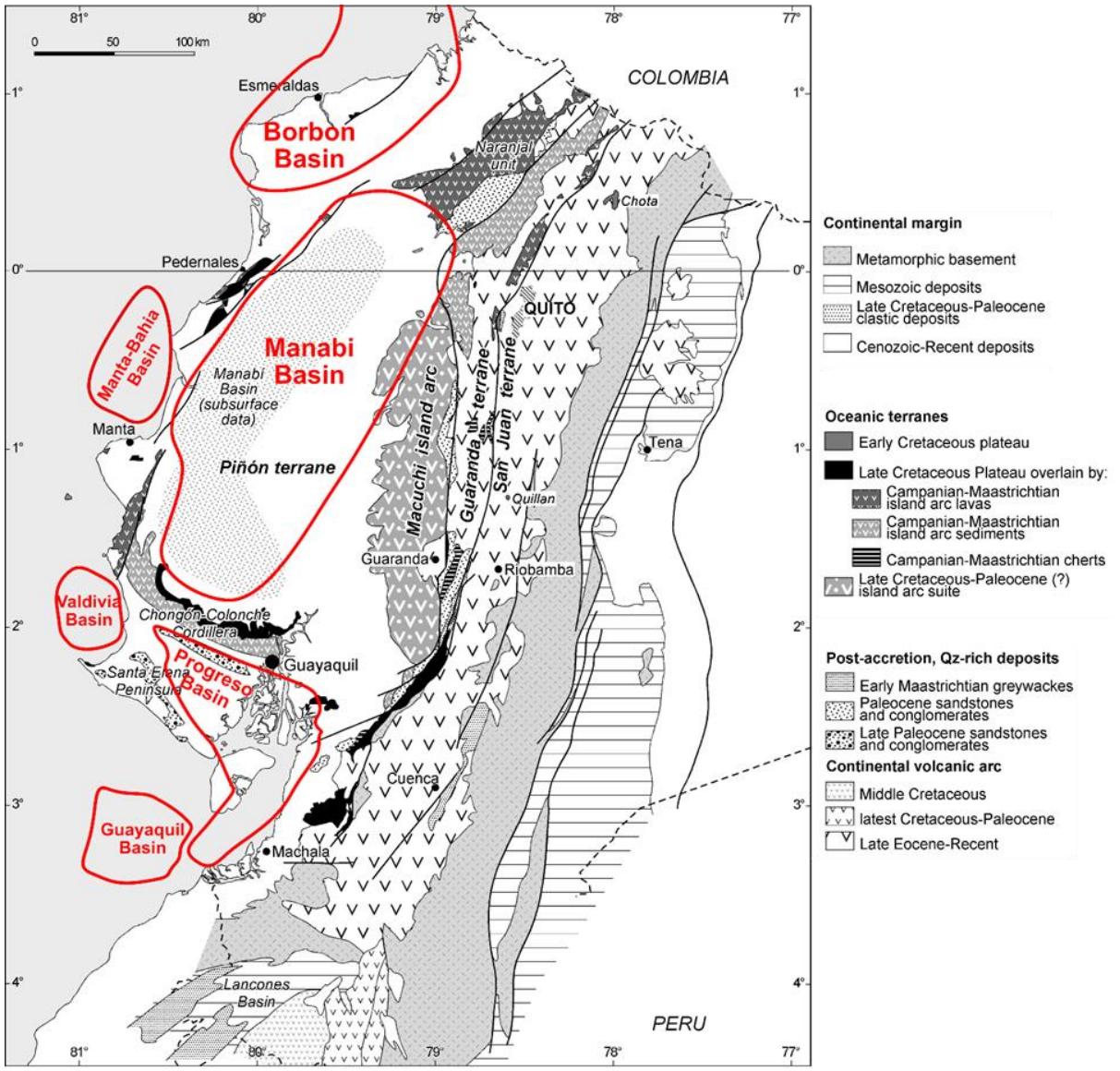

Figure 21 : Map of the main accreted terranes and geological units in continental Ecuador, modified from Jaillard et al. (2009). Rough outlines of the main sedimentary basins are shown in red (Hernandez Salazar, 2020).

In addition to the density of the upper plate, some weak upper plate transverse faults are thought to contribute to the segmentation of the margin by reducing the coupling between segments. These faults, shown in Figure 15, include the Esmeraldas fault, the Manglares fault

and the Jama fault (also known as the Cañaveral fault), which are all close to boundaries between large earthquakes (Collot et al., 2004). Splay faults may also play a role in the updip propagation of earthquakes. In the north of Ecuador, around 1.5°N, one such splay fault, seen in Figure 20, is thought to have played a role in the rupture propagation of the 1958 earthquake (Collot et al., 2004). This fault separates the inner wedge from the highly altered outer wedge, likely affected by the release of fluids from the subduction channel (Collot et al., 2008).

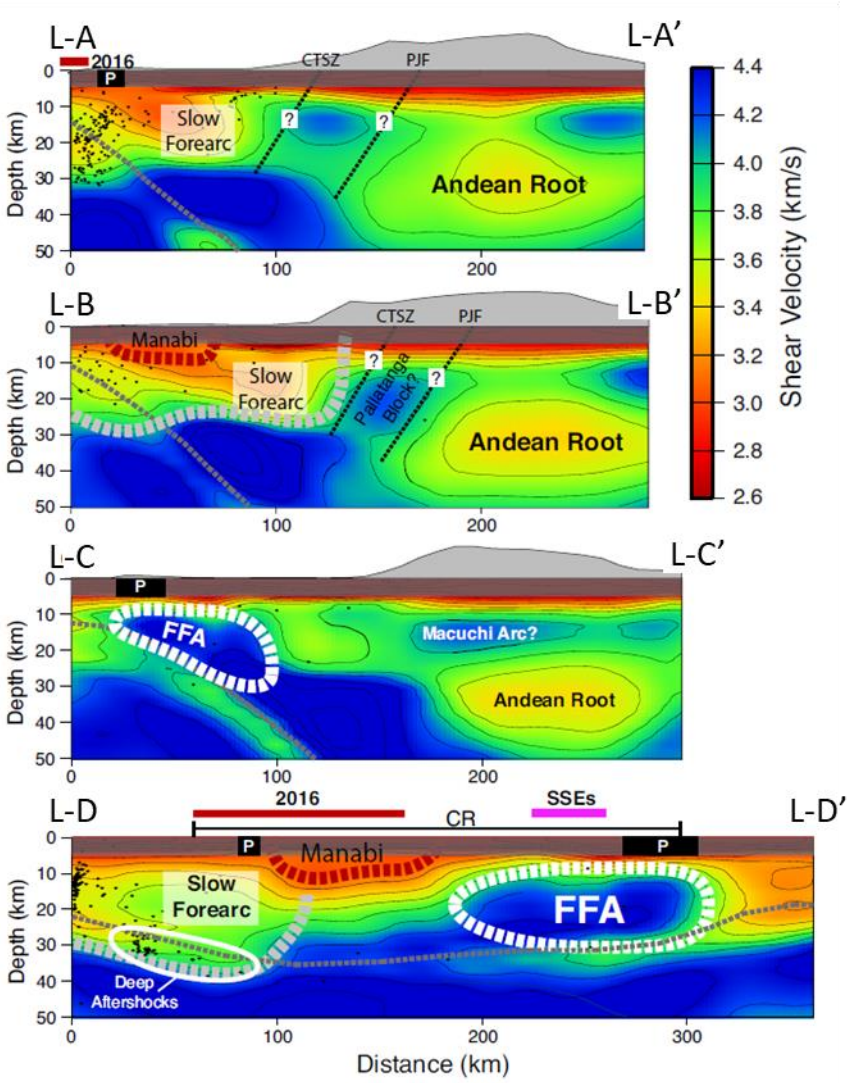

Figure 22 : Cross sections in continental Ecuador (Figure 16) of the interpreted shear-wave velocity model from Lynner et al. (2020). The extent of the 2016 Pedernales earthquake rupture zone is shown as a red line (Nocquet et al., 2017), and the deep SSE zone is shown in pink (Rolandone et al., 2018). The grey dotted line shows the location of the slab in the Font et al. (2013) starting model. Black dots are aftershocks from the 2016 Pedernales earthquake (Meltzer et al., 2019). FFA = Fast Forearc Anomaly; CTSZ = Chimbo–Toachi Shear Zone; PJF = Pujili fault system; CR = Carnegie Ridge.

2.3 Seismicity and aseismic slip along the margin

2.3.1 Intraplate seismicity

Although I will focus primarily on interplate seismicity in this thesis, it is worth remembering that the seismic hazard in Ecuador is not solely concentrated on the coast, as some intraplate seismicity occurs both within the overriding and the subducting plate. In continental Ecuador, few earthquakes occur within the North Andean Sliver (NAS, Figure 15), likely because the forearc sliver acts as a rigid undeforming block transmitting stress from the subduction to the Andes (Guillier et al., 2001). Instead, seismic moment release is largest in the Northern Andes, particularly along the inter-Andean Depression and the sub-Andean Belt (Yepes et al., 2016). Several Mw>6.5 earthquakes have been recorded over last 110 years at the NAS-SA boundary in northern Ecuador (Beauval et al., 2010, 2013; Yepes et al., 2016). Additionally, some moderate earthquakes (Mw <= 6) have also occurred west of the NAS boundary on the Quito-Latacunga fault system, a series of thrust faults on the western internal slope of the Inter-Andean depression (Alvarado et al., 2014; Beauval et al., 2010).

Some intraslab earthquakes have also occurred. In the outer rise, 150 km West of the trench, two events of magnitudes 7.2 and 7 occurred at 0°N and 2°S in 1902 and 1907, although their epicenters are poorly constrained (Font et al., 2013). Within the subducting slab itself, some earthquakes occur at intermediate or deep locations, although mostly in southern Ecuador (Yepes et al., 2016) (Figure 23). In fact, intermediate depth earthquakes occur almost exclusively south of the inland projection of the Grijalva rifted margin (Yepes et al., 2016). This implies a strong control of the different mantle rheologies of the younger Nazca lithosphere to the North and the older Farallon lithosphere to the South. One deep intraslab earthquake cluster in particular is notable: the Puyo cluster, sitting 1.5°S and 78°W near the focal point of the trench curvature, at a depth of 120 to 200 km. The focal mechanisms of earthquakes within the cluster suggest a tearing of the slab. Meanwhile, the deepening of the seismicity in this region and the rotation of focal mechanisms counterclockwise within the cluster suggest that the Farallon plate is being pinched to accommodate the curvature of the subduction zone, as Figure 23 shows (Yepes et al., 2016).

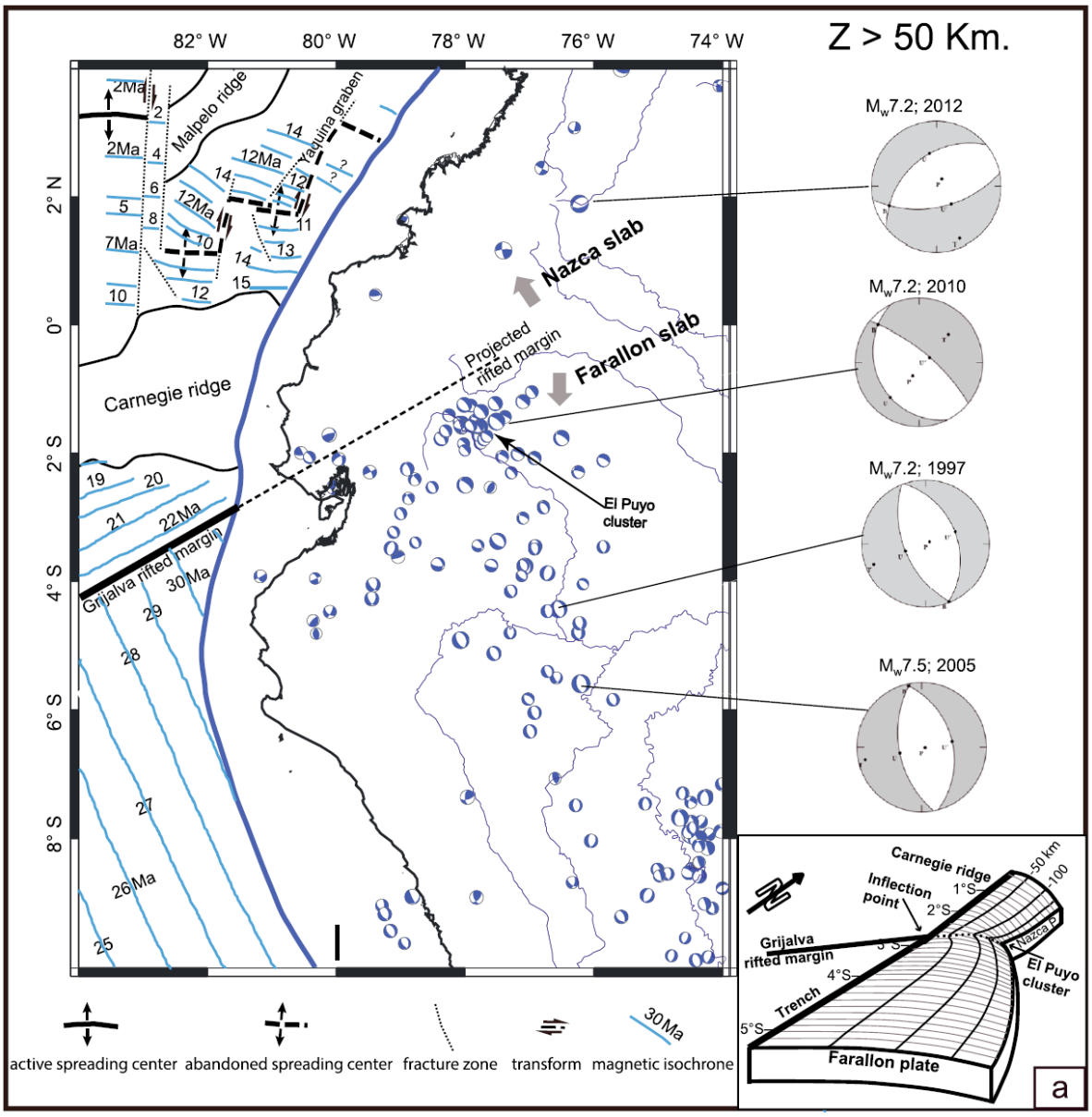

Figure 23: Map of intermediate-depth earthquake focal mechanisms (50 < Z < 300 km) from 1976 to 2013 in Ecuador and Peru, by Yepes et al. (2016). Focal mechanisms are taken from the Harvard CMT Catalogue (Dziewonski et al., 1981). *Focal mechanisms for the four largest events are shown on the side. Offshore blue lines show magnetic isochrones, with associated crustal ages in million years. (a) Sketch showing the shape of the subducting plates.*

2.3.2 Background seismicity and periodic slip at the plate interface

At the plate interface itself, as can be seen in Figure 24 and in Figure 25, there are 2 major trench-perpendicular alignments of seismicity during the interseismic period: one around 0.6°N near Punta Galera, and one around 0.25°S near Cabo Pasado (Font et al., 2013; Segovia, 2001).

Another large earthquake cluster is found near La Plata Island (Font et al., 2013; Segovia, 2001).

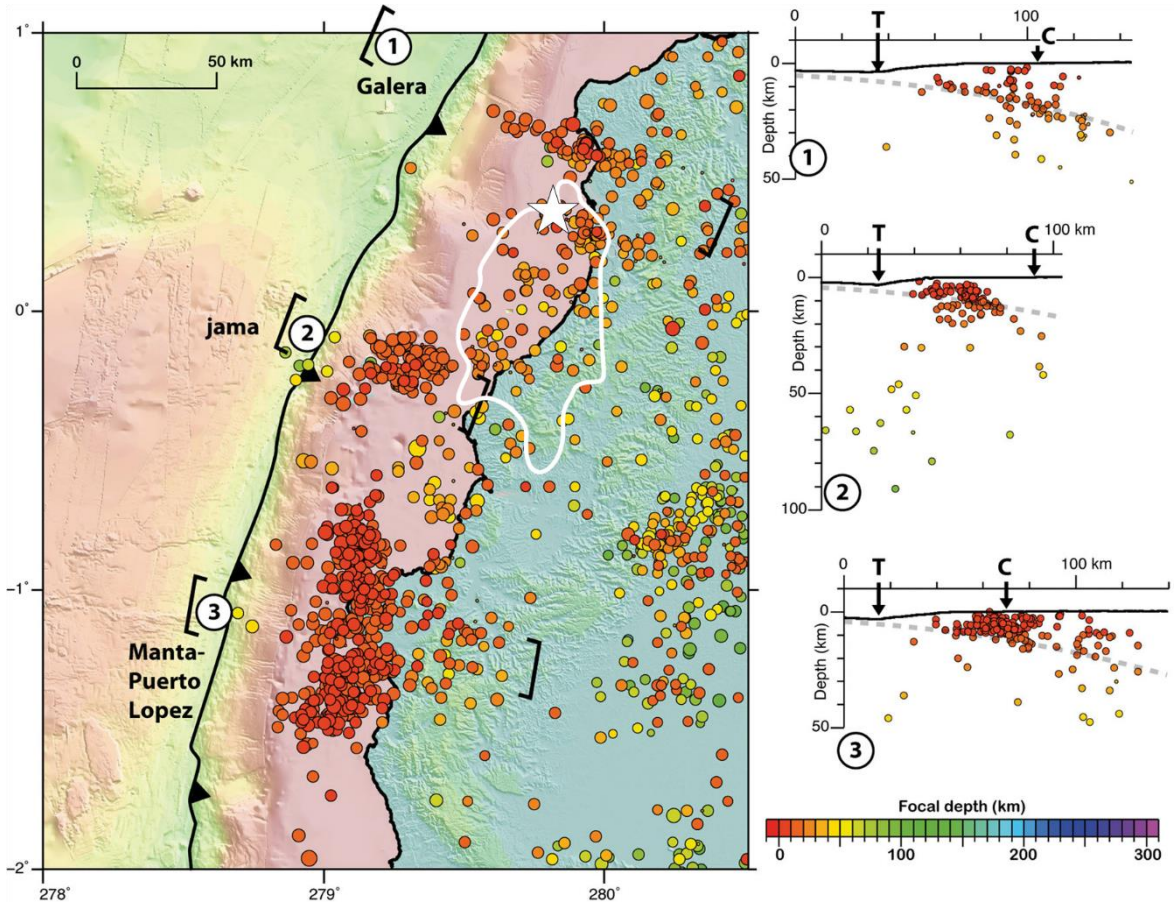

Figure 24 : Background seismicity in and around the Pedernales region between 1994 and 2007, modified from Font et al. (2013). The white star and line show the epicenter and outline of the 2016 Pedernales earthquake (Nocquet et al., 2017). Three alignments are visible: To the north, one clear trench-perpendicular alignment near Punta Galera, in the middle, a cluster near Jama-Cabo Pasado, and in the south, a trench-parallel alignment near La Plata Island (here named Manta-Puerto Lopez segment). These three clusters are shown in cross-section as well. All earthquakes were relocated in a 3D velocity model by Font et al. (2013).

The Punta Galera alignment corresponds to a site of periodic shallow slow slip events, as shown in Figure 14 (Mothes et al., 2013; Vaca et al., 2018). Two of these slow slips were detected geodetically in 2007 (Mothes et al., 2013) and 2013-2014 (Vaca et al., 2018), while swarms, which are thought to be concurrent with the SSEs, have been detected roughly every two years since 1994, lasting between a few days and two months and containing several multiplets (Vaca et al., 2018). Because of this periodic release of stress, it is thought that the region acts as a barrier to large rupture propagation (Vaca et al., 2018).

To the south, the Cabo Pasado - Jama segment also experiences frequent swarms documented by other authors, as were detected in 1996, 2000, 2010, and 2015 (Segovia, 2016), despite the strong coupling found in the area. Additionally, Rolandone et al. (2018) found bursts of multiplets at 3 different time periods since 2010 in the region, pointing to likely SSEs in the region (Figure 14).

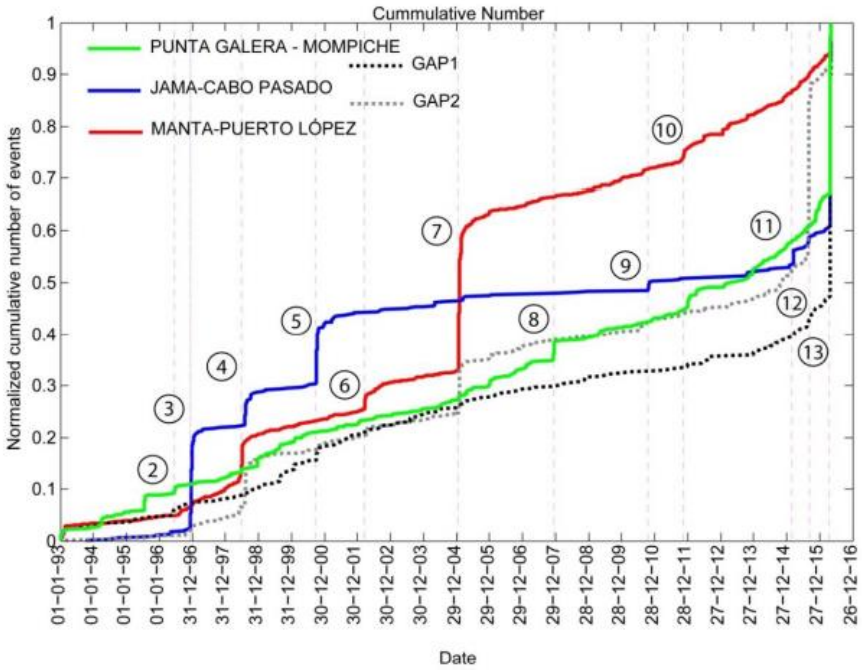

Figure 25 : Temporal evolution of the normalized cumulative seismicity in and around the Pedernales region between 1993 and 2017. Gap 1 corresponds to the seismicity between the Punta Galera and Jama-Cabo Pasado alignments, and gap 2 is the seismicity between the Jama-Cabo Pasado and Manta-Puerto Lopez region. Dashed vertical lines (and numbers) represent increases in seismicity in at least one region. Number 13 is the Pedernales earthquake. All data shown was detected and relocated by the Ecuadorian national network RENSIG, figure by Segovia (2016).

Even further south is the cluster associated with La Plata Island (referred to in Figure 24 and Figure 25 as the Manta-Puerto Lopez alignment), occurring between 0.7 and 1.5°S. The region is highly locked but marks the transition between the mostly locked subduction segment in the north and the unlocked subduction segment in the south (Chlieh et al., 2014; Nocquet et al., 2014). It hosts dense seismicity of moderate size, with magnitudes mostly below 6. This seismicity, once again, mostly occurs in swarms containing many multiplets, as in 1977, 1998, 2002, 2005, 2010, 2013 (Font et al., 2013; Holtkamp et al., 2011; Segovia et al., 2018; Vallée et al., 2013). They occur at the leading edge of the subducting oceanic seamounts, seemingly within its crust (Segovia et al., 2018). The diverse focal mechanisms further indicate that seismic activity occurs within the crust as well as at the plate interface. These swarms occur concurrently with SSEs, some of which have been detected geodetically in 2010, 2013 and 2016

(Rolandone et al., 2018; Segovia et al., 2018; Vallée et al., 2013). Some of these SSEs are shown in Figure 14.

2.3.3 Large subduction earthquakes

Several large subduction earthquakes have occurred in the north of Ecuador and the south of Colombia, all to the north of the Carnegie Ridge (Figure 14). No historical record of subduction earthquakes exists before 1896, but paleoseismological records north of Esmeraldas show that Mw > 7 earthquakes occurred at least 10 times over the last 800 years (Migeon et al., 2017). Their recurrence times appear to be between 42 and 82 years, although the 1906 earthquake appears to have been preceded by a 268 years long quiescence (Migeon et al., 2017). At least one earthquake as large as the 1906 event may have occurred 600 to 700 years ago (Migeon et al., 2017).

The 1906 event itself was a Mw 8.4-8.8 earthquake, one of the first great subduction earthquakes ever recorded and the largest in the region (Kanamori and McNally, 1982; Yoshimoto et al., 2017). It ruptured a 200 to 500 km long segment spanning northern Ecuador and southern Colombia (Kelleher, 1972). Its likely southern limit was around 0°S, immediately north of the Carnegie ridge (Kanamori and McNally, 1982; Kelleher, 1972). Based on the source model proposed by Kanamori and McNally (1982), its rupture zone has hosted four other large earthquakes of magnitudes 7-8 since 1906 (Figure 14). Despite collectively breaking the same area as the 1906 earthquake, the 1942, 1958 and 1979 earthquakes only released 20-30% of its energy, meaning other, maybe aseismic portions of the fault were likely ruptured during the 1906 earthquake (Kanamori and McNally, 1982; Ye et al., 2016). This is however a controversial point, since the 1906 magnitude and rupture zone is poorly constrained. This is in part because only very few teleseismic stations and remote tide gauges were available at the time (Kanamori and McNally, 1982). Kanamori and McNally (1982) used seismic recordings to determine that the magnitude of the earthquake was about 8.8, while Abe (1979) used far-field tsunami data to estimate the magnitude as 8.7. However, also using tsunami modelling, Yoshimoto et al. (2017) determined that the magnitude was closer to 8.4 and that the slip had concentrated near the trench without breaking the 1942, 1958, 1979 and 2016 asperities at all. It is however worth noting that tsunami modelling is inherently less sensitive to deep slip than to shallow slip, and thus this is likely a low estimate.

Following the 1906 event, three smaller events occurred in the following century that broke part of the 1906 rupture (Figure 14). The first was the 1942 earthquake, which broke the southern segment of the 1906 rupture. The magnitude of that event was once again difficult to determine as no long-period seismogram exists, but the size of the aftershock area seems to

indicate a similar magnitude to the 1958 event of about Mw 7.6-7.7 (Kelleher, 1972). It has been proposed that the event was nucleated at the leading edge of the Atacames seamounts, and propagated northward until the edge of the 1958 event (Marcaillou et al., 2016). The 1958 event itself was better recorded, and its magnitude was estimated as 7.7 from long-period seismograms (Kanamori and McNally, 1982) and 7.6 from its aftershock area (Kelleher, 1972). The event nucleated likely near a seamount (Collot et al., 2008) and was likely stopped updip by the prominent Outer Basement High (OBH, Figure 15), which seemingly caused it to propagate along a splay fault instead (SF1, Figure 20) (Collot et al., 2004; Marcaillou et al., 2006). It propagated northward before being stopped by the 1979 rupture zone (Beck and Ruff, 1984). This 1979 earthquake was the third in the sequence, with a magnitude of 8.2 calculated from far-field tsunami data (Kanamori and McNally, 1982). It ruptured a 120 - 230 km long segment, with a rupture direction again towards the northwest (Beck and Ruff, 1984; Kanamori and McNally, 1982).

Finally, three other earthquakes with magnitudes close to 7 occurred in the Bahía region: the 1896 Mw 7 earthquake, the 1956 Mw 6.95 earthquake and the 1998 Mw 7.1 event. They are thought to behave independently from the northern megathrust, although the asperity they occurred on might have ruptured during the 1906 event (Yepes et al., 2016). The only existing focal mechanism is for the 1998 event, and is poorly constrained, although compatible with a thrust faulting event (Dziewonski et al., 1981; Ekström et al., 2012; Segovia, 2001). Using the spatial extent of the early aftershocks of the 1998 event, Segovia (2001) determined that the 1998 mainshock had a roughly 80x80 km large rupture zone that overlapped in part with the Cabo Pasado locked patch. However, it seems that the earthquake mostly ruptured a seemingly currently uncoupled portion of the megathrust, and the area of maximum moment release was found on the southern border of the coupled patch (Chlieh et al., 2014; Nocquet et al., 2014; Segovia, 2001). However, too little is known about this sequence of earthquakes to confirm whether they ruptured a primarily aseismic portion of the fault or not.

2.3.4 The Pedernales earthquake and its aftermath

The 2016 Mw 7.8 Pedernales earthquake occurred on the 16th of April 2016, preceded by 11 minutes by one Mw 4.8 foreshock, and caused close to 700 deaths and widespread damage. The mainshock ruptured 2 asperities, initiating in the north and propagating south (Gombert et al., 2018; Nocquet et al., 2017). This is reflected in the distribution of slip, which occurred mostly in two patches: in the north, there was about 3 m of slip, and in the south up to 6 m. Between these two patches, there is a region of lower slip (1-2 m) (Nocquet et al., 2017). Overall, the rupture zone seemed to correlate to a region of low-density in the forearc, which

could have played a role in the propagation of the rupture (Alvarez et al., 2017). The rupture area itself appears to be the same as the 1942 earthquake (Nocquet et al., 2017; Ye et al., 2016; Yoshimoto et al., 2017), though the 1942 epicenter was south of the 2016 epicenter (Kelleher, 1972). Nocquet et al. (2017) determined that the Pedernales earthquake released more energy than had been stored since 1942. Combined with the apparent seismic quiescence before 1906 and the higher energy budget released by the1906 event compared to the sum of all subsequent large events, this points to a possible seismic supercycle in the region. Contrary to a simple earthquake cycle model, where all large earthquakes release all the strain accumulated since the last large earthquake, a supercycle implies that strain is accumulated for much longer and released by several temporally clustered large earthquakes, rather than by a single earthquake (Nocquet et al., 2017). This model is contested for the Ecuador-Colombia subduction zone, as Yoshimoto et al. (2017) argued that the earthquake's maximum slip was similar to the slip deficit accumulated since 1942. However, Gombert et al. (2018) confirmed that, assuming the 1942 and 2016 earthquake ruptured the same asperity, the accumulated moment deficit during that period was smaller than the seismic moment released by the Pedernales earthquake. But as they pointed out, the 1942 rupture is poorly constrained, and this conclusion only holds if it truly overlaps with the 2016 rupture.

The earthquake triggered both substantial afterslip and a large number of aftershocks (Figure 26). The afterslip, which appears to have been abnormally large for the earthquake size, was mostly distributed into two patches updip of the rupture and one deep region (Rolandone et al., 2018; Tsang et al., 2019). Of the two shallow afterslip regions north of -0.5°S, one was the SSE prone region near Punta Galera, while the other was the swarm-prone high-coupling region near Cabo Pasado (Figure 15) (Rolandone et al., 2018). The third region, located at 50 km depth downdip of the rupture, had also experienced SSEs prior to the mainshock (Rolandone et al., 2018). Finally, 100 km south of the rupture, at La Plata Island, an SSE was triggered a few days later by static stress changes from Pedernales (Rolandone et al., 2018; Tsang et al., 2019). These observations show how similar the phenomena of slow slip events and afterslip really are, in spite of their usual separation (Rolandone et al., 2018).

Many aftershocks were also triggered by the mainshock, primarily updip of the rupture. Most of the aftershocks have thrusting mechanisms and likely occur at the interface, between the trench and the maximum depth of the coseismic rupture (Agurto-Detzel et al., 2019). The aftershock sequence contains several swarms, as well as large events (Soto-Cordero et al., 2020). Three trench-perpendicular alignments of seismicity can be observed, two of which were observed in the interseismic period by Font et al. (2013) (Figure 24), and one around 0.4°N near Pedernales (Agurto-Detzel et al., 2019). These bands of seismicity may be composed of smaller, focused clusters containing earthquake swarms and large-magnitude aftershocks (Soto-Cordero et al., 2020). The distribution and focal mechanisms of the 2016 aftershocks also roughly correspond to those of the 1942 aftershocks, meaning they are likely linked to permanent

subducting structures (Mendoza and Dewey, 1984; Yoshimoto et al., 2017). Several clusters are linked to bathymetric subducting features, like the Carnegie Ridge and the Atacames seamounts (Agurto-Detzel et al., 2019; Soto-Cordero et al., 2020). The clusters near Punta Galera similarly correlate to residual bathymetry and gravity anomalies, confirming the influence of the structure of the downgoing plate (Agurto-Detzel et al., 2019; Soto-Cordero et al., 2020). On the other hand, the termination of the seismicity at depth near Manta is likely due to a rheological transition in the overlying plate (Soto-Cordero et al., 2020). More broadly, several clusters of seismicity line or stop at areas of rheological contrasts at depth between accreted oceanic terranes and sedimentary basins (Soto-Cordero et al., 2020).

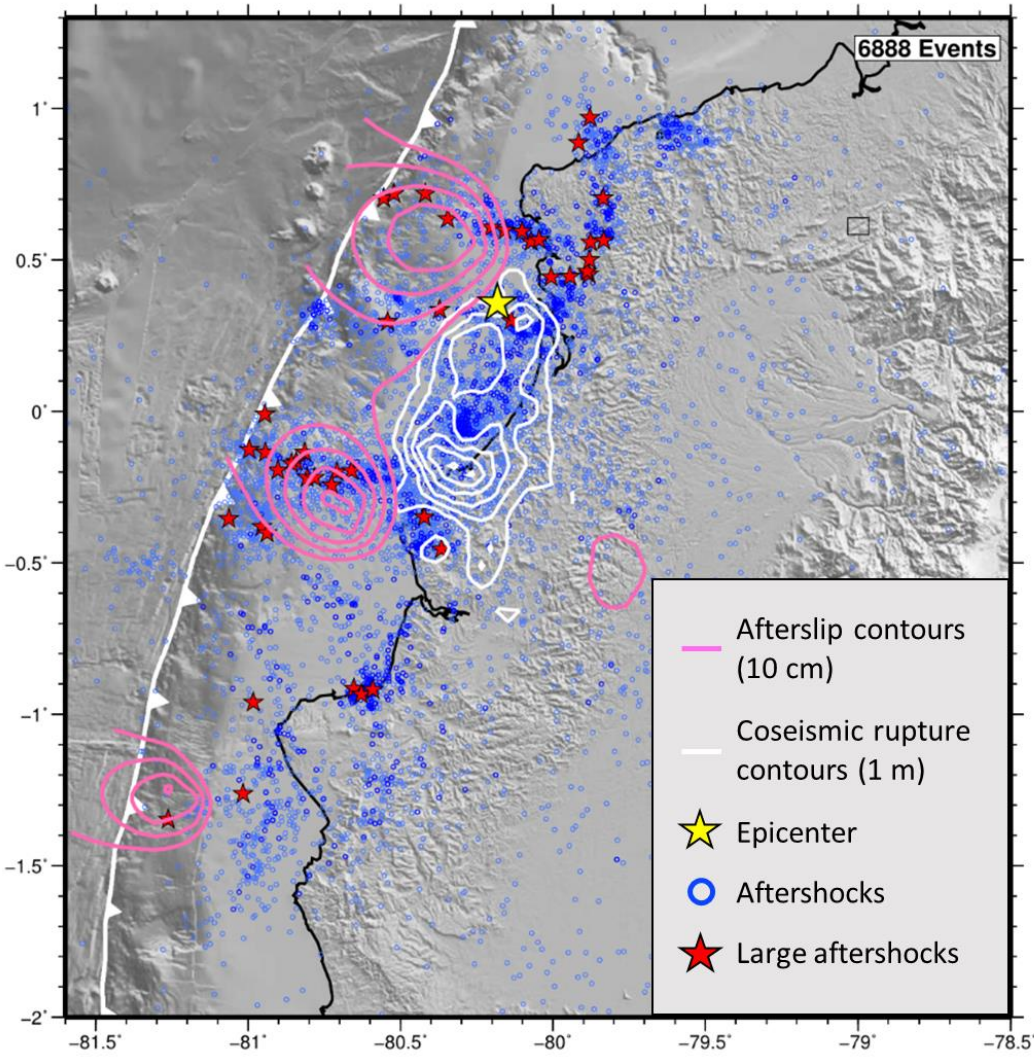

Figure 26 : Map of aftershocks and afterslip from the 2016 Pedernales earthquake, modified from Agurto-detzel et al. (2019). Small aftershocks (Ml ~2.5 - 5) are shown as blue circles, and aftershocks with Ml > 5 are shown as red stars (Agurto-Detzel et al., 2019). The epicenter of the Pedernales earthquake is shown as the yellow star, while the 1 m contours of the rupture zone are shown in white (Nocquet et al., 2017). Contours of the afterslip are shown in pink (Rolandone et al., 2018).

It seems that afterslip was a major driving force behind the aftershock expansion (Agurto-Detzel et al., 2019). This is demonstrated by the fact that their spatio-temporal evolutions are similar (Figure 27). Agurto-Detzel et al. (2019) found a semi-logarithmic migration of aftershocks along strike and dip, which they argue shows the influence of afterslip in the expansion of the aftershock sequence. Additionally, the cumulated afterslip and number of aftershocks in the first month have similar time evolutions, again demonstrating how closely the two are linked (Agurto-Detzel et al., 2019). However, Wu et al. (2017) did find that 5 of the 6 M>6 aftershocks occurred in positive Coulomb stress areas, meaning Coulomb stress changes from the mainshock were still important. But many aftershocks also fall in the stress shadow of the mainshock, making afterslip necessary to explain their locations (Jiménez et al., 2021). This influence is especially felt in the streaks of seismicity updip of the rupture.

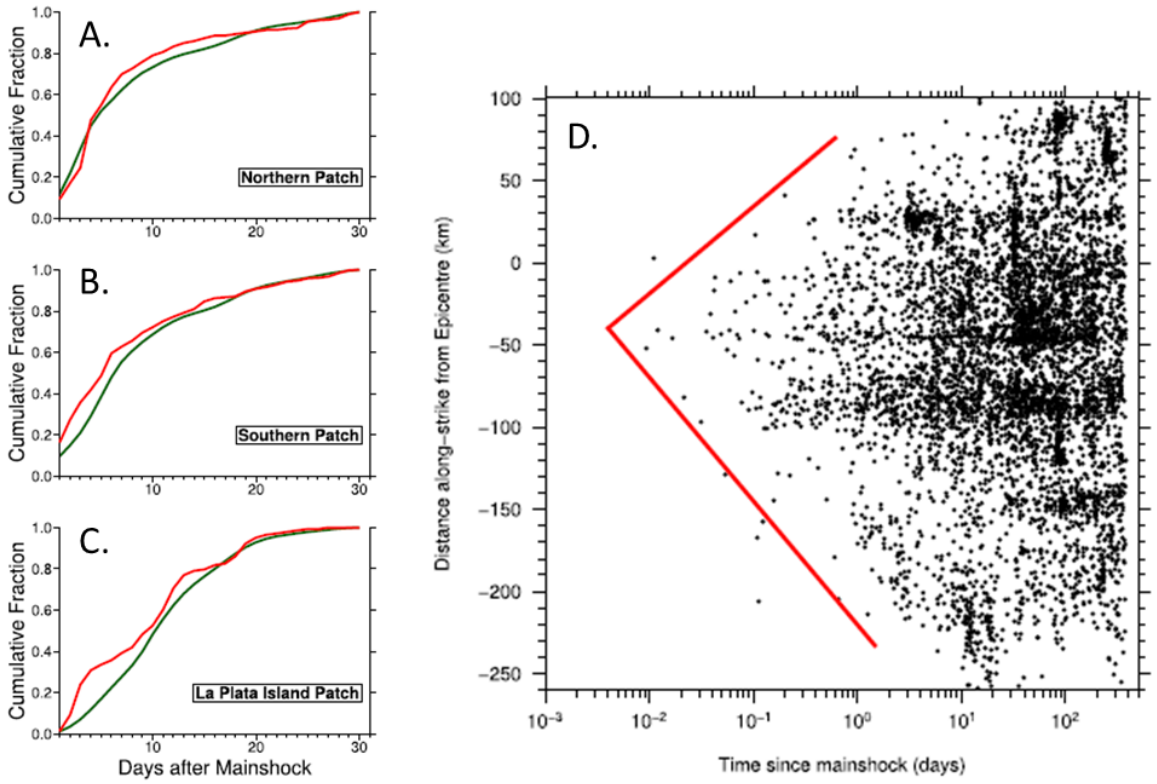

Figure 27 : Spatio-temporal evolution of aftershocks, and relationship from the afterslip, modified from Agurto-detzel et al. (2019). A-C: Cumulative number of aftershocks (in red) and cumulative afterslip (in green) as a function of time in the three main afterslip regions. D: Aftershock along-strike distance from the epicenter as a function of time. Red lines show the semi-logarithmic expansion of the aftershock region with time.

No aftershock occurs where the coseismic slip is highest, and no large aftershock with Ml > 5 occurs within the mainshock region (Agurto-Detzel et al., 2019). However; many small aftershocks concentrate inside mainshock rupture, between the two coseismic asperities (Figure

26), in an area of intermediate levels of coseismic slip (Agurto-Detzel et al., 2019). This can be explained in one of two ways. Assuming that the friction on the megathrust is very heterogeneous, it is possible that these small aftershocks occur to release the strain on the plate interface remaining after the mainshock (Agurto-Detzel et al., 2019). However, it is likely that most of these events occurred in the seismogenic volume, rather than at the interface, and that they represent off-fault damage instead (Agurto-Detzel et al., 2019).

Finally, some seismicity was triggered in the upper plate, particularly a swarms near the town of Esmeraldas (1°N, 79.6°W) (Hoskins et al., 2021). Starting two months after the mainshock, one major swarm and several small swarms occurred, almost certainly triggered by fluid diffusion and accompanied by slow slip on the upper plate faults in the region (Hoskins et al., 2021).

2.4 Outstanding questions

Several questions remain surrounding the Ecuadorian subduction zone. The first is the way in which seismic and aseismic slip coexist in the region. It seems that some creeping or slowly slipping regions may have ruptured seismically in the past. One example of this is during the 1906 earthquake, as normally creeping areas likely experienced coseismic slip. Another likely example is the 1998 Bahia earthquake, which, assuming it did happen at the plate interface, seemingly ruptured either a currently creeping portion of the megathrust, a locked patch that was found to experience afterslip after the 2016 earthquake, or a portion of the fault that also ruptured during the 2016 earthquake. In all these cases however we lack well-constrained data to confirm a change in behavior of the megathrust. Thus the question of whether and how the slip behavior of a fault can change remains. More broadly, we can also ask how frictional properties of the megathrust can evolve. Additionally, as explained before, aseismic slip often influences the seismicity rate in the region, especially after the Pedernales earthquake. We may wonder how direct this relationship is.

Another particularity of the Ecuadorian subduction zone is the way in which structural features seem to influence the seismicity. There is still debate over the influence of various features on the segmentation of the fault or the microseismicity, but it is undeniable that features like the Carnegie Ridge affect subduction. Thus we may ask how fluids and subducting features affect earthquakes and their source properties in the region.

To interrogate the relationship of seismic and aseismic slip, and the way in which the frictional properties of the megathrust evolve over time, repeating earthquakes are an ideal tool, because they are strongly associated with aseismic slip and because they recur on the same

asperity but can record frictional changes over time. I take advantage of the denser seismic network after the Pedernales earthquake to create and analyze a catalogue of repeating earthquakes in the 2015-2017 period. In this way, I am also able to evaluate the way that a large earthquake and its afterslip influenced repeating earthquakes.

Chapter 3: Data and methods

With the baseline of knowledge established in the last two chapters, we are finally ready to delve into the work performed in this study. In this chapter, I will first present the data used, before explaining the creation of the repeating earthquake catalogue. For the first part of my work, I will detail the classification process, the use of template-matching, the absolute and relative relocations, and the determination of local magnitudes. I will then discuss the computation of source processes with the use of the spectral ratios method.

3.1 Data and network

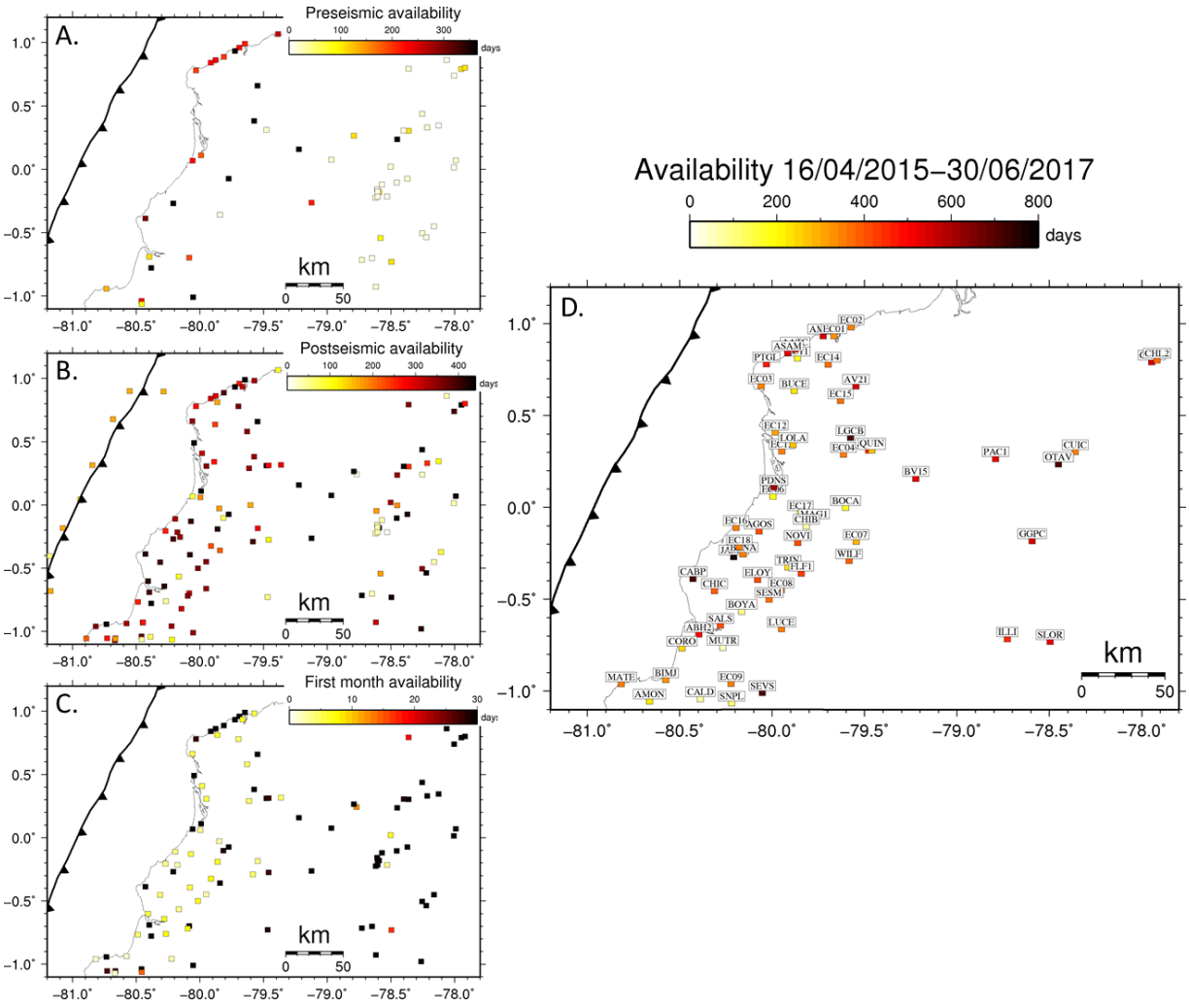

Figure 28 : Map of all stations available at various times during the study period. A: Stations available in the year before April 16th 2016. B: Stations available between April 16th 2016 and June 30th 2016. C: Stations available between April 16th

2016 and May 16th 2016. The temporary deployment of seismic stations started on May 9th 2016. D: Map of stations used in this study. The color shows the number of days each station was available during the study period, between the 16th of April 2015 and the 30th of June 2017.

Before presenting my work, I will first introduce the data I have used, along with some of its issues. Seismic instrumentation in Ecuador started in 1977 for volcano monitoring, and the seismic network was later expanded to the lowlands and the coast in the 1990s. In this study, I examined the year before and the year after the Mw 7.8 April 16th 2016 Pedernales earthquake, a time during which several seismic networks covered the region. The Permanent National Seismic Network of Ecuador (RENSIG) was active during the interseismic period and throughout the postseismic period (Alvarado et al., 2018). In 2018, this network was composed of 65 stations (Figure SB.1A) with very broadband, broadband, and short-period sensors. It also counted 2 stations belonging to the Global Seismic Network (GSN): OTAV, located ~50 km north of Quito in the Andes, and PAYG, located near Puerto Ayora in the Galápagos Islands. This allows for a coverage of the whole region, with an average distance between stations of about 30 km in the coastal region. Additionally, Ecuador has a Permanent Strong Motion Network (RENAC) composed of 117 strong motion sensors, primarily located in densely populated areas and areas with a high historical seismic hazard (Figure SB.1B). It was also in place before and after the Pedernales earthquake (Alvarado et al., 2018). Finally, in response to the April 2016 mainshock, there was an effort to better cover the area through an international temporary deployment of seismic stations, which was supported by the Instituto Geofísico at the Escuela Politécnica Nacional (IG-EPN) in Quito, different French institutions (IRD and INSU-CNRS), the US Seismic Rapid Response program and the NERC (UK) (Meltzer et al., 2019). 55 land stations were deployed starting on the 9th of May 2016, and most of the stations were removed in the middle of May 2017, while 12 were left until August 2017 (Figure SB.1C). 35 of these sensors were broadband, 14 intermediate-period and 6 short-period. Finally, 10 Ocean Bottom Seismometers (OBS) were deployed between the end of May and November 2016.

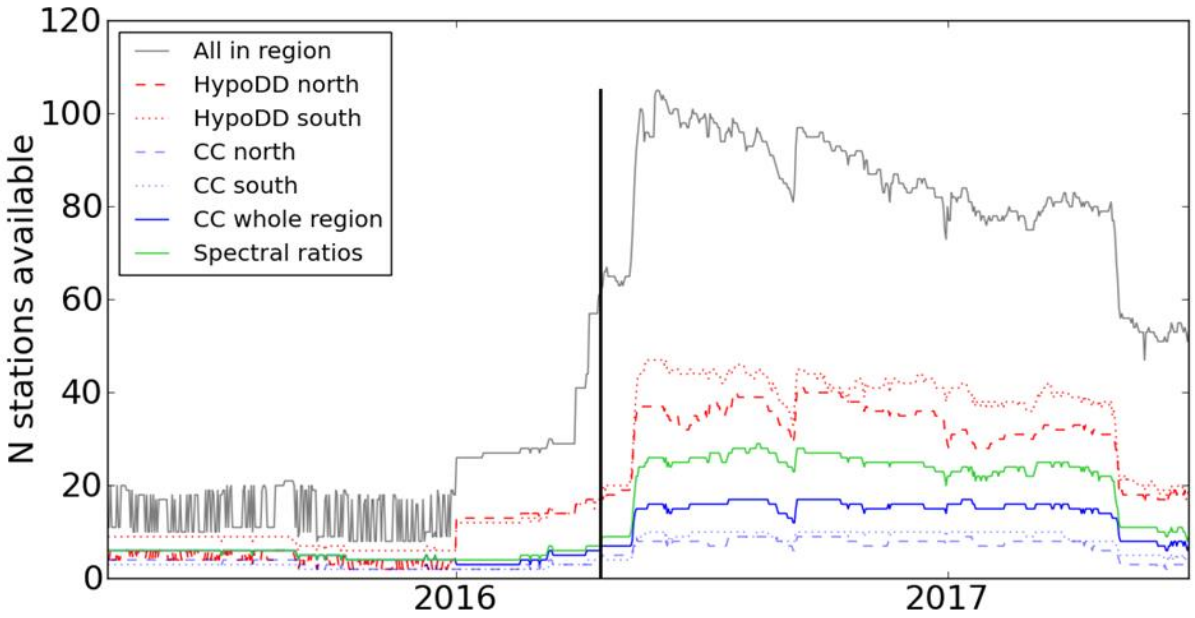

Figure 29 : Number of active stations as a function of time. The vertical black line is the time of the mainshock. The grey line shows the number of stations in the region shown in Figure 28 active on a given day. The red lines show the number of stations used for relocation with hypoDD available on a given day. The blue lines show on a given day the number of stations used for the classification of aftershocks into families of repeaters. The dotted and dashed blue lines show the number of stations for the preliminary classifications in the south and north respectively, while the full blue line shows the number of stations for the final classification over the whole region.

Successive deployments generate considerable variation in the station coverage over my study period, as I show in Figure 28, Figure 29 and Figure SB.2. The stations I have used are shown in Figure 28D. They were selected based on a few criteria. The first was the overall availability of the station, to ensure homogeneity for my study. Particular importance was paid to whether the station was available during the first month following the mainshock, as that is when the aftershock rate is highest but the station coverage is still poor. I also included stations which were available before the mainshock when possible. Second, I checked the quality of the station. For this, I made average spectra of the Z component for all candidate stations. I show these average spectra using all earthquakes within 140 km of the station (ex: Figure 30), with the exception of OTAV for which no distance limit is enforced (Figure 31). These average spectra allowed me to both find high-quality stations and decide on their frequency range for the rest of my work.

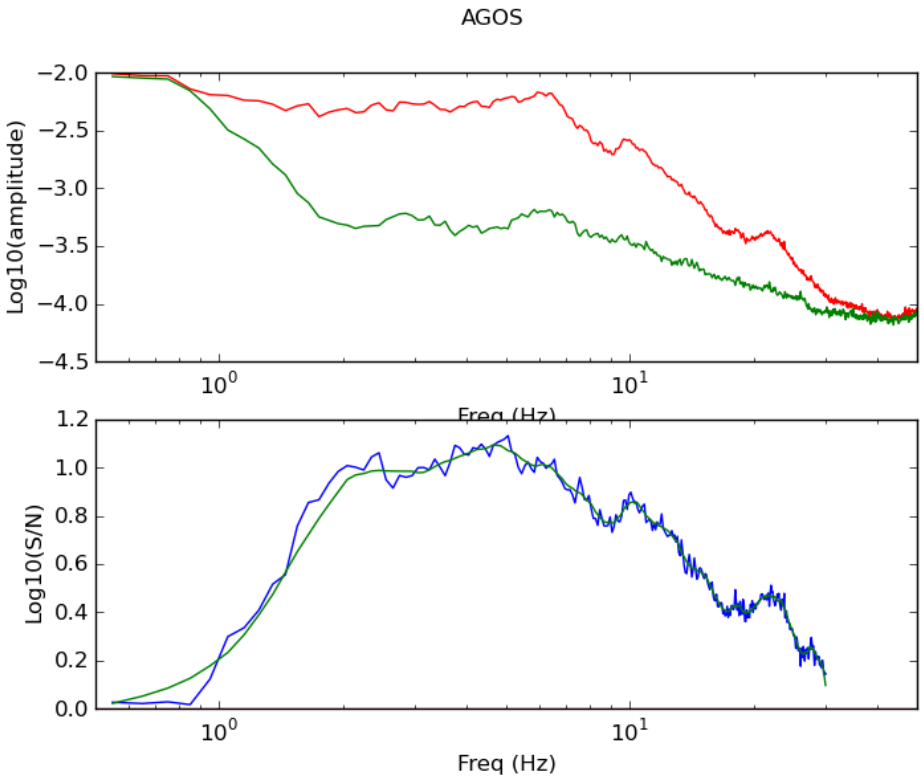

Figure 30 : Top panel: average spectrum of the vertical component of AGOS station, for 30 s of earthquake recordings (red) and for 30 s of noise ending 10 s before the P arrival (green). Bottom panel: average signal-to-noise ratio as a function of frequency (blue). The green curve is the smoothed average.

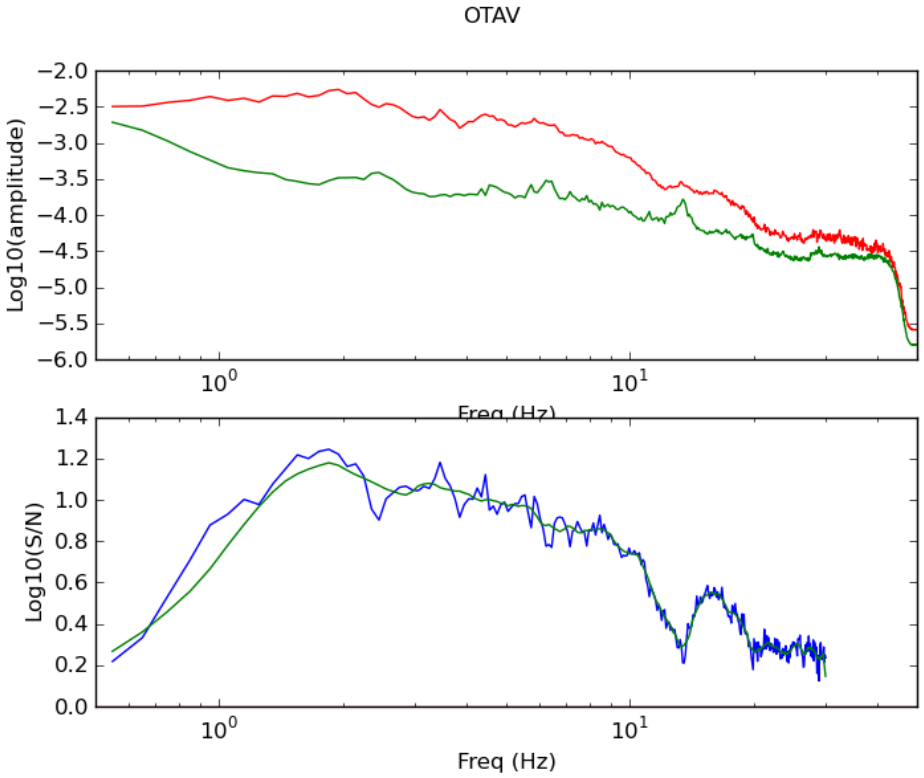

Figure 31 : Top panel: average spectrum of the vertical component of OTAV station, for 30 s of earthquake recordings (red) and for 30 s of noise ending 10 s before the P arrival (green). Bottom panel: average signal-to-noise ratio as a function of frequency (blue). The green curve is the smoothed average.

Due to the sparsity of stations with both continuous coverage and high quality, some stations with notable issues were used. I will now briefly list the issues encountered for stations that were still used for parts of my analysis. The first is the issue of distance, specifically for OTAV, which is far away from the coast. Despite this, I decided to use OTAV as it is almost always active and of very high quality. The second issue I encountered was the clock delays of ELOY station. The ELOY station clock starts having a delay 320 days after the mainshock, which gradually increases after that point. After 360 days, this delay stabilizes at around 7 seconds. (Figure SB.3). Despite this issue, the signal quality of the station remains very high, which is why I still used it for part of my study. The delay means the station is unusable for relocation in 2017, but for other uses I applied a rough clock correction based on the delays obtained in Figure SB.3 and the manual pick delays. I started with a correction of 1 s 260 days after the mainshock, and after 317 days I gradually increased the correction before stabilizing it at 7 s after 360 days. Doing so allowed me to use the station for template-matching, correlation calculations and spectral ratio fitting. Another issue that I ran into was the fact that some stations had an unusable component. One such station is CABP, whose Z component seems to be random noise before the 26th of April 2016. It can therefore not be used during that period, although the horizontal components can be used to calculate spectra (Figure 32). Similarly, the N component of LGCB has frequent spikes and is therefore unusable, so only the E component is used when calculating horizontal spectra. (Figure 32). During the interseismic period, PDNS and LGCB also have a lot of small data gaps and spikes on the Z component, which render them difficult to use. Noise at specific frequencies was also an issue. Notably, NOVI station intermittently has high frequency noise (Figure 32). When calculating correlations, this was not an issue as the filter corner frequency is low enough to suppress it. For the calculation of spectral ratios, this was dealt with by cutting off high frequencies if either the signal or the noise had a higher average amplitude in the 12-20 Hz band than in the 4-10 Hz band. Finally, the last problem encountered was the sampling rate of CHIB, which changes from 200 Hz to 100 Hz after the 8th of July 2016. This led me to avoid using the station past that point.

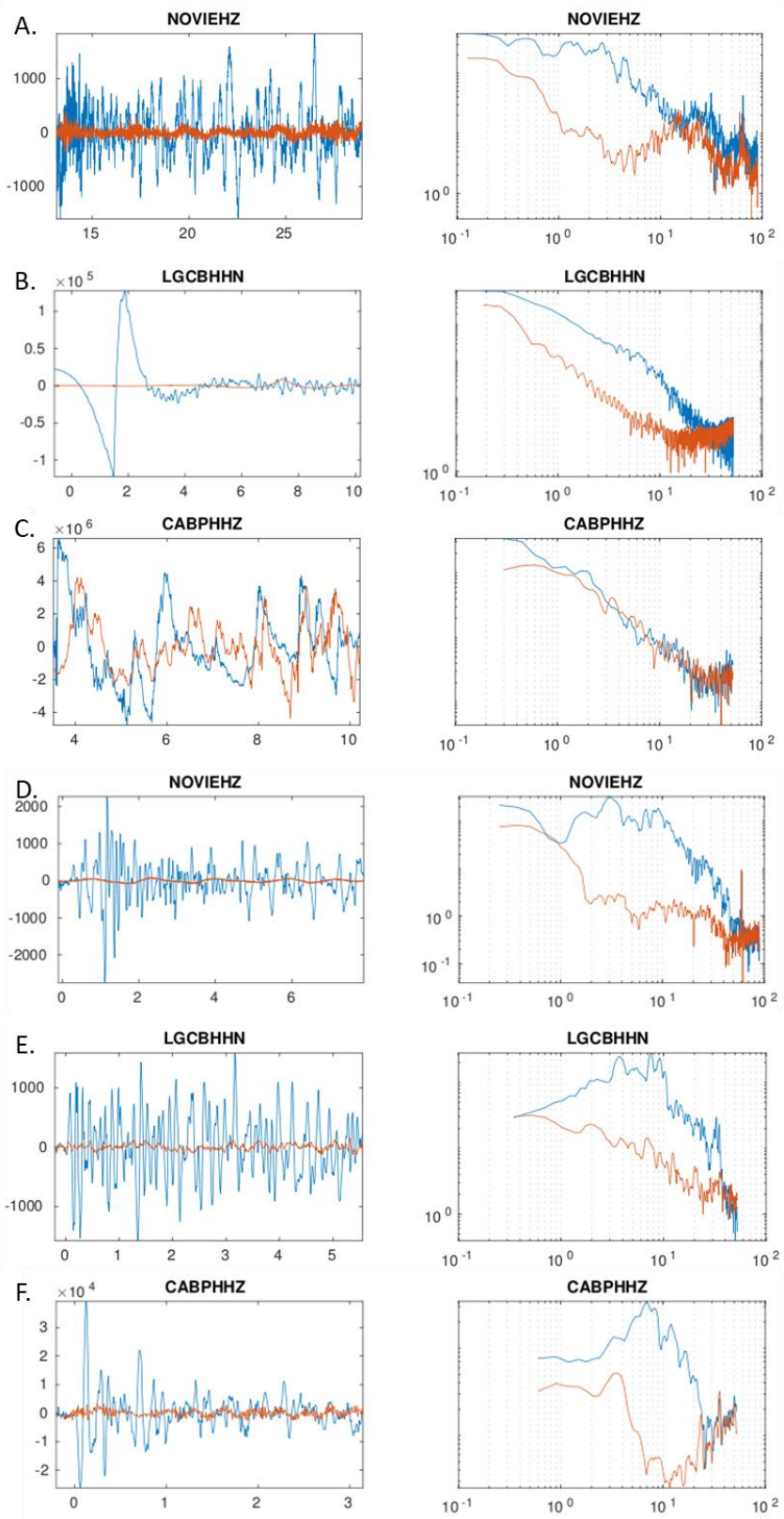

Figure 32 : Examples of seismic signals for P (B, D, E and F) and S (A and C) waves. Blue lines are the signal and red lines are noise. On the left panel is the seismogram and on the right is the spectrum. A-C: Stations with issues on one or more component. D-F: Good signal from these same stations.

As a basis for my analysis, I used the catalogue of 7326 aftershocks detected between April 16, 2016 and April 30, 2017 by Agurto-Detzel et al. (2019). They constructed this catalogue using a mix of manual and automatic picks obtained using SeisComP3 (https://www.seiscomp.de/seiscomp3/). For P phases, they obtained arrival times using a standard STA/LTA algorithm, while for S phases the AIC picker implemented in SeisComP3 was used. In both cases the data was filtered, either between 1 and 10 Hz for seismometers or between 1 and 8 Hz for accelerometers and OBS. SeisComP3 was used to associate, locate, and calculate the magnitude of seismic events. Around 800 automatically detected events were then manually picked during the first month of aftershocks to improve the quality of the catalogue. Agurto-Detzel et al. (2019) later relocated events using NonLinLoc (Lomax et al., 2000) and a simplified velocity model shown in Table 1 (Agurto-Detzel et al., 2019), which I used in my study for the sake of consistency. This catalogue has local magnitudes ranging between 1 and 6, although 80% of earthquakes have magnitudes between 1.8 and 3.6, and a magnitude of completeness of 2.5 (Figure 33) (Agurto-Detzel et al., 2019). Most aftershocks are situated updip of the rupture zone in the three regions of Punta Galera, Cabo Pasado and La Plata Island, or in the upper crust within and north of the rupture zone (Agurto-Detzel et al., 2019). However, as I concentrated on a smaller region than Agurto-Detzel et al. (2019), I only used a subset of 4767 events from the catalogue for the rest of this work.

Velocity model		
Depth of layer top (km)	Vp (km/s)	Vs (km/s)
0	5,07	2,85
20	6,76	3,82
30	7,43	3,92
120	8,81	5,22

Table 1: Velocity model from Agurto-Detzel et al. (2019) used in this study.

Having arrival time estimates for all events was necessary for the rest of this analysis, particularly when computing correlations between events and calculating spectral ratios. Because some earthquakes have no manual picks, I used NonLinLoc with this velocity model and the catalogue locations to create synthetic picks, which were then corrected using station delay terms obtained from the relocation of manually picked earthquakes. The sometimes poor locations of the original catalogue mean that these synthetic picks can have large errors. When comparing synthetic picks based on an automatic earthquake location to manual picks, the average difference is 0.4 s for the P wave and 0.7 s for the S wave. However, 1% of P synthetic picks have an error greater than 2 s and 1% of S synthetic picks have an error greater than 3.4

s. This is why I also picked some events manually to improve their accuracy, as will be discussed later.

I have introduced the seismic stations used in this study along with some of their issues, as well as the aftershock catalogue used for the rest of this study. Using this seismic data, the identification of repeating earthquakes can be further carried out, as introduced by the following sections.

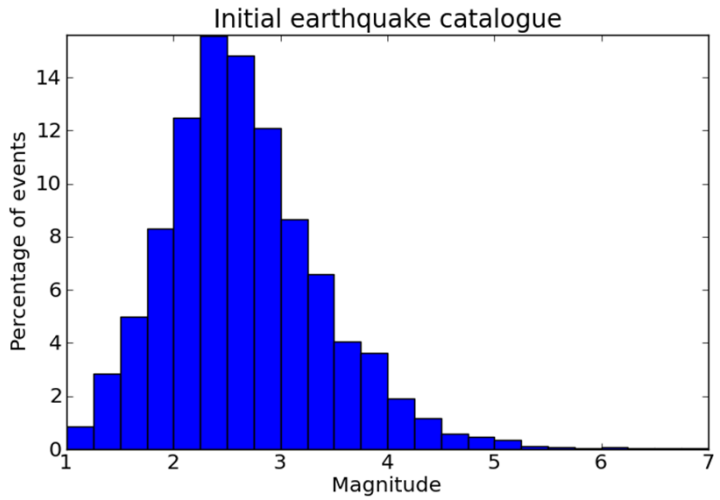

Figure 33 : Histogram of magnitudes in the catalogue of Agurto-Detzel et al. (2019) for the study region.

3.2 Classification of repeaters

The first step of my work was the creation of a repeating earthquake catalogue for the year following the Pedernales earthquake. Here I explain how I found families of repeating earthquakes within the subset of 4767 events in the region from the catalogue of Agurto-Detzel et al. (2019). The processing presented in this section is summarized in Chapter 4, and a simplified flowchart of the process is shown in Figure 34.

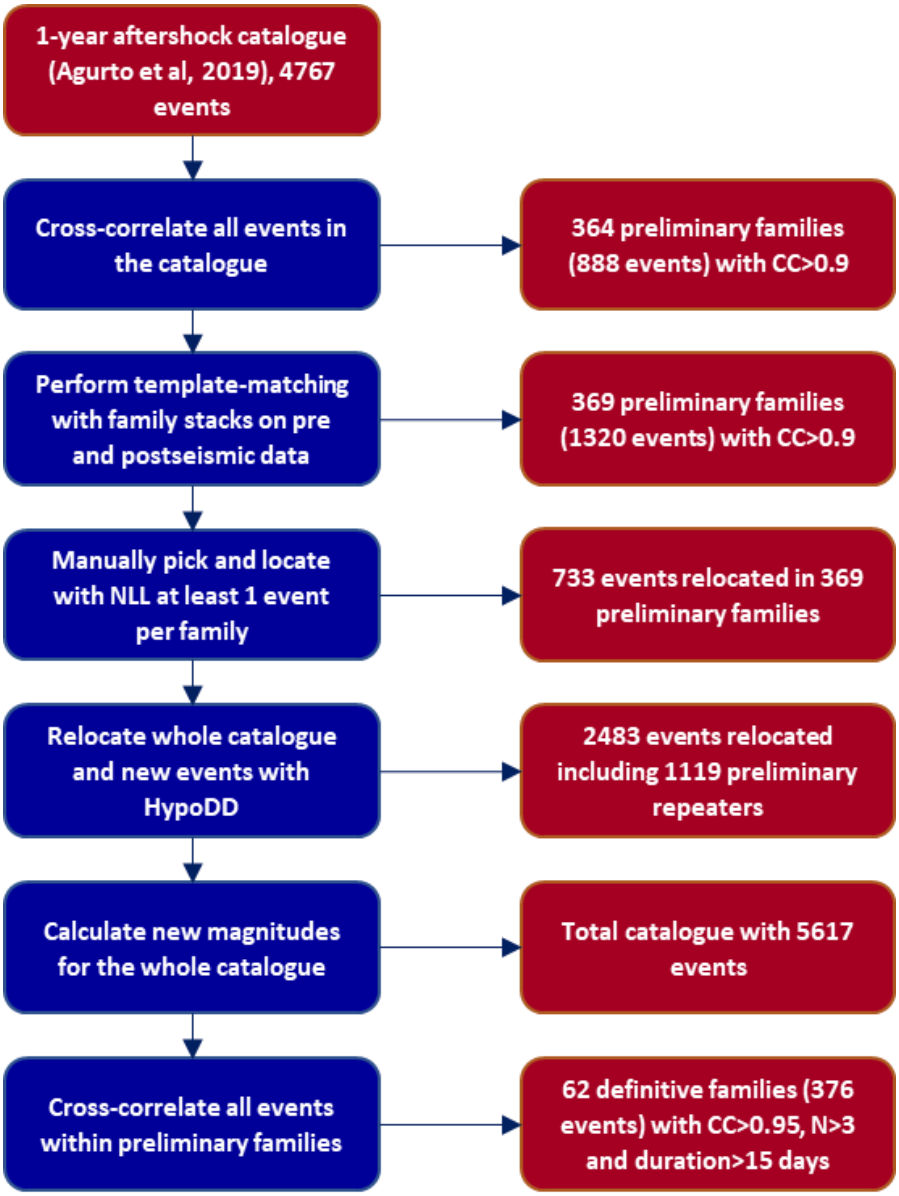

Figure 34 : Flowchart showing the main steps of the data processing done to obtain a catalogue of repeaters, by Chalumeau et al. (2021).

My initial goal was to correlate the 4767 aftershocks from the Agurto-Detzel et al. (2019) catalogue which occurred within my study region and derive repeating families from that catalogue, which would then be completed by using template-matching and further refined using double-difference relocation. However, only a small region in the north was initially analyzed. This was done both to make the initial analysis computationally easier, and to test and validate the methodology. The work was later extended to the south, and I show in Figure 35 these two groups of earthquakes. As a result of this initial separation, the calculation of correlations was performed twice, once in the north and south separately, and then over the whole study region. Initially, repeating families were constituted within the north and south regions using different stations, which were used for template-matching as well. However, after

relocating the families and merging the two regions, I realized that new correlations needed to be computed using a common set of station over the whole area, in order to obtain a homogeneous catalogue of repeaters. For this final calculation, only earthquakes that had previously been classified in families with correlation coefficients above 0.9 were examined. From now on, I will refer to the initial families obtained in the north and south as preliminary families, and to the families obtained from the correlations over the whole region as the final families.

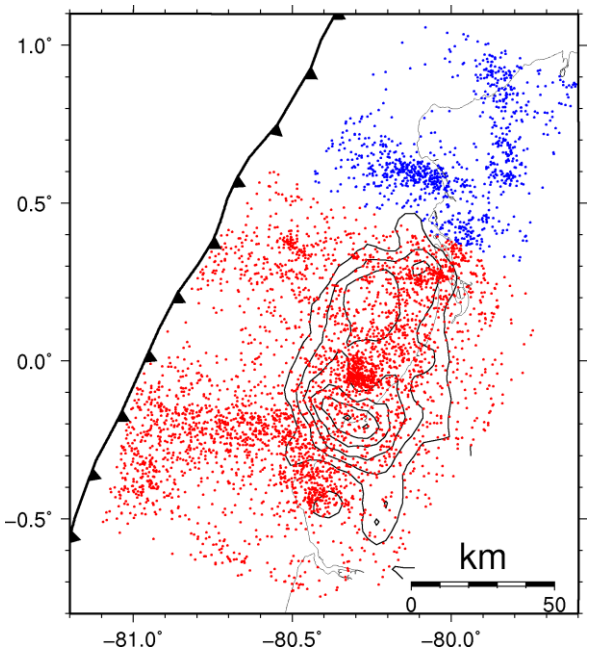

Figure 35 : Map of initial locations of aftershocks used in this study, initially in the catalogue of Agurto-Detzel et al. (2019). Blue events are events from the northern region, and red events are events from the southern region. The 1m contours of the 2016 Pedernales earthquake are shown in black (Nocquet et al., 2017).

I show the stations used and their availabilities in Figure 36. When calculating correlations, I decided to give stations different frequency bands to maximize the detection capability, especially since the network is uneven in space and time. When deciding on an appropriate frequency band, I considered the frequencies at which the average S/N ratio was high, though the threshold depended on the station. However, the upper boundary also needed to be high enough to separate two distinct nearby events, while remaining below the corner frequency to avoid dealing with source complexities (Uchida, 2019). Two events generally cannot be separated using correlation coefficients when the hypocenters are within a quarter of the dominant wavelength (Geller and Mueller, 1980). According to Eshelby (1957), the source radius is given by $R = (\frac{16\Delta\sigma}{7M_0})^{1/3}$ with $\Delta\sigma$ as the stress drop. Assuming a stress drop of 3 MPa typical in a subduction zone (Allmann and Shearer, 2009), and a local magnitude equal to the

moment magnitude, a Mw 1.8 earthquake with a circular source area would have a source radius of about 45 m. Therefore, with an average shear wave velocity of 3.7 km/s (León-Ríos et al., 2019), an upper boundary of 10 Hz should be able to separate two completely distinct repeaters. Meanwhile, corner frequencies are given as $f_C = k\beta(\frac{16\Delta\sigma}{7M_0})^{1/3}$ from Eshelby (1957) and Brune (1970), with β the S wave velocity, and a k constant equal to 0.38 for P waves and 0.26 for S waves (Kaneko and Shearer, 2014). I expect a Mw 3.6 earthquake to have a P corner frequency of 3.9 Hz and an S corner frequency of 2.7 Hz. In spite of the likely variability of stress drops and rupture velocities, I therefore expect my chosen frequency bands, with a low frequency of 1.5-3.5 Hz and a high frequency of 9-10 Hz (TABLE SA) to be able to detect most repeaters.

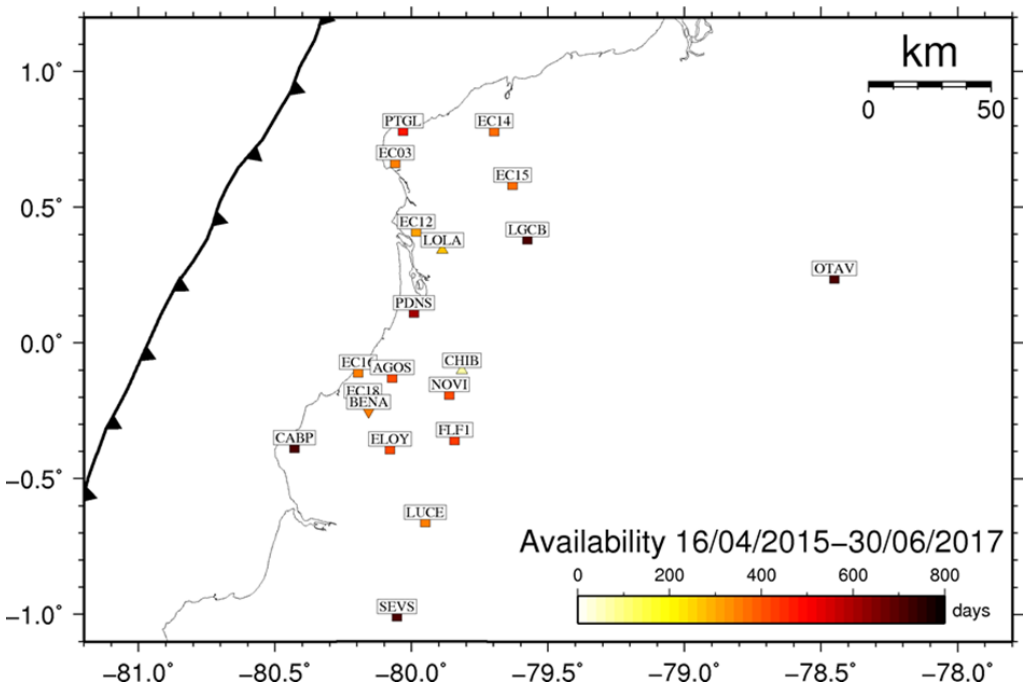

Figure 36 : Map of stations used for the correlation coefficient calculations. Squares are stations used in the final classification over the whole region. Triangles were used only for the initial classification in the north, and inverted triangles were used only for the initial classification in the south.

I decided to calculate correlation coefficients over a time period including both P and S waves to find repeating earthquakes. For this purpose, I used a 30 s window starting 2 seconds before the P wave for the final calculation for all stations except OTAV, for which I used a 57 s recording also starting 2 seconds before the P wave. P arrivals were determined using either manual or synthetic picks, and I calculated the correlation coefficient of two earthquakes by sliding the two windows sample by sample over 10 seconds to ensure that no event was left out due to a wrong location or timing.

The correlations resulting from the preliminary inversions are shown in Figure 37 and Figure 38. In both regions the mean correlation is very low, but the maximum correlation tends to be high, and there is a sudden increase in maximum correlation coefficient above 0.9. This demonstrates the specific presence of repeating earthquakes as a category separate from regular earthquakes, and informs the choice of threshold correlation coefficient used to sort earthquakes into preliminary families. Classification of repeating earthquakes is often done based on two parameters: cross-correlation, which requires a good S/N, and inter-event distance, which requires very low relative location errors, typically achieved with double difference relocation. My initial goal was to first use cross correlations to sort earthquakes into families, then add undetected events with template-matching, and finally refine this classification with double difference relocations. Because the goal was to use both locations and correlations, I initially decided on a threshold of 0.9 for the preliminary classification in the north and south, to allow for low S/N events to be included, while remaining in a range of correlations that most studies use (Uchida, 2019). However, I realized later on that location errors and incomplete relocations made it impossible to use inter-event distance to discriminate between real and apparent repeaters. I therefore used a higher correlation coefficient of 0.95 for the final classification over the whole region, since it was my only selection criterion.

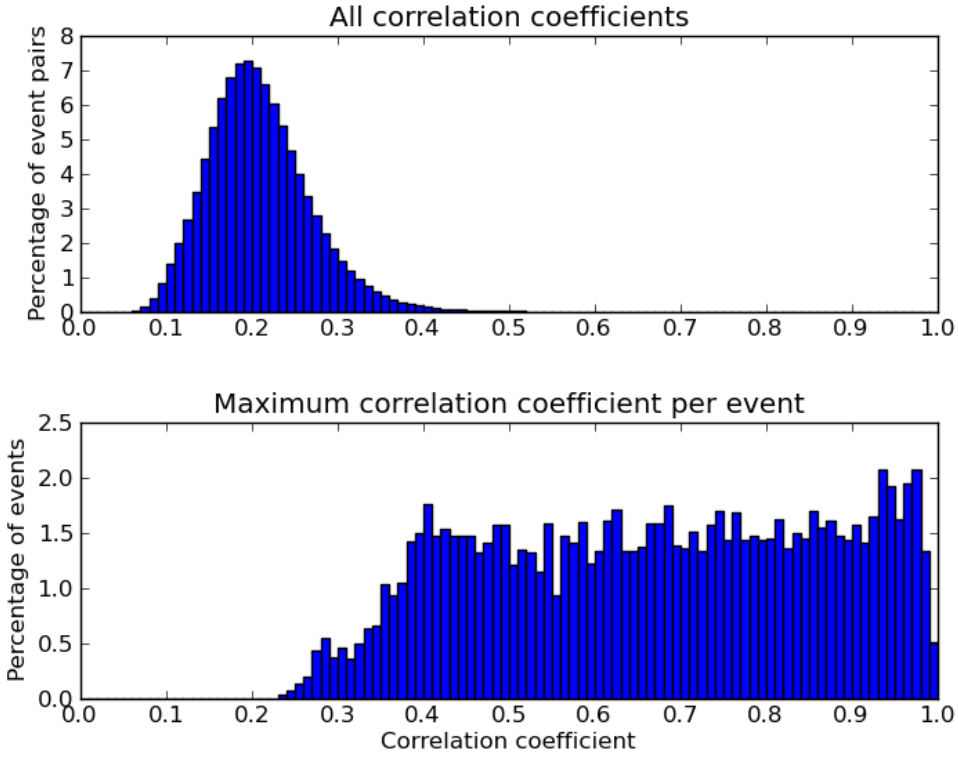

Figure 37 : Correlation coefficients calculated between aftershocks in the northern region. The top panel shows every correlation coefficient calculated in the region, for all stations and all event pairs in the catalogue. The bottom panel shows, for every event in the catalogue and for every station, the maximum correlation coefficient obtained with another event.

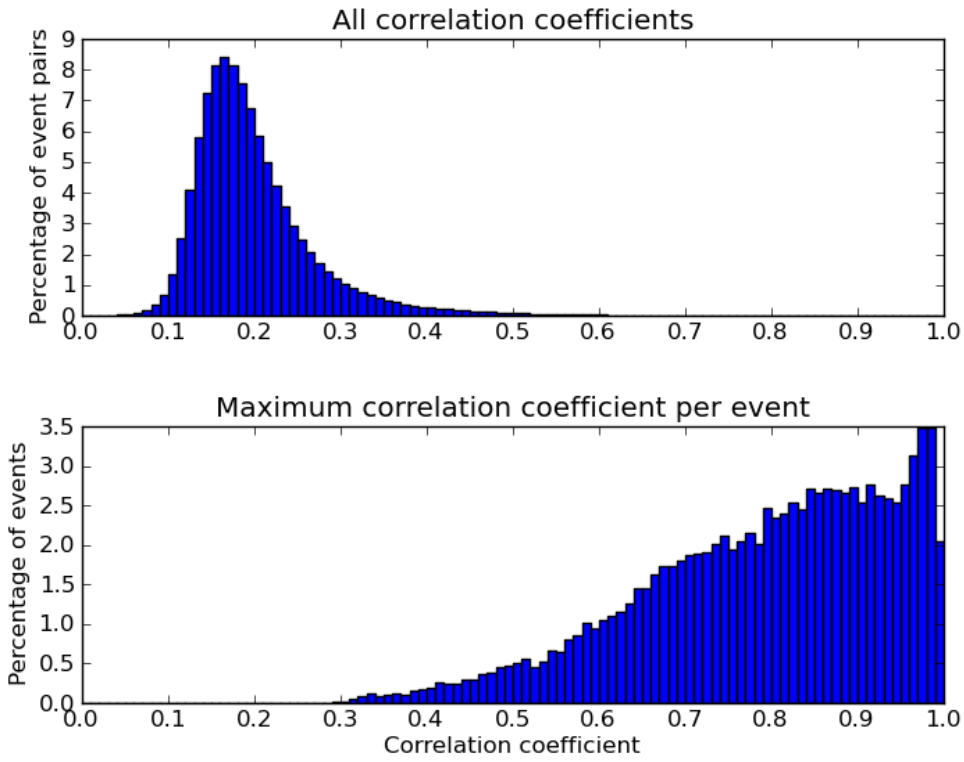

Figure 38 : Correlation coefficients calculated between aftershocks in the southern region. The top panel shows every correlation coefficient calculated in the region, for all stations and all event pairs in the catalogue. The bottom panel shows, for every event in the catalogue and for every station, the maximum correlation coefficient obtained with another event.

When gathering repeaters into families, events were included within a family if they had a high correlation coefficient with at least 2/3 of the events already within a family for at least 1/3 of the stations in common with those other events. I decided on 1/3 as the minimum number of stations due to the uneven network and heterogeneous quality, which made having a fixed station minimum impossible, and meant that the event-station distance in the first month in particular was often large. Additionally, families are merged if their stacks had a correlation coefficient above the correlation threshold for at least one third of stations present. At the preliminary stage, no limit on size was put on families of repeaters. However, after the template matching and the final classification over the whole region, families of 2 or 3 events were removed, as well as families spanning less than 15 days. This was done to remove families composed only of near-consecutive ruptures, as those were likely to be earthquakes occurring on neighboring patches rather than on the same asperity (Lengliné and Marsan, 2009). I am also more confident in families with more earthquakes, as the classification relies on more cross-correlation measurements. One example of waveforms for one family is shown in Figure 39.

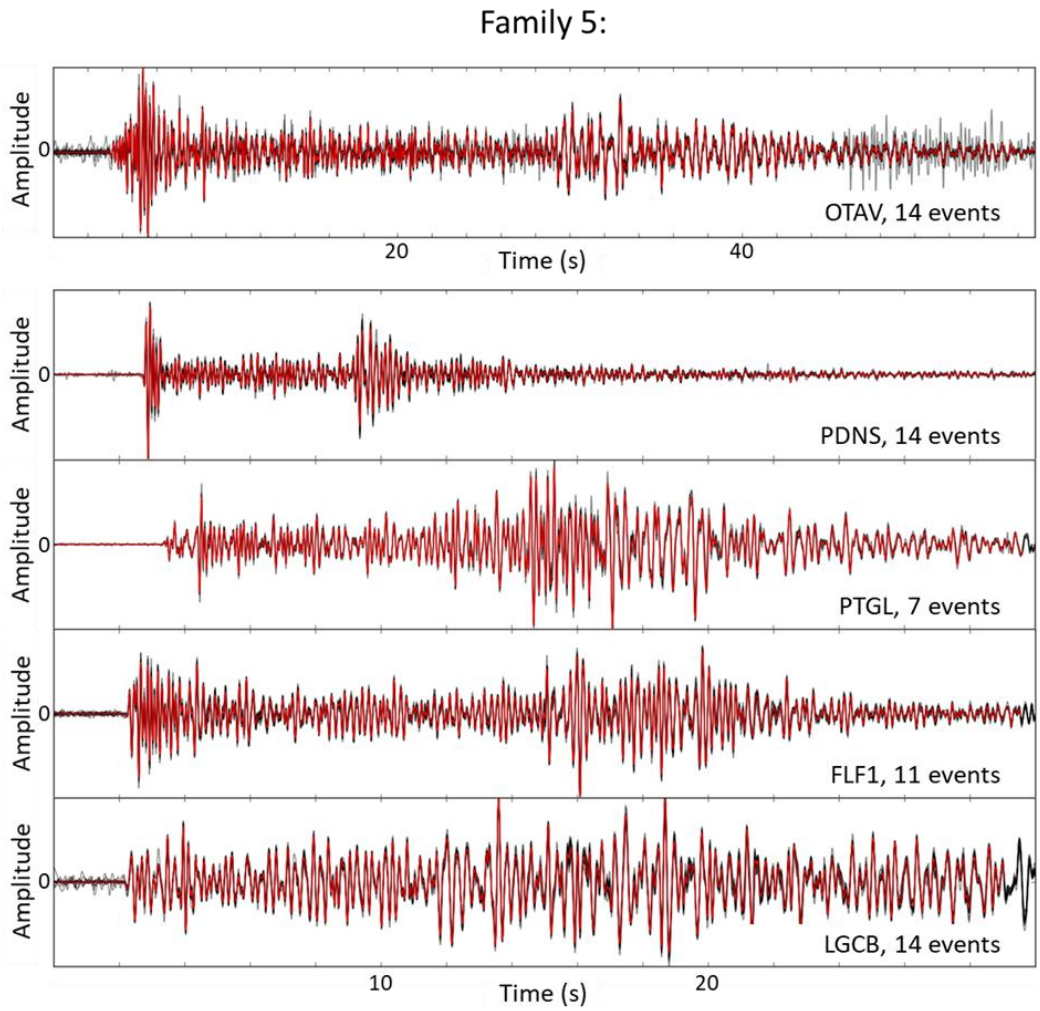

Figure 39 : Example of waveforms of repeating earthquakes for one family. All available individual event waveforms are shown in grey and the stack of all available waveforms is shown in red.

The number of families and repeating events found by the different inversions is shown in Table 1. The two initial inversions in the north and south yielded 409 families for a total of 1046 repeating earthquakes. These were, however, incomplete families, and template-matching was necessary to find missing repeaters. The final inversion on the whole region, which was done on the whole region with a complete catalogue, yielded 62 families of 4 to 15 repeating earthquakes.

	Correlation calculations summary		
Region	North	South	Whole region
Number of stations used	10	10	17
Maximum event-station distance (km)	-	-	140 (280 for OTAV)

Maximum lag (s)	5	5	4
Time window (s)	22	26	30 (57 for OTAV)
Minimum CC	0,9	0,9	0,95
Number of families	90	319	62
Number of repeaters (before template matching)	195	851	-
Number of repeaters (after template matching)	386	1629	376
Doublets and triplets removed	No	No	Yes

Table 2: Summary of the preliminary and final classifications of repeating earthquakes performed first in the north and south and later over the whole region.

3.3 Template matching

I conducted template-matching in the area with the goal of finding repeating earthquakes that had been omitted from the catalogue and to extend the analysis to the interseismic period. Template-matching was conducted between the 16th of April 2015 and the 15th of June 2017 using the code Fast Match Filter (Beaucé et al., 2017). I decided to scan the year before the mainshock in an attempt to find out families that had been active during the interseismic period, and, if possible, to obtain their recurrence time. However, because very few stations were active in 2015, I decided against continuing my search before that. I used template-matching until the 30th of June 2017, at which date a Mw 6.3 earthquake happened off the coast of Cabo Pasado.

Template-matching is often used to detect any missing earthquakes, whereas I specifically looked for repeating earthquakes, using only them as templates. In studies where repeaters have been detected, the largest events within a family are often used as the template, which can then make it easier to calculate magnitudes by using it as reference (Frank and Abercrombie, 2018; Gibbons et al., 2007). However, because of the uneven network, most earthquakes were not recorded by every station, making the use of several earthquakes per family inevitable when creating templates. I therefore used a stack of every earthquake within a given family available at a given station as template. Doing so also allowed me to reduce noise for my templates, leading to better detection capacities. For this reason, events with anomalously low S/N were not included when stacking, to avoid worsening the final stack.

Along with templates, Fast Match Filter takes template moveouts as input, which refer to the templates' delays relative to the origin time, and station weights. These are necessary when using all stations at the same time. However, I elected not to do so, instead scanning the data

station by station. While this was undoubtedly slower and greatly increased the size of the code output compared to using all stations at once, it also gave me more control on the results. I did, however, estimate moveouts for each template at each station. Although not strictly necessary when performing template-matching station by station, they were useful in retrieving accurate origin times, which were needed to associate the detections of a single event at different stations. In order to calculate moveouts, I correlated templates with recordings of all the earthquakes within the family, eliminating those with low correlations due to noise, and then I took the median of the stations' moveouts. Thanks to this, in most cases the origin times predicted by different stations detecting an earthquake with the same template were within 0.05s of each other.

In order to optimize calculation and storage I decided to downsample the data. I tried different sampling frequencies above 20 Hz, since stations' upper frequencies could be up to 10 Hz and found a downsampling to 60 Hz provides accurate CCs.

When scanning the data, I singled out earthquakes with a CC higher than 0.9 with one template. Detections within 5 s of each other were grouped together, which ensured that the same event detected by two different templates was not classified in two different families. In cases where two templates were highly correlated with an event, the event was assigned to the family with the maximum number of stations detecting it. If the number of stations was the same, then whichever template had the largest maximum correlation coefficient determined the family of the new earthquake. Once the earthquakes were detected, they were compared to events already in the catalogue. If they were within 12 s of another event, then the two were considered to be the same event. New repeaters were then assigned their family number and the average family location.

Using my existing template-matching files, I attempted to detect new events during the year before the mainshock, with the hope of finding repeating families absent from the postseismic period. This is a more typical way of performing template-matching, when any correlation with a template event above a certain correlation threshold is considered a newly detected earthquake. I set for each station the detection threshold as 10 times the median absolute deviation (MAD) of the daily correlation coefficient, which is within the range of thresholds used in the literature (Shelly et al., 2016; Walter et al., 2016; Jing Wu et al., 2017). For a randomly distributed variable with a normal distribution, the standard deviation is equal to 1.4826 MAD. Therefore, the probability of randomly exceeding 10 times the MAD is $7.66*10^{-12}$. In the south, 3 stations were active in the interseismic period and 315 templates were used, making the probability of a random false detection about 4% per day. In the north, where 4 stations were active in the interseismic period and 84 templates were used, the probability of a random false detection is about 1% per day. I was therefore satisfied that random detections would remain rare. I did, however, have to contend with a lot of false

detections due to spikes in the filtered and downsampled data, particularly for LGCB and PDNS stations, which some templates detected, almost always with the same correlation coefficient. After careful inspection and removal of certain detections, and the increase of the detection threshold to 0.6 for PDNS, I considered that any event detected at a minimum of one station with a minimum time difference of 15 s from another detection was an earthquake. I correlated these events together to find 6 families of 2 to 4 events each in the north and 6 families of 2 to 3 events each in the south.

Thus I used template-matching to add a total of 969 events to the catalogue. Among them, 134 events were classified as repeaters in the final inversion over the whole period.

3.4 Relocation

It was necessary for my analysis to have accurate relative and absolute locations for repeating earthquakes at least, in order to best constrain the spatial relationship of repeaters to afterslip. For this, earthquakes were relocated in two steps: first I performed absolute relocation using NonLinLoc with all manually picked earthquakes, then I relocated as much of the catalogue as possible with double difference relocation. These steps and their results are shown in Figure 40 and Figure 41.

Absolute relocations using NonLinLoc were performed before the template-matching, which improved the estimations of origin time. I either picked or added picks for 580 events, which brought the total number of manually picked events to 766 out of 4767 events in the catalogue for the region. At least one earthquake in every preliminary family was picked and relocated to ensure every family location was well constrained, and after the relocation I allocated the average family location to all non-relocated earthquakes within a family. Additionally, I allocated the average cluster location to all earthquakes belonging to a cluster where CC > 0.8, as I did not expect these earthquakes to be more than a few hundred meters apart, and this improved their locations considerably. Interseismic families were a particular concern, as only few stations were present to pick them. I relocated all interseismic repeaters with resolvable hypocenters, although most events only had 6 picks or less, making their location uncertainties very high.

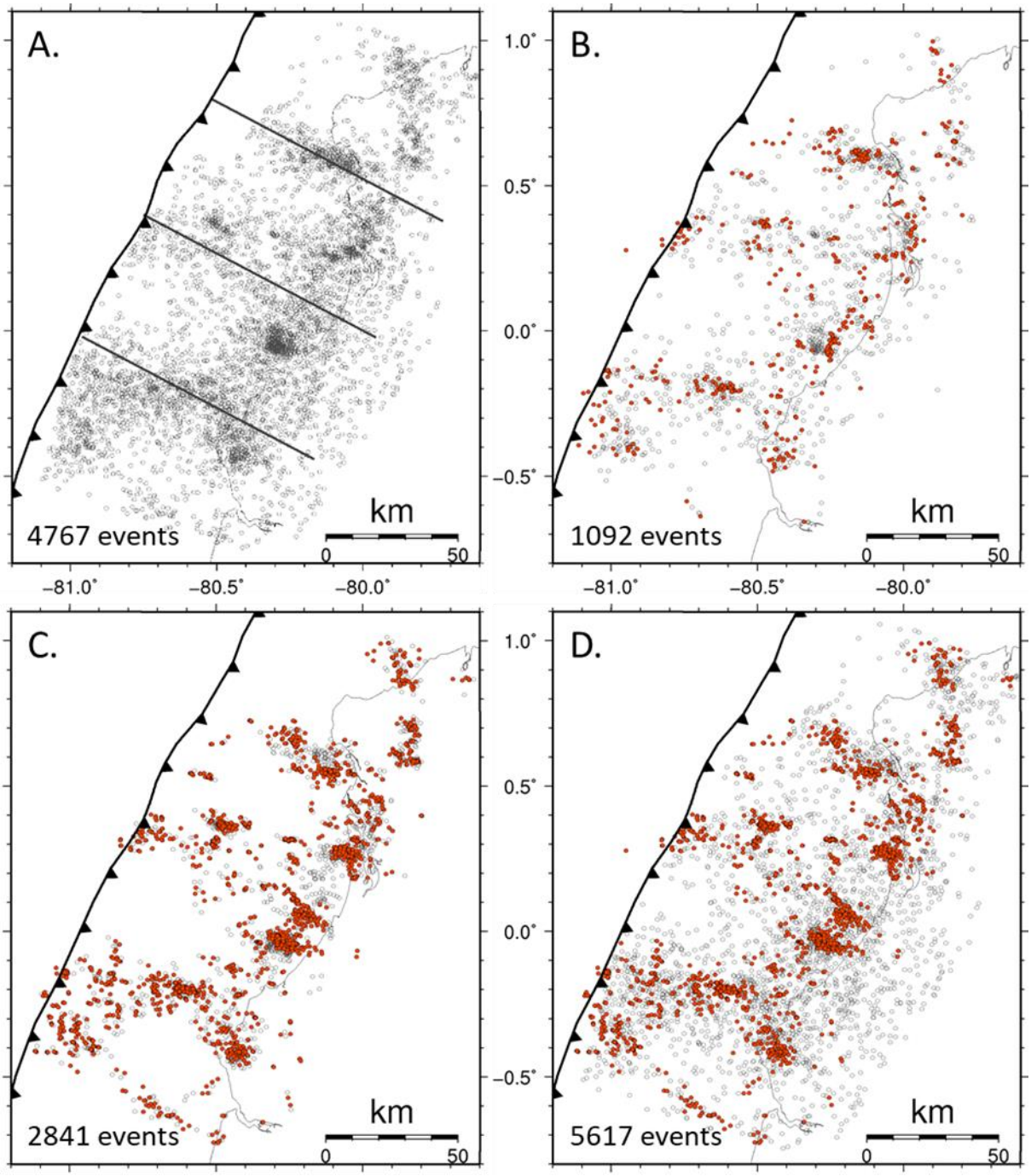

Figure 40 : Relocation of the catalogue. A: Initial positions of all events used (open grey circles). The three lines show the location of the three cross sections shown in Figure 41. B: Events relocated with NonLinLoc using manually picked arrival times (red circles). The figure also shows events that were not relocated, but that belong to clusters of earthquakes with correlation coefficients above 0.8. These events were assigned the average location of the cluster's relocated events. The initial locations of all displayed events are shown as open grey circles. C: Events relocated with HypoDD (red circles). Again, the initial locations of all displayed events are shown as open grey circles. D: Full catalogue after relocations and merging. Filled red circles are relocated earthquakes and open grey circles are non-relocated earthquakes.

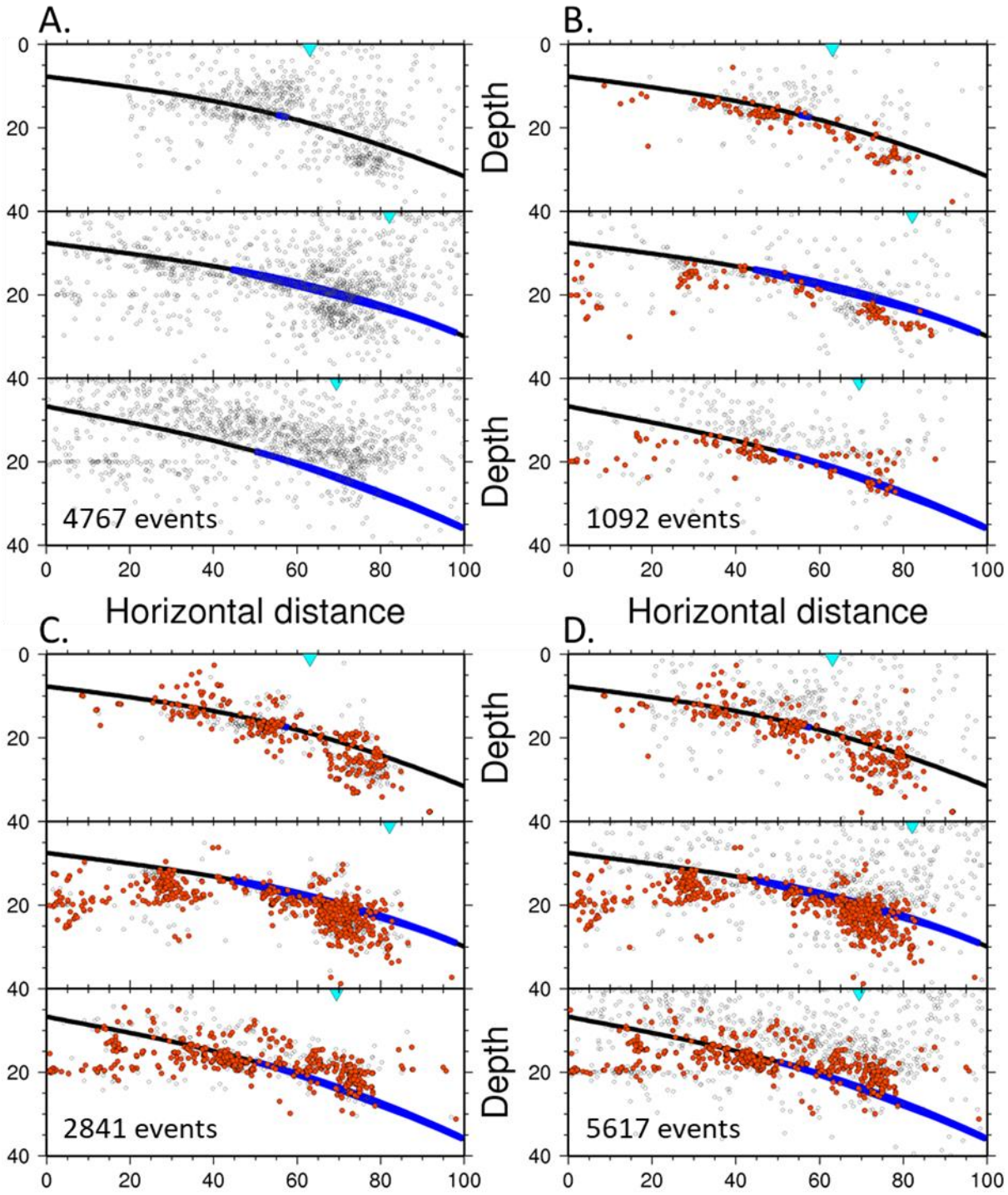

Figure 41 : Relocation of the catalogue in depth. The black line is slab 1.0 (Hayes et al., 2012). The blue line is the portion of the megathrust that slipped by more than 1 m during the mainshock. The blue inverted triangle is the coastline. A: Initial positions of all events used (open grey circles). B: Events relocated with NonLinLoc using manually picked arrival times (red circles). The figure also shows events that were not relocated, but that belong to clusters of earthquakes with correlation coefficients above 0.8. These events were assigned the average location of the cluster's relocated events. The initial locations of all displayed events are shown as open grey circles. C: Events relocated with HypoDD(red circles). Again, the initial locations of all displayed events are shown as open grey circles. D: Full catalogue after relocations and merging. Filled circles are relocated earthquakes and open circles are non-relocated earthquakes.

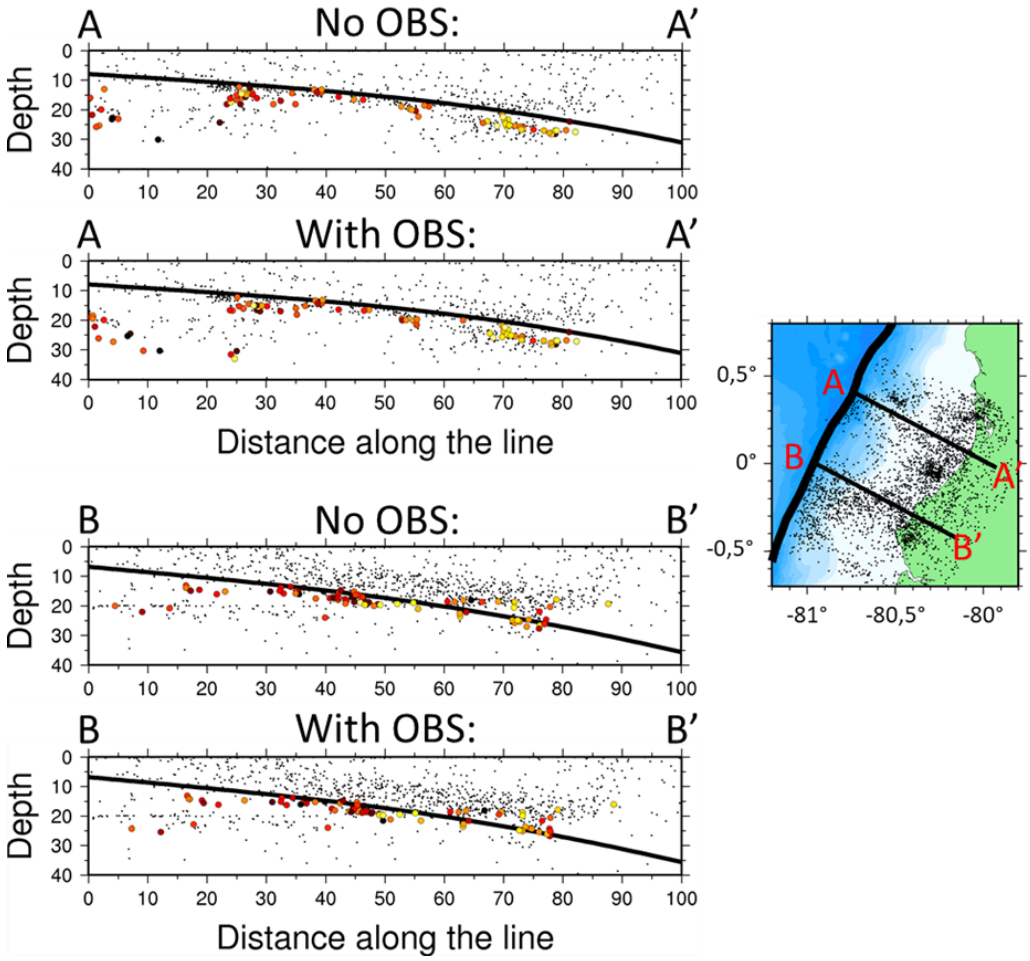

Figure 42 : Relocation in the south with or without the OBS. Black dots are the unrelocated catalogue, colored circles are the relocated preliminary families of the southern region.

When performing relocations, I decided not to use OBS stations for two reasons. First, some, like XE09, probably had clock issues, as XE09 had an average P arrival time delay of over 4 s. Second, the 1D velocity model I used was completely inappropriate for the OBS, leading to significantly larger depths for events near to trench, particularly in the south (Figure 42).

Picking earthquake arrivals manually significantly improved the earthquake locations, which are more clustered than in their original locations (Figure 40 and Figure 41). According to the NonLinLoc software, the average location error is 4.7 ± 3.9 km, with a smaller lateral error of 1.7 ± 1.3 km and a larger depth error of 4.3 ± 3.7 km (Figure 43). However, near the trench and especially in the south, earthquakes are stuck at 20 km, which is almost certainly an error due to the velocity model, since at this depth the P wave velocity jumps from 5.1 to 6.8 km/s.

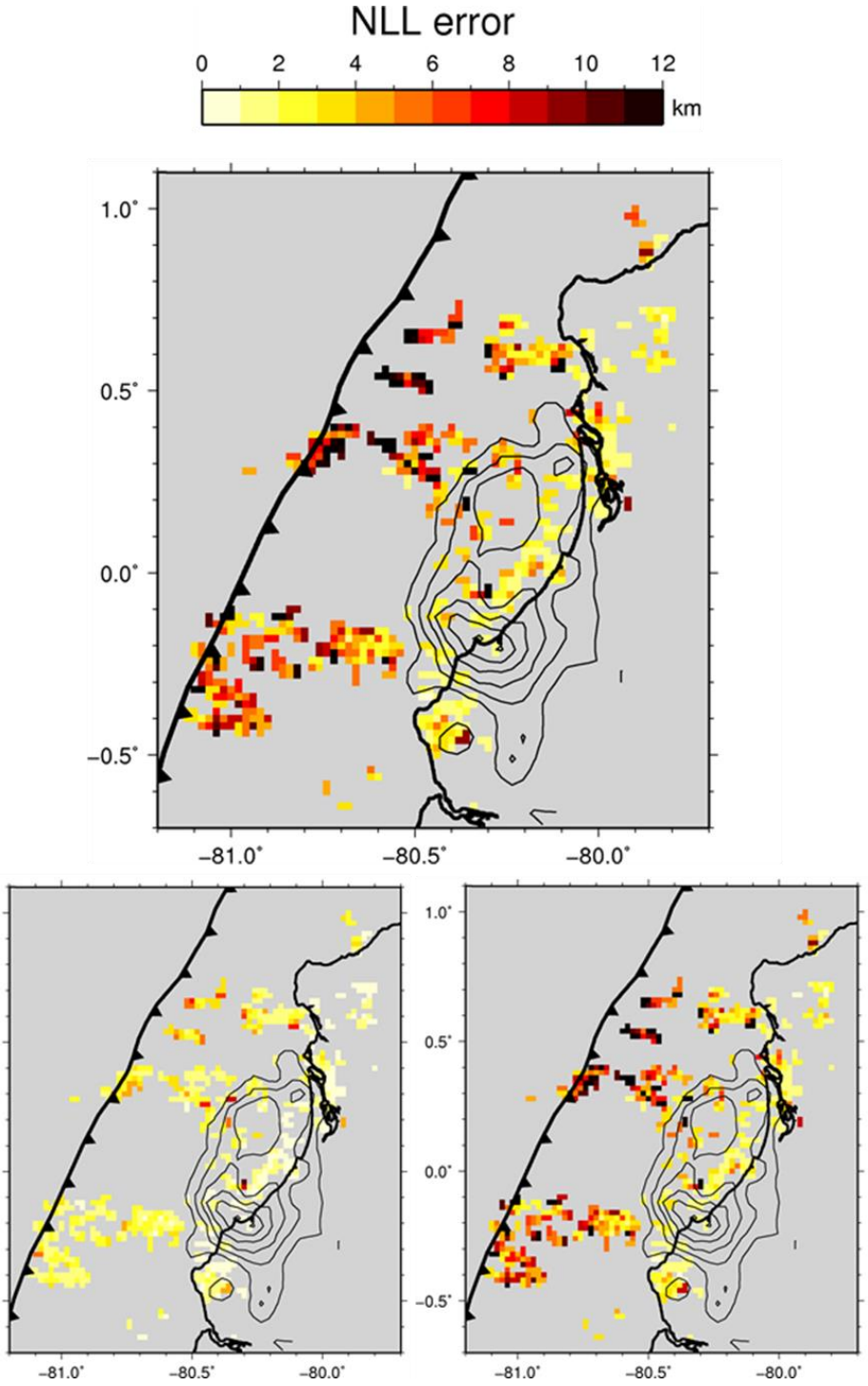

Figure 43 : Absolute relocation error calculated by NonLinLoc for events with manual picks. The top panel is the total error, the bottom left panel is the horizontal error and the bottom right panel is the error in depth. Note that these are errors calculated by the software itself, which do not take into account uncertainties of the velocity models.

To further improve locations, particularly relative locations, I used the hypoDD software (Waldhauser and Ellsworth, 2000). This method requires the computation of relative arrival times through correlation for both the P and S waves for a large number of stations. The delay in arrival times between pairs is then used to derive their relative placement. Because of this,

hypoDD locations tend to improve when many delay times are used within large clusters, rather than when attempting to locate events in small clusters. This is why I used all events available in each region, including non-repeaters and events with automatic picks and locations. This posed an additional difficulty. In the north, the 1112 events obtained after template matching could be relocated in one go. However, the southern region, which comprised of 4502 events, needed to be subdivided into 3 subregions to decrease computation time (Figure 44). I made those three subregions overlap so that clusters would not be cut in half, and I placed the boundaries of the subregions in areas where the density of preliminary repeating earthquakes was low. In total, the southernmost subregion had 2088 events, the middle subregion had 1704 events and the northernmost subregion had 1133 events.

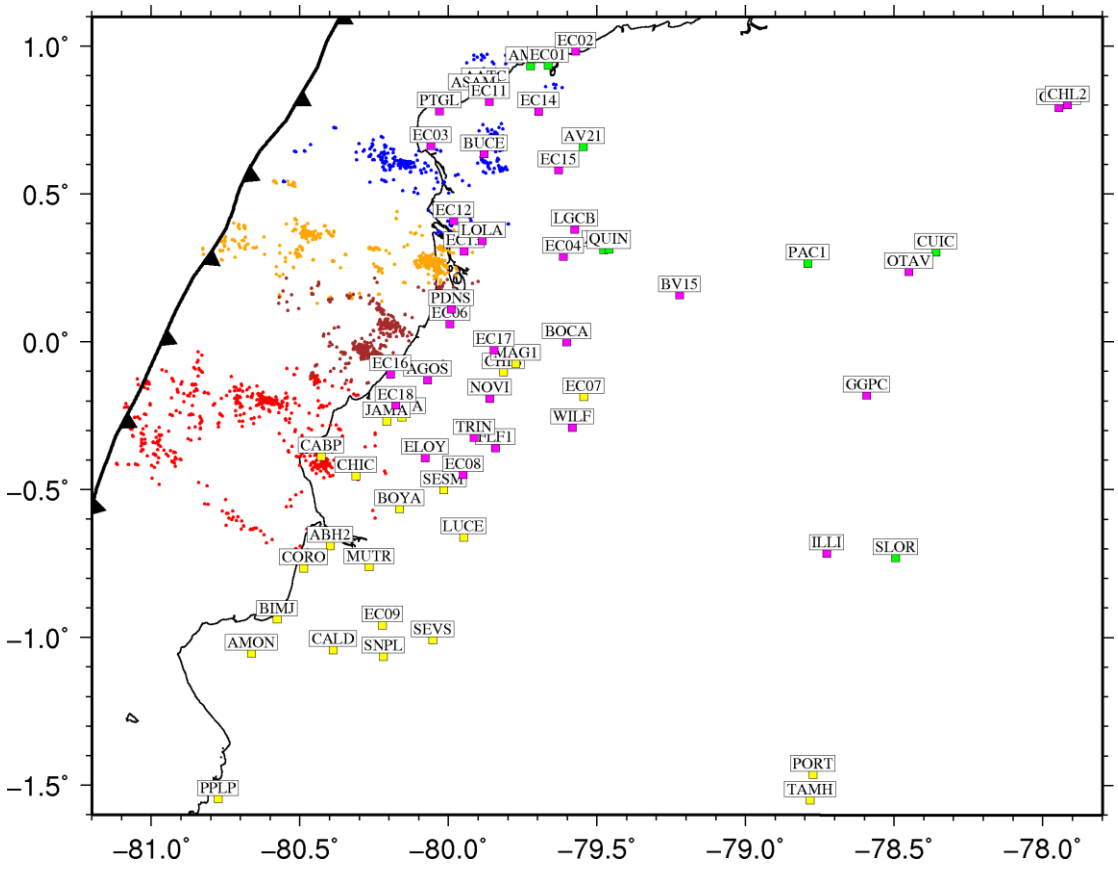

Figure 44 : Map of stations used for relocation with HypoDD. Blue dots are events in the northern region relocated by HypoDD. The southern region is divided into three subregions for the HypoDD relocation: the orange dots are events in the upper subregion, the brown dots are events in the middle subregion and the red dots are events in the southernmost subregion. Although they are divided for computational efficiency, all subdivisions of the southern region use the same subset of stations. Yellow squares are stations used for the relocation only in the southern region. Green squares are stations used for the relocation only in the northern region. Pink squares are stations used for the relocation in both regions.

I used a large number of stations (Figure 44), as the quality of the signal did not need to be as high as in the previous section. Instead, I tried to include as many useable stations as possible.

In particular, stations of lower quality that were available during the first month or before the mainshock were included to attempt to improve coverage. For this reason, the frequency band used to find the time delay through correlation was allowed to vary more significantly between stations. However, the upper boundary needed to be above 6 Hz, and the lower boundary below 4 Hz, and the frequency band needed to be more than 5 Hz. These frequency bands were kept the same for the P and S waves, which were dealt with separately when calculating correlations. The time window, which I chose individually by station and by phase, was usually around 5-6 s in total, large enough to account for errors in the P and S arrivals around the synthetic picks (TABLESB and SC).

Once correlation coefficients were calculated, I used the differential times to relocate events with hypoDD. When using hypoDD, one is given the option to use catalogue picks, correlation picks, or both. I chose the latter option, using catalogue picks for all manually picked events. Events with catalogue picks were paired if their initial locations were less than 8 km apart. For the relative times obtained with correlation, I set the correlation coefficient threshold at 0.7 to create event pairs. Above this threshold, the differential time was used in the inversion, weighted by the square of the correlation. With both correlation and catalogue picks, I calibrated HypoDD so that for two events to be paired together, they needed a minimum of 8 observation pairs between them. HypoDD then creates clusters of events, within which earthquakes are relocated relative to each other. I set the minimum number of events in a cluster to 2 and the maximum distance between clusters and stations to 250 km.

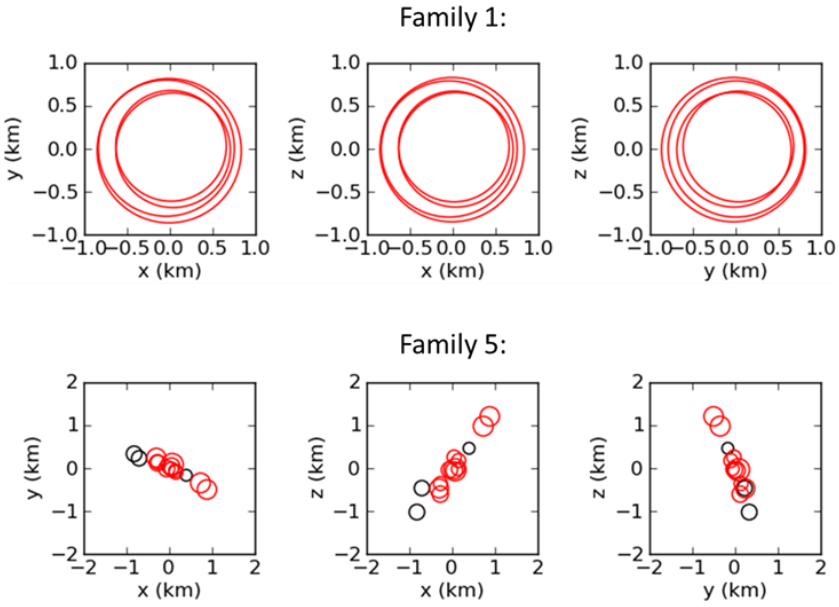

Figure 45 : Examples of HypoDD relocation within two families of repeating earthquakes. Repeaters are plotted as circles, whose diameter is determined as $D = 2 \times (\frac{16\Delta\sigma}{7M_0})^{1/3}$. *X represents the horizontal distance of the earthquake from the center of the family in the E-W direction, y represents the horizontal distance of the earthquake from the center of the family in the*

N-S direction, and z represents the horizontal distance of the earthquake from the center of the family in depth. Red circles are events which are in contact with at least one other repeater in the family, while black circles are isolated events.

When relocating events, I used the least-squares method rather than the SVD method, which would typically be considered more accurate, but which cannot work with as many earthquakes as I have. For each run of HYPODD, I used several groups of iterations with different weights, cutoffs and damping parameters to ensure that the solution converges well (TABLE SD). I separated my different iteration groups in an attempt to best relocate the events. The first groups focus on relocating events with catalogue picks, to improve the absolute location, with the second group getting rid of picks with large residuals. Then events are relocated with primarily CC picks to get finer locations. As picks with large time residuals or location errors are gradually removed, the damping is increased to avoid overfitting the data. The relocation results are shown in Figure 40C and Figure 41C, while examples of the result of the relative relocation within families of repeating earthquakes are found in Figure 45.

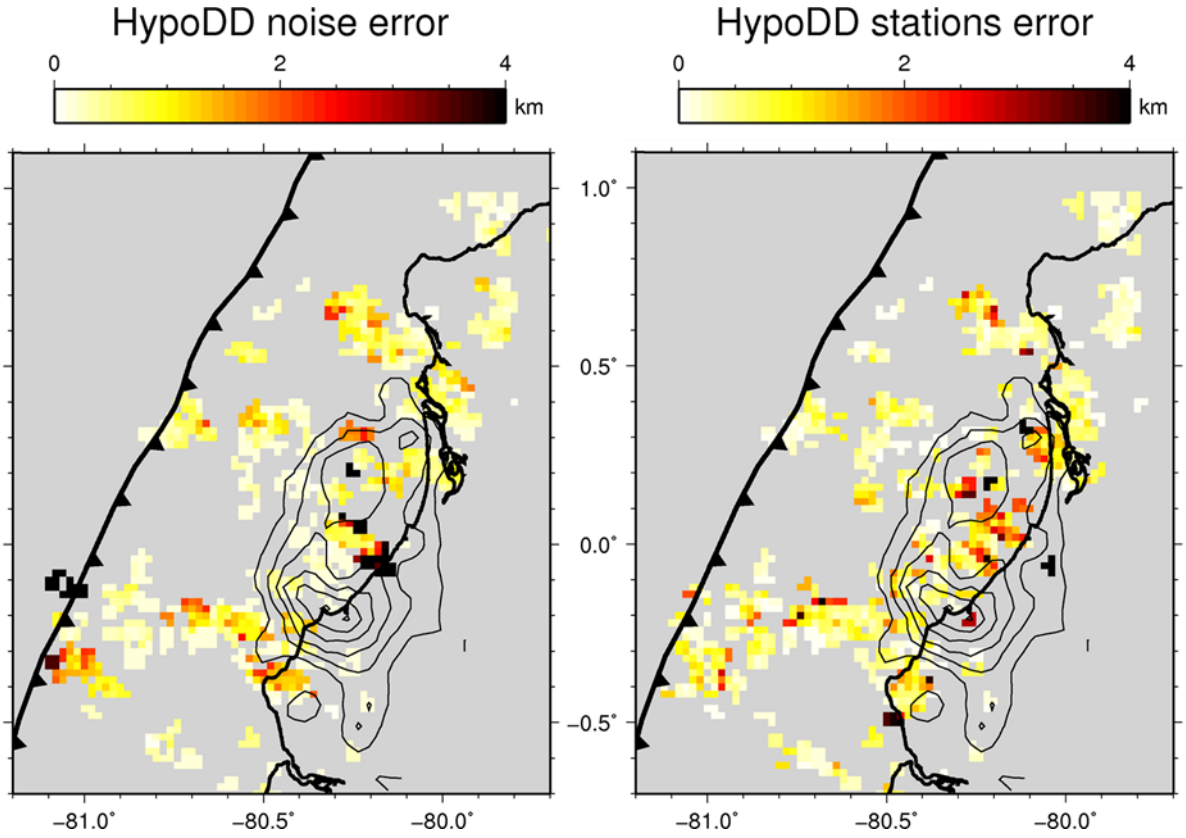

Figure 46 : Map of HypoDD errors calculated from bootstrapping. On the left, the error linked to noise in the arrival times, calculated by introducing random time delays to the station times. On the right, the error linked to the unevenness of the network, calculated by randomly removing stations for each event pair.

Finally, I merged the hypoDD relocation results from different subregions together. When an event was in two clusters from two different subregions, the clusters were merged together. Using the average absolute difference in location for all common events, the smaller cluster had its absolute location adjusted. In this way, events common to two clusters could keep their relative position in both.

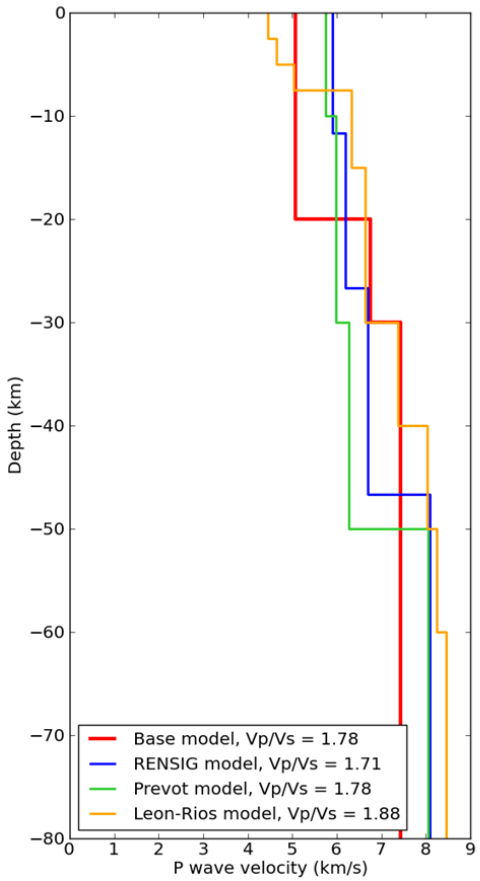

Figure 47 : Velocity models used for comparison to the base model in the HypoDD relocation. The base model (thick red line) is from Agurto-Detzel et al. (2019). The RENSIG model (blue) is the one developed by the Instituto Geofisico of Ecuador based on Andean geology (Font et al., 2013). The Prevot model (green) is from Prevot et al. (1996). The Leon-Rios model (orange) is from León-Ríos et al. (2019).

At the end of the inversion, variations in location are on the order of 10 m. However, that is not the real uncertainty associated with hypoDD. Unfortunately, when using the least squares method, HypoDD does not give accurate error estimates, which can only be retrieved through bootstrapping methods. I calculated the errors stemming from two different issues, which I show in Figure 46. First, I calculated the average error from noise in the correlation delays by launching 100 iterations in which I introduced a random perturbation in the original travel time data. This random perturbation was taken from the range of time residuals I obtained from my

initial inversion. The corresponding error was found to be around 750 m on average. I then evaluated the effect of the changing network of stations on my data. To do so, I performed 50 iterations during which I randomly took out one station for each earthquake pair, and obtained an average error of 580 m, with the largest error seemingly being associated with events within the rupture zone (Figure 46). This may be in part because that region experienced changes in seismic velocity over time as a result of the damage and recovery process (Agurto-detzel et al., 2020), and the relative relocation method relies on the assumption of a constant velocity structure. Additionally, earthquakes in this region are smaller on average (1.5 < Ml < 5), and thus can have low S/N ratio possibly contributing to their having larger errors.

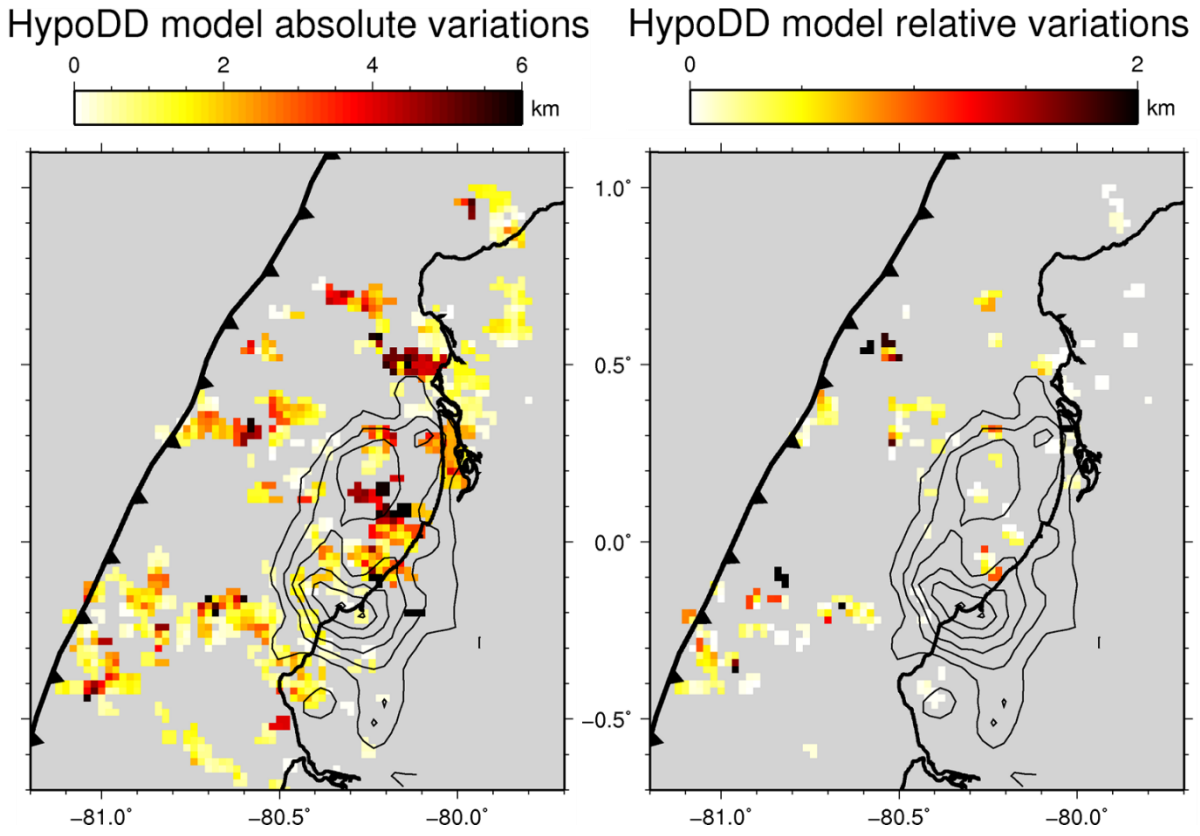

Figure 48 : Map of variations in HypoDD locations obtained using different 1D velocity models. On the left is the variation in absolute locations of earthquakes. On the right, the variation in locations of repeaters relative to other repeaters within a single family.

In addition to these sources of error, I also evaluated the impact of the velocity model in hypoDD, by comparing results from my velocity model (Agurto-Detzel et al., 2019) to those of other existing models (Figure 47). The first is the RENSIG model, constructed by the *Insituto Geofisico* using Andean geology and therefore probably limited in my coastal region (Font et al., 2013). The second model does correspond to my region, but was built largely using Andean stations and events, and is therefore also probably poorly constrained (Prévot et al., 1996). The

third model was constructed more recently using the Pedernales aftershock sequence, and is likely the most accurate (León-Ríos et al., 2019). Overall, the average distance between clusters when using these three models is about 1.8 km. However, within individual repeating family, the average error linked to the velocity model is about 520 m (Figure 48).

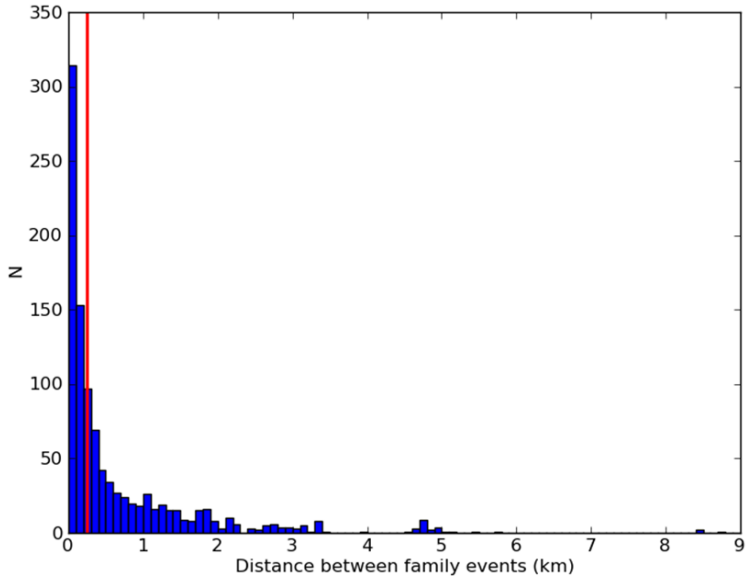

Figure 49 : Histogram of distances between repeating earthquakes belonging to a single family, calculated after relocation with HypoDD. The red line is the estimated median earthquake diameter of 250 meters, calculated as $D = 2 \times (\frac{16\Delta\sigma}{7M_0})^{1/3}$. *For comparison, the median inter-event distance between two repeating earthquakes within a family is also 250 meters, while the error is at least 750 meters.*

Ultimately, in the definitive families with a correlation coefficient above 0.95, the average inter-event distance is 680 m, with a median of 250 m (Figure 49). This is within the errors I calculated, but above the average size of a repeater. Due to these large errors, HypoDD locations could not be used as a criterion for family classification. This was compounded by the fact that 61 out of 376 repeating earthquakes from the final classification could not be relocated with HypoDD (Figure 50).

In total, 2925 events had their locations improved using either NonLinLoc and HypoDD. These more accurate locations made it possible to improve magnitude estimations as well.

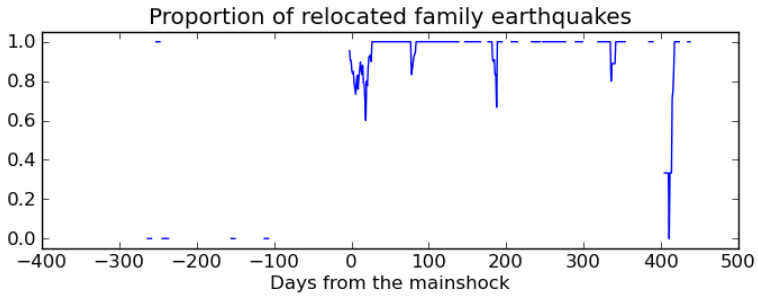

Figure 50 : Proportion of repeating earthquakes relocated with HypoDD as a function of time, with smoothing over a 5-day window.

3.5 Local magnitude calculations

After template matching, it was necessary to calculate the magnitudes of new events, with the goal of making them consistent with the existing catalogue. Local magnitudes are given as:

$$M_L = log_{10}(A) + a_0 + a_1 log_{10}(D)$$

Where A is the peak amplitude, D is the distance to the station and a_0 and a_1 are constants. The a_1 term, linked to distance, is the same used by SeisComP3 and by Agurto-Detzel et al. (2019). I obtained the a_0 term for each station by calculating the magnitude of relocated events already in catalogue station by station. For this, 1092 events that had been relocated with either NonLinLoc or HypoDD were used. This allowed me to obtain for each station a relationship between the newly calculated local magnitude and the catalogue local magnitude. I used this as a station correction term to calculate the new events' local magnitudes, ensuring that the new magnitudes are consistent with the catalogue ones. I compare the catalogue magnitudes with the newly calculated magnitudes in Figure 51 and Figure 52. These figures show that the old and new magnitudes of earthquakes already in the catalogue are very similar. It can therefore be inferred that the magnitudes of the new events found by template-matching are consistent with the rest of the catalogue.

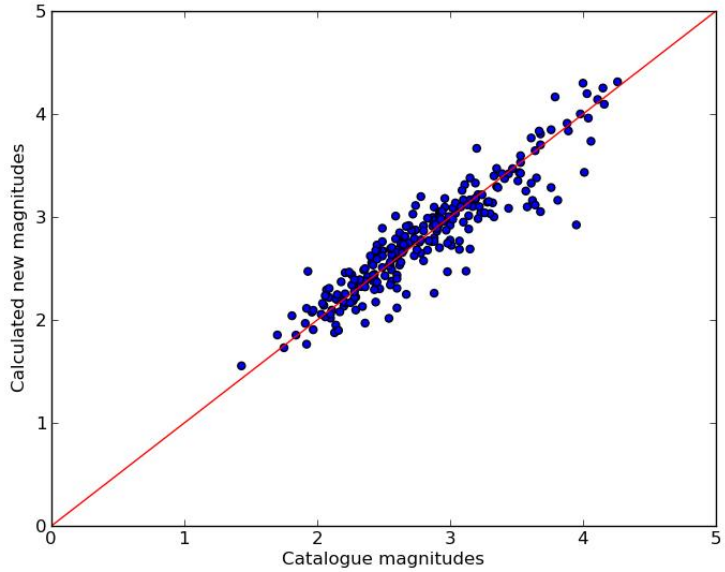

Figure 51 : Newly calculated Vs catalogue magnitude for relocated events in the north. The red line is the 1:1 line.

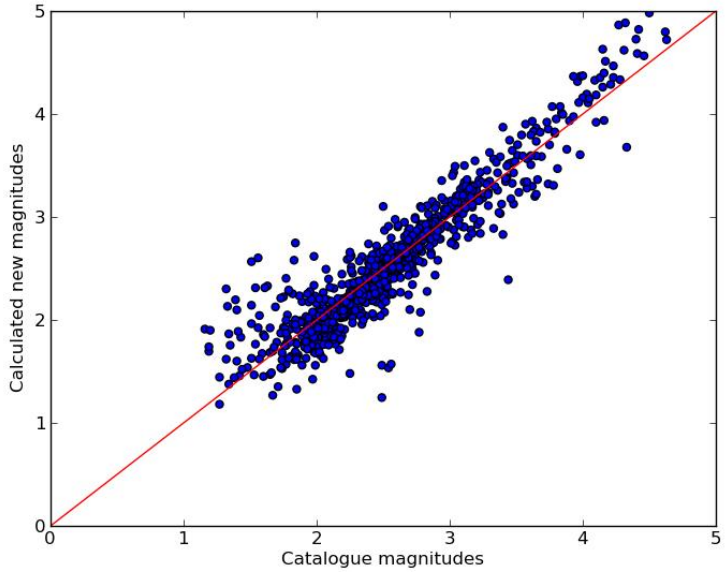

Figure 52 : Newly calculated Vs catalogue magnitude for relocated events in the south. The red line is the 1:1 lines.

Having cross-correlated events from the original aftershock catalogue, created families and completed them using template-matching, relocated families and individual events and calculated missing local magnitudes, I obtained a catalogue of repeating earthquakes for the aftermath of the Pedernales earthquake. The results of this part of the study are presented in Chapter 4.

3.6 Computing source properties with spectral ratios

Having created a catalogue of repeating earthquakes, my next goal was to calculate their source properties in order to analyze their evolution over the postseismic period, and through it the evolution of the frictional properties of the megathrust. I decided to compute the source properties of non-repeaters as well, in order to better understand their spatial distribution.

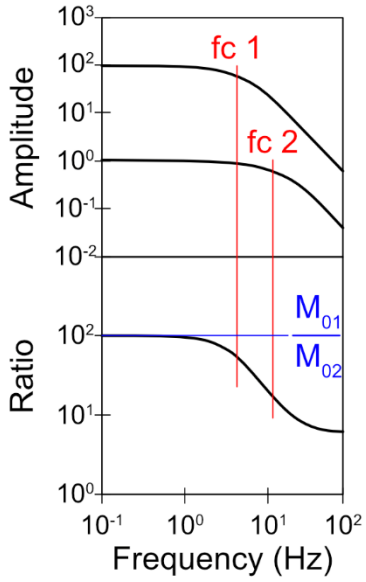

Figure 53 : Spectral ratio method. The spectra of two neighboring earthquakes are calculated at a given station, and one is divided by the other. Doing so removes the path and station components of the seismic signal, leaving a ratio of the source spectra. If the seismic sources are simple, then the ratio can be modelled, and the corner frequencies retrieved, along with the ratio of seismic moments between the two events.

I used the spectral ratios method to recover seismic moments and corner frequencies of aftershocks. By dividing the spectra of two closely located earthquakes, I was able to remove the effects of attenuation common to both, and recover the seismic moment difference between the two, as well as their corner frequencies (Figure 53). I did so at 30 different stations (Figure 54). The method presented in this section is elaborated on in Chapter 5, so I will summarize the main points and add further details as necessary. I gathered 1514 relocated aftershocks into 55 clusters with a maximum inter-event distance of 9 km, containing either repeating earthquakes or a minimum of 7 events with a maximum Ml difference above 1. Within each cluster at a given station, the P time window was defined as 0,6 * $(Ts - Tp)_{\text{cluster average}}$ seconds starting 0.1 second before the P arrival. I chose this to avoid any contamination from the S wave, since 5% of theoretical $(Ts - Tp)_{\text{average}}$ have an error of 20% (1.66 s) or more. The S time window was

defined as 1.2 * (Ts – Tp) $_{\text{cluster average}}$ seconds starting 0.1 second before the S arrival, while noise windows were calculated using the same window lengths, ending 2 s before the P arrival. Any window smaller than 2 s was discarded, along with any event with $(Ts - Tp)_{average}$ less than 2.5 s. This is because, even after relocation, the median absolute errors are 0.36 and 0.63 s for the P and S synthetic arrivals respectively, but can reach as high as 1.5 s for the P ad 2.5 s for the S (95% threshold). To limit the impact of errors in arrival times, I moved the time window by 0.5 to 2.5 seconds depending on the picking error, in order to find the starting point for which the window contains the most signal.

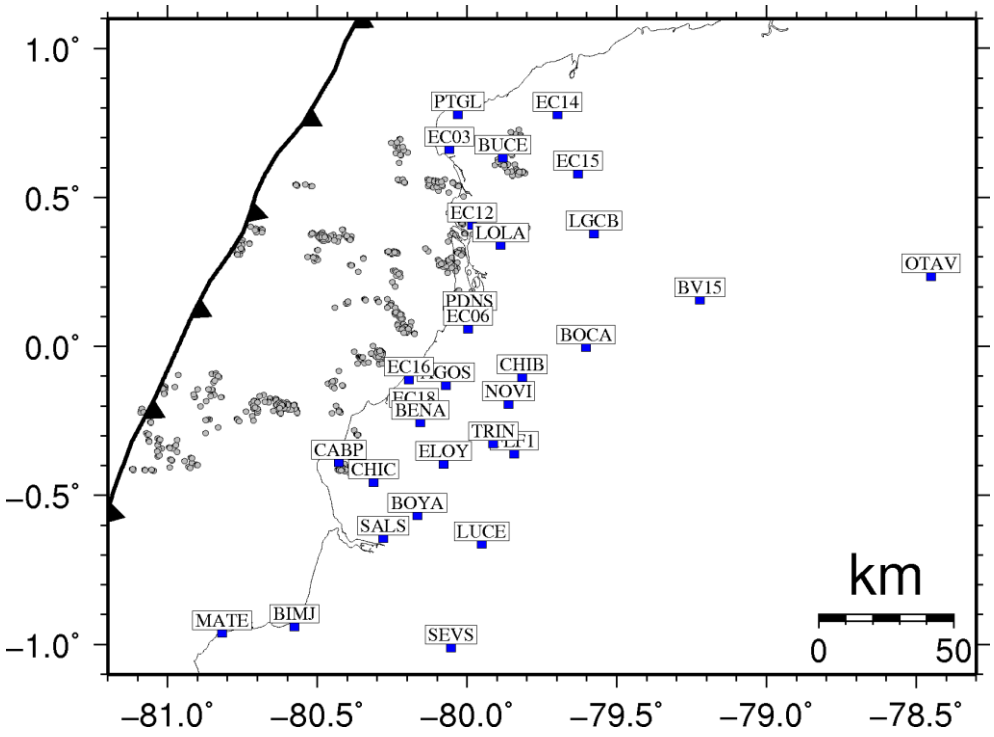

Figure 54 : Stations used for spectral ratios (blue squares). Grey dots are the earthquakes whose source properties are examined.

For the calculation of spectral ratios, I used the spectrum of the vertical component for the P wave and the average spectrum of the horizontal component for the S wave, both of which were calculated using the multitaper code developed by Prieto et al. (2009). I discarded the S spectrum if the average S/N over the 2-20 Hz frequency band changes by a factor of 2 or above between the two horizontal components, as I found this to lead to bad ratios later on. Spectra were then resampled to 0.0025 in the log domain to ensure higher frequencies did not get weighed more than lower ones. I later smoothed the average spectrum with a window of 0.4, then decimated the data so that the interval between 2 points became 0.05 in the log domain. Spectral ratios were computed exclusively on the part of the spectrum where S/N >= 4, on the condition that the log of that frequency interval was over 0.7. Additionally, I also ensured that

the ratio of the signal of event 1 to the noise of event 2, and the signal of event 2 to the noise of event 1, were both higher than 4 in the entirety of that interval.

As preparation for the inversion, absolute seismic moments were calculated using the part of the displacement spectra where S/N > 3. I used them as starting values for the inversion, with corresponding starting corner frequencies calculated using the equation $f_C = k\beta(\frac{16\Delta\sigma}{7M_0})^{1/3}$ from Eshelby (1957) and Brune (1970) with an a priori stress drop of 2 MPa, an S wave velocity β of 3690 m/s, and a k constant equal to 0.38 for P waves and 0.26 for S waves (Kaneko and Shearer, 2014). Correlation coefficients were then computed between events filtered below the lowest corner frequency in the portion of the spectra where S/N >= 3. I discarded the spectral ratio of an event pair if their correlation coefficient exceeded 0.8 at two thirds or more of available stations or their correlation coefficient exceeded 0.8 at the station examined (Abercrombie, 2015).

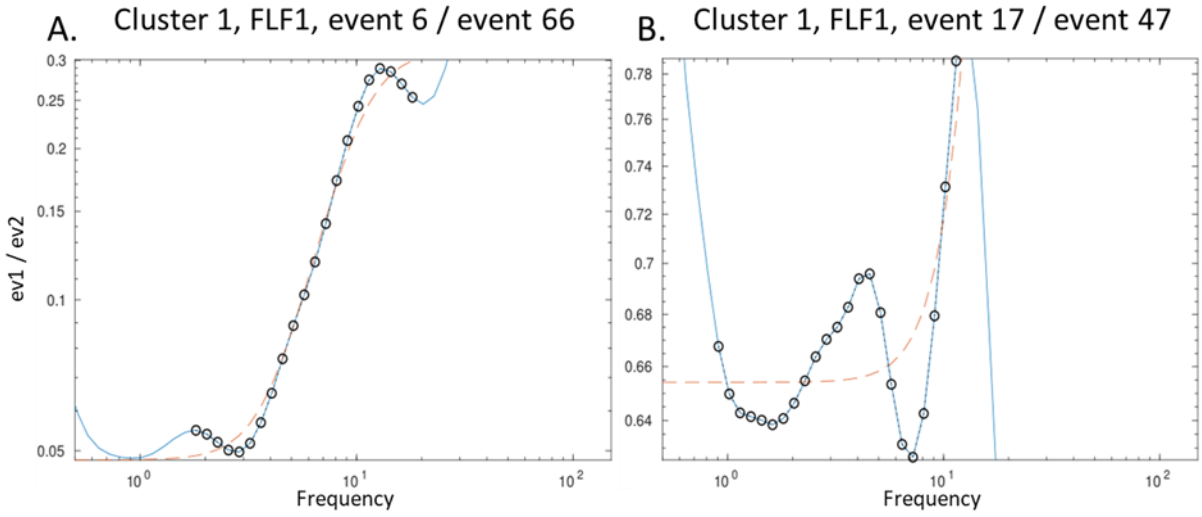

Figure 55 : Examples of two individual spectral ratios, one that was included in the inversion (A) and one rejected as its shape could not be modelled (B). The blue line is the spectral ratio over the full spectrum, including regions where the signal/noise ratio is too low. The open black circles are the points at which the ratio is modelled. The dashed red line is the best-fit model of the ratio.

Furthermore, to ensure that my inversion would converge, I first modelled individual spectral ratios using the equation:

$$\frac{S_1(f)}{S_2(f)} = \frac{M_{01}}{M_{02}}\left(\frac{1+(\frac{f}{f_{c2}})^{\gamma n}}{1+(\frac{f}{f_{c1}})^{\gamma n}}\right)^{\frac{1}{\gamma}}$$

I used the Boatwright model (Boatwright, 1980) with $\gamma = 2$ and n = 2. Modelling individual ratios allowed me to remove those with poor fits before the final inversion (examples shown in Figure 55). Events were removed if the modelling yielded complex numbers for the frequency corners, moments, or errors, if the two modelled corner frequencies or moments were both unrealistically large or small, if the two modelled corner frequencies both fell well outside the examined frequency range, or if the fit was too poor. The fit of the model was calculated using the residual RMS divided by the interval between the 90th percentile and the 10th percentile of the log of the ratio. The ratio was discarded if its RMS/interval was above 0.15. This was decided through visual inspection of the data, by looking at 279 ratios from P and S waves at different stations and grading them on a scale of 0 to 3 with 0 = the ratio cannot be fit by the model at all, 1.5 = undecided and 3 = the ratio is perfectly fit by the model. The threshold of 0.15 was used as it maximized the number of ratios with grades 2 or above while minimizing the number of ratios with grades 1 or below (Figure 56). Although studies often impose a minimum magnitude difference, I decided not to do so, as I found that there is no adequate threshold at which ratios go from well to poorly fit by the Boatwright model (Figure 57). Some ratios had small magnitude differences (0.1 or below) but were well modelled, while others had large magnitude differences (0.5 or above) but were poorly modelled.

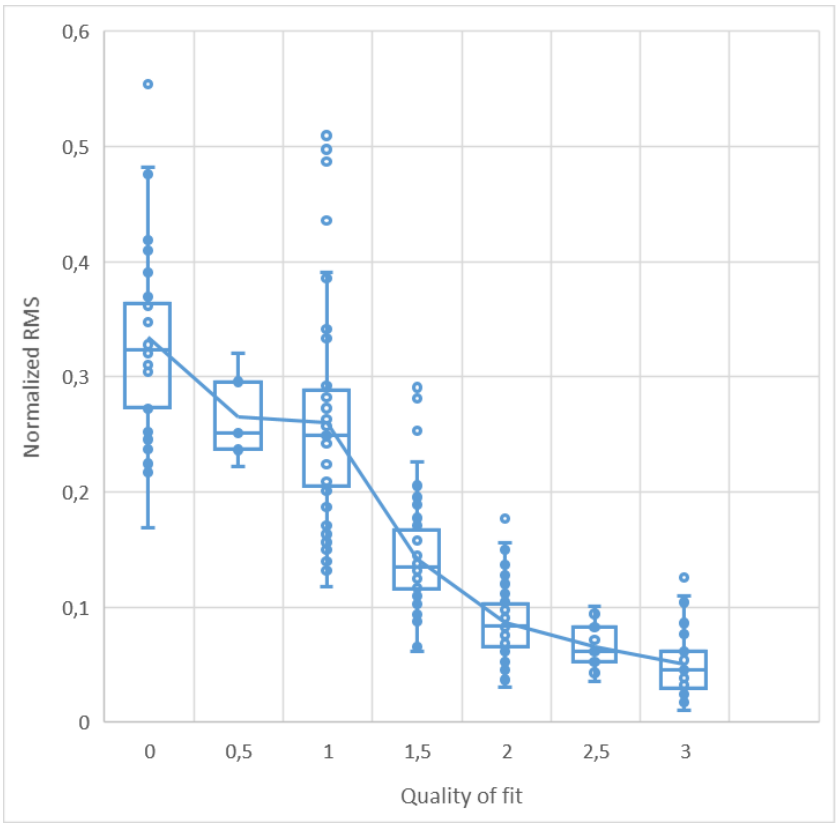

Figure 56 : Normalized residual RMS as a function of how well the ratio is fit by the Boatwright model. Each ratio is modelled independently with the Boatwright model, from which the residual RMS is obtained. The RMS is normalized by the interval between the 90th percentile and the 10th percentile of the log of the ratio. The fit of each ratio is then evaluated through visual inspection, with 0=worst fit and 3=best fit. As can be seen, 0.15 is a threshold below which most ratios are considered to fit the Boatwright model and above which most ratios are considered not to fit the Boatwright model.

Finally, I modelled all spectral ratios for a cluster at a single station together to determine corner frequencies and seismic moments. In order to constrain the absolute values of seismic moment, I used the logarithmic mean of the previously calculated preliminary seismic moments, which then remained fixed during the inversion. I used the nlinfit function in MATLAB to fit all spectral ratios together in the log domain. I ran several iterations with different starting parameters either until the number of successful iterations (defined as iterations that converge to realistic values of corner frequencies between 0.01 and 100 and seismic moments between 10^5 and 10^{25}) exceeded 7, or until the total iteration number exceeded 35. If none of the 35 iterations converged, I removed problematic events and inverted the data again. Starting parameters for the initial iteration were the previously calculated preliminary seismic moments, and corner frequencies, while starting parameters for later iterations were determined randomly within the range of corner frequencies and seismic moments derived for each event when individual ratios were modelled. Using different starting parameters in this manner very rarely yielded different results, but it often made the inversion more likely to converge. Ultimately, my results are taken to be the ones from the iteration with the smallest error.

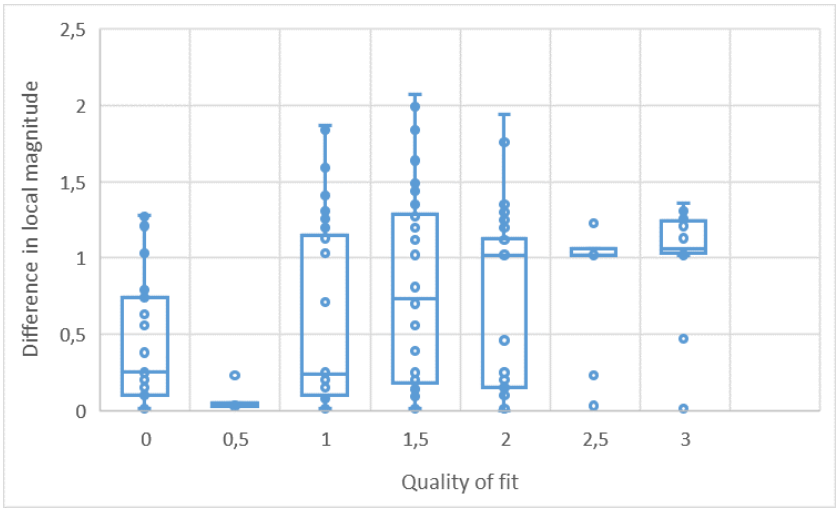

Figure 57 : Difference in local magnitude between earthquakes as a function of how well their spectral ratio is fit by the Boatwright model. Each ratio is modelled independently with the Boatwright model, and its fit is evaluated through visual inspection with 0=worst fit and 3=best fit. This is compared to the difference in local magnitude of the two events examined. It seems that the magnitude difference between two events does influence how well their ratio can be fit by the Boatwright

model. However, there is no clear threshold to determine what minimum magnitude difference should be used, and some well-fit ratios have small magnitude differences while some poorly fit ratios have large magnitude differences.

For events modelled at several stations, I defined the seismic moment and P and S corner frequencies as the median between all the values obtained at different stations. To ensure the quality of my results, I first removed corner frequencies below the minimum frequency examined, as well as corner frequencies above half of the maximum frequency examined (see Appendix C for more detail). I then calculated static stress drops as $\Delta\sigma = \frac{7}{16}(\frac{f_c}{k\beta})^3 M_0$ from Eshelby (1957) and Brune (1970). I took the logarithmic mean of the P and S stress drop as the event stress drop. Finally, I calculated uncertainties by performing a jackknife test on the data, removing 20% of individual data points in 100 iterations and finding the standard deviation of source parameters.

Through this work, I was able to retrieve good quality seismic moments, corner frequencies and stress drops for 597 aftershocks of the Pedernales earthquake, including 187 repeating earthquakes. The results of this section are presented in Chapter 5.

Thus I was able to create a catalogue of postseismic repeating earthquakes, and in most instances I was able to recover their source properties, along with those of many aftershocks. These results are presented and discussed separately in the following two chapters, and further discussed in tandem in Chapter 6.

Chapter 4: Results from classification, template-matching and relocation

This chapter introduces the catalogue of repeaters obtained in the previous chapter. It was published as a scientific article in 2021[1].

Here, we focus on the relationship between repeating earthquakes and afterslip, and we explore the limits of using repeaters to quantify aseismic slip. We find that repeating earthquakes are present primarily within large clusters of aftershocks at the edge of the two main afterslip regions, where the afterslip gradient is high. We also attempt to use the relationship between seismic moment and slip determined by Nadeau and Johnson (1998) to quantify afterslip, but find that the slip derived from repeaters is not representative of large-scale aseismic slip. Combining these two observations, we show that quantifying afterslip from repeating earthquakes is not straightforward. We also suggest that the accumulation of stress at the edges of the afterslip region may be linked to the behavior of repeaters.

[1] See https://doi.org/10.1029/2021JB021746

Repeating earthquakes at the edge of the afterslip of the 2016 Ecuadorian M_W7.8 Pedernales earthquake

Caroline Chalumeau, Hans Agurto-Detzel, Louis De Barros, Philippe Charvis, Audrey Galve, Andreas Rietbrock, Alexandra Alvarado, Stephen Hernandez, Susan Beck, Yvonne Font, Mariah C. Hoskins, Sergio Leon-Rios, Anne Meltzer, Colton Lynner, Frederique Rolandone, Jean-Mathieu Nocquet, Marc Régnier, Mario Ruiz, Lillian Soto-Cordero, Sandro Vaca, Monica Segovia

4.1 Abstract

Repeating earthquakes repeatedly rupture the same seismic asperity and are strongly linked to aseismic slip. Here, we study the repeating aftershocks of the April 16, 2016 MW 7.8 Pedernales earthquake in Ecuador, which generated a large amount of afterslip. Using temporary and permanent stations, we correlate waveforms from a one-year catalog of aftershocks. We sort events with a minimum correlation coefficient of 0.95 into preliminary families, which are then expanded using templatematching to include events from April 2015 to June 2017. In total, 376 repeaters are classified into 62 families of 4–15 events. They are relocated, first using manual picks, and then using a double difference method. We find repeating earthquakes during the whole period, occurring primarily within large aftershock clusters on the edges of the areas of largest afterslip release. Their recurrence times, shortened by the mainshock, subsequently increase following an Omori-type law, providing a timeframe for the afterslip's deceleration. Although they are linked temporally to the afterslip, repeater-derived estimates of slip differ significantly from GPS-based models. Combined with the fact that repeaters appear more spatially correlated with the afterslip gradient than with the afterslip maxima, we suggest that stress accumulation at the edge of the afterslip may guide repeater behavior.

4.2 Introduction

Subduction zones host the largest, most destructive earthquakes, along with a large variety of seismic and aseismic slip processes. Understanding these processes, and the relationships between them, is necessary to better constrain the mechanical properties of the fault and to better assess seismic hazard. For this purpose, repeating earthquakes are an important seismological tool, able to link aseismic slip and seismic behavior.

Repeating earthquakes (or repeaters) are families of two or more events, usually of small magnitude, that represent repeated ruptures on a single seismic asperity through time (Ellsworth, 1995; Nadeau et al., 1994; Vidale et al., 1994). They are identified by their nearly identical waveforms and overlapping rupture areas. Over the last 25 years, they have been observed in a large variety of tectonic settings, from strike-slip faults (Nadeau and Johnson, 1998) and normal faults (Duverger et al., 2018), to reverse faults (K. H. Chen et al., 2008) and megathrust faults (Dominguez et al., 2016; Uchida et al., 2003). In all these settings, repeaters are associated with aseismic slip, be it creep, afterslip, or slow slip events (SSEs). The recurrence of these earthquakes suggests that a seismic asperity is being continually loaded, likely by aseismic slip, and breaking at regular intervals (T. Chen and Lapusta, 2009). This makes repeaters ideal tools to probe the properties of a fault and its slip history.

Repeaters are usually quasi-periodic during the interseismic period, with log(Tr) proportional to $\log(M_0^{1/6})$ (where Tr is recurrence time and M_0 is seismic moment). This relationship seems to be universal across tectonic contexts, further suggesting that repeaters depend on tectonic loading rates (K. H. Chen et al., 2007). This makes them useful to estimate creep at depth (K. H. Chen et al., 2008; Nadeau and Mcevilly, 1999). Since repeaters likely represent slip on an isolated asperity being loaded by surrounding creep, repeaters measure slip directly on the fault, independently from GPS surface measurements. They can therefore complement geodetic models, which have their own uncertainties linked to instrument location, fault geometry, model smoothing, and other parameterization.

Afterslip is a transient aseismic process that occurs in response to a large earthquake, usually in conjunction with aftershocks. Both geodetic and repeating earthquake data can be used to estimate afterslip (Uchida, Yui, et al., 2009). They offer complementary constraints on the geographical extent and amplitude of afterslip. Repeaters are an especially powerful tool along subduction margins as they provide additional insights into afterslip occurring in offshore regions. Recurrence times of repeaters drop after a mainshock, then slowly increase following an Omori-type law (Marone et al., 1995; Peng et al., 2005; Schaff et al., 1998; Taira et al., 2009). This study aims to better characterize the relationship between repeaters and afterslip in the context of the Ecuador-Colombia subduction zone by looking at the post-seismic sequence of the 2016 Mw 7.8 Pedernales megathrust earthquake in Ecuador.

The Ecuador-Colombia subduction zone is a complex, spatially heterogeneous region that exhibits a wide variety of slip behaviors, from aseismic slip to large megathrust earthquakes. Over the last century, five earthquakes with magnitudes above 7.5 have occurred in the area. The 1906 Mw 8.4-8.8 earthquake (Kanamori and McNally, 1982; Yoshimoto et al., 2017) is the largest known earthquake in the region. It is thought to have ruptured a 200 to 500 km long segment from central Ecuador to southern Colombia (Kelleher, 1972). During the following 70 years, 3 earthquakes of magnitude 7.7 – 8.2 each ruptured a distinct ~200 km portion of this segment, starting with the southern segment in 1942, then the middle segment in 1958 and the northern segment in 1979 (Beck and Ruff, 1984; Kanamori and McNally, 1982). These formed a northward sequence that may only have released as little as a fifth of the moment released by the 1906 earthquake, suggesting that the latter broke through not only the three smaller asperities together, but also some adjacent creeping portions of the megathrust (Beck and Ruff, 1984; Kanamori and McNally, 1982).

The April 16th 2016 Mw 7.8 Pedernales earthquake was the latest in the along-strike megathrust sequence. It ruptured a highly coupled patch of the subduction interface (Chlieh et al., 2014; Nocquet et al., 2014) corresponding to the approximate rupture area of the 1942 earthquake (Nocquet et al., 2017). Some studies have argued that the moment released by the Pedernales earthquake represents the entirety of the strain accumulated since 1942, meaning each megathrust earthquake that occurs in this area completely resets the fault loading (Ye et al., 2016; Yoshimoto et al., 2017). Others have proposed that the moment released by the 2016 earthquake far exceeds the strain accumulated since 1942 (Nocquet et al., 2017), suggesting the existence of an earthquake supercycle in the Ecuador-Colombia subduction zone. This would explain the relative seismic quiescence before 1906 and the subsequent enhanced seismic hazard, implying that the 1906 earthquake did not fully reset the strain accumulation along the plate boundary (Nocquet et al., 2017).

In addition to megathrust earthquakes, there is a large variety of interacting slip behaviors along the Ecuadorian margin. North of the 2016 rupture zone (Figure 58), the Punta Galera region exhibits low to intermediate coupling that hosts frequent SSEs accompanied by repeating earthquakes and seismic swarms (Vaca et al., 2018). This periodic unloading via aseismic slip may cause the area to impede rupture propagation (Vaca et al., 2018). Other areas prone to slip aseismically include La Plata island, where SSEs have been observed concurrently with seismic swarms (Chlieh et al., 2014; Segovia et al., 2018; Vallée et al., 2013), the region downdip of the rupture zone where an SSE was detected in 2015 (Rolandone et al., 2018), and upper plate faults near Esmeraldas (Hoskins et al., 2021). Aseismic behavior was also found during the postseismic period of the 2016 earthquake, with several regions experiencing afterslip, imaged by GPS data (Rolandone et al., 2018). During the first month following the Pedernales earthquake, two main patches of afterslip emerged updip of the coseismic rupture zone in the north and south, about 100 km apart (Rolandone et al., 2018) (Figure 58). Both patches remain

static in space for the first month, growing in amplitude but not in area (Rolandone et al., 2018; Tsang et al., 2019). The northern patch is situated in a low interseismic coupling area (5 to 40%) while the southern patch is centered on a high interseismic coupling region (50 to 90%) (Figure 58), yet in both cases the amplitudes, dimensions and behaviors are similar, with large and rapid early slip (Rolandone et al., 2018).

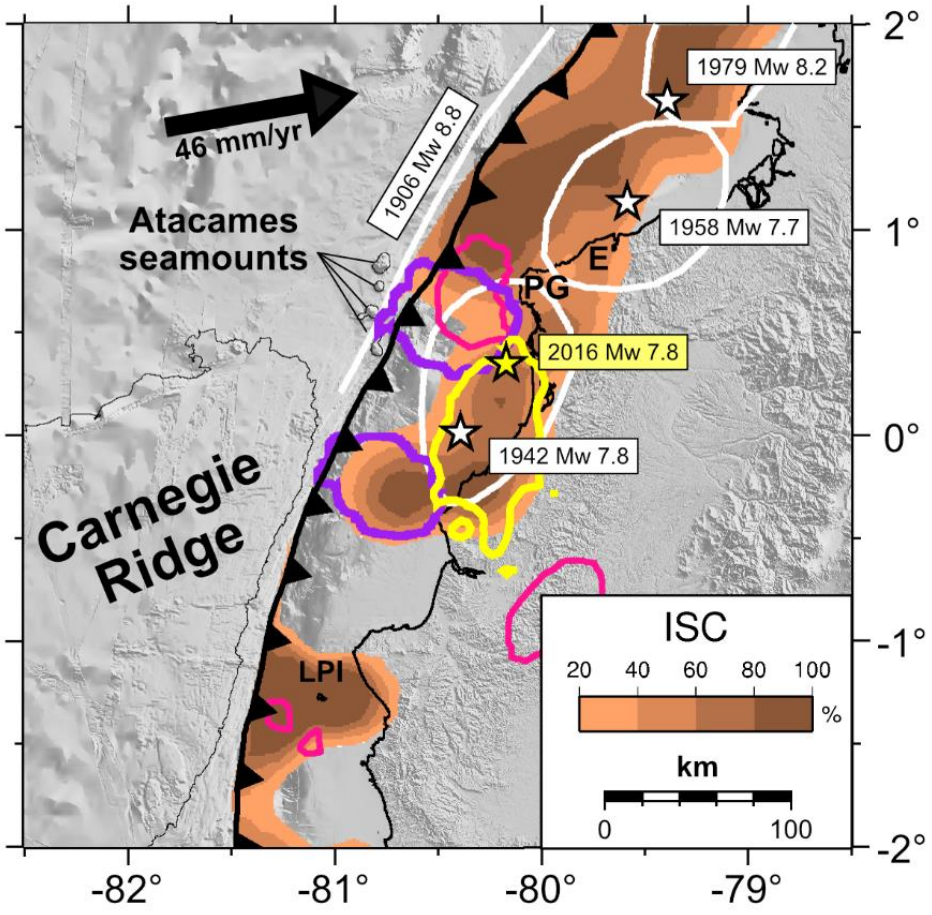

Figure 58 : Seismotectonic features in the study region. Interseismic coupling (Nocquet et al., 2014) is shown in brown color scale. SSEs shown in pink: 2013 SSE offshore Punta Galera (PG) (Vaca et al., 2018), 2013 SSEs around La Plata Island (LPI) (Segovia et al., 2018), 2015 deep SSE (Rolandone et al., 2018). The presence of a 2016 SSE near Esmeraldas (E) is suspected but not yet modelled (Hoskins et al., 2021). White stars and white lines show the epicenters and approximate rupture areas of past megathrust earthquakes (Kanamori and McNally, 1982; Mendoza and Dewey, 1984). The yellow star and yellow line show the epicenter and the 1 m contour of the rupture zone of the 2016 Pedernales earthquake (Nocquet et al., 2017). The purple lines show the 20 cm edges of the 1-month Pedernales afterslip (Rolandone et al., 2018). Plate convergence between the Nazca plate and the North Andean Sliver is from Chlieh et al., (2014).

The afterslip was accompanied by aftershocks, further highlighting the seismic-aseismic interaction already visible during the interseismic period. During the month following the mainshock, the aftershocks' spatio-temporal evolution mirrored that of the afterslip,

demonstrating that aftershock expansion was controlled primarily by afterslip (Agurto-Detzel et al., 2019). The link between seismicity and subducting oceanic relief was also highlighted (Agurto-Detzel et al., 2019; Soto-Cordero et al., 2020). The aseismic Carnegie Ridge, a 2 km high, 280 km wide, and 14-15 km thick volcanic feature, subducting between 0° and 2.5°S (Gailler et al., 2007; Michaud et al., 2009; Sallarès et al., 2005), segments the region, and prevents rupture propagation towards the south (Collot et al., 2004), while subducting seamounts also influence the distribution of seismicity (Agurto-Detzel et al., 2019; Collot et al., 2017; Marcaillou et al., 2016; Segovia et al., 2018; Soto-Cordero et al., 2020). Seismic imaging studies have also suggested that upper plate structures further segment the margin and play an additional role in preventing rupture south of 0.5°S (Koch et al., 2020; Lynner et al., 2020).

In this unique context, we explore the link between afterslip and repeating seismicity. We first extract repeaters from an existing earthquake catalog (Agurto-Detzel et al., 2019), relocate them, and enhance our detection through template matching. Repeaters are then compared with an existing afterslip model, in order to discuss the spatiotemporal relationship between them. We note that repeating earthquakes seem related to afterslip gradient rather than to afterslip itself. We therefore hypothesize that repeaters are influenced by the stress transferred from the afterslip.

4.3 Materials and Methods

To extract repeating earthquakes occurring during the postseismic phase of the Pedernales earthquake, we use both the permanent seismic network in place in Ecuador (Alvarado et al., 2018), and the one-year temporary deployment of land and ocean bottom seismic (OBS) stations deployed in the aftermath of the Pedernales earthquake (Agurto-Detzel et al., 2019; Meltzer et al., 2019). We examine 14 months of postseismic data, as well as 12 months of interseismic data. We start with the one-year long catalog produced by Agurto-detzel *et al.* (2019) using both automatic and manual picks. We calculate cross-correlations between all catalog earthquakes within the region, using them to obtain preliminary repeating earthquake families. These are later expanded through template-matching. We then relocate these earthquakes, first using manual picking to get robust preliminary locations, and then using the double-difference algorithm HypoDD to get finer relocations (Waldhauser and Ellsworth, 2000) and to calculate magnitudes. We then obtain a final classification of repeaters. A flowchart summarizing the processing steps can be found in the supplementary materials (Figure SC.1).

Between April 16th 2016 and April 30th 2017, 4762 earthquakes were catalogued in the study region. The first month of data was only recorded by the permanent seismic network,

while the temporarily deployed land stations were active from mid-May 2016 through mid-May 2017, and the OBS stations were active from the end of May to November 2016. This mismatch in coverage between permanent and temporary stations means our seismic data does not uniformly cover the month with the most earthquakes (Figure SC.2). In an effort to get a homogeneous, unbiased seismic coverage, we use a subset of 7 permanent and 10 temporary stations for repeater classification, ensuring at least 3 stations are simultaneously active at all times (Figure SC.2).

We perform time domain cross correlation on the vertical seismic component in a window starting 2 seconds before the theoretical P arrival and encompassing both the P and S waves, for all events and for all stations within a 140 km radius of the target earthquakes. The window length is fixed at 30 seconds for each station to ensure that all earthquakes' S waves are included in the correlation. Only one GSN station, OTAV, is used for earthquakes at all distances, with a window length of 57 seconds. While OTAV is farther away from the correlated earthquakes, it recorded high quality, low noise data during the entire period of interest. A different filter is used for each station based on the frequency band with the highest S/N ratio, in an effort to homogenize the various stations' detection capabilities. The parameters used to compute correlation coefficients are shown in Table S1.

We initially set a lower correlation threshold of 0.9 to find preliminary repeating families. This condition is required to be met at 2 stations if 5 or more stations are recording, or at 1 station if 4 or fewer stations are recording, to classify events as preliminary repeaters. This initial pass sorted 888 of the 4762 catalog earthquakes into 364 families. Waveforms from each family are then stacked to form a single representative template. Template-matching is then performed from the April 16th 2015 to the June 30th 2017 using the Fast-Matched Filter (FMF) code (Beaucé et al., 2017), using a correlation threshold of 0.9 and adding 432 new repeaters to our families. The use of stacks and the low correlation coefficient ensure that the catalog of repeaters is as complete as possible. We also search for new earthquakes in the year before the mainshock by lowering the detection threshold to ten times the daily average correlation between templates and the continuous data. New earthquakes are correlated together to find interseismic families, resulting in 3 new doublets.

All preliminary families are then relocated. Manual picking is first used to improve family locations with the *NonLinLoc* algorithm (Lomax et al., 2000), using the same 1-D velocity model as Agurto-Detzel et al., (2019). At least one repeater in every family is relocated, and its coordinates are used to set family locations. If several repeaters are relocated within a family, the average location is used. Cross correlations of P and S waves are later used to perform a higher precision relative relocation of the whole catalog using double-difference travel times and the HypoDD software (Waldhauser and Ellsworth, 2000). The region is separated into 4 subregions for relocation, and 63 stations are used, with 12 stations used on average to relocate

each earthquake pair. 2483 events are relocated out of 5617, including 1119 preliminary repeaters. We show examples of relocated repeaters within families in Figure SC.3. With these new locations, local magnitudes (M_L) are calculated for all earthquakes, from which seismic moments are derived (see details in Appendix B:Text S1).

Lastly, we calculate correlation coefficients again on the preliminary repeaters to enforce a stricter classification for our definitive families. The threshold correlation coefficient used to classify events as repeaters is 0.95, high enough to confirm the rupture of one single source and low enough to avoid missing events during periods with poor coverage (Uchida, 2019 and references therein). Earthquakes are sorted into families if they correlate above 0.95 at one third of available stations. We only retain families with 4 or more repeaters which span more than 15 days. These additional criteria are applied because very short-lived families (with under 15 days between the first and last repeater), and a significant portion of families with 2 or 3 events, appear to be near simultaneous events, which may be the result of nearby asperities rupturing separately, rather than one single asperity rupturing repeatedly (Lengliné and Marsan, 2009). We are confident in larger families because they are based upon more cross-correlation similarity measurements. Thus, excluding doublets, triplets, and very short-lived families, we find a total of 376 repeaters grouped into 62 families. In the interseismic period, we only identified 8 repeaters each belonging to different repeating families. Examples of family waveforms are shown in Figure 59 for the PDNS station.

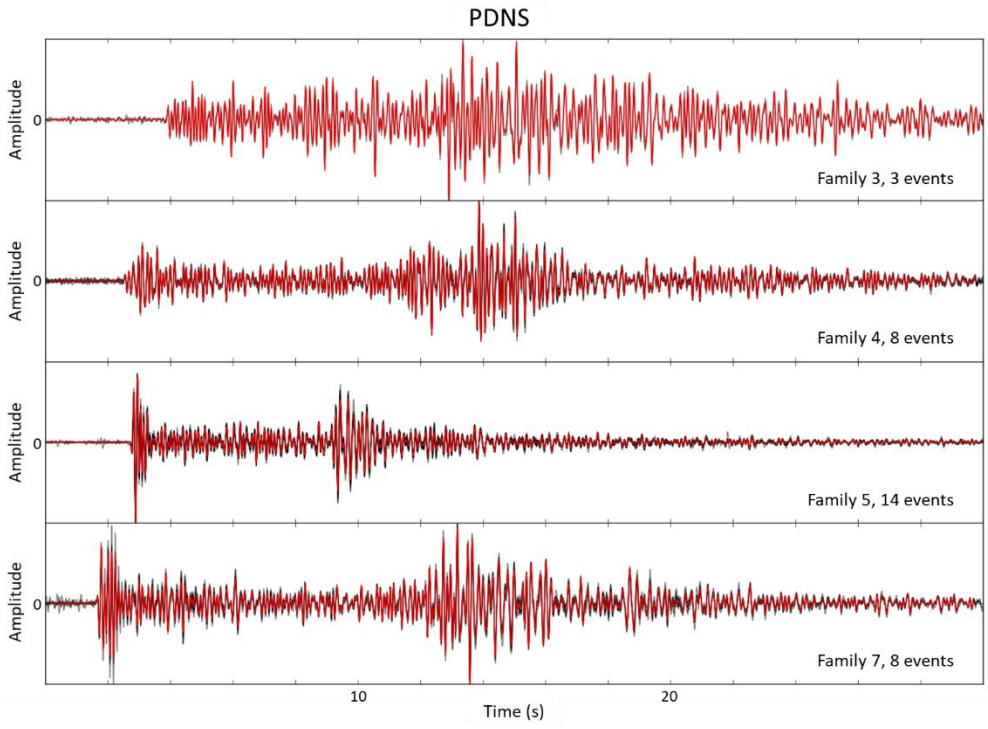

Figure 59 : Normalized waveform plots of four different families recorded at the PDNS station. Grey lines are individual repeaters' waveforms, while red lines are the stacks of all individual repeater waveforms available within a family.

Although other studies sometimes use a spatial parameter to classify repeaters, like source overlap or hypocentral distance (Uchida, 2019 and references within), we have elected to base our classification solely on correlation coefficients. This is in part because 61 out of 376 repeating earthquakes could not be relocated with HypoDD, due to the small number of stations available in the first month. It is also because the location uncertainty was too large to accurately determine whether two earthquakes shared the same source. We estimated the relative relocation average error attributable to noise in the data by introducing a random error in our original travel time data and repeating the inversion 100 times for all 2483 relocated events. That error was found to be around 750 m on average. To that we must add the errors that stem from the unevenness of the network, since most of the stations used do not cover the entire period, and since all the stations used for cross-correlation differential times are on land. We performed 50 iterations with all 2483 relocated events during which we randomly take out one station for each earthquake pair. Doing so yielded an average error of about 580 m. Since the relative location errors were an order of magnitude higher than the repeaters' source areas, it was not possible to use hypocentral distance as a classification criterion without missing a significant number of repeaters.

4.4 Results

4.4.1 Location and evolution of repeaters

The proportion of repeaters among aftershocks through time is shown in Figure 60. The catalog used as the basis for this study (Agurto-Detzel et al., 2019) stopped on day 381 after the mainshock (April 30th 2017). Any later earthquake was found exclusively with template matching, making the proportion of repeaters past day 381 biased. The proportion of repeaters shows that the increased number of stations past the first month did not lead to a sharp increase in detections, which ensures that our detection capacities remain relatively constant. Although some of the earlier aftershocks are clearly missing due to the decreased detection capabilities right after the mainshock, the proportion of repeaters seems to remain unaffected (Figure 60). Large aftershocks affect the number of repeaters and other aftershocks, but not necessarily their relative proportions, as in the first ~100 days following the Pedernales earthquake the proportion of repeaters remains relatively constant at around 0.1. This suggests that the processes driving both aftershocks and repeaters are strongly linked in the region during that time.

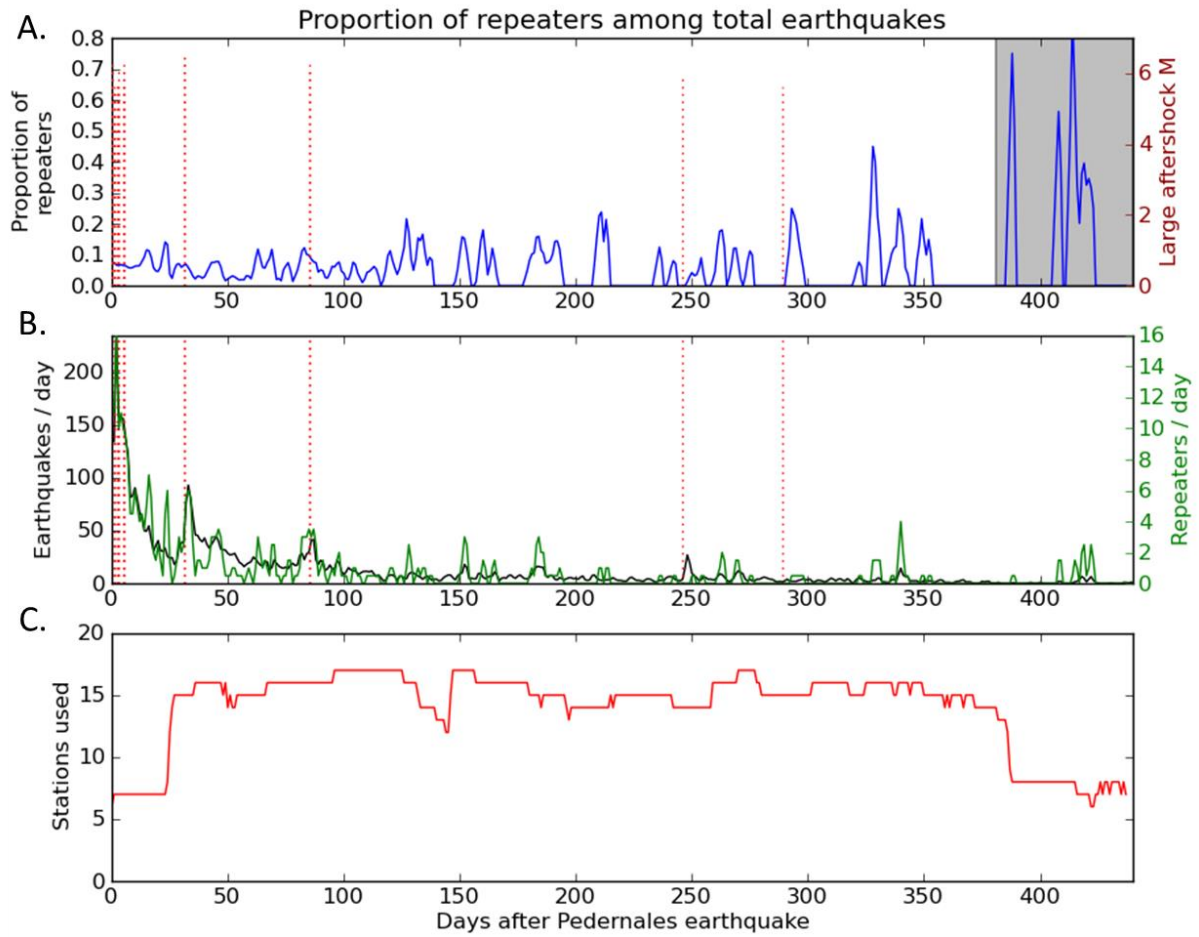

Figure 60 : Number of repeaters through time. A: proportion of repeaters detected among aftershocks per day. Note that the catalog originally stops after 1 year, so any event after that was detected through template-matching in an attempt to find new repeaters. Thus the proportion shown after 381 days (grey zone) is biased. The red dashed lines show the dates and magnitudes of large aftershocks (M>5.5). B: total number of earthquakes (in black) and repeaters (in green) per day. C: total number of stations used to detect repeating earthquakes.

As expected after a large earthquake, the recurrence times of repeating earthquakes drop, then gradually increase after the mainshock (Figure SC.4). At least 50 families of repeaters show a consistent gradual increase of recurrence time. Some families show perturbations and small decreases in recurrence time after large aftershocks with magnitudes above 6, like in May and July 2016. These perturbations tend to be accompanied by small increases in magnitude. Most families follow an Omori-type law, like what has been documented in other parts of the world (Schaff et al., 1998), with recurrence times decaying faster as we get closer to the afterslip center. This is especially apparent near the northern afterslip patch. Due to the lack of interseismic recurrence times, we cannot determine how recurrence times at the end of our study compare to interseismic ones. However, stress perturbations from the mainshock seem to still be present, because recurrence times at the end of our study are still increasing. This is

consistent with geodetic studies that suggest that postseismic slip is still happening in Ecuador in 2020 (Rolandone et al., 2020).

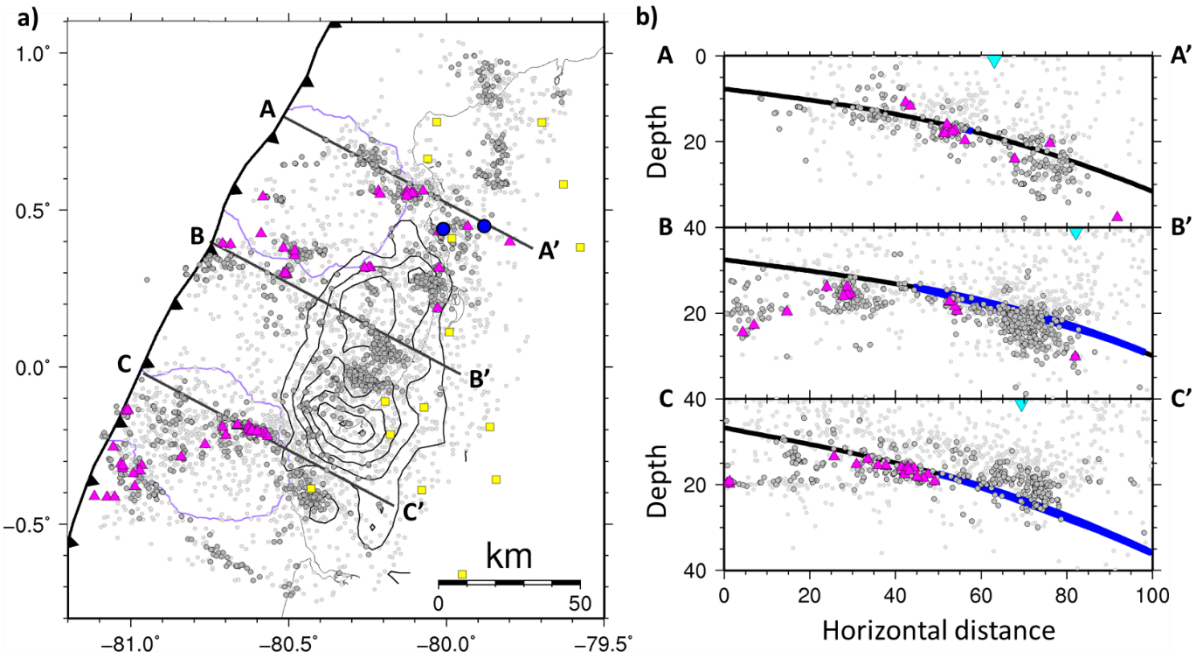

Figure 61 : Seismicity in the study region. a) Seismicity in map view. Relocated earthquakes (dark gray, 2483 events), non-relocated earthquakes (light gray, 3134 events) and repeaters (pink triangles, 62 families) are shown. Stations used for the classification of repeaters are shown as yellow squares. 1m contours of the rupture zone are shown in black (Nocquet et al., 2017). Blue circles show the two largest M6.9 and M6.7 aftershocks that occurred on May 18th 2016. The 200 mm limit of the afterslip is shown in purple (Rolandone et al., 2018). b) Seismicity in 30 km wide cross sections. The black line is the slab 1 plate interface (Hayes et al., 2012). The blue highlight corresponds to the portion of the interface that experienced more than 1 m of coseismic slip during the 2016 Pedernales earthquake (Nocquet et al., 2017). The coastline is depicted using inverted light blue triangles.

Relocated aftershocks and repeaters are shown in map and cross section view in Figure 61. Absolute aftershock relocations have a lateral uncertainty of 1.7 ± 1.3 km and a depth uncertainty of 4.3 ± 3.7 km on average. There are more significant errors in depth within 25 km of the trench, especially towards the south, where many events appear to be aligned on the 20 km depth discontinuity of the 1D velocity model. The lateral uncertainty in this region is 2.4 ± 1.1 km, while the depth uncertainty is 7.3 ± 4.2 km. A combination of poorer station coverage near the trench, especially in the first month, and a 1-D model ill-fitted for the complex velocity structure in the area likely accounts for these large errors. Earthquakes closer to the dense land network have better constrained locations, with a lateral error of about 1.5 ± 1.1 km and a depth error of about 3.3 ± 2.9 km. These events typically cluster close to the plate interface.

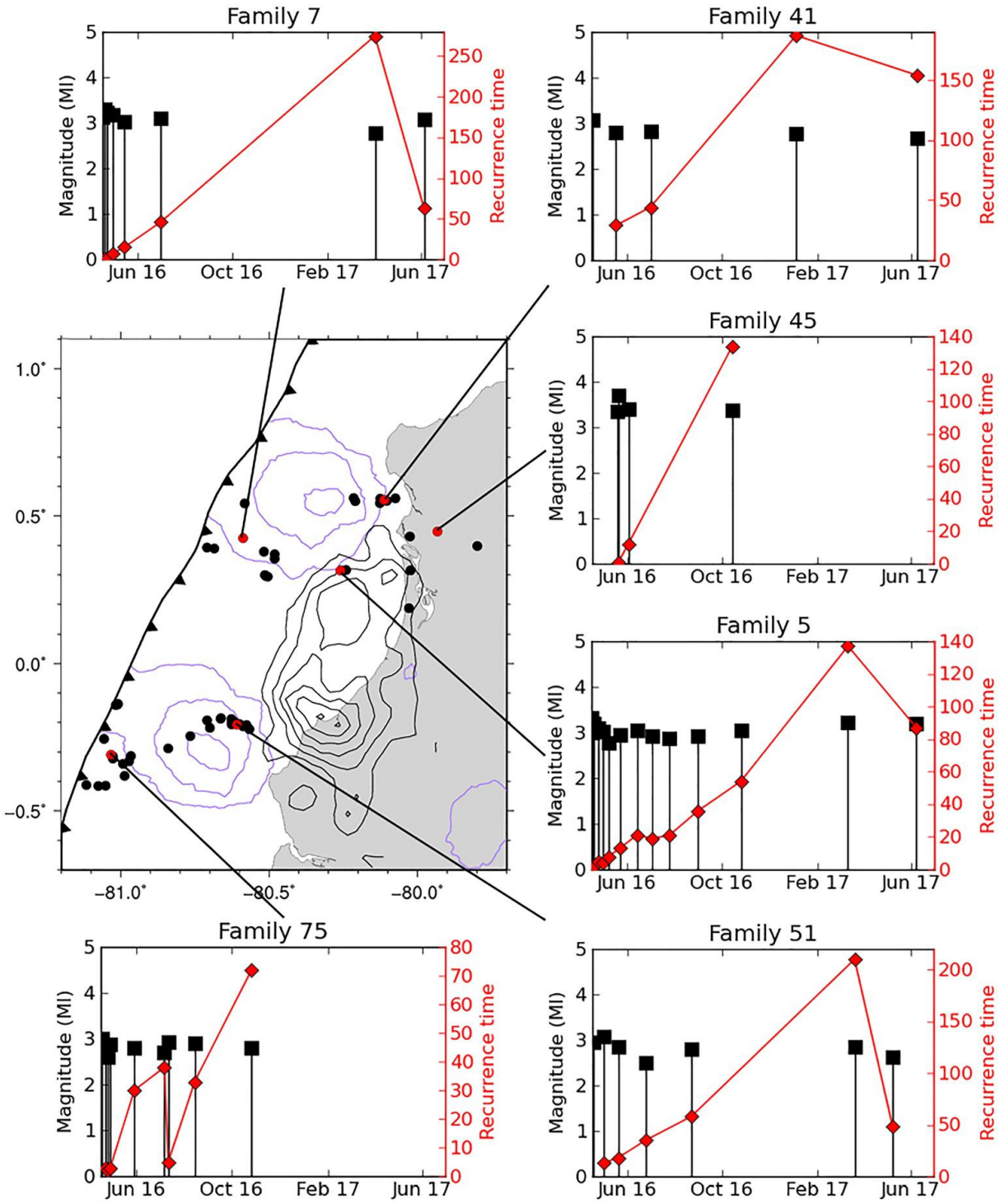

Figure 62 : Locations and evolution of six selected repeating earthquake families (red on the map). On the map, all families are shown as black dots, and 200 mm contours of the afterslip are shown in purple (Rolandone et al., 2018). For each selected family, postseismic repeaters' magnitudes (black squares) and recurrence times (red diamonds) are shown as a function of time.

In map view, repeater distribution appears to be similar to that of aftershocks. Most families are located in larger clusters, with only a few families being isolated elsewhere. This is consistent with suggestions that the Pedernales aftershocks are driven in large part by afterslip (Agurto-Detzel et al., 2019), similarly to repeaters. In fact, repeaters primarily occur updip of

the mainshock rupture, where most of the afterslip occurs (Rolandone et al., 2018; Tsang et al., 2019). With a few exceptions north-east of the coseismic rupture, both repeaters and aftershocks are contained within three trench-perpendicular seismicity streaks that stretch between the coseismic rupture zone and the trench. These are permanent features in the area, visible in both the interseismic and postseismic periods (Agurto-Detzel et al., 2019; Font et al., 2013). This area between the rupture zone and the trench is subject to only small coseismic Coulomb stress changes from the mainshock (Figure SC.5a). Repeaters in particular mostly experience small stress increases. About 10% of repeaters and 20% of non-repeaters in the first month experience more than 10 bars of coseismic stress increase from the mainshock (Figure SC.5b). Overall, the median stress increase experienced by repeaters is 3.5 bars, enough for coseismic stress changes to induce short-term triggering for some repeaters (K. H. Chen et al., 2013). However, the pattern of repeaters' and earthquakes' distribution is very different from the distribution of coseismic stress changes (Figure SC.5a).

Three main regions contain repeaters: the northern afterslip patch (A-A' and B-B', Figure 61), the southern afterslip patch (C-C'), and the area north-east of the main coseismic rupture zone (near blue circles, Figure 61). Repeaters are present around the northern patch of afterslip throughout the whole period (Figure 62). This includes observations near the trench. This area experienced SSEs during the interseismic period, though their slip amplitude was about ten times lower than that of the 2016 afterslip (Vaca et al., 2018). While the 2013 SSEs did cause possible repeaters (Vaca et al., 2018), neither they nor the repeaters we detected in the year before the mainshock, occurred closer than 40 km from the trench (Figure SC.6).

Similarly, most repeaters in the south occur around the slip maximum of the southern patch of afterslip. Unlike in the north, this patch sits on a highly coupled region (Figure 58). While the repeaters in the cluster closest to the center of the patch are more numerous, and their magnitudes are generally higher, overall repeaters behave similarly in the northern and southern afterslip patches. One difference is that families near the trench in the south mostly stop after ~200 days, while trenchward families in the north remain active until the end of the study period. In the cluster closest to the southern slip maximum, however, families are numerous and repeaters occur for at least ~300 days (Figure 62). This cluster was also active before the mainshock, as two families were activated there during the year preceding the mainshock.

Finally, the region north-east of the rupture contains a few repeaters, along with many aftershocks. It is likely that these repeaters, along with the other earthquakes, are caused directly by the M6.9 and M6.7 aftershocks on May 18th 2016, as they are only activated after the first month. Repeating families in this region, in addition to being sparse, stop after less than 200 days. This may reflect the short duration of the aseismic slip that occurred in the area, although we cannot know as no afterslip model exists past the first month.

Several regions have a high density of aftershocks but no repeaters. There is a high density of aftershocks between the two coseismic slip maxima, as well as at the southern end of the rupture zone, but no repeaters occur there. Within the coseismic rupture zone, it is likely that aseismic slip is prevented by the nearly total stress release during the mainshock. Even aftershocks within the rupture area may not occur at the plate interface, although this cannot be confirmed given the depth uncertainties and the lack of focal mechanisms (Agurto-Detzel et al., 2019; Soto-Cordero et al., 2020). The other clusters without repeaters are located north of the rupture, at -79.90°W (Figure 61a). Aftershocks north of 0.8°N mostly occur in December of 2016, starting on December 2nd, in the overlying plate (Soto-Cordero et al., 2020) and are not likely to be directly linked to afterslip. These events do not seem to directly relate to the aftermath of a large earthquake, although three earthquakes above magnitude 5 occur in that region between December 12th and December 20th, during the peak of seismic activity. They may be related to a swarm occurring in the Esmeraldas sequence 30 km to the east, itself happening on a crustal fault and probably in concurrence with aseismic slip, which starts on November 28th (Hoskins et al., 2021). Meanwhile, aftershocks in the cluster between 0.6°N and 0.8°N are primarily associated with the large M6.9 and M6.7 aftershocks of May 18th 2016 and the M6 and M6.2 earthquakes on July 11th 2016.

4.4.2 Repeaters and afterslip

Repeaters identified in this study seem strongly associated with the two main afterslip patches. We aim at quantifying that relationship by using the GPS-derived 30-days afterslip model developed by Rolandone *et al.* (2018). Since no geodetic afterslip model currently exists past the first month, we primarily focus on families that are active within that time period. To calculate slip from repeaters, we use the equation developed by Nadeau and Johnson (1998), henceforth referred to as the NJ equation:

$$\log(d) = 0.17 \log(M_0) - 2.36$$

Here the seismic moment M_0 is in dyne-cm and the slip d is in cm. Although the equation is an empirical relation based on geodetic data from Parkfield, California, it has been used successfully in several subduction settings, including Japan (Igarashi, 2020; Matsubara et al., 2005; Nomura et al., 2017; Uchida et al., 2016; Uchida, Nakajima, et al., 2009; Uchida, Yui, et al., 2009; Uchida and Matsuzawa, 2013) and Chile (H. Huang et al., 2017; Kato et al., 2016; Meng et al., 2015). The model has been criticized in different studies as being physically implausible (Beeler et al., 2001; Sammis and Rice, 2001), as it assumes that no aseismic slip occurs on the asperities and that stress drop is a function of magnitude, therefore predicting unrealistic stress drops for small earthquakes (Beeler et al., 2001; Sammis and Rice, 2001). A

competing model developed by Beeler et al., (2001) would not materially alter our estimates, since it tends to give similar results to the NJ equation (Igarashi et al., 2003; Mavrommatis et al., 2015). We therefore feel confident in using the NJ equation here.

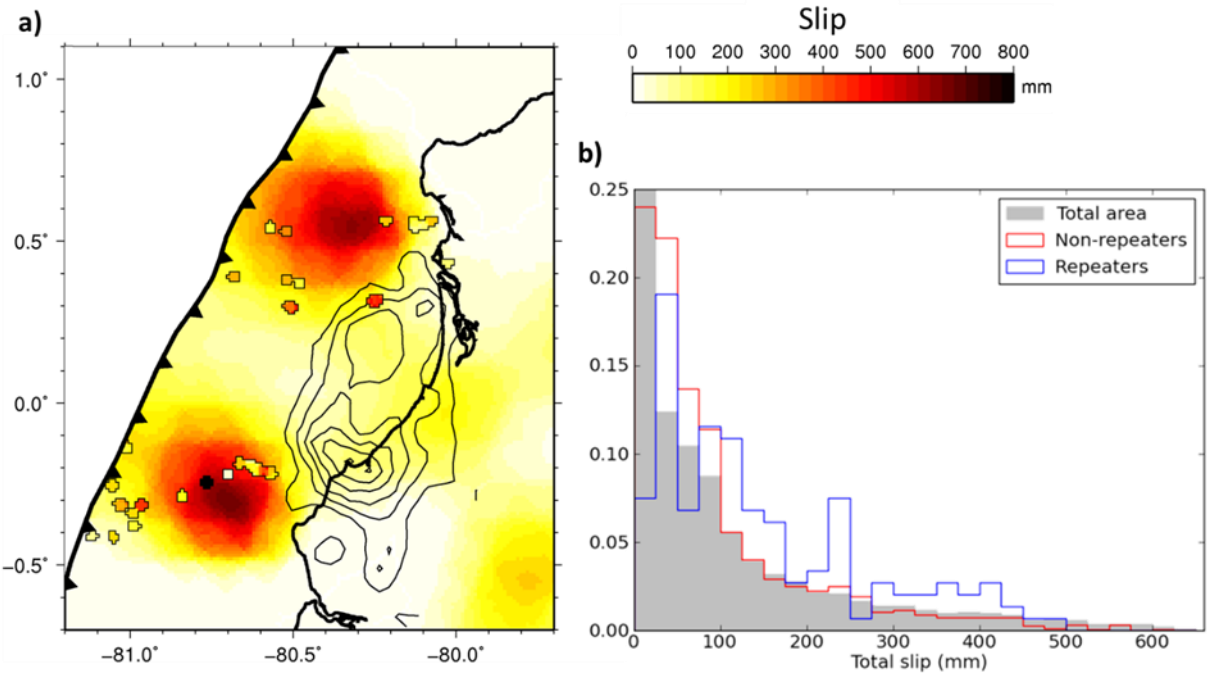

Figure 63 : Positioning of repeaters with regards to the afterslip, and comparison between repeaters' estimated slip and the GPS model of afterslip from Rolandone et al., (2018). a) Total aseismic slip after 1 month (Rolandone et al., 2018). Outlined patches represent slip calculated from repeating families with 2 or more events in the first month, using the NJ equation. For easier comparison both among families and with the geodetic model, NJ slip from each family was extrapolated to one month, using the ratio of slip calculated using the NJ equation to slip modeled by GPS between the first and last repeater of the month. Each cell averages slip from families within a 2 km radius. b) Percentage of first month repeaters and non-repeaters located in areas experiencing a given amount of afterslip (sampled over 5 km²), as estimated from the GPS model (Rolandone et al., 2018). The total slip is the amount of afterslip experienced between the mainshock and the time of a given earthquake at that location, according to the GPS model. Non-repeaters are shown in red and repeaters are shown in blue. The grey bars show the percentage of the total study area experiencing a given amount of afterslip.

The resulting slip estimates are shown in space and time in Figure 63a and Figure 64. From the geodetic model of afterslip (Rolandone et al., 2018), we estimate the amount of slip that occurred between the first and last repeater of the month within a family. Some agreement is found in the spatial distribution of slip from repeaters and GPS (Figure 63a), as well as with its temporal evolution (Figure 64). The shape of the curves showing the evolution of slip with time for GPS and repeaters are similar, in both the northern and the southern slip regions. Absolute estimates of the average slip differ by a factor of 0.5 to 0.95 from geodetic estimates, which is in the same range of uncertainties as in other studies (Igarashi et al., 2003; Uchida, Yui, et al., 2009). There is also a good temporal agreement between smaller-scale surges in GPS-derived

slip and in repeater-derived slip, around days 5, 10 and 15, although these perturbations appear slightly later in the GPS data. However, upon closer inspection of individual families, the relationship between GPS and repeater-derived slip breaks down. First, there is a lot of spatial heterogeneity in the slip calculated (Figure 63a). This is true even when considering long-term slip (Figure SC.7). More explicitly, GPS and repeater-derived slip of individual families do not appear to have a strong relationship (Figure 65a), even when considering families only from one region. We confirm this by plotting the average moment of individual families against their average experienced slip as modelled from GPS data (Figure 65b). We find a large scatter and a poor correlation, despite a similar overall trend to the repeaters at Parkfield (Figure 65b).

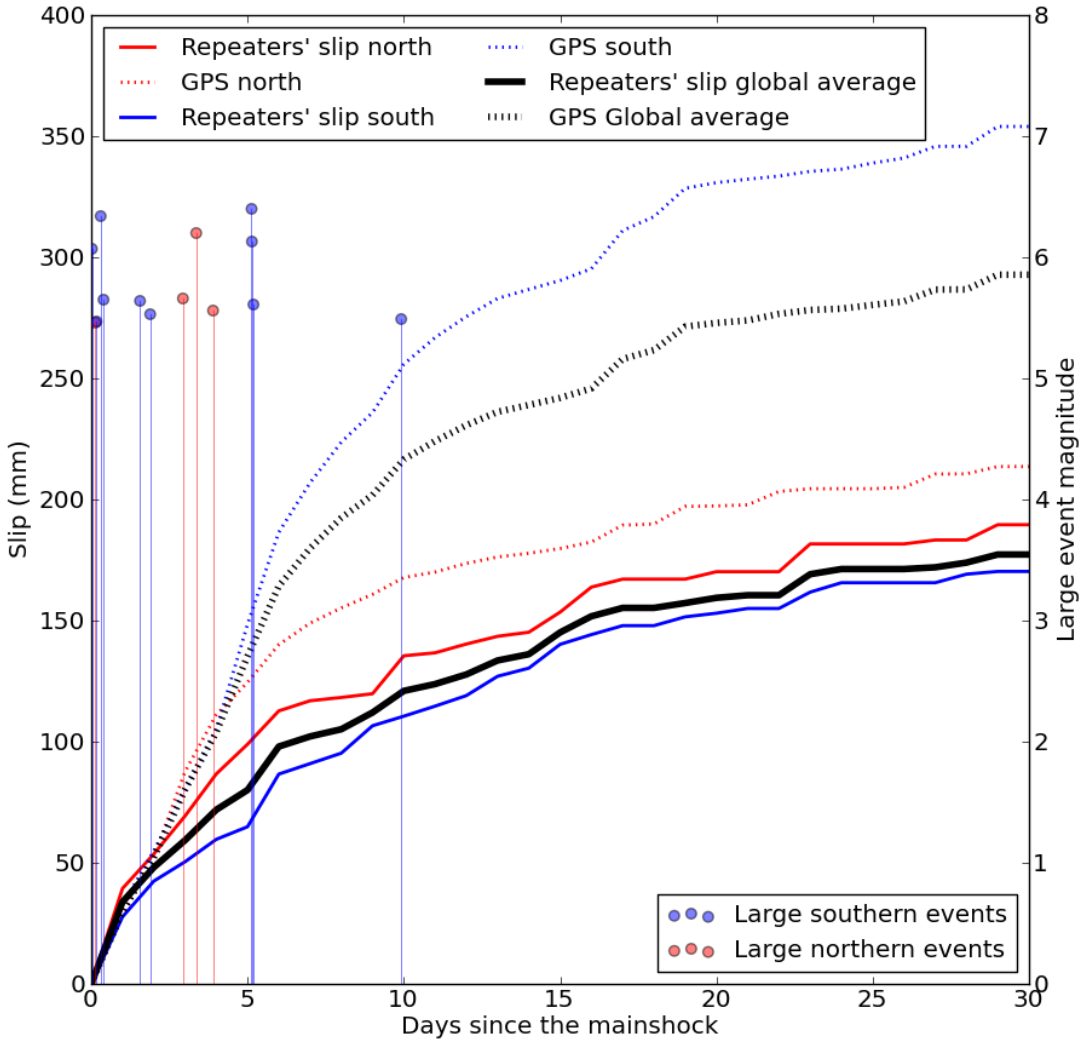

Figure 64 : Average cumulative afterslip experienced in the first month by repeating families within 50 km of the northern (red) and southern (blue) patch, and over the whole area (black). Full lines represent the average calculated slip experienced

by families. The dotted lines show the average slip from the geodetic model at the locations of the families (sampled over 5 km²). Red and blue circles represent earthquakes with Ml>5.5 occurring in the north and south respectively.

The complexity of the slip/repeaters relationship is reinforced by the absence of repeaters in areas with maximum afterslip as well as in areas with no slip (Figure 63). The distribution of non-repeaters follows the slip distribution, at least for slip values larger than 100 mm, which are better resolved. Repeaters are more concentrated in areas of moderately large slip, between 100 and 450 mm. They are however absent from areas which experienced more than 500 mm of slip. In map view, it is apparent that repeaters mostly surround the two afterslip maxima (Figure 63a). This is true in the southern as well as the northern slip regions, although the different coupling values may imply different asperity densities and productivity of seismicity. This reinforces the idea that something beyond simply the amount of slip is influencing the repeaters and their distribution. Since repeaters appear to be mostly on the edges of the main patches of afterslip, afterslip gradient is a likely candidate mechanism.

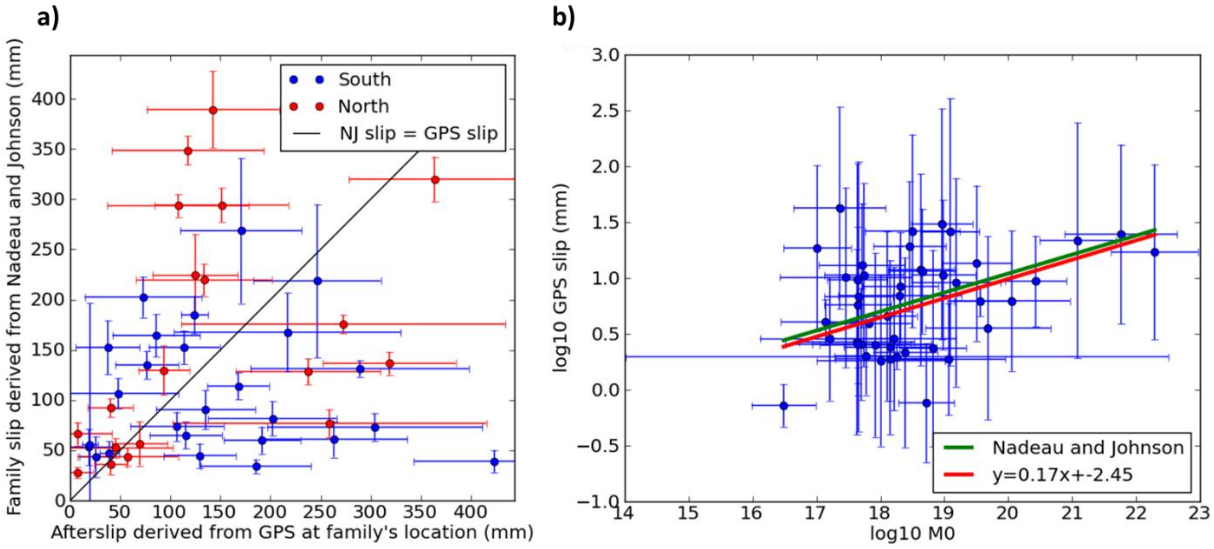

Figure 65 : Comparison of slip derived from repeaters and GPS a) Aseismic slip experienced by a family between the first and the last repeater of the first month, estimated from the geodetic model versus estimated using the NJ equation. Only families with 2 or more events in the first month, and more than a day between the first and the last event of the month, are used. Families within 50 km of the northern and southern afterslip patch are shown in red and blue respectively. b) Comparison of average family seismic moment and average slip experienced. The green line is the linear relationship predicted by the NJ equation. The red line is the least squares fit through the data.

4.4.3 Repeaters and afterslip gradient

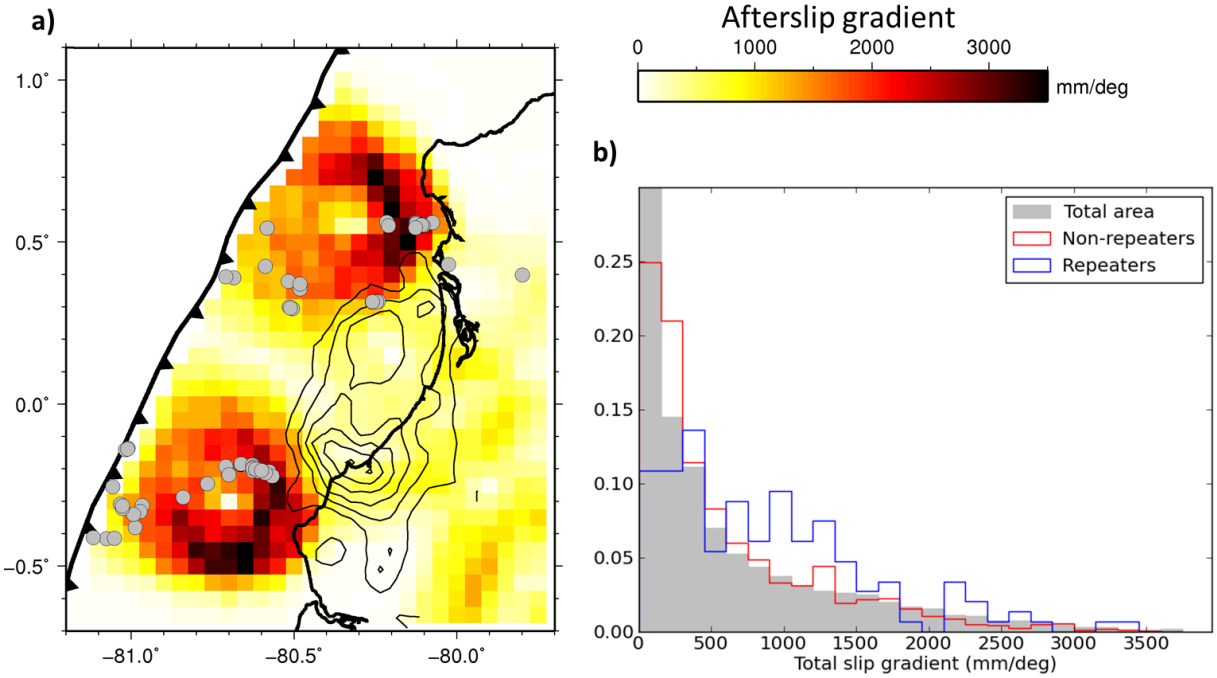

Figure 66 : Afterslip spatial gradient experienced by repeaters. a) Map of first month repeating families (in grey) and the spatial gradient of the cumulative one month afterslip from Rolandone et al. (2018). b) Percentage of first month repeaters and non-repeaters located in areas experiencing a given amount of afterslip gradient (sampled over 5 km²). The slip gradient is the amount of afterslip gradient experienced between the mainshock and the time of a given earthquake at that location, according to the GPS model. Non-repeaters are shown in red and repeaters are shown in blue. The grey bars show the percentage of the study area experiencing a given amount of afterslip gradient.

Repeaters seem to concentrate in areas with large afterslip gradients, and the gradient associated with repeaters is higher than for the aftershock population (Figure 66). More generally, it seems non-repeaters are present at all gradient values, while repeaters occur only where gradient is moderate to high. To better illustrate this, and since the afterslip patches are roughly concentric circles, we plot the distribution of earthquakes and repeaters against distance from the center of the slip patch at the end of the month (Figure 67C and D). We see that the distribution of repeaters has a stronger correlation than non-repeaters with the afterslip gradient, in the south especially. In both the north and south, there are almost no earthquakes at the center of the patch where the slip is highest. Were the amount of slip to most strongly influence the location of repeaters or non-repeaters, their numbers would be highest at the center and decay with distance, but that is not the case. Instead, in the north and south the number of repeaters peaks at 25 and 15 km away from the center of the patch respectively, which is nearer to where the afterslip gradient peaks. Since the two main patches of afterslip remain relatively stationary throughout the month, their edges remain fixed in space (Figure SC.8). As a result, afterslip gradient, which is largest at these edges (Figure 66a), grows consistently throughout the month,

while its spatial extent remains near constant. This implies that the location of repeaters with regards to slip is constant over the whole month. Overall, this suggests that aseismic slip gradient may be a major control on the distribution of repeaters.

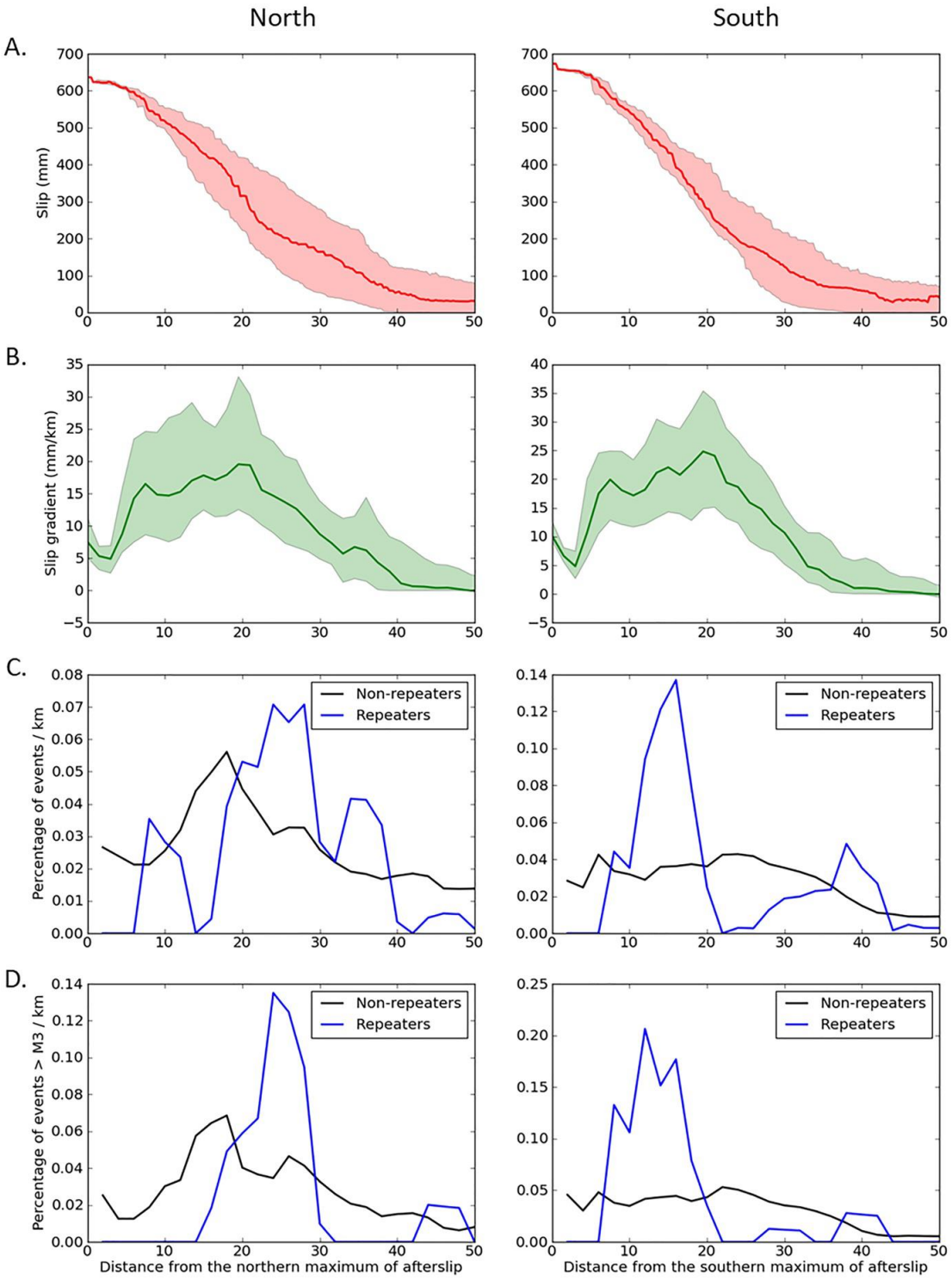

Figure 67 : Average afterslip, afterslip gradient and seismicity distribution with regards to distance from the center of the northern (left) and southern (right) patch of afterslip at the end of the first month. The top panels (A) show the evolution of geodetic afterslip with distance. The panels below (B) show the average afterslip gradient as a function of distance. Half of

all radial profiles fall within the shaded area. The third panels (C) show the distribution of all repeaters (blue) and non-repeaters (black) with regards to distance. The bottom panels show only repeaters from families with median magnitudes above 3 and minimum magnitudes above 2.7 (blue), and non-repeaters with magnitudes above 3 (black).

4.5 Discussion

We have found repeating families in the aftershock sequence of the Pedernales earthquake, which qualitatively appear to be associated with afterslip, both spatially and temporally. These repeaters are mainly located primarily at the edges of the two main afterslip patches, where afterslip gradient is highest, rather than at their center, where slip is highest. Slip gradient seems to be an important factor controlling repeaters. We will now explore this relationship in detail.

4.5.1 Influence of uncertainties on the results

Before interpreting our results, it is important to assess their robustness by evaluating the impact of uncertainties. While gaps in station coverage (Figure SC.2b) have been shown to be in large part mitigated, errors in repeater detection and classification are a potential issue. We mitigate errors by using a high correlation threshold. This likely means that some repeaters are missing from the dataset, but it ensures we have high confidence in the families that we do interpret. Our dataset is additionally limited by the repeaters' magnitudes. While the total catalog local magnitudes are mostly between 1.5 and 3.5, repeaters' local magnitudes are concentrated between 2.2 and 3.4 (Figure SC.9a), suggesting that repeating families with magnitudes lower than 2.2 are likely incomplete or undetected. This could affect the spatial distribution of repeaters in areas where the average magnitude is low, like northeast of the mainshock rupture and within the mainshock area. The latter 2 regions, however, have a magnitude of completeness of 2 and 1.5 respectively (Figure SC.9b), so it is less likely that repeating families were missed there. A lack of completeness within a family could lower its slip estimate, and may explain low values when compared to GPS-derived slip. On the other hand, some non-repeaters may have been missclassified as repeaters due to an inadequate upper threshold of the filter used for correlation. This may be an issue for small-magnitude earthquakes with corner frequencies significantly above the filter's upper frequency boundary (Uchida, 2019 and references within). However, even when examining families with median magnitudes larger than 3 and minimum magnitudes larger than 2.7 (Figure SC.10), there still is no visible relationship between slip estimations from GPS and repeaters. The placement of repeaters with regards to slip and gradient also remains similar (Figure 67)

Since we compare the distribution of repeaters to that of non-repeaters, any repeater that has been falsely identified as a non-repeater might also impact on our analysis. To avoid this issue, we exclude from the group of non-repeaters every earthquake that has a correlation coefficient above 0.9 with another earthquake. The threshold of 0.9 is chosen as it is used by some studies to classify repeaters (e.g. Uchida, 2019 and references within), and thus the nature of these earthquakes as repeaters or non-repeaters is uncertain. Thus we ensure that the repeaters group and the non-repeaters group are truly distinct.

The different sensitivities of GPS and repeaters necessarily impact our comparisons with GPS models. The GPS slip model is smooth by necessity, while the repeaters' slip estimates are not. A highly heterogeneous slip at the interface would be smoothed when recorded at the surface and therefore be poorly resolvable by GPS models, but would explain the high degree of heterogeneity of the repeaters' slip estimates. However, if families did concentrate in small heterogeneous areas of higher-than-average slip unresolvable by the GPS, we would probably expect repeaters to overestimate of the overall slip, which is seemingly not the case here.

GPS models themselves have uncertainties to take into account. We consider the center of the southern patch of afterslip to be well constrained, as a different afterslip model shows it to remain within 5 km (Figure SC.11) (Tsang et al., 2019). In the north, the center of the afterslip deviates by 10 km, but the landward edge of the patch remains in place, leaving the trenchward side as the most uncertain (Figure SC.11).

Another source of error is the uncertainty of earthquake locations. Although lateral earthquake location errors are small on average, they have to be combined with errors in the geodetic model of afterslip, especially near the trench, in order to ensure our observations regarding the relationship of repeaters to slip and to slip gradient is correct. For example, the underestimation of slip from an earthquake cluster close to the center of an afterslip patch compared to one given by the GPS model (Figure 63a), could be explained by the cluster being wrongly located too close to the afterslip patch center. In fact, most of the repeaters within the high slip areas tend to have low estimations of slip compared to the GPS, while the families further from the patch tend to have slip estimations that are higher than the GPS (Figure 63a). If we were to assume that our repeaters' slip estimations are correct, and this discrepancy is due entirely to location errors, then if anything, this confirms that repeaters should be more concentrated on the edges and less in regions of high slip. Alternatively, the regularization parameters used to derive the GPS model could have led to an overconcentration of slip at the center of the two slip patches (Rolandone et al., 2018). A more spread out slip may explain some of the regional discrepancies between the GPS and family slip, although it would still not explain why repeaters remain located on the edge of the afterslip. To account for location and geodetic model errors and smoothing, we give each family an error for GPS slip that corresponds to the standard deviation of the GPS slip within a 15 km radius of the family's

location (Figure 65a). Even when taking the average of both NJ slip and GPS over a 30 km region, the agreement between the two is still poor (Figure SC.12), suggesting that location errors are neither the reason for the lack of repeaters near the center of the afterslip, nor the cause of the discrepancy between repeaters and GPS slip.

4.5.2 What controls repeaters occurrence?

We have shown a significant correlation between the location of repeaters and the gradient of the afterslip. Additionally, we have found that the relationship of geodetic slip estimates to repeaters is not linear in the region, even taking uncertainties into account. These findings hint at afterslip gradient being an important factor controlling repeaters. We will now discuss how feasible that statement is, in light of studies in other regions.

A few factors are widely recognized as influencing the locations of repeaters. The most important factor is the presence of aseismic slip (Waldhauser and Schaff, 2008). This means repeating earthquakes are typically outside, or around, historic large earthquake rupture zones and highly coupled regions (Chaussard et al., 2015; Igarashi et al., 2003; Ryder and Bürgmann, 2008; Templeton et al., 2009; Uchida et al., 2003; Uchida, Yui, et al., 2009), although on occasion they have been found inside past (Uchida and Matsuzawa, 2013) or future rupture zones (Uchida and Matsuzawa, 2011). In Ecuador, repeaters are indeed found in slipping areas outside of the rupture zone, although interseismic coupling appears to have only a limited bearing on the locations of repeaters, which seemingly occur at all values of coupling (Figure SC.13). Another common observation that fits with our data is the location of repeaters within areas containing dense microseismicity (Kato and Igarashi, 2012; Ryder and Bürgmann, 2008). Repeaters can only occur on asperities that are seismogenic, meaning that frictional features always remain the primary factor controlling their distribution. As such, repeaters cannot occur in completely aseismic areas, any more than they can occur in locked areas.

To our knowledge, there are no studies examining specifically the locations of repeaters with regards to afterslip gradient. However, repeaters occurring primarily away from the aseismic slip center is not a unique observation. Along the San Andreas fault (California), earthquakes, including repeaters, tend to align along horizontal streaks (Lengliné and Marsan, 2009; Rubin et al., 1999). These streaks have been proposed to be boundaries between seismic and aseismic slip (Sammis and Rice, 2001), although they are more generally thought to have a geological origin (Rubin et al., 1999). Joint geodetic and seismological studies show that repeaters appear to be absent from areas that slip the most, preferring instead areas of intermediate slip (Chaussard et al., 2015; Templeton et al., 2009). As a result, studies using only repeaters can underestimate the total slip, since they do not sample the slip maximum

(Templeton et al., 2009). While the NJ relationship was derived first in Parkfield, its application is not straightforward in the whole of California. There is always some small-scale heterogeneity, so that in some cases the M_0-Tr relationship only weakly follows the NJ trend (Lengliné and Marsan, 2009). When comparing InSAR models to repeaters slip, slip profiles tend to agree, but are different in detail (Ryder and Bürgmann, 2008), with sometimes large scattering in the calculated Vs InSAR rates (Chaussard et al., 2015). In some cases, particularly for short-term, faster creep, the parameters of the NJ equation need to be changed to better reflect the data (Khoshmanesh et al., 2015), suggesting that the relationship of M_0 to slip is not the same everywhere at every time.

The most studied subduction zone with regards to repeating earthquakes is northeastern Japan. During interseismic times, repeaters appear to be located in slow and fast creeping areas within the seismogenic zone (Igarashi et al., 2003), with a good agreement between GPS measurements and repeaters' slip (Nomura et al., 2017), and relatively small scatter (Igarashi et al., 2003). After the 2011 Tohoku earthquake, however, the density of repeaters appears to have been low within patches of significant afterslip, according to several afterslip models (Iinuma et al., 2016; Silverii et al., 2014; Uchida and Matsuzawa, 2013).

It is perhaps best to compare our study to repeating earthquakes occurring after a large earthquake, to determine whether they do tend to organize around the afterslip maxima or not. On the one hand, the aftermath of the 2015 Mw8.4 Illapel earthquake clearly shows repeaters occurring largely within the area of maximum afterslip, and the slip estimates from repeaters agree well with the GPS models (H. Huang et al., 2017). In this case, however, the afterslip was low in amplitude, staying below 50 cm, and large in extent (H. Huang et al., 2017; Shrivastava et al., 2016), meaning there likely was not a large regional slip gradient anywhere. On the other hand, the 2012 Mw7.6 Nicoya earthquake offers a clear case of repeaters being located on the afterslip edge. Costa Rican repeaters exist largely between the two main patches of afterslip (Chaves et al., 2020; Hobbs et al., 2017; Yao et al., 2017), despite the fact that some non-repeating earthquakes occur closer to the two slip centers (Yao et al., 2017). Like in Ecuador, the two patches of afterslip in Costa Rica both have a high amplitude, here up to 1 m, and a small spatial extent, less than 50 km, meaning the slip gradient would be very high (Figure SC.14). There is also a poorer agreement between the slip derived from repeaters using the NJ equation and the slip from the GPS model, further highlighting the similarities between Costa Rica and Ecuador (Figure SC.14).

It therefore seems that cases similar to ours exist elsewhere, and that the behavior of repeaters with regards to slip and gradient may be dictated by the amplitude of the spatial gradient. The question remains of the extent to which slip gradient influences repeater behavior. There are two main explanations that we can propose. The first is that gradient is simply the indicator of a change in the mechanical properties of the fault, which are themselves responsible

for the occurrence of repeaters. The second is that gradient, or the stress that accompanies it, is directly controlling repeaters.

The first possibility is that the high gradient results from aseismic slip is being stopped by a large locked asperity, with repeaters nucleating at its edge. This idea was proposed by Sammis and Rice (2001) as a way to explain the relationship between repeating earthquakes' recurrence times and seismic moments as proposed by Nadeau and Johnson (1998) without requiring uncommonly high stress drops for repeating earthquakes. This model implies that slip on a repeating asperity is not directly related to overall aseismic slip. It is instead being controlled largely by the presence of the large asperity. Similarly, Anooshehpoor and Brune (2001) model repeaters as asperities within creeping patches inside of larger asperities, invoking slip velocity shielding to explain the scaling of repeaters moment to the overall measured aseismic slip. Both models, however, necessitate the concentration of repeaters along the boundary between large asperities and creeping regions, which is not true for most of our repeaters (Figure SC.13).

A similarly high gradient could be observed if, rather than being stopped by a single large asperity, aseismic slip was slowed down by a multitude of smaller, concentrated asperities. This may still result in slip velocity shielding between asperities of different sizes, explaining heterogeneities between families and a complex relationship of repeaters to slip. In particular, it would explain why, in some regions, nearby repeating aftershocks have very different behaviors but still, when averaged, follow Omori's law and the NJ scaling relationship (Lengliné and Marsan, 2009). However, in our case, slip averaged over a region still does not match with slip derived from geodetic models, putting into question the direct relationship of slip to repeaters (Figure SC.12).

More generally, the absence of repeaters close to the afterslip maxima could be explained by that region being completely aseismic and therefore unable to produce any earthquakes. In that case, the high spatial gradient could be a passive indicator of a rheology change that allows for the presence of earthquakes and repeaters. Like with the previous possibility, this offers no explanation as to why the fit of geodetically-derived and repeater-derived is so poor. More importantly, it raises the question of why repeaters would be present in areas where the afterslip is moderate but the interseismic coupling is close to 0% (Figure SC.13), yet absent from areas where the interseismic coupling and the afterslip are both higher. The transition of repeater-prone to completely aseismic regions would need to be more closely investigated for this to be answered conclusively.

It is also possible that stress transferred from the afterslip, which is directly related to the gradient, is a driving force behind repeaters in the region. While stress is released within the afterslip patches, it induces local stress concentrations at its edges (Andrews, 1976; Rice, 1993; Scholz, 2019; Wynants-Morel et al., 2020). Since the edges of the afterslip patch, along with the areas experiencing the largest slip gradient, remain static throughout the whole period, a

recurrent loading of asperities through continuous stress increase at the edge is possible. We know that stress increase from SSEs can trigger seismic swarms at their edges, as has been shown in Hawaii (Segall et al., 2006) and in New Zealand (Bartlow et al., 2014). No study has currently looked at the applicability of that model for repeaters, but it may be worth investigating in detail. This link between gradient and repeaters has important implications for the estimation of slip using repeaters. Although the presence of repeaters itself remains an indication of aseismic slip occurring in its vicinity, the fact that repeaters occur preferentially at the edges of the slip, and not at its peak, necessarily makes it difficult to accurately quantify the total slip. Additionally, if stress from the afterslip does indeed drive repeaters, then getting an accurate estimation of slip from the latter would likely be challenging.

4.6 Conclusion

We have conducted a systematic search for repeating earthquakes in 14 months of postseismic data of the Mw7.8 2016 Pedernales earthquake in Ecuador, as well as 12 months of interseismic data. Repeating earthquake families were found in the vicinity of the two main patches of afterslip in the 14 months following the mainshock. We show that there appears to be a spatial relationship between the location of repeaters and the spatial gradient of the afterslip. Repeating earthquakes seem to concentrate primarily on the edges of the afterslip, where slip gradient is high, rather than at its center, where slip is high. While structural controls undoubtedly remain the most important factor leading to the presence of repeaters, our results suggest that stress accumulation on the edges of the afterslip may be a driving force behind repeater activity.

Chapter 5: Results from source property calculations

This chapter shows the stress drops, seismic moments and corner frequencies of repeating earthquakes and regular aftershocks determined using spectral ratios. It was written and formatted as a scientific article and is intended for publication in 2022.

Stress drops carry information on the state of stress on a fault, and thus by recovering stress drops we hope to better understand some of the complexity of the megathrust. One of our primary results in this chapter is indeed an anomaly in stress drops near the trench, which we interpret as a region of high pore-fluid pressure, or possibly of distinct frictional properties. Additionally, studying the source properties of repeating earthquakes in particular can provide insight into processes like fault healing and the time evolution of friction on a fault. We find that in most of the study region, the stress drops and corner frequencies of repeating earthquakes have very different evolutions, with even neighboring families behaving differently in time. However, near the trench, stress drops are initially high and all decrease over the postseismic period. We link this behavior to a likely increase in pore fluid pressure over that time.

Spatio-temporal evolution of small earthquakes' source properties in the aftermath of the 2016 Pedernales earthquake

5.1 Abstract

Subduction zones are highly heterogeneous regions capable of hosting large earthquakes. To better constrain the processes at depth, we analyze the source properties of 1514 aftershocks of the April 16th, 2016 Mw 7.8 Pedernales earthquake (Ecuador) using spectral ratios. We are able to retrieve accurate seismic moments, stress drops, and P and S corner frequencies for 597 aftershocks, including 187 events belonging to families of repeating earthquakes. We find that, for the studied magnitude range (Mw 2-4), stress drops appear to increase as a function of seismic moment. They are also found to depend on their distance to the trench. This is in part explained by the increase in depth, and therefore normal stress, away from the trench. However, even accounting for the shallow depths of earthquakes, stress drops appear to be anomalously low near the trench, which is best explained either by a high pore fluid pressure or by different frictional properties in that region. We are also able to examine the temporal evolution of source properties thanks to the presence of repeating earthquakes. We find that the variations of source properties within repeating earthquake families are not uniform, and are highly spatially variable over most of the study area. This is not the case near the trench, however, where stress drops systematically decrease over time. We suggest that this reflects an increase in pore fluid pressure near the trench over the postseismic period.

5.2 Introduction

Subduction zones are home to some of the largest and most damaging earthquakes on Earth. These regions often present a complex slip behavior, as areas of slow aseismic slip can neighbor earthquake rupture. This slip behavior is mostly controlled by the geometry, the structural heterogeneity and the stress state of the megathrust. To know whether a large and damaging earthquake can occur on a given portion of a fault, we therefore need to characterize the fault properties and processes acting upon it in detail. Retrieving the source properties of small to moderate earthquakes can allow us to gain key insights into the large-scale mechanical properties of an active fault. In particular, stress drop ($\Delta\sigma$) indicates the difference in stress

levels between the start and end of an earthquake, and can therefore be an indicator of the initial stress heterogeneities on the fault, as well as its shear strength.

On average, stress drop is thought to be constant across scales (Abercrombie, 1995; Aki, 1967; Allmann and Shearer, 2009). However, in detail, variations in stress drops have been observed and linked to a variety of factors. Some studies have found an increase in stress drops with magnitudes on regional scales (Bindi et al., 2020), and other studies have found that stress drops increase with magnitude but plateau at high magnitudes (Drouet et al., 2011). This remains a controversial point, as observed trends may result from errors in stress drop calculations (Abercrombie, 2021). Tectonic setting can also affect stress drops, as intraplate earthquakes in stable regions typically have higher stress drops than interplate earthquakes (Viegas et al., 2010). Similarly, faulting type seems to influence stress drops, as some studies show strike-slip earthquakes tend to have higher stress drops (Allmann and Shearer, 2009), although other studies find that thrust faulting earthquakes have higher stress drops than strike-slip ones at depth (Hardebeck and Aron, 2009).

Some authors have found a degree of correlation between stress drops of microearthquakes and the coseismic slip areas of large earthquakes: stress drops were sometimes found to be high around past rupture zones and low within them (Yamada et al., 2021), although that correlation is ambiguous (Allmann and Shearer, 2007; Shearer et al., 2006). Similarly, Hardebeck and Aron (2009) found that stress drops of earthquakes in and around locked zones were higher on average than those on creeping portions of the Hayward fault (California) at similar depths, suggesting a link to coupling. Stress drops have also sometimes been found to increase with depth in the crust as a consequence of the increase in vertical stress (Boyd et al., 2017; Hardebeck and Aron, 2009; Huang et al., 2017), including in subduction zones (Oth, 2013; Uchide et al., 2014). Stress drops depending primarily on applied shear stress is consistent with both their increase with depth and their relationship to fault locking and faulting type (Hardebeck and Aron, 2009). Finally, pore fluid pressure can decrease stress drops by reducing the effective normal stress (Goertz-Allmann et al., 2011).

Variations of stress drops with time have also been observed, especially after large earthquakes. However, there is no unique behavior expected after a mainshock, as both increases and decreases in stress drop have been observed (X. Chen and Shearer, 2013). Shear stress changes induced by the mainshock may account for some of the observed changes in stress drop after a large earthquake (Allmann and Shearer, 2007).

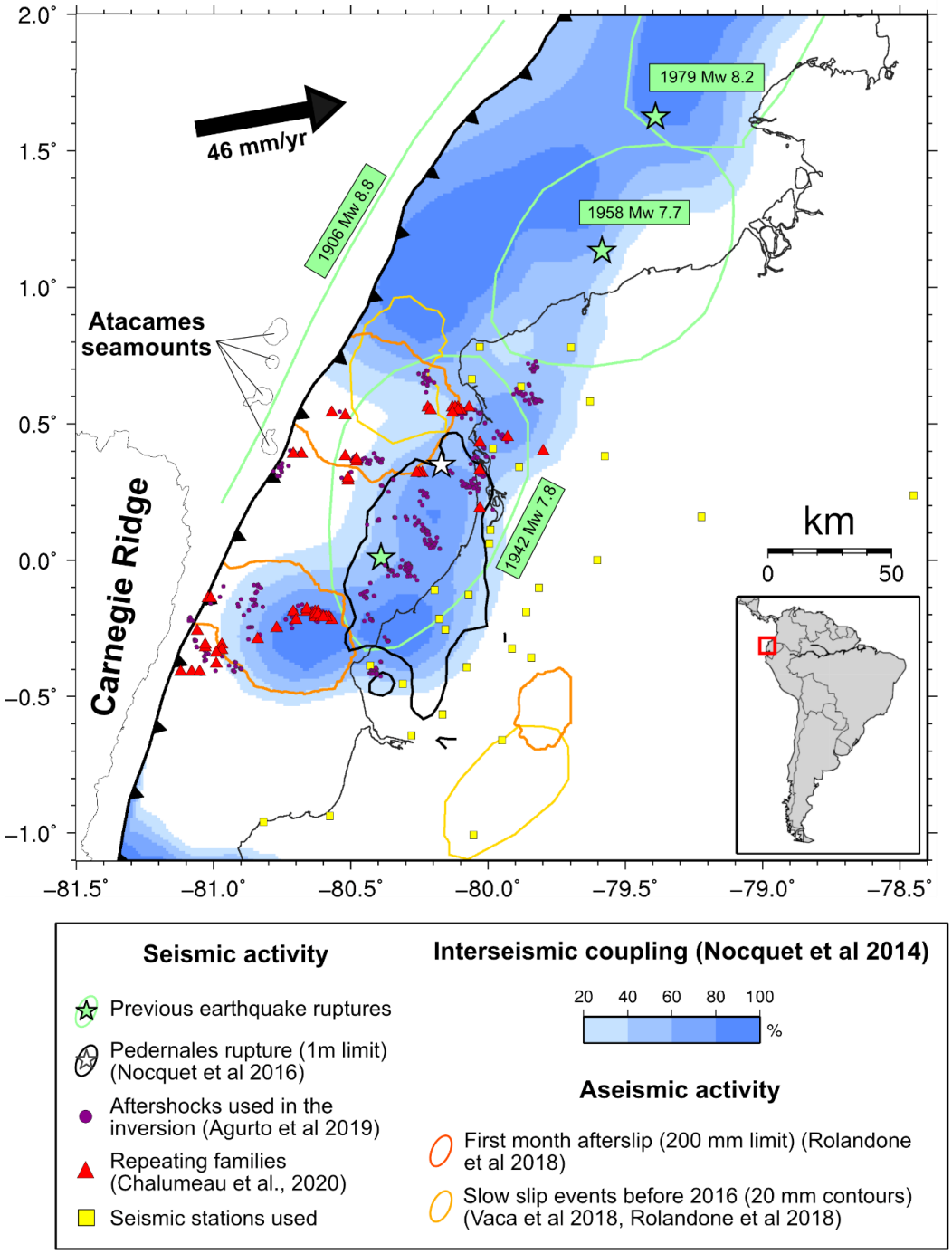

Figure 68 : Seismotectonic features of the study region. The main bathymetric features of the incoming plate are labeled, along with the plate convergence rate between the Nazca plate and the North Andean Sliver from Chlieh et al. (2014). Stars show the epicenters of the Pedernales earthquake (in white) and previous megathrust earthquakes (in green). The green circles show the rough outlines of past megathrust earthquakes (Kanamori and McNally, 1982; Mendoza and Dewey, 1984) while the black line shows the geodetically derived rupture zone of the 2016 Pedernales earthquake (Nocquet et al., 2017). The orange lines show the 20 cm edges of the Pedernales afterslip during the first month (Rolandone et al., 2018). Yellow lines show the 20 mm edges of geodetically observed slow slip events occurring prior to 2016 (Rolandone et al., 2018; Vaca et al., 2018).

When studying temporal variations in source properties, repeating earthquakes are ideal tools, as they are thought to represent the repeated rupture of a single asperity due to loading from surrounding aseismic slip (Ellsworth, 1995). They can therefore be used as proxy to study the temporal evolution of the frictional properties of the fault (Vidale et al., 1994). Large earthquakes greatly impact repeating earthquakes, causing a significant decrease followed by an increase in recurrence times, as well as a change in seismic moment that can be positive or negative, and sometimes the emergence of new repeating families (K. H. Chen et al., 2010; T. Chen and Lapusta, 2009; Hatakeyama et al., 2017; Peng et al., 2005). Some rupture processes of repeating earthquakes are remarkably similar, maintaining a consistent rupture direction and velocity and occasionally a consistent stress drop (Abercrombie et al., 2012). In other cases, repeating earthquake stress drops have decreased and gradually recovered after a large earthquake (Abercrombie, 2014; Chaves et al., 2020). This has been explained by the decrease in healing time after a large earthquake leading to a decrease in its static coefficient of friction (Abercrombie, 2014; Chaves et al., 2020; Scholz, 1998).

In this paper, we aim to use both repeating and non-repeating aftershocks to understand the spatial and temporal variability of source properties in the aftermath of a large megathrust earthquake. Our study focuses on the postseismic period of the Mw7.8 2016 Pedernales earthquake in Ecuador (Figure 68). The Pedernales earthquake occurred in a region of varying interseismic coupling that hosts both large earthquakes and slow slip events. It was the fifth event above magnitude 7.5 that occurred in the region since 1900. The first and largest was the Mw 8.4-8.8 1906 event (Kanamori and McNally, 1982; Yoshimoto et al., 2017), which ruptured a 200-500 km-long portion of the Ecuador-Colombia subduction zone (Kelleher, 1972). Three other Mw 7.7-8.2 earthquakes occurred in the 20th century, all within the 1906 rupture zone. The 1942 earthquake ruptured its southern portion, the 1958 earthquake ruptured its middle portion and the 1979 earthquake ruptured its northern portion. The Pedernales earthquake broke the highly coupled southern segment, similar to the 1942 earthquake (Chlieh et al., 2014; Nocquet et al., 2014, 2017). It may have released all of the strain stored since 1942 (Ye et al., 2016; Yoshimoto et al., 2017), or may have released more strain than what was accumulated since 1942, thus hinting at the existence of an earthquake supercycle and explaining the apparent quiescence of the Ecuador-Colombia subduction zone before 1906 (Nocquet et al., 2017).

Aseismic slip controls a large portion of the seismicity in the region, as was highlighted in the aftermath of the Pedernales earthquake. In the month following the mainshock, the aftershock expansion and moment release were controlled primarily by the afterslip (Agurto-Detzel et al., 2019). The seismicity was arranged into three streaks going from the rupture zone to the trench, which are permanent features of the background seismicity (Font et al., 2013). These streaks contained a large number of repeating earthquakes, which occurred primarily at the edge of the two afterslip patches (Chalumeau et al., 2021). These patterns of seismicity are

likely controlled primarily by the subducting features on the Nazca plate, although variations in upper plate composition and structure has also been found to possibly control megathrust rupture extent (Koch et al., 2020; Lynner et al., 2020). The subducting Atacames seamounts likely participate in reducing the interseismic coupling and may act as barriers preventing large ruptures from propagating up-dip (Marcaillou et al., 2016). Meanwhile, to the south, the Carnegie Ridge, a 2 km high, 280 km wide, and 14 - 19 km thick volcanic feature, subducting between 0° and 2.5°S, likely limits rupture propagation in this direction (Collot et al., 2004; Gailler et al., 2007; Graindorge et al., 2004; Michaud et al., 2009; Sallarès et al., 2005).

In this context, we explore not only what features control the spatial distribution of microearthquakes' stress drops, but also the evolution of their source properties in the aftermath of a large subduction earthquake. Through this, we hope to better understand the evolution of the frictional properties of the megathrust, and the recovery process after the mainshock. For this purpose, we use the spectral ratios method to recover seismic moments, corner frequencies and stress drops of both repeaters and regular aftershocks of the Pedernales earthquake. We find that stress drops increase with moment magnitude. Furthermore, we note that earthquakes near the trench have on average lower and decreasing stress drops. Elsewhere, stress drops remain highly heterogeneous, with no clear pattern of evolution.

5.3 Data and Methods

We examine 14 months of postseismic data of the Pedernales earthquake, using both the permanent Ecuadorian seismic network (Alvarado et al., 2018), as well as the temporary seismic stations deployed for one year after the Pedernales earthquake (Agurto-Detzel et al., 2019; Meltzer et al., 2019). We use the aftershock catalogue published by Agurto-Detzel et al. (2019) using both automatic and manual detections and located with a 1D model (Figure 69). Within this catalogue, 2925 events were partially relocated with both NonLinLoc (Lomax et al., 2000) and HypoDD (Waldhauser and Ellsworth, 2000) by Chalumeau et al. (2021). 1514 of these events are sorted into 55 clusters of 7 or more earthquakes with a maximum distance of 9 km, corresponding to twice the average absolute location error for our relocated earthquakes (Chalumeau et al., 2021). We use these earthquakes for our inversion. As for repeating earthquakes, we use the catalogue of 376 repeaters sorted into 62 families of 4 to 15 events detected by Chalumeau et al. (2021) (Figure 68 and Figure 69). This catalogue was constructed using cross-correlation with a threshold of 0.95, and was completed using template-matching to ensure the completeness of families.

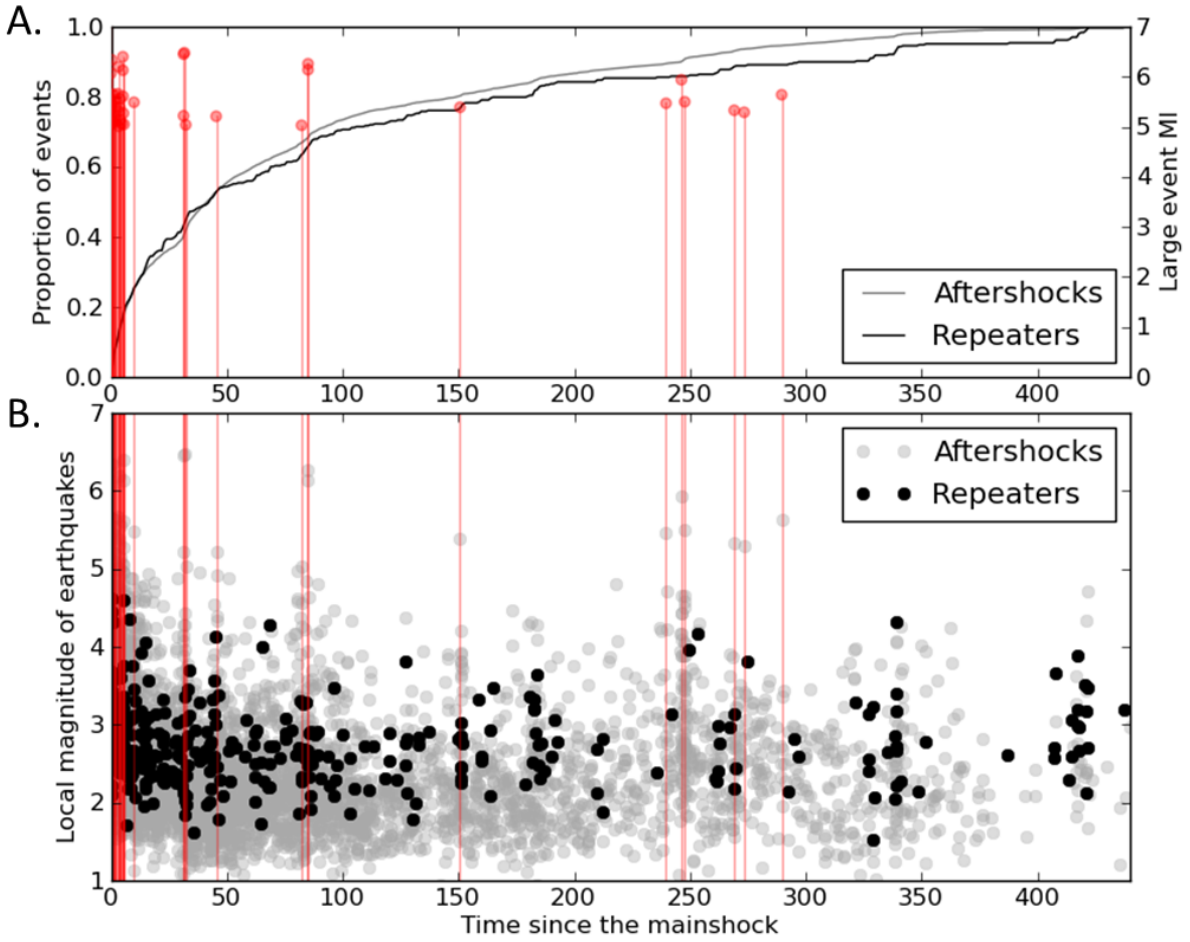

Figure 69: Time and magnitude of earthquakes in the initial catalogue. In gray are aftershocks from the Agurto-Detzel et al. (2019) catalogue, and in black are the repeaters from the Chalumeau et al. (2021) catalogue. The red lines and circles are the large-magnitude earthquakes with local magnitudes above 5. A: Cumulative number of aftershocks and repeaters as a function of time, normalized by the total number of aftershocks and repeaters. B: Local magnitudes of aftershocks and repeaters as a function of time.

To infer source properties, we use the spectral ratios method, also known as the multiple empirical Green's function (meGf) method, developed by Ide and Beroza (2003) and based on an approach by Hough (1997), to obtain seismic moments and corner frequencies. This method works as follows. A seismogram can be written as S(t) = E(t) * G(t) * I(t) where E is earthquake source, G is propagation (Green's function) and I is instrument response, which we know. According to the Boatwright spectral model (Boatwright, 1980), the source displacement spectrum is given by: $E(f) = (\frac{\Omega}{1+(f/f_c)^{\gamma n}})^{\frac{1}{\gamma}}$, where Ω is the low-frequency asymptote, f_c the corner frequency and γ and n are two constants assumed to be γ = 2 and n = 2. Meanwhile, G is unknown. However, for two closely located events, the path from event to station, and therefore G, should be the same. So by taking a ratio of the two events at the same station in

the frequency domain, we can remove propagation effects and be left with only the source information:

$$\frac{S_1(f)}{S_2(f)} = \frac{M_{01}}{M_{02}} \left(\frac{1 + (f/f_{c2})^{\gamma n}}{1 + (f/f_{c1})^{\gamma n}}\right)^{\frac{1}{\gamma}} \quad (1)$$

Often, this method is used to recover the source properties of one large event using one or several much smaller events as empirical Green's functions. However, this requires not only a large number of small events, but also large magnitude differences between collocated events, which we do not have in many places. We instead elect to invert the ratios of all suitable earthquake pairs within a cluster, regardless of magnitude difference, as was done by Lengliné et al. (2014) and Agurto-detzel et al. (2017).

We use 30 stations with sampling rates of 100 Hz, 125 Hz, or 200 Hz. These stations (Figure SD.1) are chosen based on their quality, their azimuthal coverage and their availability. However, even with these precautions, the first and last months, which fall outside the temporary deployment (Meltzer et al., 2019), have significantly fewer stations available, which makes events during that time less well constrained. At all times however, at least 7 stations are present.

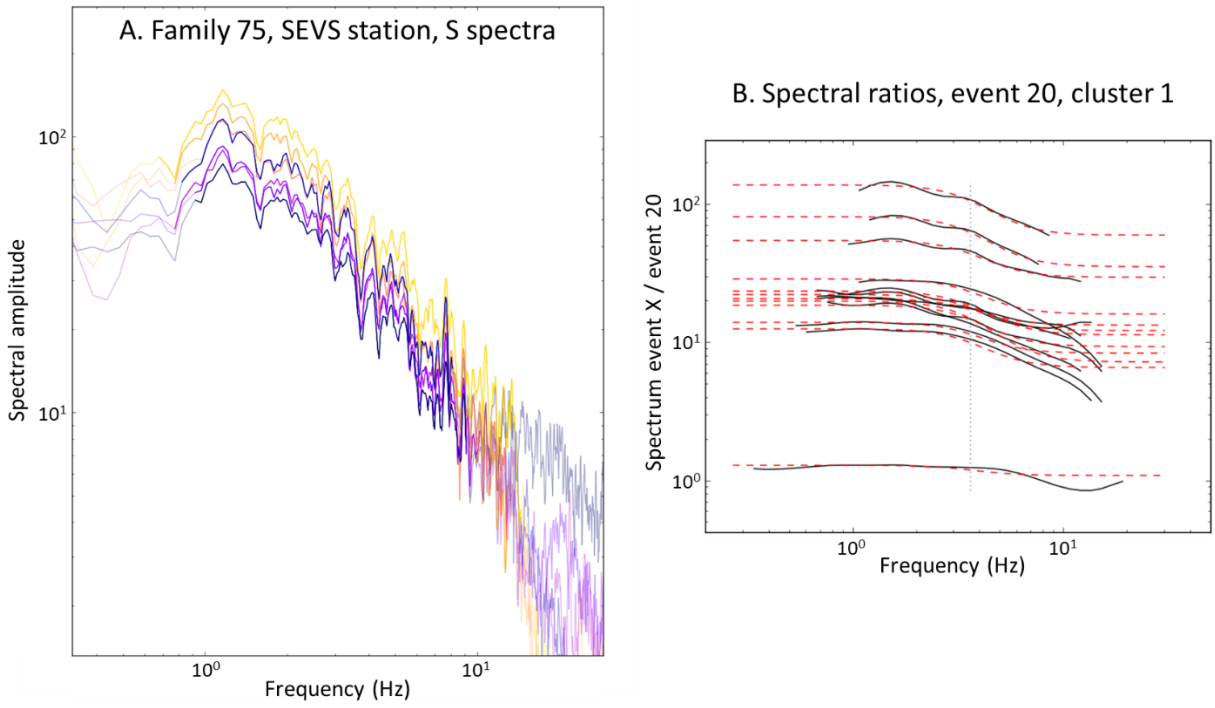

Figure 70 : Examples of spectra and spectral ratios. A: S velocity spectra of repeating earthquakes in family 75 at SEVS station. Faded lines are areas of the spectrum that are excluded from spectral ratio modelling as S/N < 4. B: Spectral ratios used to calculate source properties for the S phase of event 20 in cluster 1 with SEVS station. Full black lines are the real spectral ratios and dashed red lines are the modelled spectral ratios. The dotted grey line is the event's corner frequency.

We separate the P and S waves throughout the whole process, as stations are far enough that the two phases are usually distinct. Within a single cluster and for a given station, we keep the lengths of P and S time windows constant as 0.6 * $(Ts - Tp)_{average}$ and 1.2 * $(Ts - Tp)_{average}$ respectively, starting 0.1 s before the P and S arrivals. To avoid contamination from one phase to another, and to account for errors in theoretical arrivals, we discard any window smaller than 2 s, and any cluster-station pair with $(Ts - Tp)_{average}$ smaller than 2.5 s. Using these time windows, we calculate P spectra on the vertical component and S spectra on the horizontal ones using the multitaper code developed by Prieto et al. (2009). An example of S wave spectra for a repeating earthquake family is shown in Figure 70. Noise spectra are also calculated using the same window lengths but ending 2 s before the P arrival. These spectra are smoothed and resampled in log space to ensure that higher frequencies do not weigh more than lower ones in the inversion.

Before the inversion, we use the displacement spectra of each earthquake to calculate preliminary seismic moments. We fit this general model to the part of the spectrum where S/N >= 3, using the equation:

$$D(f) = \frac{\Omega e^{-\pi f t/Q}}{(1 + (f/f_c)^{\gamma n})^{\frac{1}{\gamma}}} \qquad (2)$$

Where t is the phase travel time and Q is the frequency-independent quality factor, left free in the inversion but around 700 on average for the P wave and 900 for the S wave over the whole region. Using the modelled Ω, we calculate seismic moment as $M_0 = \frac{4\pi\rho c^3 r\Omega}{U}$ (Shearer, 2009) where ρ is density, c is phase velocity, r is the event-station distance and U is the radiation pattern, which depends on the focal mechanism but can be averaged to 0.52 for P waves and 0.63 for S waves (Boore and Boatwright, 1984). These values of M_0 are later used as starting values for the inversion, with corresponding starting corner frequencies calculated by assuming a 2 MPa stress drop.

Before calculating spectral ratios, correlation coefficients are computed between events within a cluster. An event pair is used in the final inversion at a given station if it has a correlation coefficient above 0.8 at more than a third of stations where correlations can be calculated and at the station examined. Having high correlation coefficients like this ensures that the events are collocated, which in turn is necessary to obtain accurate results (Abercrombie, 2015).

In order to avoid introducing errors, we elect not to convert our data to displacement when calculating spectral ratios. The spectral ratios are only computed over the part of the spectrum where S/N >= 4, on the condition that log(fmax) – log(fmin) >= 0.7.

Before inverting for all corner frequencies and seismic moments, each individual spectral ratio is modelled, and those that are poorly fit by equation 1 or that yield unrealistic results are discarded (fc below 0.1 or above 100 or M_0 below 10^6 or above 10^{20}). We also discard spectral ratios when both corner frequencies fall well outside the frequency range of the data.

Finally, we invert all remaining spectral ratios for a cluster at a single station together. In order to constrain the absolute values of seismic moment, we use the logarithmic mean of the preliminary seismic moments, which is kept constant during the inversion. We run the inversion several times with different starting M_0 and fc, and keep the results with the smallest numerical error. If the inversion cannot converge, we remove problematic events. We show an example of inverted spectral ratios for one event in Figure 70. We take an event's seismic moment and corner frequency to be the median between available stations. From seismic moments, we calculate moment magnitudes using the equation by Hanks and Kanamori (1979):

$$M_w = 2/3\ (log_{10}(M_0) - 9.1) \qquad (3)$$

We also calculate static stress drops as:

$$\Delta\sigma = \frac{7}{16}\left(\frac{f_c}{k v_s}\right)^3 M_0 \qquad (4)$$

From Eshelby (1957) and Brune (1970). Here v_s is the S wave velocity, given as 2900 m/s, the average S wave velocity at our earthquakes' depth (Agurto-Detzel et al., 2019). k is a constant which differs between P and S and depends on rupture velocity (Kaneko and Shearer, 2014). As discussed later, we set k_P as 0.33 and k_S as 0.26. This model assumes that the rupture

is circular, and therefore that any change in fc is due to a change in size of the rupture. The event stress drop is taken to be the logarithmic mean of the P and S stress drop.

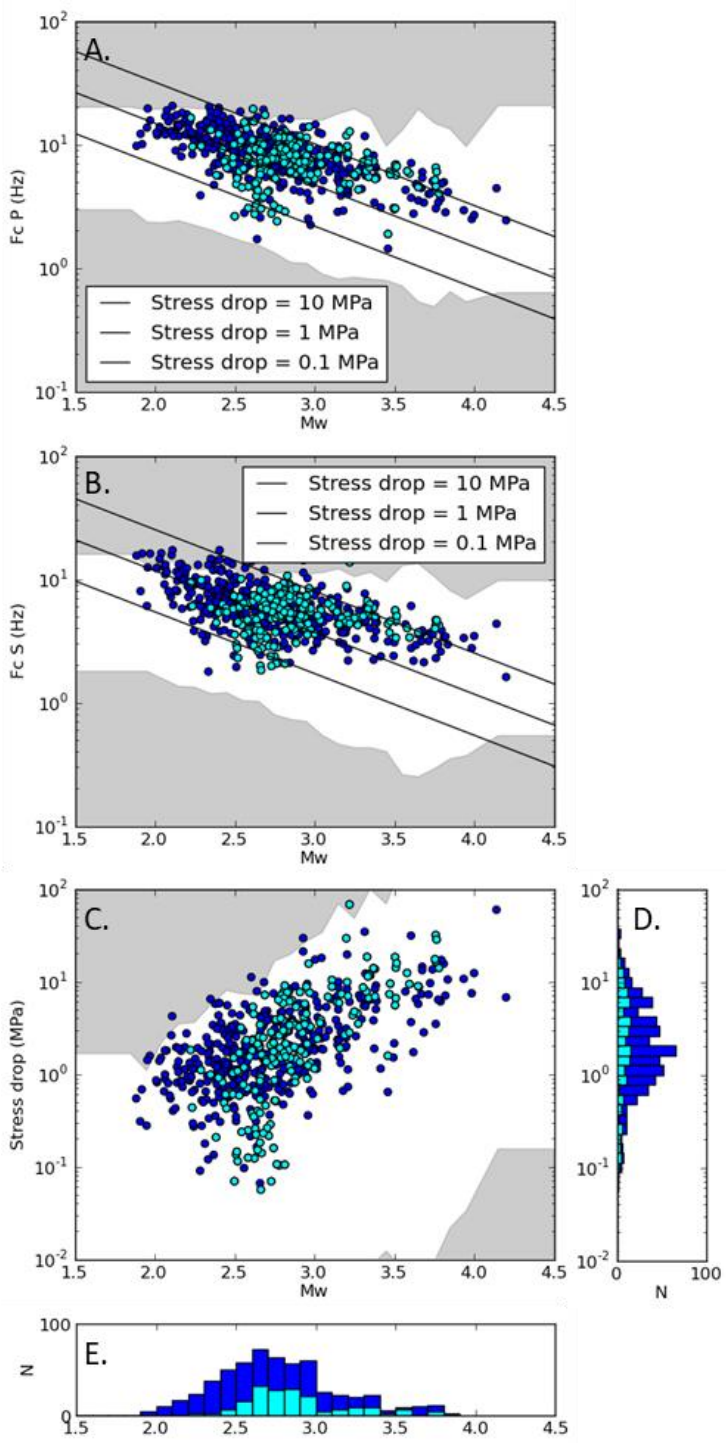

Figure 71 : Panels A-C show source properties (corner frequencies inferred from P-waves and S-waves, stress drop) as a function of moment magnitude. Panels D and E show the distribution of stress drops and magnitudes respectively. Light blue represents repeaters and dark blue represents non-repeaters. The grey shaded areas show for a given magnitude the median upper and lower frequency limits between which corner frequencies can be resolved.

We calculate uncertainties by performing a jackknife test on our data (Agurto-detzel et al., 2017; Prieto et al., 2007). For each cluster and each station, we run 100 inversions where we resample the spectral ratio data, removing 20% of data points within spectral ratios. We estimate the error as the standard deviation of the logarithms of seismic moments, corner frequencies, and stress drops obtained. For this study, we only keep events which have errors below $10^{0.5}$ for stress drop, $10^{0.2}$ for fcP, $10^{0.2}$ for fcS and 0.2 for Mw.

Since every ratio has its own frequency range of analysis, there are no frequency limits common to all earthquakes beyond which corner frequencies cannot be resolved. However, we determine that corner frequencies that exceed half of the maximum frequency at which a ratio is calculated are underestimated, and therefore discarded (Text SD.1 and Figure SD.5). We do however keep the estimation of magnitude from these earthquakes, since it relies on low-frequency signal.

Finally, we ensure that the use of earthquakes from different times after the mainshock, hence with possible medium velocity and attenuation variations, does not significantly bias our results (Text SD.2 + Figure SD.12).

5.4 Results

5.4.1 Source properties within the general population of earthquakes

Out of 1514 aftershocks examined, we recover the source properties of 850 events using P waves, and 861 events using S waves, of which 597 events have acceptable errors on both P and S source properties. Due to the uneven station coverage, first month events are more likely to be missing. Corner frequency, moment magnitude and stress drop distributions are shown in Figure 71. About 90% of corner frequencies are within 3 to 15 Hz for the P wave and 3 to 12 Hz for the S wave, with median values of 8 and 6 Hz respectively.

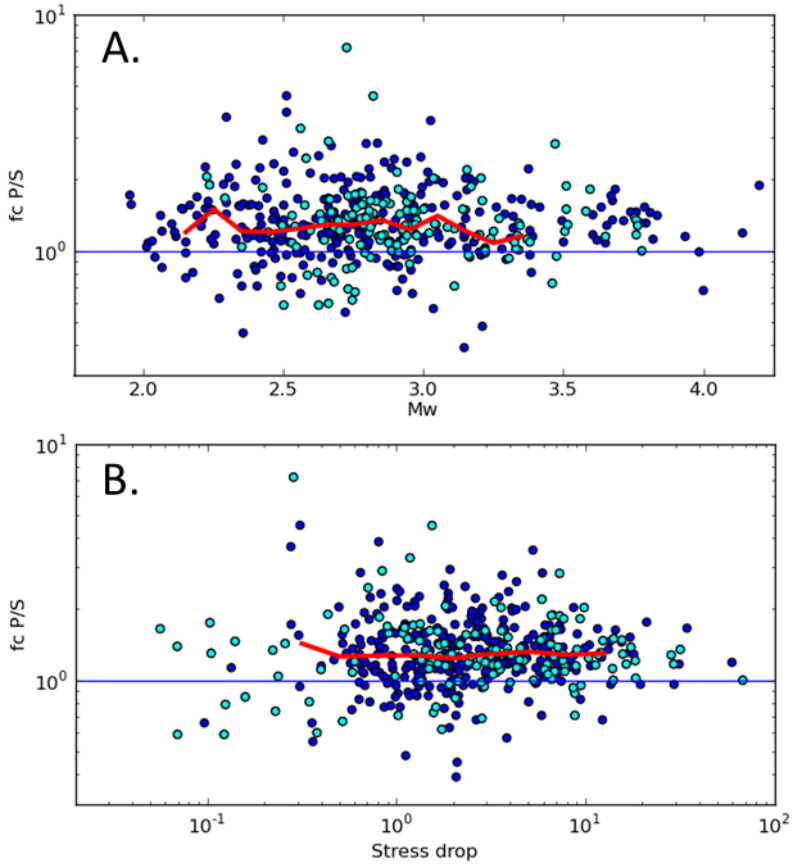

Figure 72 : P/S corner frequency ratio as a function of Mw (top) and stress drop (bottom). Light blue represents repeaters and dark blue represents non-repeaters. The red line is the median.

The median P/S corner frequency ratio is 1.27 (Figure SD.3). This ratio appears to be constant with corner frequency, stress drop and magnitude (Figure 72). Since $f_c = kv_s/L$ (Brune, 1970), where k is a constant linked to the rupture process, the P/S corner frequency ratio must be equal to k_P/k_S. According to Kaneko and Shearer (2014), k_P, k_S and k_P/k_S are affected by the rupture velocity and the geometry of the rupture (Kaneko and Shearer, 2015). Since rupture geometries are likely very diverse at such a large scale, the average k_P/k_S ratio probably reflects the average velocity of rupture. A ratio of 1.27 corresponds to a rupture velocity of about $0.75v_s$, so we set k_P as 0.33 and k_S as 0.26 (Kaneko and Shearer, 2014) to compute the stress drops (4). Other studies have found similar v_r/v_s based on P/S corner frequency ratios in subduction zones (Yamada et al., 2021). Note however that this ratio is an average in space and time, and therefore the scattering can be explained by varying rupture velocities and geometries among events.

Our moment magnitudes vary between 2.2 and 3.6 with a median of 2.7, while stress drops are mostly log-normally distributed and vary between 0.2 and 12 MPa with a median of 1.9 MPa (Figure 71D-E). This is within the expected range for a subduction zone (Abercrombie et al., 2017; Oth et al., 2010; Yoshida et al., 2017). Overall, while repeaters tend to have higher

magnitudes than non-repeaters, they generally seem to have the same magnitude-stress drop distribution as non-repeaters at this scale. For both repeaters and non-repeaters, we see an increase of stress drop with moment magnitude (Figure 71C). This could be a result of selection bias, since corner frequencies above half of the high frequency bandwidth limit were discarded, or it could reflect a real change in source properties with magnitude. In Figure 71A-C, shaded areas represent frequencies below the median lower frequency limit and above half of the median upper frequency limit. These areas are lacking events, as earthquakes falling within them are more likely to have unresolvable corner frequencies.

If there is an increase of stress drops with magnitude beyond our sampling bias, then it must be possible for the 917 events that were discarded during the inversion to fully compensate the observed trend, assuming stress drops to be log-normally distributed at every magnitude range (Allmann and Shearer, 2009). While the distribution of stress drops in the lower magnitude range appears truncated (Figure SD.6), there are too few discarded events to explain our observed increase of stress drops with magnitude while assuming that the average stress drop remains above 9 MPa (as it is for events with magnitudes above 3.5).

Our corner frequency estimates may also be biased. When modelling spectral ratios, if one of the corner frequencies is too close to the edge of the bandwidth, allowing that corner frequency as a free parameter may contaminate the corner frequency estimation of the other event (Shearer et al., 2019). We ensure this is not the cause of our trend by inverting for the spectral ratios of low-corner frequency events, while assuming a corner frequency corresponding to a stress drop of 2 MPa for all the high frequency events. Doing so does not remove the trend, meaning the increase in stress drops with magnitudes is likely real (Figure SD.7).

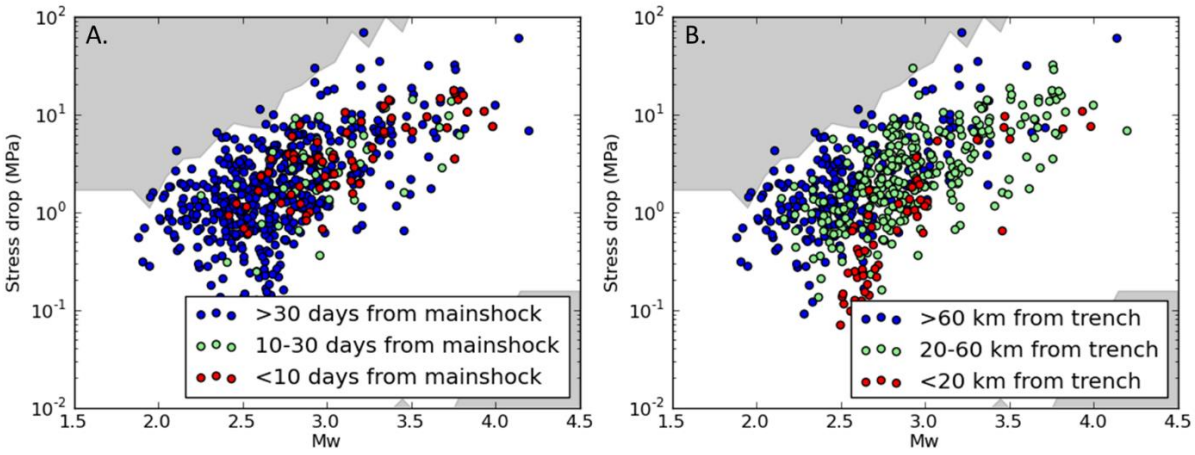

Figure 73 : Distribution of stress drops as a function of magnitude. A: Events colored by time. The timing of repeaters does not influence the stress drop Vs magnitude trend. B: Events colored by distance to the trench. The grey shaded areas show for a given magnitude the median upper and lower frequency limits between which corner frequencies can be resolved.

Thus since stress drop most probably increases with magnitude for our catalogue, we investigate the cause of this increase. Both location and timing could affect magnitudes and stress drops, and could therefore be creating this trend. However, when coloring earthquakes with respect to time (Figure 73A), we see that early and late earthquakes have the same trend and have similar stress drops in the high magnitudes, although there are fewer low-magnitude earthquakes in the first month of aftershocks due to fewer stations being available, making the detection threshold higher. Therefore, timing is unlikely to explain the magnitude vs stress drop trend. Event location, particularly depth, is another candidate to explain this relationship. Because depth itself is poorly resolved, particularly near the trench, we consider distance from the trench as a general proxy for depth, assuming earthquake hypocenters are close to the plate interface. We see that distance to the trench has an impact on the Mw versus stress drop relationship (Figure 73B). Events 20 km or under from the trench stand apart, with lower stress drops and a steeper trend. Events in the 20-60 km group have the same trend but lower stress drops compared to events in the >60 km group. However, for all three groups, we see that stress drops increase with magnitudes. Therefore, although distance to the trench influences stress drop, it cannot explain why stress drops increase with magnitude.

The dependence of stress drops on magnitudes, combined to the spatially variable magnitude of completeness, means that the dependence of stress drops on depth is complex to see in map view (Figure 74A). However, we do see that stress drops are clearly lower near the trench, especially in the south where stress drops increase from the trench to the transition between the rupture zone and the southern afterslip patch. On average, the median stress drop is observed to increase with depth (Figure 74C). This increase with depth is not linked to an increase of magnitudes (Figure 74B), in part because the magnitude of completeness near the trench is much lower. A slight variation of stress drop is also observed with the coupling (Figure 74D). However, as the coupling is globally increasing away from the trench, this variation is likely attributable to depth. Away from the trench, stress drops do not show large anomalies or any significant variations with the afterslip areas. Stress drops might be slightly lower within the rupture zone, although it is likely that events in that area occur distributed within the seismogenic volume, making comparisons to interplate earthquakes difficult (Agurto-Detzel et al., 2019). What we mainly see is significant spatial variability in stress drops, even among very close events, meaning that local heterogeneities likely control stress drops. Such spatial variability has already been documented in other regions, including subduction zones (Abercrombie et al., 2017; Baltay et al., 2013).

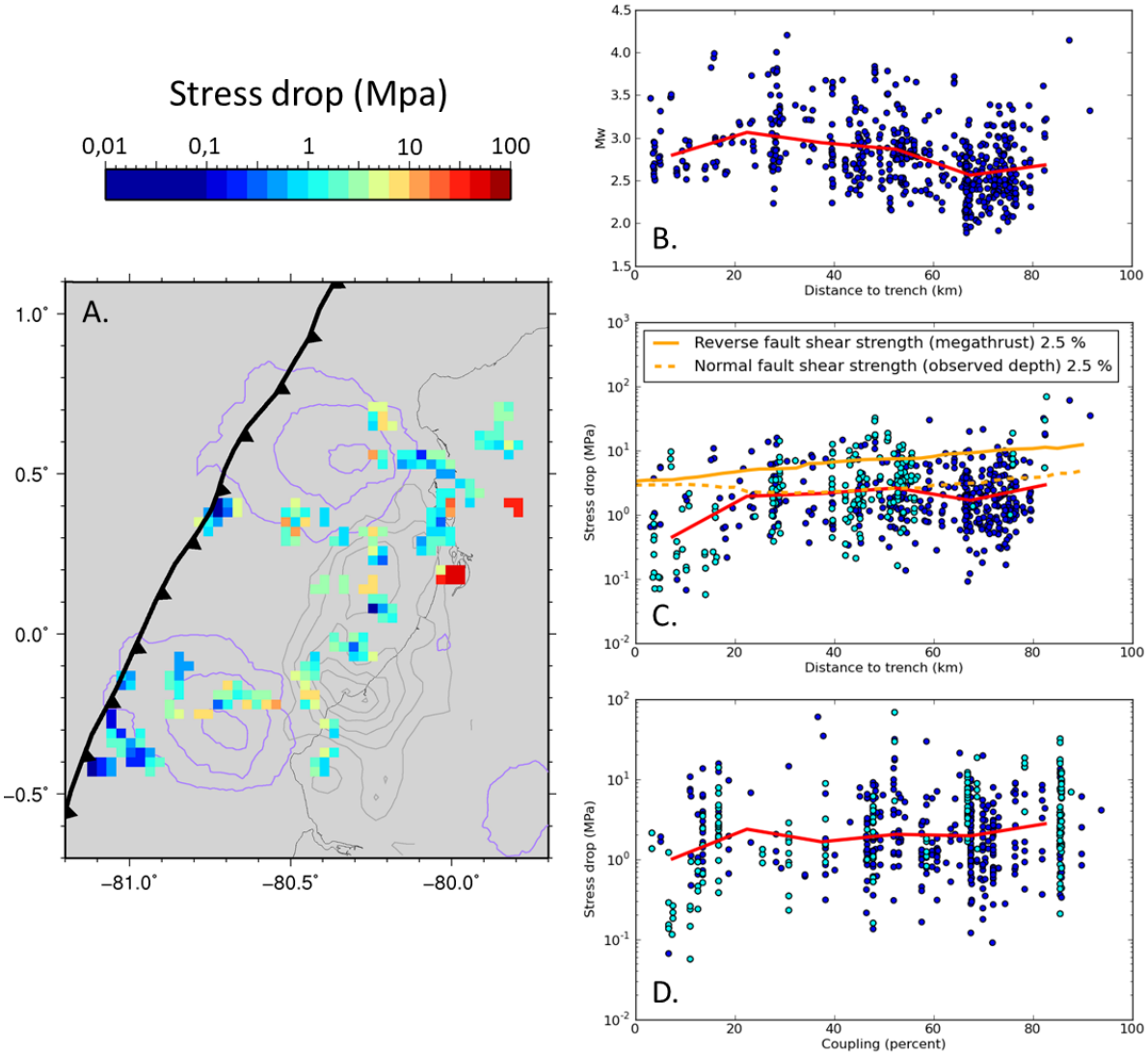

Figure 74 : Spatial distribution of stress drop. A shows a map of all stress drops calculated, with colors representing their logarithm. B shows the magnitude of events with full source properties as a function of distance to the trench. C shows stress drop as a function of distance from the trench, with the orange lines showing the expected shear strength based on earthquake depth, and the depth of the interface (Hayes et al., 2012). D shows the relationship of stress drops to coupling. In B, C and D, the red line is the median.

Thus, stress drops appear highly heterogeneous in space and show a dependency on depth and magnitudes. In order to fully characterize the evolution of source properties with time, we look at changes at a single location within repeating earthquake families.

5.4.2 Source properties within families of repeaters

Out of the 376 repeaters identified by Chalumeau et al. (2021), we recover source properties from 187 events. We look for global trends in the evolution of source properties in time by normalizing each family of repeaters by the source properties of its last fully recovered event, which should be the closest to the background response (Figure 75). We also show source properties as a function of recurrence times in Figure SD.11, but because in most cases recurrence times increase with time (Chalumeau et al., 2021), there are no significant differences between these two analyses. For all events, we normalize properties station by station, to limit the impact of our evolving network on the results. Seismic moment appears high right after the mainshock and decreases with time, while corner frequencies remain on average constant but very scattered (Figure 75). Consequently, stress drops are also very scattered but tend to decrease with time, like the moment magnitude. Overall, the large scatter in these plots indicates that families exhibit many different behaviors.

Out of the 62 families of repeaters, 51 have at least 3 magnitudes and 3 stress drops calculated, or have more than 5 magnitudes. We show their individual evolutions over time in Figure SD.9. Overall, P and S corner frequencies usually change together and demonstrate a wide variety of behavior. Corner frequencies increase with time in 5 families, decrease in 12, and are stable in 13. Additionally, there are cases where the evolution of corner frequencies is more complicated, as well as cases where the number of resolved corner frequencies within the family is too low to have a reliable trend. Meanwhile, out of the 26 families with visible trends in Mw with time, 6 have increasing Mw while 20 have decreasing Mw, confirming that there is less variability in the changes of magnitudes with time. Consequently, the stress drops increase with time for 3 families and decrease with time for 18 families with visible trends.

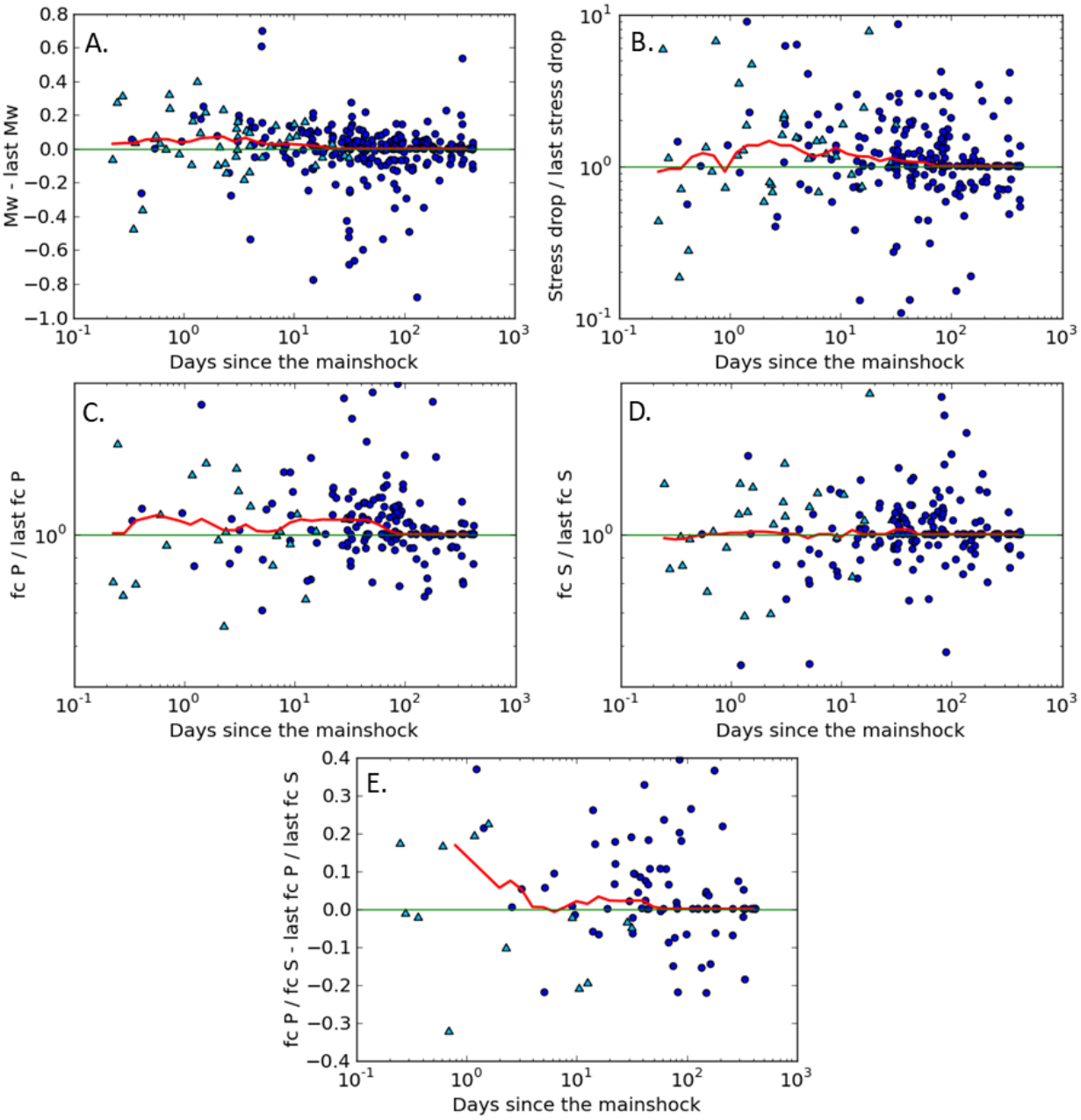

Figure 75 : Evolution of normalized source properties within families. Panel A shows normalized moment magnitudes, panel B shows normalized stress drops, panels C and D show normalized P and S corner frequencies, and panel E shows the normalized P/S corner frequency ratio. Each event within a family is normalized by the last event of that family with all source properties determined. The red line is the median computed using a sliding window 1 in log space. Triangles represent the first event after the mainshock within a family.

Overall, families that are very close can have very different stress drops and different time variations of stress drops. We do however see regional patterns in the time evolution of source properties in the region near the trench (Figure SD.8). In this area, all 6 families with resolvable stress drop changes see a decrease in stress drop throughout the whole period, and all 8 families with distinct trends in moment magnitude also have decreasing moments. An example of S

wave spectrum for one such family is shown as an example in Figure 70, where the difference in moment is immediately evident. Many families in this region have corner frequencies that are difficult to resolve. Nevertheless, provided that we assume that P and S corner frequencies behave similarly, then corner frequencies are either stable or decrease in the region. This might reflect a measurement bias due to an increase in attenuation over time. Such a change in attenuation would need to account for changes in seismic moments as well as corner frequencies. Using a similar method to Kelly et al. (2013) and assuming that all repeaters within a family have the same corner frequency, then we have:

$$ln\frac{S_1(f)}{S_2(f)} = ln\frac{M_{01}}{M_{02}} + (\frac{t}{Q_2} - \frac{t}{Q_1})\pi f \quad (5)$$

Where t is the travel time and Q is the quality factor along the path to the station. For a given family, we fit all spectral ratios below the lowest corner frequency with this equation, first leaving the seismic moment to vary within a family, then assuming that it remains constant (Figure SD.10). The data cannot be fit without variations in seismic moment, meaning that attenuation alone cannot explain the variations in stress drop that we observe in the region.

5.5 Discussion

Having recovered 597 stress drops within our region, we find that they are influenced primarily by magnitude and distance to the trench, with little influence from coupling or the location of slow slip. Additionally, the evolution of source properties with time on single asperities is heterogeneous, except near the trench, where stress drops are widely seen to decrease.

5.5.1 Relationship of stress drops with magnitude

On average, the stress drops of all aftershocks appear to increase with magnitude, as observed in other parts of the world (Bindi et al., 2020). Lin and Lapusta (2018) suggest that apparent scaling of stress drop with M_0 could be due to heterogeneities on the fault. Large strength variations would lead to some portions of a fault patch not slipping, meaning the earthquake rupture would have a complex shape. Event duration, and therefore corner

frequency, is controlled by the rupture length, while event magnitude depends on the rupture area. This implies that events of similar duration may have very different magnitudes, if their shape is very different. Elongated ruptures in particular can have low magnitudes but similar corner frequencies to circular ruptures if the rupture length is the same. In this way, assuming a circular rupture leads to an underestimation of the stress drop. Therefore, in some cases an apparent stress drop increase with magnitude could simply reflect a larger proportion of complex rupture shapes for low magnitudes (Lin and Lapusta, 2018). Such elongated rupture shapes would lead to lower P/S corner frequency ratios compared to what is expected from a circular rupture (Lin and Lapusta, 2018). However, we find no dependence of the P/S corner frequency ratio on either estimated stress drop or magnitude (Figure 72), leading us to conclude that rupture shape or velocity variation is not the cause of our dependence of stress drop on magnitude.

We saw in Figure 73 that the magnitude-stress drop relationship holds during different time periods, implying that it is not caused by the temporal variations of these two parameters. Therefore, the observed scaling implies that earthquakes are not self-similar within the range of magnitudes studied here. Going back to Eshelby (1957):

$$\Delta\sigma = \frac{7}{16}\frac{M_0}{R^3} \qquad (6)$$

Where R is the radius of the rupture. Because we have $M_0 = \mu DA$ (Aki, 1966), where μ is the shear modulus, D is the displacement and A is the area of the rupture, having larger stress drops for larger magnitudes implies that the displacement increases faster than the size of the asperity. This increase is shown in Figure 76A, where we see that coseismic displacement seems to be proportional to $M_0^{2/3}$, rather than the expected $M_0^{1/3}$.

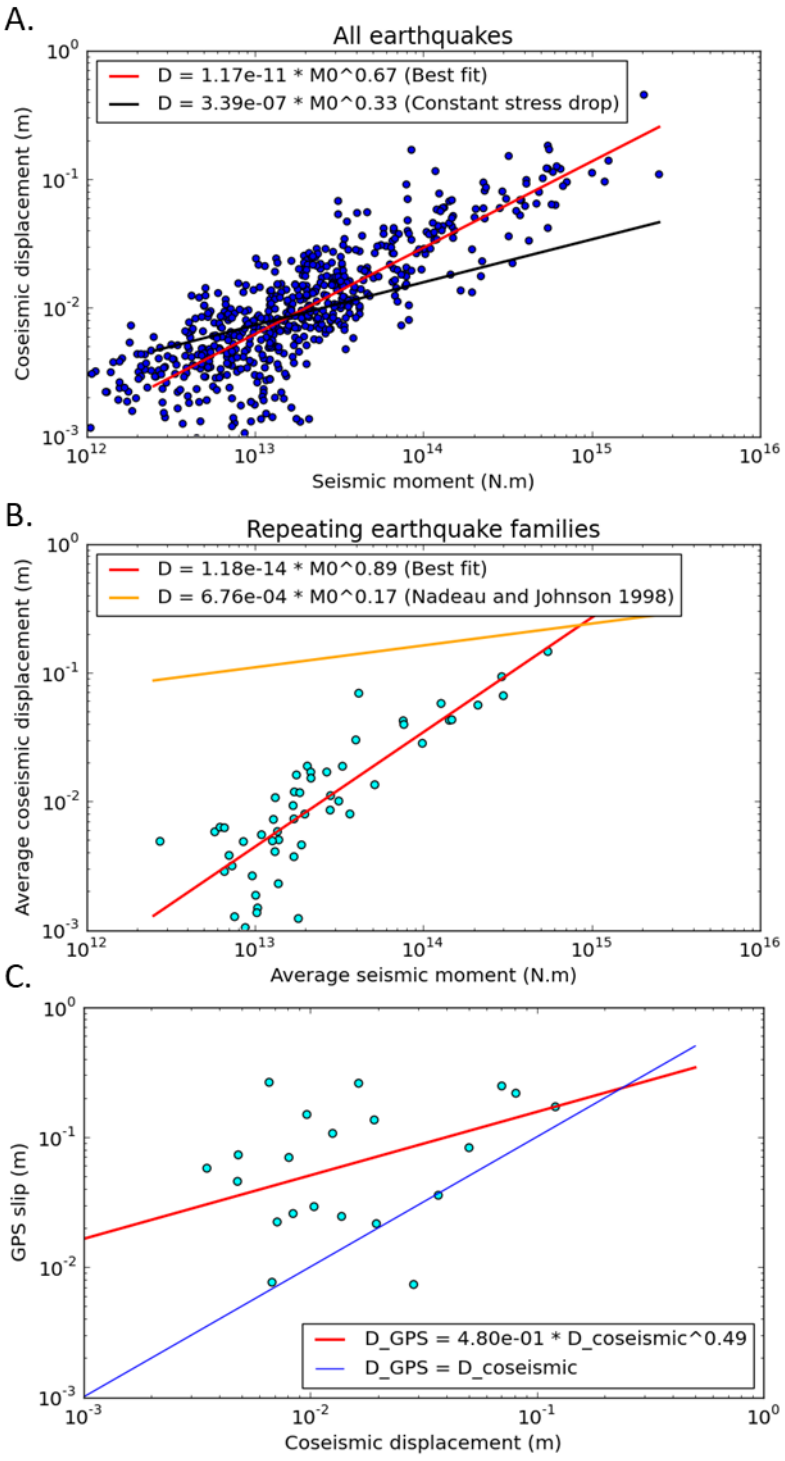

Figure 76: A: Coseismic displacement as a function of seismic moment, for all earthquakes. The red line shows the best fit for the data, while le black line shows the theoretical increase of displacement with moment when assuming a constant stress drop of 1.9 MPa.

B: Average coseismic displacement as a function of average moment within families of repeating earthquakes. The red line is the best fit. The orange line is the relationship derived by Nadeau and Johnson (1998) using quasi-periodic repeaters on the creeping portion of the San Andreas fault.

C: Average geodetically measured slip (Rolandone et al., 2018) as a function of average coseismic displacement for families of repeating earthquakes active during the first month. The red line is the best fit, while the blue line shows the line where the GPS slip is equal to the coseismic slip.

Looking specifically at repeating earthquakes in Figure 76B, we see that the relationship of seismic moment to displacement is similar for repeaters and non-repeating aftershocks. This is notable, as it is very different to the displacement predicted by the Nadeau and Johnson (1998) model. They assume that all the displacement on a repeating earthquake asperity occurs coseismically, and thus that coseismic displacement is proportional to $M_0^{1/6}$ for repeating earthquakes. This is however not verified in California, where the model was developed (Beeler et al., 2001), and we see here that this model does not hold in our context either. In fact, the GPS displacement occurring on asperities hosting repeating earthquakes seems to be almost always larger than the coseismic displacement (Figure 76C), implying as Beeler et al. (2001) suggested that a portion of the slip occurring on the asperity is aseismic. Additionally, the smaller repeating earthquake asperities seem to host a higher proportion of aseismic slip than the larger asperities, which is again compatible with the model of Beeler et al. (2001). Therefore, the presence of a varying aseismic slip component in the asperity slip may explain the dependency between stress drop and moment.

5.5.2 Lower stress drops near the trench

One striking observation regarding the spatial distribution of stress drops is their low values near the trench, particularly in the south, despite the higher magnitude of completeness in the region. This hints at a dependency of stress drops with depth in our study area. Depth in this region is poorly constrained, and 3D tomography studies have located most earthquakes in this region within the subducting plate (León-ríos et al., 2021). However, most focal mechanisms that were previously calculated near the trench show thrust faulting (Agurto-Detzel et al., 2019). Thus, for simplicity in the absence of depth constraints, we cautiously assume that earthquakes in the region occur primarily near the interface. We therefore investigate the likely causes of an increase in stress drop with depth.

Previous studies have often found a dependence of stress drop (Oth, 2013) or source duration (Bilek, 2007; Bilek and Lay, 2002; Lay et al., 2012) on depth in subduction zones. Because there is a tradeoff between rupture velocity variations and stress drop variations (Lay and Bilek, 2007), our observation of low stress drops near the trench could reflect slow rupture velocities. Bilek and Lay (2002) suggested that these slow rupture velocities could be explained by the region being conditionally stable with asperities embedded in it. Slow earthquake ruptures would then be due to a large portion of the rupture propagating into the conditionally stable portion of the megathrust. However, while Tolga Şen et al. (2015) observed a decrease in normalized source duration with depth for both interplate and intraplate earthquake of Mw

4.0-6.5, they concluded that special frictional conditions near the trench were not required to explain the data. Instead, a variation of rigidity combined with an increase of stress drop with depth could well explain their observations.

We test whether the normal stress increase with depth in the Earth is enough to account for most of our observed increase in stress drop with depth, as has been the case for other studies (Huang et al., 2017). To test this, we show in Figure 74C the shear strength as a function of depth. This curve is constructed by making the same assumptions as Huang et al. (2017): a coefficient of friction of 0.6 and hydrostatic pore pressure. We show 2 separate curves: The first curve corresponds to an estimate of the shear strength for reverse faults at the plate interface, where we expect most repeaters to be. However, due to uncertainties in depth it is possible for earthquakes near the trench to be associated with normal faulting in the slab. We therefore show a second profile of shear strength for normal faulting at the average hypocentral depth. We find that stress drops follow the increase of shear strength with depth of the interface quite well between 20 and 60 km from the trench. Stress drops seem to represent around or below 2.5% of the shear strength (Figure 74C), which is predictably lower than what is found for intraplate earthquakes (Huang et al., 2017). It could mean that shear strength is overestimated, due to a fluid pressure higher than the hydrostatic one or to a friction coefficient lower than 0.6. After 60 km, stress drops are lower on average, likely because a lot of earthquakes in this region occur in the rupture zone, both at the interface and within the seismogenic volume (Agurto-Detzel et al., 2019). At this distance, repeating earthquakes, which occur outside of the rupture zone and likely on the interface, have higher stress drops, comparable to what we expect if stress drop increases with depth. Meanwhile, within 20 km of the trench, stress drops span a wider range, but are on average too low to be explained by the lower strength caused by the shallower depth. This means that either a higher pore fluid pressure or a different coefficient of friction are necessary to explain the low values of stress drop near the trench.

The thinned and highly fractured upper lithosphere imaged by Marcaillou et al. (2016) where the Atacames seamounts enter subduction may help explain why the stress drops in that region would be low. It may significantly alter the stiffness of the medium, and possibly the friction. Marcaillou et al. (2016) also finds that the subduction channel between the subducted seamounts is likely filled with overpressurized fluids, which may also contribute to the low stress drops. However, as this is linked to the subduction of the Atacames seamounts, it cannot explain why the stress drops are similarly low in the south, unless the oceanic relief associated with the Carnegie Ridge has a similar effect.

5.5.3 Postseismic changes in repeating earthquake sources

We observe some patterns in the evolution of the source properties of repeating earthquakes with time. For many of our families of repeating events, we find that the seismic moment decays with time after the mainshock. This has been observed in several places (Chaves et al., 2020; K. H. Chen et al., 2010; Uchida et al., 2015), although lower magnitudes after a mainshock have been observed as well (K. H. Chen et al., 2010). These variations have been interpreted as a balance between two processes (Chaves et al., 2020; K. H. Chen et al., 2010; Uchida et al., 2015). On the one hand, recurrence times tend to be smaller after a mainshock, which decreases the static coefficient of friction and therefore lowers the stress drops. On the other hand, the increase in strain rate in the aftermath of the mainshock can cause transient embrittlement, which increases rupture areas and therefore lowers corner frequencies. This can occur if the nucleation length of the earthquake is initially of a similar size to the velocity-weakening patch, and is therefore more likely for smaller magnitudes (K. H. Chen et al., 2010). According to this model, if the area of slip grows sufficiently, it can compensate for the lower stress drops, and the seismic moment of the repeater increases. Otherwise, the seismic moment will be lower due to the decreased stress drop.

However, in our study area, high seismic moments after the mainshock are rarely associated with a lower corner frequency. Most families have either constant or negative trends of corner frequency with time, which means that, if the source size does change, it is unlikely to be larger at the start rather than the end of the period. Therefore, transient embrittlement is unlikely to affect most of our repeating sources and cannot account for the larger magnitudes immediately after the mainshock. On the other hand, most families have larger stress drops right after the mainshock, which then decrease with time. This refutes the idea that lower recurrence times necessarily lead to a widespread decrease in fault strength, since our recurrence times increase with time. At the scale of individual asperities, some transient embrittlement or fault weakening may occur, but they cannot explain the general behavior of families in our dataset. In fact, most regions have widespread heterogeneity with no link to large scale properties, like slow slip or coupling, meaning that very local processes likely dictate the response of repeaters to the mainshock, with the exception of the near-trench region.

5.5.4 Decrease in stress drops with time near the trench

As we have discussed, the near-trench region appears distinct from the rest of the study area. Not only is it a region of lower stress drops, but we also observe throughout the postseismic period a decrease in stress drops, seismic moments, and sometimes corner frequencies with time within families of repeating earthquakes. We have established that neither transient embrittlement nor fault weakening can explain such behavior, as recurrence times also increase with time. This change could alternatively be related to the presence of fluids, as the low vp and high vp/vs ratio in this region point to the presence of a large volume of fluids (León-ríos et al., 2021). The change in stress drops might therefore be linked to an increase in pore fluid pressure during the period. Lengliné et al. (2014) found that, in the context of fluid injections, repeaters can have very similar corner frequencies but very different stress drops likely linked to rapid changes in pore fluid pressure. Cauchie et al. (2020) made similar observations in the same region at a different date, although in both cases there was no specific trend of stress drops with time. Other studies looking at non-repeaters have found a dependence of stress drops on pore fluid pressure in injection sites as well (Staszek et al., 2017).

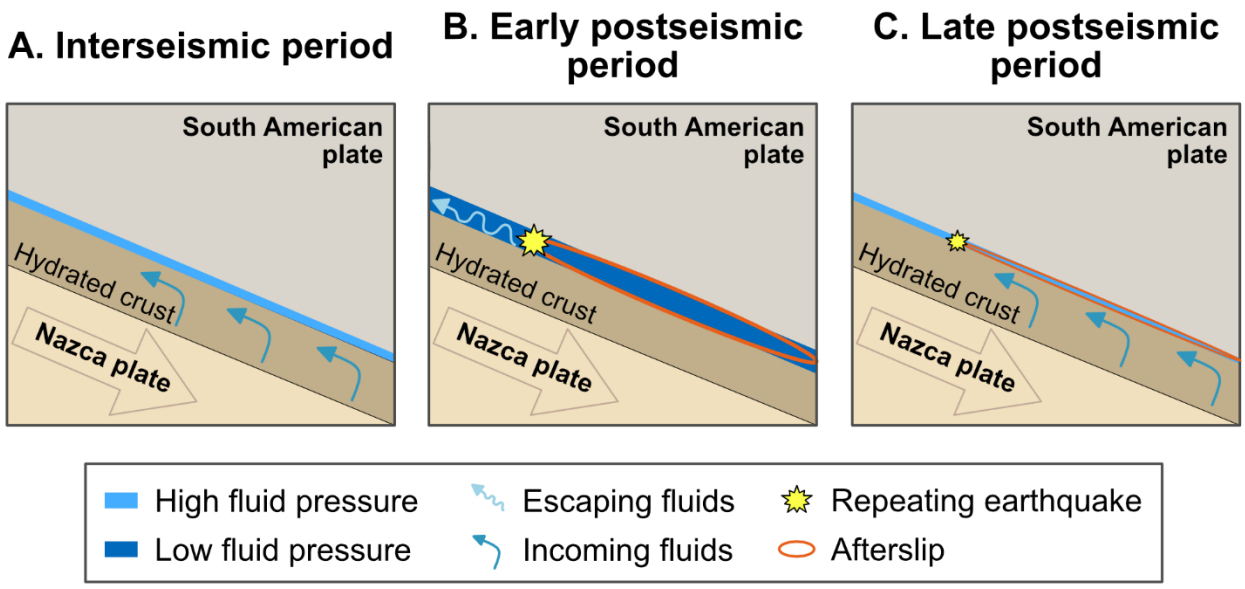

Figure 77: Schematic diagram of the evolution of pore fluid pressure near the trench during the postseismic period. A: Interseismic period: Fluid pressure is high as fluids are trapped at the plate interface. B: Early postseismic period: Fluid pressure is low as afterslip causes dilation and fluids escape the interface. C: Late postseismic period: Fluid pressure increases again as the afterslip slows down.

We propose that our observed stress drop decrease is due to an increase in pore fluid pressure linked to fault-valve behavior (Husen and Kissling, 2001; Sibson, 1990), as we explain in Figure 77. This would mean that before the mainshock, the subduction interface acted as a low-permeability zone, leaving fluid pressure to build up. The afterslip, by dilatancy effects or by breaking the seal, may have lowered pore fluid pressure. However, as afterslip decreased, slab fractures and the subduction interface were gradually resealed by precipitate-hosting fluid advection and diffusion, leading to a new increase in pore fluid pressure and a subsequent decrease in frictional strength. This behavior has been documented in subduction zones after both megathrust earthquakes (Husen and Kissling, 2001; Magee and Zoback, 1993) and SSEs (Nakajima and Uchida, 2018; Warren-Smith et al., 2019), and is visible in the geological record (Cerchiari et al., 2020). The decrease in stress drops that we are observing is therefore likely the last stage of this process, associated with fluid-pressure build up. This idea might be further supported by the fact that no repeating earthquake has been detected near the trench in the south in the year before the mainshock, and only two occur in the second half of the study period (Chalumeau et al., 2021). Meanwhile, down-dip of this region, two repeaters occur in the year before the mainshock, and repeaters continue to occur throughout the subsequent 440 days (Chalumeau et al., 2021). Additionally, the near-trench region saw little activity during the interseismic period compared to the postseismic period, even from regular earthquakes (Font et al., 2013; Soto-Cordero et al., 2020). It is therefore possible that most of the near-trench seismicity, repeating and not, emerged as a result of low pressure linked to the afterslip activity, and disappeared as afterslip slowed down and pressure increased again.

5.6 Conclusion

We computed the corner frequencies, seismic moments and stress drops of 597 small Mw 2-4 earthquakes along the Ecuadorian subduction zone in the aftermath of the Mw7.8 2016 Pedernales earthquake. Stress drops were found to increase with magnitude, as well as with distance to the trench. When examining the variation of source properties within repeating earthquakes, we find that in most of the region they are spatially variable with no clear pattern of evolution, and likely influenced by local processes. Near the trench, however, earthquake stress drops systematically decrease over time, likely reflecting changes in pore fluid pressure associated with the decay of the afterslip. Thus our work allows us to image changes in friction of the megathrust in space and time.

Chapter 6: Discussion and conclusion

Over the course of this study, I compiled a catalogue of repeating earthquakes between 2015 and 2017, which I relocated using manual picks and double difference time arrivals. However, the location uncertainties led me to rely solely on cross-correlation to constitute families of repeaters, which may affect the robustness of the classification (Uchida, 2019). I mitigated this issue by using a high correlation coefficient of 0.95 and by removing families of only 2 or 3 events, as well as short-lived families of burst-type repeaters. I found that repeating earthquakes occur primarily in regions with abundant microseismicity. They do not, however, occur in areas experiencing the largest amount of afterslip. Instead, repeaters are located primarily at the edges of the afterslip regions, where the afterslip gradient is high. This differs somewhat from the classical model of repeaters as isolated asperities embedded within creeping regions and thus driven by the slip around (Uchida and Bürgmann, 2019). Additionally, using the Nadeau and Johnson (1998) model to estimate the amount of aseismic slip occurring on the megathrust proved to be ineffective. My results show large differences in slip between neighboring families, and a poor correlation between the slip derived from the repeaters and from the geodetic measurements.

I also computed some of the source properties of repeating earthquakes as well as regular aftershocks, with several features worth noting. The first is the dependence of stress drop on seismic moment and on distance from the trench in the region. Earthquakes near the trench have particularly low stress drops, which may reflect a difference in frictional properties or pore fluid pressure in the region. Additionally, when looking at the evolution of source properties with time within families of repeating earthquakes, I found that the near-trench region is the only one where a significant trend can be found. In this region, a decrease in stress drop can be found over the year after the mainshock, in all of the families present with resolvable source properties. This large-scale change may reflect an increase in pore fluid pressure as afterslip decays and the fault gradually heals.

In the following section, I will address some outstanding points, and put the results from the last two chapters together to better understand the processes and structure of the plate interface.

6.1 Correlation coefficient dependence on inter-event distance

As previously stated, the lack of precision in earthquake locations forced me to base the classification of repeaters solely on correlation coefficients, as is still widely done (Chaves et al., 2020; Dominguez et al., 2016; Duverger et al., 2018; Yao et al., 2017). It is justified a posteriori by the fact that, as seen in Figure 37 and Figure 38 from Chapter 3, high-correlation earthquakes form a clear and distinct population from the rest of the catalogue, highlighting that repeaters belong to a different class of events than the rest of the aftershocks. Like most studies, I assumed that highly correlated events must be separated by less than a quarter of the wavelength of the highest frequencies of the signal. However, it is worth questioning these assumptions to ensure that my classification is robust. Thus in this section, I will investigate the relationship of correlation with inter-event distance, and show how correlations are affected by the number and distance of the stations used.

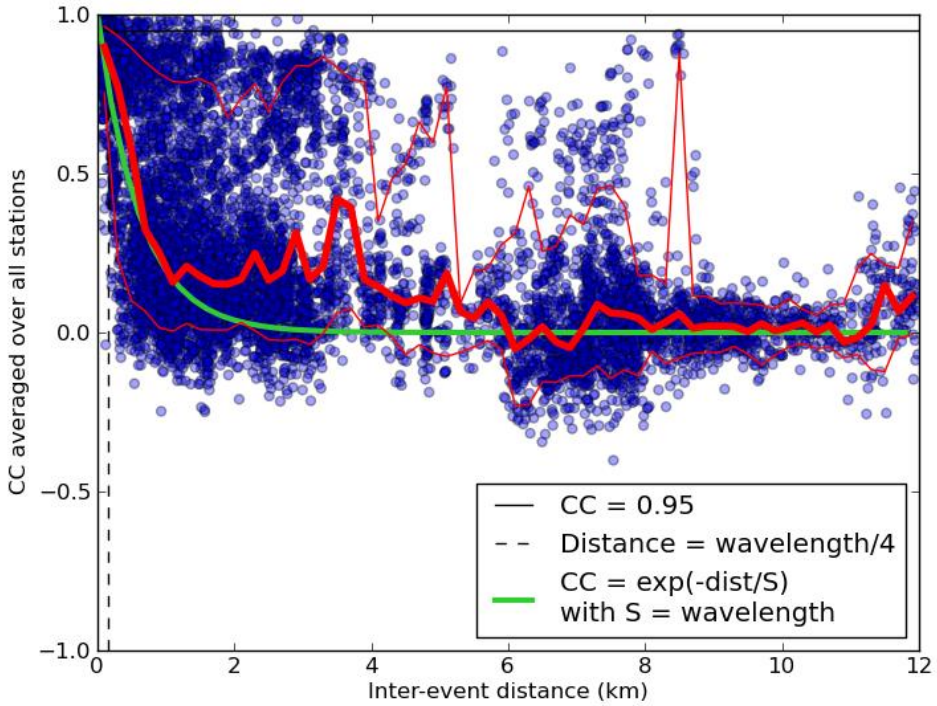

Figure 78 : Correlation coefficient averaged over at least four stations as a function of inter-event distance (blue circles). Only event pairs with an error in distance below 300 m are shown in the plot. The thick red line shows the median correlation while the thin red lines show the 10th and 90th percentiles. The green line is the relation derived by Menke (1999), with S being the wavelength associated with the upper corner frequency of the filter. Because events were filtered between 1.5 and 6 Hz, and assuming a seismic velocity of about 3.7 km/s (León-Ríos et al., 2019), the wavelength is about

600 meters. The dashed vertical black line shows the quarter of the wavelength, which corresponds to the minimum distance resolvable by cross correlation (Geller and Mueller, 1980). The horizontal black line shows the 0.95 threshold.

In theory, correlation coefficient decays exponentially with distance. Menke (1999) suggested that $CC = e^{-d/s}$ where d is distance and s is a frequency-dependent correlation length, taken to be the wavelength of the dominant frequency. This is however only a first-order approximation, as several studies have demonstrated with numerical modelling that the medium heterogeneity, time window and source-receiver geometry also affect the way correlation decays with distance (Baisch et al., 2008; Han et al., 2014). I explore this relationship using my dataset. To do so, using my already-calculated correlations is problematic for several reasons. The first is that I have used different filters for different stations, and so cannot combine them. Additionally, my average inter-event distance errors are on the order of 500 m to 1 km, which is higher than the S wavelength at 9Hz, the upper boundary of the lowest filter used for correlations. This means that the decay of correlation with inter-event distance is likely to be difficult to resolve for data filtered up to 9 or 10 Hz. The second issue is that source complexity affects correlations above the corner frequency (8 and 6 Hz for P and S waves on average), even for collocated events with similar focal mechanisms, thus making the correlation-distance link less clear (Nakahara, 2004; Uchida, 2019). To remedy this, I correlate a sample of well-relocated event pairs with high signal/noise ratio filtered between 1.5 and 6 Hz, to determine how correlation coefficient in general is affected by distance between earthquakes and event-station distance. The relationship of correlation with inter-event distance, shown in Figure 78, is close to the one predicted by Menke (1999). This confirms that when averaging correlation coefficients over a large number of stations, and when filtering signal below the corner frequency, correlation is indeed primarily dependent on inter-event distance and on the upper boundary of the filter. However, while this is true for the median correlation coefficient, significant variability exists. In particular, some pairs have very high correlations but large inter-event distance, showing the limitation of the method. In addition, some closely located events are poorly correlated, likely due to differences in focal mechanisms. This is not the case for events within 150 m of each other, which overwhelmingly have high correlations, perhaps indicating that velocity structure and focal mechanisms do not vary much over this length scale.

I also examine the relationship between correlation and event-station distance (Figure 79). I find that, for events with inter-event distances smaller than the quarter of the upper wavelength of the filter, the event-station distance has little impact on the correlation coefficient, beyond the likely introduction of noise. However, for events with larger separations, correlation coefficients tend to be larger when the station is close, and are generally more variable. This might be explained by the fact that inter-event vertical separation is better resolved when the station is far, particularly for a deep source (Gao et al., 2021). However, the fact that collocated

events' correlation coefficients are not dependent on station-event distance is important, since this study's stations and events tend to be far apart.

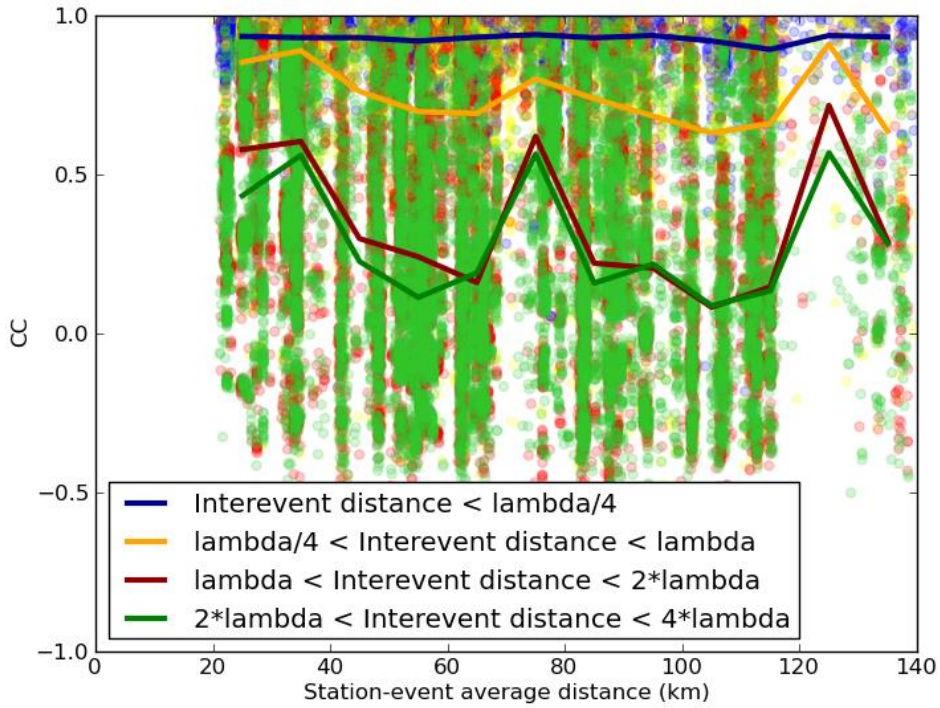

Figure 79 : Correlation coefficients as a function of station-event distance. Four subgroups of event pairs are considered: those separated by less than a quarter of the dominant wavelength (150 m) in blue, those separated by one to two wavelength (600-1200 m) in red, those separated by two to four wavelengths (1200-2500 m) in green, and those separated by four to eight wavelengths (2500-4900 m) in yellow. The median variation of correlation coefficient with station-event distance for these four groups is shown as thick blue, brown, green and orange lines respectively.

I am therefore confident that correlation coefficient is a good proxy for distance, although significant variations exist between stations. These variations are not linked to the epicentral distance when both the average correlation coefficient and the signal to noise ratio are high. Overall, I can be confident that correlation coefficients are enough to find robust families of earthquakes.

6.2 Relationship between repeaters' displacements and large-scale slip

With confidence in the results, and having calculated source properties of a lot of repeaters, I can revisit briefly the relationship between the slip experienced by repeaters and the large-scale displacement measured by GPS. I showed in Chapter 4 that the Nadeau and Johnson equation (Nadeau and Johnson, 1998) did not accurately predict the GPS slip that occurred on an asperity. However, since at the time I had no seismic moment for repeating events at the time, I had used the equation from Agurto-Detzel et al. (2019) to estimate them, which as seen in Chapter 5 was actually inappropriate for this dataset. Thus, it may be that the bad fit of the Nadeau and Johnson curve was in part linked to this miscalculation of seismic moments. However, when I calculate again the fit using the new M_L-M_w relation, I find that it is no better suited to the data (Figure 80). The Nadeau and Johnson equation overestimates slip for families far from the afterslip centers in particular, which might reflect an issue with the geodetic model, or with the use of the Nadeau and Johnson equation in the first place. This poor fit is not unique to this dataset, as some other studies of aftershock sequences in subduction zones also yield similarly poor and heterogeneous estimates (Yao et al., 2017).

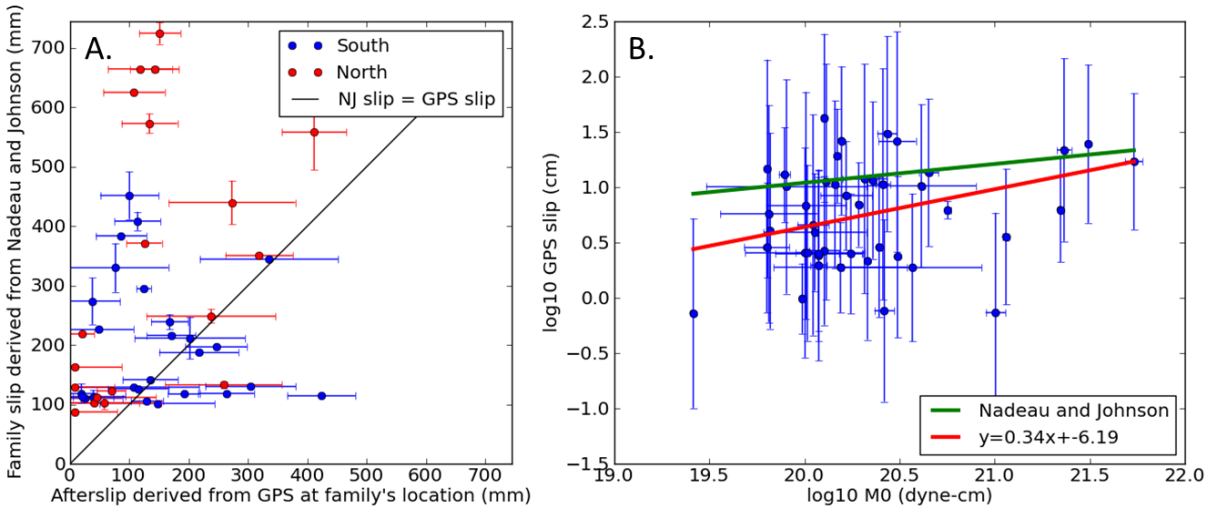

Figure 80 : A: Aseismic slip experienced by a family between the first and the last repeater of the first month, estimated from the geodetic model (Rolandone et al., 2018) versus estimated using the Nadeau and Johnson equation. This time, I use seismic moments calculated directly from spectral ratios when available. Otherwise, I convert local to moment magnitudes using the formula derived in Appendix C: $M_W = 0.6 \times M_L + 1.1$. Only families with 2 or more events in the first month, and more than a day between the first and the last event of the month, are used. Families within 50 km of the northern and southern afterslip patch are shown in red and blue respectively. B: Comparison of average family seismic moment and

average slip measured geodetically (Rolandone et al., 2018). The green line is the linear relationship predicted by the Nadeau and Johnson equation. The red line is the least squares fit through the data.

One possible explanation is that the Nadeau and Johnson equation was elaborated during the interseismic period in California, when the variability between repeaters occurring at different times is small. However, repeating aftershocks' source properties are rarely constant with time during the postseismic period (Chapter 5). Additionally, the assumption made by the Nadeau and Johnson (1998) model of small earthquakes stress drops being larger than large earthquakes stress drops is not correct here. Thus to better understand the relationship of repeaters to afterslip, I consider whether the coseismic displacement of repeaters, calculated using available stress drops, is linked to the large scale slip derived through geodesy.

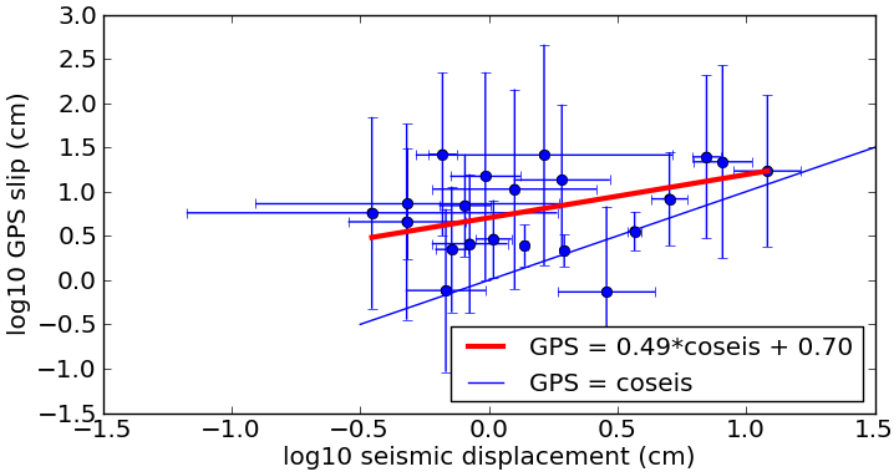

Figure 81 : Average coseismic slip experienced by a repeater within a family versus average afterslip estimated geodetically (Rolandone et al., 2018). Only events with well-resolved source properties are used to calculate the averages. The red line shows the best fit trend, while the blue line shows the 1:1 line.

I show in Figure 81 that the measured geodetic slip increases weakly with the amount of coseismic displacement occurring on an asperity, although the sum of repeaters' displacements is generally lower than the slip modelled with GPS. This is also true in other regions like Costa Rica, where Yao et al. (2017) find the coseismic slip of repeaters to be significantly smaller than the calculated afterslip, assuming a 3 MPa stress drop. It can be explained by the presence of aseismic slip on repeating earthquake asperities, a feature which was theorized by Beeler et al. (2001) and has since been modelled numerically (T. Chen and Lapusta, 2009).

The Beeler model also states that the amount of slip accommodated aseismically should decrease as the seismic moment of the family increases, which appears to be true here. However, when trying to fit the data to the Beeler model, I find that the ratio of coseismic to

total displacement (estimated from GPS) on an asperity cannot be accurately modelled (Figure 82). Once again, the ratio of seismic to aseismic slip that I observe is significantly more variable than what the Beeler model predicts, and for a few families the coseismic displacement appears to be larger than the geodetically measured slip on the fault, although this is likely due to uncertainties in the calculation of both geodetic and coseismic slip.

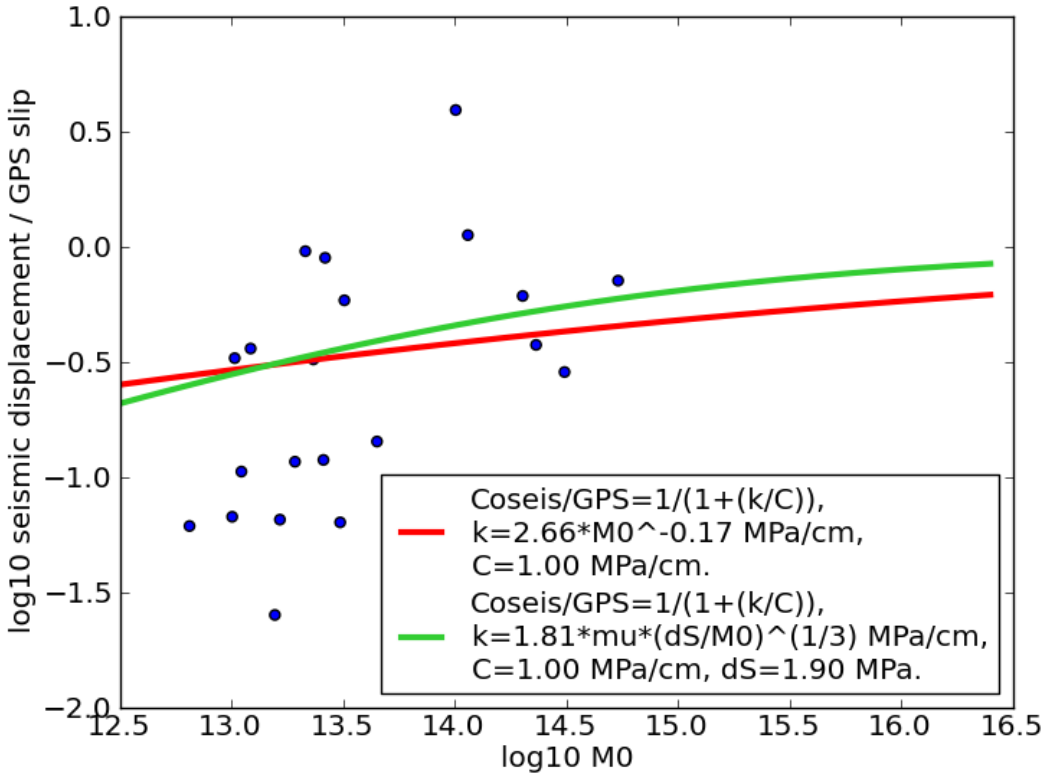

Figure 82 : Average ratio of coseismic slip to geodetically-measured displacement experienced by families, as a function of average seismic moment. Only events with well-resolved source properties are used to calculate the averages. The red and green curve show two different fits of the data using the Beeler model. The green line uses a stiffness that varies as a function of $M_0^{-1/3}$, as is generally assumed, and uses a stress drop of 1.9 MPa, which is the average stress drop of the catalogue. The red line uses a stiffness that varies as a function of $M_0^{-0.17}$, which was determined based on the stress drops and coseismic displacements available in the whole catalogue.

Thus the large scatter and lack of agreement between the data and models linking repeaters and aseismic slip appears real, and requires explanation. One way to test whether geodetic and repeaters measurements are compatible would be to invert these two datasets jointly, as was done in a few other places (Mavrommatis et al., 2015). Because geodetic models of slip tend to smooth the experienced slip and only represent large-scale tendencies, while repeaters represent slip on a hundred-meter scale asperity, the discrepancy in slip measurements may be explained by the structural and frictional complexity of the megathrust and the aseismic slip occurring on it.

6.3 Influence of subducting structures and small-scale heterogeneities on repeaters slip

When considering whether repeaters can be used as proxies for large-scale slip, I assumed the megathrust to be a single plane on which repeaters occur. However, this is a simplification.

Two aspects of subduction zone structure in particular would help explain why repeaters slip is so heterogeneous and so difficult to link to larger-scale slip. The first is that, until now, I have neglected the possibility of off-fault damage. While repeaters, when well located, appear to be aligned along the megathrust, some may still be occurring at the intersection between the megathrust and intraplate faults. Repeaters may particularly occur in the overriding plate near subducted relief like the subducted Atacames seamounts (Marcaillou et al., 2016), which are associated with faulting in the upper plate. The occurrence of repeaters in upper plate faults associated with seamounts is documented at the Hikurangi subduction zone (Hughes et al., 2021; Shaddox and Schwartz, 2019), and can help explain discrepancies between overall displacement measured by GPS and repeater slip. This possibility should be examined further by calculating focal mechanisms for repeaters, although they cannot fully confirm whether slip occurs along the megathrust or on a conjugate rupture. We could examine in more detail where repeaters occur relative to the seamount, and how aseismic slip is triggered during seamount subduction.

Additionally, it is worth considering that the megathrust itself is a complex structure, which could explain discrepancies between repeaters and large-scale faults. In another context, Williams et al. (2019) found that the mismatch between repeaters' and geodetic fault displacement near Parkfield, California could be explained by fault complexity. In their model, repeaters occur on small parallel fault strands existing within the fault zone which each contribute to the large-scale deformation, thus explaining why the coseismic displacement of repeaters is always inferior to the long-term large-scale displacement.

The study region, of course, is a subduction zone rather than a continental transform fault. However, the idea that fault zone complexity could lead to the displacement of repeaters being smaller than the large-scale deformation is applicable, and may explain why there is a lot of heterogeneity in the slip. In a subduction zone, deformation at the megathrust occurs within a meters to kilometers thick shear zone rather than a simple plane of contact, as evidenced by geology (Fagereng and Sibson, 2010). This subduction channel is composed of sheared sediments saturated with fluids and fragments of oceanic crust and the overriding plate, forming

a mix of competent and incompetent material that gives the subduction zone mechanical properties different from those of a simple plane (Fagereng and Sibson, 2010). This leads to a heterogeneous strain rate, shear strength, viscosity and faulting style in the channel, and produces three end-member behaviors (Fagereng and Sibson, 2010). On one end, when high-competence material is dominant in the mix, shearing is localized along discontinuities and nucleation of large earthquakes is possible. On another end, when low competence material is dominant, deformation is distributed and faults can creep or slip slowly. When both competent and incompetent material are present, then both discrete and distributed deformation can occur.

Indirect evidence of this mix of lithology exists for active subduction zones using seismic imaging. In Hikurangi, the pre-trench sediments were drilled, and the shallow subduction was imaged in an area prone to slow slip (Barnes et al., 2020). By doing so authors were able to image this geometric complexity, and to infer the rheological heterogeneity likely found at the plate interface at multiple scales. Meanwhile, in Costa Rica, Kirkpatrick et al. (2020) were able to image in 3D both the geometrical roughness and the heterogeneous mechanical properties on the megathrust, hinting at this heterogeneous structure. They also found in their region that earthquakes with small rupture zone have highly variable, often small stress drops compared to earthquakes with larger rupture zones, which have larger and less variable stress drops. They explain this as small earthquakes being more sensitive to stress heterogeneities as they rupture only one asperity. While I cannot make definitive conclusions due to the limitations of the dataset, this might mean that the spatial variability found in stress drops at the Ecuadorian margin could also reflect the roughness and heterogeneity of the megathrust.

Having established the heterogeneous nature of the subduction channel, I can explain its importance for estimations of slip based on repeating earthquakes. We currently do not know how localized deformation truly is within the subduction channel. Repeating micro-earthquakes in particular may actually occur within competent lenses of material, surrounded by slowly deforming incompetent material (Collettini et al., 2011). This means that they may not reflect all of the deformation occurring at the plate interface. The ratio of seismic to aseismic slip may depend not only on the size of the competent lens on which the repeating earthquake occurs, but also on its orientation, its position relative to other competent material, or the thickness of the deforming zone. While this is currently outside the scope of this present work, exploring this possibility further would help bridge the gap between geological observations of subduction zones in the field and seismological observations of micro-earthquakes. Doing so would require accurate focal mechanisms, but would ideally be paired with high-resolution 3D imaging extending to regions where repeating microseismicity is abundant.

6.4 Differences between up-dip and down-dip repeaters

Beyond the small-scale heterogeneity found among repeaters, I have also demonstrated a large-scale difference in behavior between events close to the trench and events further away. Like regular earthquakes, repeaters near the trench have anomalously low stress drops. Additionally, repeating earthquake stress drops near the trench decrease over time, unlike the stress drops of deeper repeaters, which have much more variable evolutions. Both of these observations may be controlled by fluid pressure in the region. In this section, I will further detail the observable differences between shallow and deep repeaters.

The spatio-temporal characteristics of repeating earthquakes differ depending on their distance to the trench. The largest earthquake clusters are between 20 and 60 km from the trench. In that region, families exist close together in those tight clusters. By comparison, families near the trench are more spread out, and aftershocks in general are less clustered. The timing of repeaters is also different near the trench. To illustrate this, I have separated the region into three subregions: one further than 60km from the trench, one from 20 to 60 km from the trench and one from 0 to 20 km from the trench. I show earthquakes in these subregions in Figure 83, Figure 84, and Figure 85.

Only five repeating earthquake families exist further than 60 km (Figure 83), spread out in space with seemingly no interaction among themselves. They start either right after the mainshock, or right after one of the large aftershocks in the region, and they tend to be short-lived, as only one repeater occurs more than 200 days after the mainshock. The late starting date of some families suggest that they occurred in regions unlocked by the large aftershocks, and the early end to most of the families further implies that the region was quickly locked again, only experiencing aseismic slip for a short time. There is only one repeater which occurs at the end of the period, during the suspected June 2017 SSE in the north (Chalumeau et al., 2021 and personnal communications). However, in the absence of a slip model for this SSE, I cannot say if it affected the deeper region, or was confined to the northern afterslip area that had previously hosted SSEs (Vaca et al., 2018).

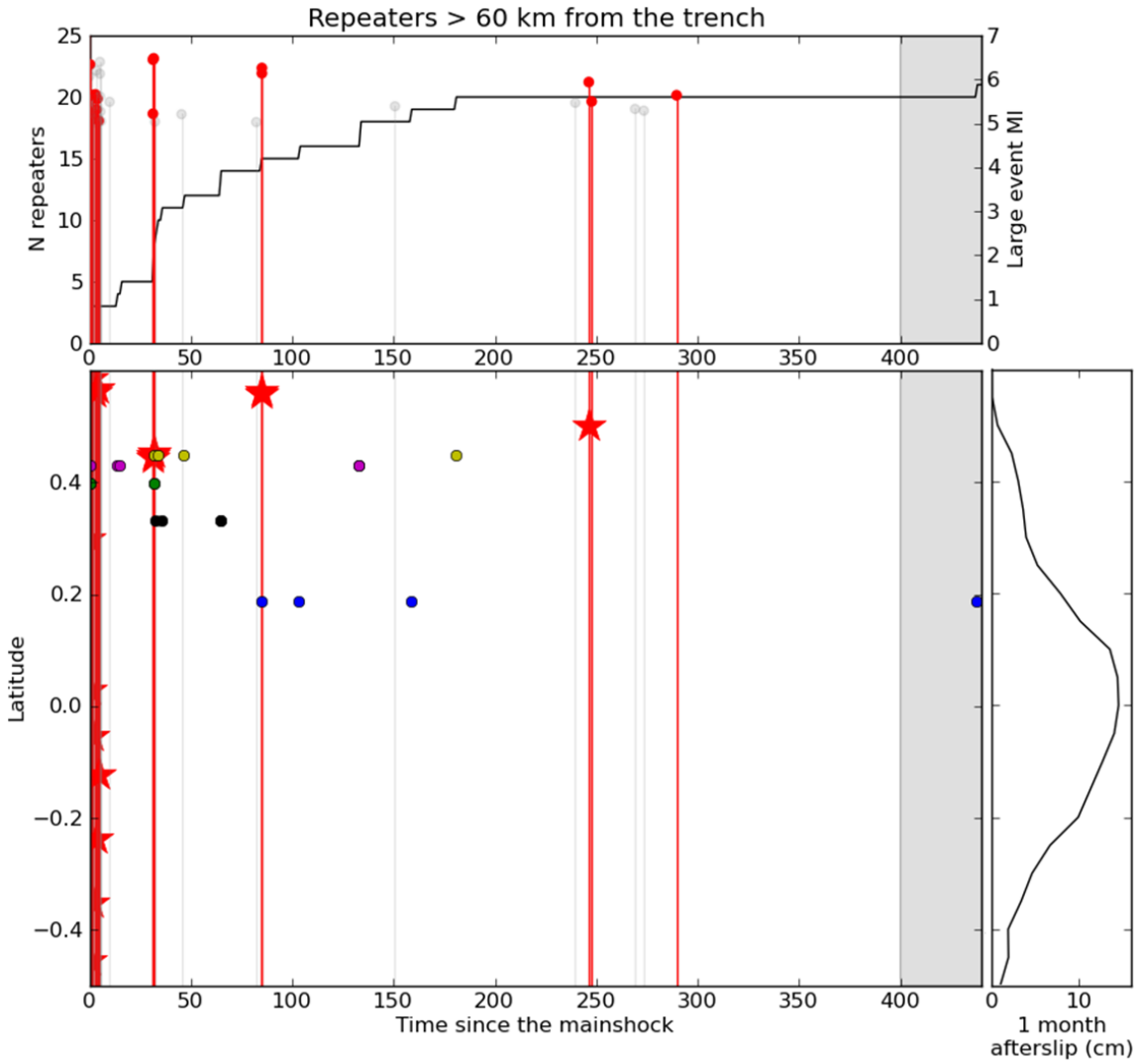

Figure 83 : Occurrence of repeating earthquakes as a function time in the region further than 60 km away from the trench. The full black line (top panel) shows the cumulative number of repeaters with time. The vertical red and grey lines show the earthquakes with local magnitudes above 5 happening within and further than 5 km away from the region, respectively, with their local magnitudes given in the top panel (circles). Red stars (bottom panel) show the latitude of earthquakes within 5 km of the region. Repeating earthquakes are shown as colored circles (bottom panel). The grey shaded area corresponds to the approximate time of the slow slip event occurring at the end of the period (Chalumeau et al., 2021 and personnal communications). Its spatial extent is currently undetermined, so the shading extends to all latitudes. The panel on the right shows the average amount of afterslip that occurred in the region in the first month as a function of latitude (Rolandone et al., 2018).

By contrast, repeaters between 20 and 60 km from the trench occur throughout the period (Figure 84), and a few also occur before the mainshock. While repeaters are sometimes triggered by nearby larger earthquakes, this is not seen consistently, and the effect is often small. Conversely, some earthquakes of magnitude 5-5.5 are seemingly preceded by an increase in repeating activity, like near day 45 or near day 270, which may indicate preseismic slip. Once again, after day 400 a large number of families are activated due to the slow slip. Overall, the

picture is one of repeating seismicity that interacts with itself and with larger earthquakes, However, the cumulative number of repeaters still has a logarithmic shape until the end of the period, with only small bursts to disrupt the decline in seismicity rate.

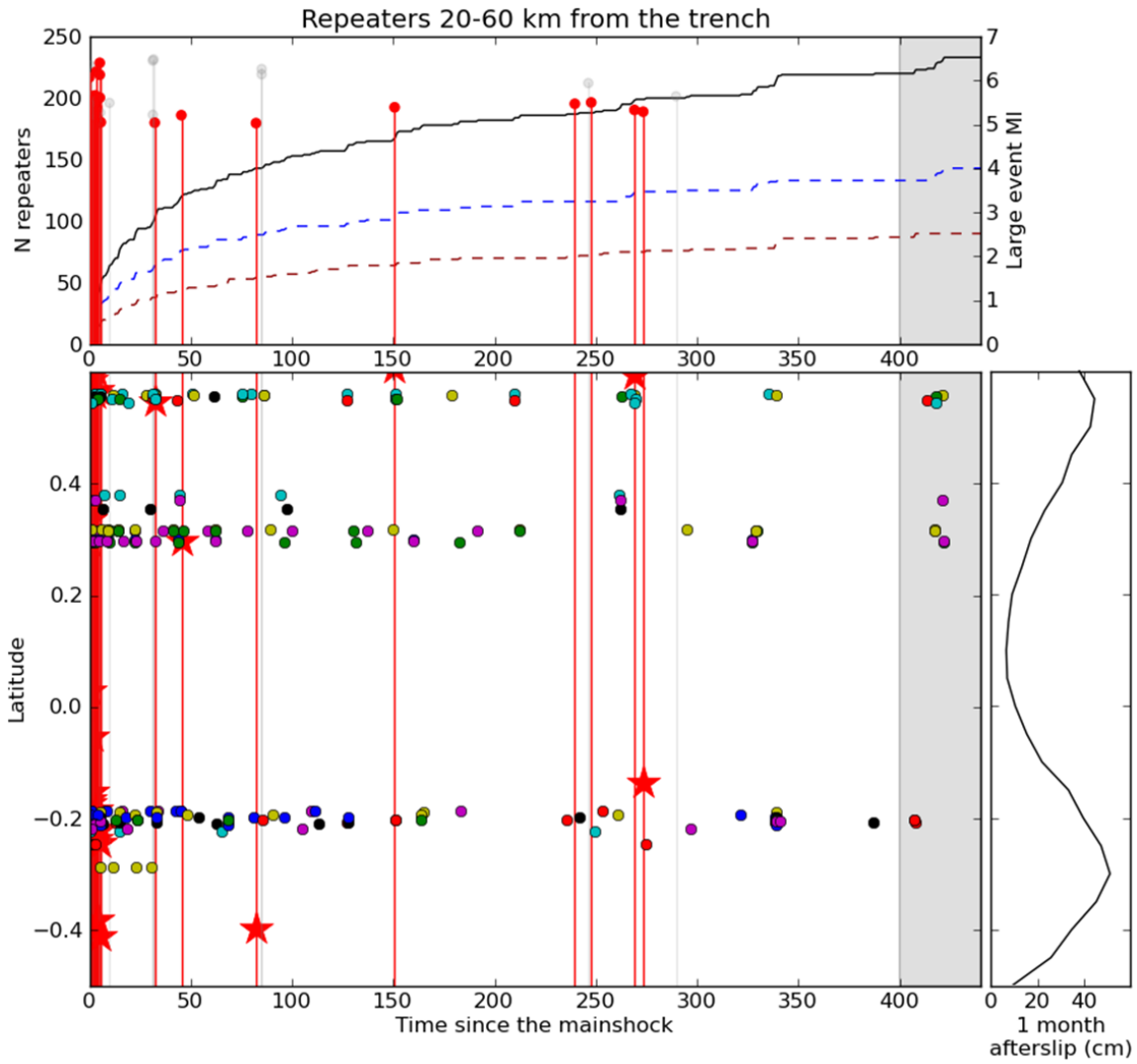

Figure 84 : Occurrence of repeating earthquakes as a function time in the region between 20 and 60 km from the trench. The black line (top panel) shows the total cumulative number of repeaters with time, with the dashed blue and red lines showing the cumulative number of repeaters in the north and south respectively. The vertical red and grey lines show the earthquakes with local magnitudes above 5 happening within and further than 5 km away from the region, respectively, with their local magnitudes given in the top panel (circles). Red stars (bottom panel) show the latitude of earthquakes within 5 km of the region. Repeating earthquakes are shown as colored circles (bottom panel). The grey shaded area corresponds to the approximate time of the slow slip event occurring at the end of the period (Chalumeau et al., 2021 and personnal communications). Its spatial extent is currently undetermined, so the shading extends to all latitudes. The panel on the right shows the average amount of afterslip that occurred in the region in the first month as a function of latitude (Rolandone et al., 2018).

Within 20 km of the trench, repeaters are much more clustered in time, despite their larger spatial separations (Figure 85). There are two distinct episodes of significantly increased repeating seismicity around day 80 and day 185. In the former case, an event of magnitude > 5 occurs, but cannot fully explain the increase in repeating seismicity, which starts before that earthquake. There is therefore a likely increase in slip rate, although it seems completely confined to the near-trench region. The second increase in seismicity around day 185 is not associated with any moderate or large event, regional or otherwise. Notably, it is linked to the activity of many trench repeaters in the south, but also the activation of 3 out of the 4 families of trench repeaters in the north, which potentially implies an interaction over at least 70 kilometers. This might be explained by an increase in aseismic slip in the near-trench region, but, again, no corresponding increase in activity occurs further than 20 km from the trench. After this episode, most trench repeaters become inactive until the SSE after day 400 in the north. Similarly, it seems that no repeater occurs near the trench in the year before the mainshock, although the detection capacities during that time are poor. As discussed briefly in Chapter 5, the fact that repeating earthquake activity nearly stops in the second half of the period could be explained by a high fluid pressure gradually shutting down families. The activation of repeating families during the 2017 SSE could be an indication of a temporary change in fluid pressure in the region again.

This shows that there are significant differences between the shallow and deeper regions of the subduction zone, and that those regions can be activated independently (day 185) or together (day 400 onward) during likely slow slip events. These differences, revealed by repeating earthquakes, are likely linked to frictional properties or pore-fluid pressure. Based on the work by León-ríos et al. (2021), the region 20-30 km from the trench has an elevated vp/vs ratio, indicating that the region is highly hydrated. This is similar to other regions like southern Chile, where a high vp/vs ratio is observed near the trench along with a lack of background seismicity at the plate interface (Haberland et al., 2009; Hicks et al., 2014). Such a difference between shallow and deep portions of the megathrust can also be seen in Central Chile, where Frank et al. (2017) was able to quantify the evolution of rheology with depth using the 2015 Illapel aftershock catalogue. They find a change in rheology with depth, which can correspond to a decrease of a-b with depth or to anomalously high pore pressure at shallow depths.

It would be interesting to quantify the amount and movement of pore fluids at shallow depths, in order to better understand the differences of behavior at different depths. Part of this may be done through geophysical imaging techniques, but seismology could also help further this question. If the near-trench region is saturated with fluids, then unconventional signals like non-volcanic tremors and very low frequency earthquakes should be observed, as they are in other subduction zones (Baba et al., 2021; Nakano et al., 2018). Detecting and tracking them could therefore be a useful tool to track fluid movements and better understand the role of fluids in the seismic cycle.

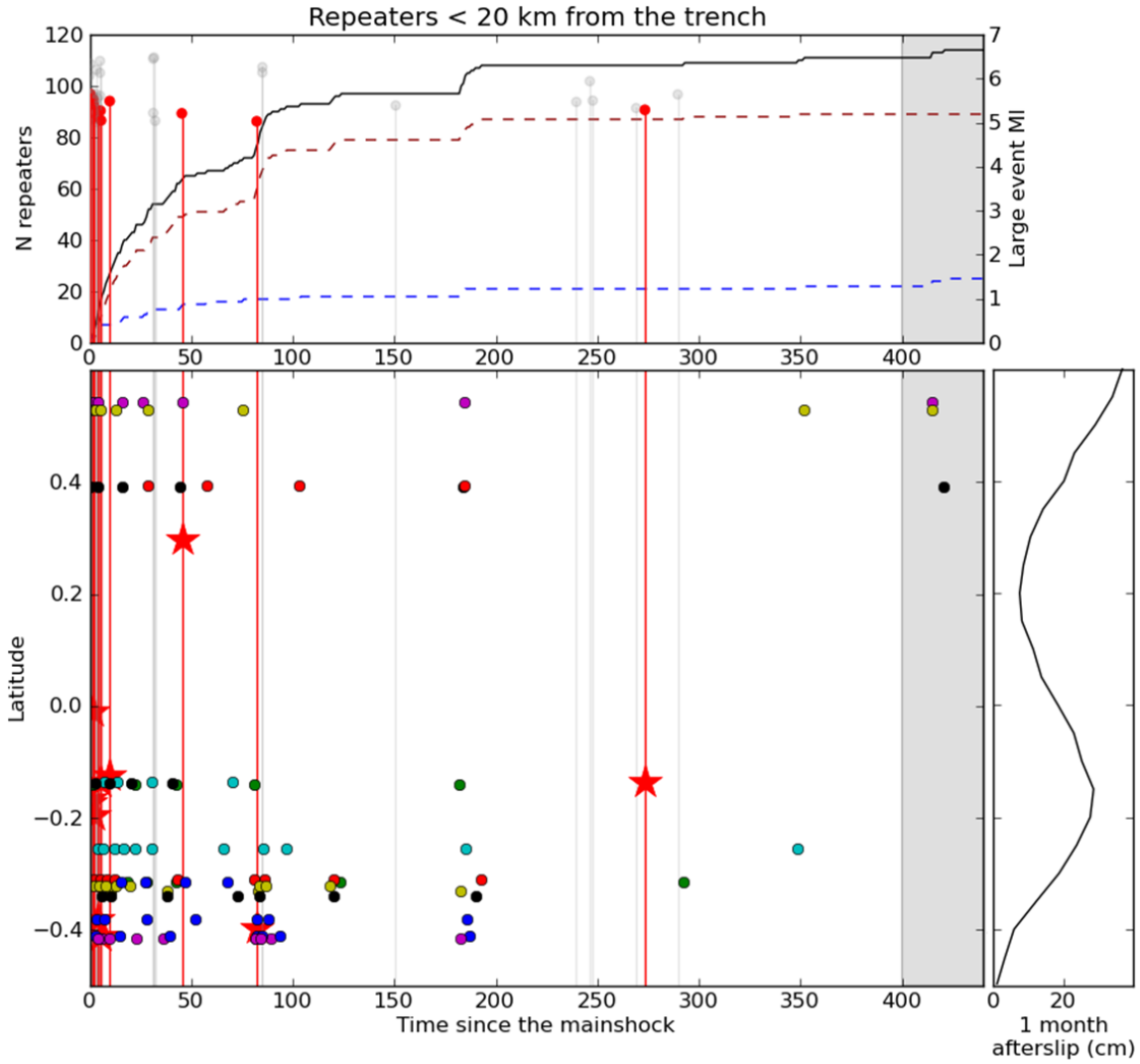

Figure 85 : Occurrence of repeating earthquakes as a function time in the region closer than 20 km from the trench The black line (top panel) shows the total cumulative number of repeaters with time, with the dashed blue and red lines showing the cumulative number of repeaters in the north and south respectively. The vertical red and grey lines show the earthquakes with local magnitudes above 5 happening within and further than 5 km away from the region, respectively, with their local magnitudes given in the top panel (circles). Red stars (bottom panel) show the latitude of earthquakes within 5 km of the region. Repeating earthquakes are shown as colored circles (bottom panel). The grey shaded area corresponds to the approximate time of the slow slip event occurring at the end of the period (Chalumeau et al., 2021 and personnal communications). Its spatial extent is currently undetermined, so the shading extends to all latitudes. The panel on the right shows the average amount of afterslip that occurred in the region in the first month as a function of latitude (Rolandone et al., 2018).

6.5 Conclusion and future prospects

Studying seismicity, particularly repeating earthquakes, in the aftermath of the Pedernales earthquake allowed us to learn more about the subduction process in Ecuador. Repeating earthquakes were found to exist primarily around the main afterslip regions, thus possibly highlighting frictionally heterogeneous regions acting as barriers to the propagation of aseismic slip, or otherwise indicating an accumulation of stress at the edges of the afterslip. The heterogeneity of slip measured by repeating earthquakes, along with their poor agreement with large-scale geodetic models, hint at the complexity of slip on the megathrust, likely caused by small-scale structural features. I am additionally able to see a larger-scale segmentation in depth between different regions within the coseismic zone. In particular, the behaviors and stress drops of repeaters and aftershocks reveal that the near-trench region is likely fluid-filled and subject to changes in pore pressure. It also seems to experience confined episodes of transient slip.

These findings should be investigated further, ideally with the help of geodetic modelling and geophysical imaging along with seismological studies. The question of how seismic and aseismic behavior changes over the whole seismic cycle is particularly important, and requires that this analysis be performed over a longer timeframe. Obtaining focal mechanisms for repeating earthquakes especially would also improve our understanding of megathrust structure and the location of aseismic slip on or off the fault. Finally, the role of fluids at different depth in the subduction is still to be elucidated, likely using other seismic signals along with geophysical imaging.

Bibliography

Abe, K. (1979). Size of Great Earthquakes of 1837-1974 Inferred From Tsunami Data. *Journal of Geophysical Research*, *84*(B4), 1561–1568.

Abercrombie, R. E. (1995). Earthquake source scaling relationships from 1 to 5 Ml using seismograms recorded at 2.5 km depth. *Journal of Geophysical Research*, *100*(B12), 24015–24036.

Abercrombie, R. E. (2014). Stress drops of repeating earthquakes on the San Andreas Fault at Parkfield. *Geophysical Research Letters*, *41*, 8784–8791. https://doi.org/10.1002/2014GL062079.Received

Abercrombie, R. E. (2015). Investigating uncertainties in empirical Green's function analysis of earthquake source parameters. *Journal of Geophysical Research: Solid Earth*, *120*, 4263–4277. https://doi.org/10.1002/2015JB011984.Received

Abercrombie, R. E. (2021). Resolution and uncertainties in estimates of earthquake stress drop and energy release. *Philosophical Transactions Royal Society*, *379*.

Abercrombie, R. E., Antolik, M., Felzer, K., & Ekström, G. (2001). The 1994 Java tsunami earthquake: Slip over a subducting seamount. *Journal of Geophysical Research*, *106*(B4), 6595–6607.

Abercrombie, R. E., Bannister, S., Ristau, J., & Doser, D. (2017). Variability of earthquake stress drop in a subduction setting, the Hikurangi Margin, New Zealand. *Geophysical Journal International*, *208*(1), 306–320. https://doi.org/10.1093/gji/ggw393

Abercrombie, R. E., Chen, X., & Zhang, J. (2012). Repeating Earthquakes with Remarkably Repeatable Ruptures on the San Andreas Fault at Parkfield. *Geophysical Research Letters Supporting*, *47*(47), 1–15. https://doi.org/10.1029/2020GL089820

Agurto-detzel, H., Bianchi, M., Prieto, G. A., & Assumpção, M. (2017). Earthquake source properties of a shallow induced seismic sequence in SE Brazil. *Journal of Geophysical Research: Solid Earth*, *122*. https://doi.org/10.1002/2016JB013623

Agurto-Detzel, H., Font, Y., Charvis, P., Régnier, M., Rietbrock, A., Ambrois, D., Paulatto, M., Alvarado, A., Beck, S. L., Courboulex, F., De Barros, L., Deschamps, A., Hernandez Salazar, M. J., Hernandez, S., Hoskins, M. C., León-Ríos, S., Lynner, C., Meltzer, A., Mercerat, E. D., … Soto-cordero, L. (2019). Ridge subduction and afterslip control aftershock distribution of the 2016 Mw 7.8 Ecuador earthquake. *Earth and Planetary Science Letters*, *520*, 63–76. https://doi.org/10.1016/j.epsl.2019.05.029

Agurto-detzel, H., Rivet, D., & Charvis, P. (2020). *Seismic velocity changes in the epicentral area of the Mw 7.8 Pedernales (Ecuador) earthquake from cross-correlation of ambient seismic noise*.

Aizprua, C., Witt, C., Brönner, M., Johansen, S. E., Barba, D., & Hernandez Salazar, M. J. (2020). Forearc Crustal Structure of Ecuador Revealed by Gravity and Aeromagnetic Anomalies and Their Geodynamic Implications. *Lithosphere*.

Aki, K. (1966). Generation and propagation of G waves from the Niigata earthquake of June 16, 1964. Part 2. Estimation of earthquake moment, released energy and stress-strain drop from G wave spectrum. *Bulletin of the Earthquake Research Institute*, *44*, 73–88.

Aki, K. (1967). Scaling law of seismic spectrum. *Journal of Geophysical Research*, *72*(4), 1217–1231. https://doi.org/10.1029/JZ072i004p01217

Allmann, B. P., & Shearer, P. M. (2007). Spatial and temporal stress drop variations in small earthquakes near Parkfield, California. *Journal of Geophysical Research*, *112*(April). https://doi.org/10.1029/2006JB004395

Allmann, B. P., & Shearer, P. M. (2009). Global variations of stress drop for moderate to large

earthquakes. *Journal of Geophysical Research*, *114*(November 2008), 1–22. https://doi.org/10.1029/2008JB005821

Alvarado, A., Audin, L., Nocquet, J.-M., Jaillard, E., Mothes, P. A., Jarrín, P., Segovia, M., Rolandone, F., & Cisneros, D. (2016). Partitioning of oblique convergence in the Northern Andes subduction zone: Migration history and the present-day boundary of the North Andean Sliver in Ecuador. *Tectonics*, *35*, 1048–1065. https://doi.org/10.1002/2016TC004117.Received

Alvarado, A., Audin, L., Nocquet, J.-M., Lagreulet, S., Segovia, M., Font, Y., Lamarque, G., Yepes, H., Mothes, P. A., Rolandone, F., Jarrín, P., & Quidelleur, X. (2014). Active tectonics in Quito, Ecuador, assessed by geomorphological studies, GPS data, and crustal seismicity. *Tectonics*, *33*, 67–83. https://doi.org/10.1002/2012TC003224.Received

Alvarado, A., Ruiz, M., Mothes, P. A., Yepes, H., Segovia, M., Vaca, M., Ramos, C., Enríquez, W., Ponce, G., Jarrín, P., Aguilar, J., Acero, W., Vaca, S., Singaucho, J. C., Pacheco, D., & Córdova, A. (2018). Seismic, Volcanic, and Geodetic Networks in Ecuador: Building Capacity for Monitoring and Research. *Seismological Research Letters*. https://doi.org/10.1785/0220170229

Alvarez, O., Folguera, A., & Gimenez, M. (2017). Rupture area analysis of the Ecuador (Musine) Mw = 7.8 thrust earthquake on April 16, 2016, using GOCE derived gradients. *Geodesy and Geodynamics*, *8*(1), 49–58. https://doi.org/10.1016/j.geog.2017.01.005

Andrews, D. J. (1976). Rupture Velocity of Plane Strain Shear Cracks. *Journal of Geophysical Research*, *81*(32), 5679–5687.

Anooshehpoor, A., & Brune, J. N. (2001). Quasi-Static Slip-Rate Shielding by Locked and Creeping Zones as an Explanation for Small Repeating Earthquakes at Parkfield. *Bulletin of the Seismological Society of America*, *91*(2), 401–403.

Araki, E., Saffer, D. M., Kopf, A., Wallace, L. M., Kimura, T., Machida, Y., & Ide, S. (2017). Recurring and triggered slow-slip events near the trench at the Nankai Trough subduction megathrust. *Science*, *356*, 1157–1160.

Audet, P., Bostock, M. G., Christensen, N. I., & Peacock, S. M. (2009). Seismic evidence for overpressured subducted oceanic crust and megathrust fault sealing. *Nature*, *457*, 76–78. https://doi.org/10.1038/nature07650

Avouac, J.-P. (2011). The lessons of Tohoku-Oki. *Nature*, *475*, 300–301. https://doi.org/10.1029/2009gl039276

Avouac, J.-P. (2015). From Geodetic Imaging of Seismic and Aseismic Fault Slip to Dynamic Modeling of the Seismic Cycle. *Annual Review of Earth and Planetary Sciences*, *43*(1), 233–271. https://doi.org/10.1146/annurev-earth-060614-105302

Baba, S., Obara, K., Takemura, S., Takeo, A., & Abers, G. (2021). Shallow Slow Earthquake Episodes Near the Trench Axis off Costa Rica. *Journal of Geophysical Research : Solid Earth*, *126*. https://doi.org/10.1029/2021JB021706

Bablon, M. (2018). *Reconstruction de l'histoire des volcans de l'arc équatorien : contraintes pour l'évolution chronologique de l'arc andin et pour l'évaluation du risque volcanique*. Uni- versité Paris Saclay (COmUE).

Baisch, S., Ceranna, L., & Harjes, H. (2008). Earthquake Cluster: What Can We Learn from Waveform Similarity? *Bulletin of the Seismological Society of America*, *98*(6), 2806–2814. https://doi.org/10.1785/0120080018

Baltay, A. S., Hanks, T. C., & Beroza, G. C. (2013). Stable Stress-Drop Measurements and their Variability: Implications for Ground-Motion Prediction. *Bulletin of the Seismological Society of America*, *103*(1), 211–222. https://doi.org/10.1785/0120120161

Barnes, P. M., Wallace, L. M., Saffer, D. M., Bell, R. E., Underwood, M. B., Fagereng, A., Meneghini, F., Savage, H. M., Rabinowitz, H. S., Morgan, J. K., Kitajima, H., Kutterolf, S., Hashimoto, Y., Oliveira, C. H. E. De, Noda, A., Crundwell, M. P., Shepherd, C. L., Woodhouse, A. D., Harris, R.

N., … LeVay, L. J. (2020). Slow slip source characterized by lithological and geometric heterogeneity. *Science Advances*, *6*.

Bartlow, N. M., Wallace, L. M., Beavan, J., Bannister, S., & Segall, P. (2014). Time-dependent modeling of slow slip events and associated seismicity and tremor at the Hikurangi subduction zone, New Zealand. *Journal of Geophysical Research : Solid Earth*, *119*, 734–753. https://doi.org/10.1002/2013JB010609.1.

Beaucé, E., Frank, W. B., & Romanenko, A. (2017). Fast Matched Filter (FMF): An Efficient Seismic Matched-Filter Search for Both CPU and GPU Architectures. *Seismological Research Letters*, *89*(1), 165–172. https://doi.org/10.1785/0220170181

Beauval, C., Yepes, H., Bakun, W. H., Egred, J., Alvarado, A., & Singaucho, J. C. (2010). Locations and magnitudes of historical earthquakes in the Sierra of Ecuador (1587–1996). *Geophysical Journal International*, *181*, 1613–1633. https://doi.org/10.1111/j.1365-246X.2010.04569.x

Beauval, C., Yepes, H., Palacios, P., Segovia, M., Alvarado, A., Font, Y., Aguilar, J., Troncoso, L., & Vaca, S. (2013). An Earthquake Catalog for Seismic Hazard Assessment in Ecuador. *Bulletin of the Seismological Society of America*, *103*(2A), 773–786. https://doi.org/10.1785/0120120270

Beck, S. L., & Ruff, J. (1984). The Rupture Process of the Gmat 1979 Colombia Earthquake: Evidence for the Asperity Model. *Journal of Geophysical Research*, *89*(B11), 9281–9291.

Beeler, N. M., Lockner, D. L., & Hickman, S. H. (2001). A Simple Stick-Slip and Creep-Slip Model for Repeating Earthquakes and its Implication for Microearthquakes at Parkfield. *Bulletin of the Seismological Society of America*, *91*(6), 1797–1804.

Bilek, S. L. (2007). Using Earthquake Source Durations along the Sumatra – Andaman Subduction System to Examine Fault-Zone Variations. *Bulletin of the Seismological Society of America*, *97*(1), 62–70. https://doi.org/10.1785/0120050622

Bilek, S. L. (2010). Invited review paper: Seismicity along the South American subduction zone: Review of large earthquakes, tsunamis, and subduction zone complexity. *Tectonophysics*, *495*(1–2), 2–14. https://doi.org/10.1016/j.tecto.2009.02.037

Bilek, S. L., & Lay, T. (2002). Tsunami earthquakes possibly widespread manifestations of frictional conditional stability. *Geophysical Research Letters*, *29*(14).

Bilek, S. L., & Lay, T. (2018). Subduction zone megathrust earthquakes. *Geosphere*, *14*(4), 1468–1500. https://doi.org/10.1130/GES01608.1

Bindi, D., Spallarossa, D., Picozzi, M., & Morasca, P. (2020). Reliability of Source Parameters for Small Events in Central Italy : Insights from Spectral Decomposition Analysis Applied to Both Synthetic and Real Data. *Bulletin of the Seismological Society of America*, *110*(6). https://doi.org/10.1785/0120200126

Boatwright, J. (1980). A spectral theory for circular seismic sources; simple estimates of source dimension, dynamic stress drop, and radiated seismic energy. *Bulletin of the Seismological Society of America*, *70*(1).

Boore, D. M., & Boatwright, J. (1984). Average body-wave radiation coefficients. *Bulletin of the Seismological Society of America*, *74*(5), 1615–1621.

Boyd, O. S., Mcnamara, D. E., Hartzell, S., & Choy, G. (2017). Influence of Lithostatic Stress on Earthquake Stress Drops in North America. *Bulletin of the Seismological Society of America*, *107*(2), 856–868. https://doi.org/10.1785/0120160219

Brune, J. N. (1970). Tectonic Stress and the Spectra of Seismic Shear Waves from Earthquakes. *Journal of Geophysical Research*, *75*(26).

Bürgmann, R. (2018). The geophysics, geology and mechanics of slow fault slip. *Earth and Planetary Science Letters*, *495*, 112–134. https://doi.org/10.1016/j.epsl.2018.04.062

Calahorrano, A., Sallarès, V., Collot, J.-Y., Sage, F., & Ranero, C. R. (2008). Nonlinear variations of

the physical properties along the southern Ecuador subduction channel: Results from depth-migrated seismic data. *Earth and Planetary Science Letters*, *267*(3–4), 453–467. https://doi.org/10.1016/j.epsl.2007.11.061

Cauchie, L., Lengliné, O., & Schmittbuhl, J. (2020). Seismic asperity size evolution during fluid injection: case study of the 1993 Soultz-sous-Forêts injection. *Geophysical Journal International*, *221*, 968–980. https://doi.org/10.1093/gji/ggaa051

Cerchiari, A., Remitti, F., Mittempergher, S., Festa, A., Lugli, F., & Cipriani, A. (2020). Cyclical variations of fluid sources and stress state in a shallow megathrust-zone mélange. *Journal of the Geological Society*, *177*(3), 647–659. https://doi.org/10.1144/jgs2019-072

Chalumeau, C., Agurto-detzel, H., De Barros, L., Charvis, P., Galve, A., Rietbrock, A., Alvarado, A., Hernandez, S., Beck, S. L., Font, Y., Hoskins, M. C., León-Ríos, S., Meltzer, A., Lynner, C., Rolandone, F., Nocquet, J.-M., Régnier, M., Ruiz, M., Soto-cordero, L., … Segovia, M. (2021). Repeating Earthquakes at the Edge of the Afterslip of the 2016 Ecuadorian Mw 7.8 Pedernales Earthquake. *Journal of Geophysical Research: Solid Earth*, *126*. https://doi.org/10.1029/2021JB021746

Chaussard, E., Bürgmann, R., Fattahi, H., Johnson, C. W., Nadeau, R. M., Taira, T., & Johanson, I. (2015). Interseismic coupling and refined earthquake potential on the Hayward-Calaveras fault zone. *Journal of Geophysical Research: Solid Earth*, *120*, 8570–8590. https://doi.org/10.1002/2015JB012230.Received

Chaves, E. J., Schwartz, S. Y., & Abercrombie, R. E. (2020). Repeating earthquakes record fault weakening and healing in areas of megathrust postseismic slip. *Science Advances*, *6*. https://doi.org/10.1126/sciadv.aaz9317

Chemenda, A., Lallemand, S., & Bokun, A. (2000). Strain partitioning and interplate friction in oblique subduction zones: Constraints provided by experimental modeling. *Journal of Geophysical Research*, *105*(B3), 5567–5581.

Chen, K. H., Bürgmann, R., & Nadeau, R. M. (2010). Triggering Effect of M 4-5 Earthquakes on the Earthquake Cycle of Repeating Events at Parkfield, California. *Bulletin of the Seismological Society of America*, *100*(2), 522–531. https://doi.org/10.1785/0120080369

Chen, K. H., Bürgmann, R., & Nadeau, R. M. (2013). Do earthquakes talk to each other? Triggering and interaction of repeating sequences at Parkfield. *Journal of Geophysical Research: Solid Earth*, *118*(1), 165–182. https://doi.org/10.1029/2012JB009486

Chen, K. H., Bürgmann, R., Nadeau, R. M., Chen, T., & Lapusta, N. (2010). Postseismic variations in seismic moment and recurrence interval of repeating earthquakes. *Earth and Planetary Science Letters*, *299*, 118–125. https://doi.org/10.1016/j.epsl.2010.08.027

Chen, K. H., Chen, I., & Kim, A. (2016). Can slip heterogeneity be linked to earthquake recurrence? *Geophysical Research Letters*, *43*(13), 6916–6923. https://doi.org/10.1002/2016GL069516.Received

Chen, K. H., Nadeau, R. M., & Rau, R.-J. (2007). Towards a universal rule on the recurrence interval scaling of repeating earthquakes? *Geophysical Research Letters*, *34*(16), 1–5. https://doi.org/10.1029/2007GL030554

Chen, K. H., Nadeau, R. M., & Rau, R.-J. (2008). Characteristic repeating earthquakes in an arc-continent collision boundary zone: The Chihshang fault of eastern Taiwan. *Earth and Planetary Science Letters*, *276*(3–4), 262–272. https://doi.org/10.1016/j.epsl.2008.09.021

Chen, T., & Lapusta, N. (2009). Scaling of small repeating earthquakes explained by interaction of seismic and aseismic slip in a rate and state fault model. *Journal of Geophysical Research: Solid Earth*, *114*(1), 1–12. https://doi.org/10.1029/2008JB005749

Chen, X., & Shearer, P. M. (2013). California foreshock sequences suggest aseismic triggering process. *Geophysical Research Letters*, *40*, 2602–2607. https://doi.org/10.1002/grl.50444

Chlieh, M., Mothes, P. A., Nocquet, J.-M., Jarrín, P., Charvis, P., Cisneros, D., Font, Y., Collot, J.-Y., Villegas-Lanza, J. C., Rolandone, F., Vallée, M., Régnier, M., Segovia, M., Martin, X., & Yepes, H. (2014). Distribution of discrete seismic asperities and aseismic slip along the Ecuadorian megathrust. *Earth and Planetary Science Letters*, *400*, 292–301. https://doi.org/10.1016/j.epsl.2014.05.027

Clift, P., & Vannucchi, P. (2004). Controls on tectonic accretion versus erosion in subduction zones: implications for the origin and recycling of the continental crust. *Review of Geophysics*, *42*. https://doi.org/10.1029/2003RG000127.1.INTRODUCTION

Collettini, C., Niemeijer, A., Viti, C., Smith, S. A. F., & Marone, C. (2011). Fault structure, frictional properties and mixed-mode fault slip behavior. *Earth and Planetary Science Letters*, *311*(3–4), 316–327. https://doi.org/10.1016/j.epsl.2011.09.020

Collot, J.-Y., Agudelo, W., Ribodetti, A., & Marcaillou, B. (2008). Origin of a crustal splay fault and its relation to the seismogenic zone and underplating at the erosional north Ecuador–south Colombia oceanic margin. *Journal of Geophysical Research*, *113*. https://doi.org/10.1029/2008JB005691

Collot, J.-Y., Charvis, P., Gutscher, M. A., & Operto, S. (2002). Exploring the Ecuador-Colombia Active Margin and Interplate Seismogenic Zone. *Eos*, *83*(17), 185–190.

Collot, J.-Y., Marcaillou, B., Sage, F., Michaud, F., Agudelo, W., Charvis, P., Graindorge, D., Gutscher, M. A., & Spence, G. (2004). Are rupture zone limits of great subduction earthquakes controlled by upper plate structures ? Evidence from multichannel seismic reflection data acquired across the northern Ecuador – southwest Colombia margin. *Journal of Geophysical Research*, *109*(11), 1–14. https://doi.org/10.1029/2004JB003060

Collot, J.-Y., Sanclemente, E., Nocquet, J.-M., Leprêtre, A., Ribodetti, A., Jarrín, P., Chlieh, M., Graindorge, D., & Charvis, P. (2017). Subducted oceanic relief locks the shallow megathrust in central Ecuador. *Journal of Geophysical Research: Solid Earth*, *122*, 3286–3305. https://doi.org/10.1002/2016JB013849

Demets, C. (1995). Plate motions and crustal deformation. *Review of Geophysics*, 365–369.

Den Hartog, S. A. M., Peach, C. J., Matthijs De Winter, D. A., Spiers, C. J., & Shimamoto, T. (2012). Frictional properties of megathrust fault gouges at low sliding velocities: New data on effects of normal stress and temperature. *Journal of Structural Geology*, *38*, 156–171. https://doi.org/10.1016/j.jsg.2011.12.001

Dessa, J.-X., Klingelhoefer, F., Graindorge, D., André, C., Permana, H., Gutscher, M. A., Chauhan, A., Singh, S. C., & Team, S.-O. S. (2009). Megathrust earthquakes can nucleate in the forearc mantle: Evidence from the 2004 Sumatra event. *Geological Society of America*, *37*(7), 659–662. https://doi.org/10.1130/G25653A.1

Dominguez, L. A., Taira, T., & Santoyo, M. A. (2016). Spatiotemporal variations of characteristic repeating earthquake sequences along the Middle America Trench in Mexico. *Journal of Geophysical Research: Solid Earth*, *121*(12), 8855–8870. https://doi.org/10.1002/2016JB013242

Drouet, S., Bouin, M.-P., & Cotton, F. (2011). New moment magnitude scale, evidence of stress drop magnitude scaling and stochastic ground motion model for the French West Indies. *Geophysical Journal International*, *187*, 1625–1644. https://doi.org/10.1111/j.1365-246X.2011.05219.x

Duverger, C., Lambotte, S., Bernard, P., Lyon-caen, H., Deschamps, A., & Nercessian, A. (2018). Dynamics of microseismicity and its relationship with the active structures in the western Corinth Rift (Greece). *Geophysical Journal International*, *215*(1), 196–221. https://doi.org/10.1093/gji/ggy264

Dziewonski, A. M., Chou, T., & Woodhouse, J. H. (1981). Determination of Earthquake Source Parameters From Waveform Data for Studies of Global and Regional Seismicity. *Journal of Geophysical Research*, *86*(B4), 2825–2852.

Eguez, A., Alvarado, A., Yepes, H., Machette, M. N., Costa, C., & Dart, R. L. (2003). *Database and Map of Quaternary faults and folds of Ecuador and its offshore regions*.

Ekström, G., Nettles, M., & Dziewonski, A. M. (2012). The global CMT project 2004–2010: Centroid-moment tensors for 13,017 earthquakes. *Physics of the Earth and Planetary Interiors*, *201*. https://doi.org/10.1016/j.pepi.2012.04.002

Ellsworth, W. L. (1995). Characteristic earthquakes and long-term earthquake forecasts: implications of central California seismicity. In *Urban Disaster Mitigation: The Role of Engineering and Technology*.

Eshelby, J. D. (1957). The determination of the elastic field of an ellipsoidal inclusion, and related problems. *Proceedings of the Royal Society of London*, 376–396.

Fagereng, Å., & Sibson, R. H. (2010). Mélange rheology and seismic style. *Geology*, *38*(8), 751–754. https://doi.org/10.1130/G30868.1

Fitch, T. J. (1972). Plate Convergence, Transcurrent Faults, and Internal Deformation Adiacent to Southeast Asia and the Western Pacific. *Journal of Geophysical Research*, *77*(23), 4432–4460.

Font, Y., Segovia, M., Vaca, S., & Theunissen, T. (2013). Seismicity patterns along the Ecuadorian subduction zone: new constraints from earthquake location in a 3-D a priori velocity model. *Geophysical Journal International*, *193*(1), 263–286. https://doi.org/10.1093/gji/ggs083

Frank, W. B., & Abercrombie, R. E. (2018). Short Note Adapting the Matched-Filter Search to a Wide-Aperture Network: An Aftershock Sequence and an Earthquake Swarm in Connecticut. *Bulletin of the Seismological Society of America*, *108*(1), 524–532. https://doi.org/10.1785/0120170190

Frank, W. B., Poli, P., & Perfettini, H. (2017). Mapping the rheology of the Central Chile subduction zone with aftershocks. *Geophysical Research Letters*, *44*(11), 5374–5382. https://doi.org/10.1002/2016GL072288

Gailler, A., Charvis, P., & Flueh, E. R. (2007). Segmentation of the Nazca and South American plates along the Ecuador subduction zone from wide angle seismic profiles. *Earth and Planetary Science Letters*, *260*(3–4), 444–464. https://doi.org/10.1016/j.epsl.2007.05.045

Gao, D., Kao, H., & Wang, B. (2021). Misconception of Waveform Similarity in the Identification of Repeating Earthquakes. *Geophysical Research Letters*, *48*. https://doi.org/10.1029/2021GL092815

Geller, R., & Mueller, C. (1980). Four similar earthquakes in central California. *Geophysical Research Letters*, *7*(10), 821–824.

Gibbons, S. J., Bøttger, M., Harris, D. B., & Ringdal, F. (2007). The detection and location of low magnitude earthquakes in northern Norway using multi-channel waveform correlation at regional distances. *Physics of the Earth and Planetary Interiors*, *160*, 285–309. https://doi.org/10.1016/j.pepi.2006.11.008

Goertz-Allmann, B. P., Goertz, A., & Wiemer, S. (2011). Stress drop variations of induced earthquakes at the Basel geothermal site. *Geophysical Research Letters*, *38*. https://doi.org/10.1029/2011GL047498

Gombert, B., Duputel, Z., Jolivet, R., Simons, M., Jiang, J., Liang, C., Fielding, E. J., & Rivera, L. (2018). Strain budget of the Ecuador–Colombia subduction zone: A stochastic view. *Earth and Planetary Science Letters*, *498*, 288–299. https://doi.org/10.1016/j.epsl.2018.06.046

Graindorge, D., Calahorrano, A., Charvis, P., Collot, J., & Bethoux, N. (2004). Deep structures of the Ecuador convergent margin and the Carnegie Ridge, possible consequence on great earthquakes recurrence interval. *Geophysical Research Letters*, *31*(4), L04603. https://doi.org/10.1029/2003GL018803

Grevemeyer, I., Ranero, C. R., & Ivandic, M. (2018). Structure of oceanic crust and serpentinization at subduction trenches. *Geosphere*, *14*(2), 395–418. https://doi.org/10.1130/GES01537.1

Guillier, B., Chatelain, J.-L., Jaillard, E., Yepes, H., Poupinet, G., & Fels, J. F. (2001). Seismological evidence on the geometry of the orogenic system in central-northern Ecuador (South America). *Geophysical Research Letters*, *28*(19), 3749–3752.

Haberland, C., Rietbrock, A., Lange, D., Bataille, K., & Dahm, T. (2009). Structure of the seismogenic zone of the southcentral Chilean margin revealed by local earthquake traveltime tomography. *Journal of Geophysical Research*, *114*. https://doi.org/10.1029/2008JB005802

Han, L., Wu, Z., Li, Y., & Jiang, C. (2014). Cross-correlation Coefficients for the Study of Repeating Earthquakes: An Investigation of Two Empirical Assumptions/Conventions in Seismological Interpretation Practice. *Pure and Applied Geophysics*, *171*, 425–437. https://doi.org/10.1007/s00024-012-0515-3

Hanks, T. C., & Kanamori, H. (1979). A Moment Magnitude Scale. *Journal of Geophysical Research*, *84*, 2348–2350. https://doi.org/10.1029/JB084iB05p02348

Hardebeck, J. L., & Aron, A. (2009). Earthquake Stress Drops and Inferred Fault Strength on the Hayward Fault, East San Francisco Bay, California. *Bulletin of the Seismological Society of America*, *99*(3), 1801–1814. https://doi.org/10.1785/0120080242

Hatakeyama, N., Uchida, N., Matsuzawa, T., & Nakamura, W. (2017). Emergence and disappearance of interplate repeating earthquakes following the 2011 M9.0 Tohoku-oki earthquake: Slip behavior transition between seismic and aseismic depending on the loading rate. *Journal of Geophysical Research: Solid Earth*, *122*(7), 5160–5180. https://doi.org/10.1002/2016JB013914

Hayes, G. P., Wald, D. J., & Johnson, R. L. (2012). Slab1.0: A three-dimensional model of global subduction zone geometries. *Journal of Geophysical Research*, *117*. https://doi.org/10.1029/2011JB008524

Hensen, C., Wallmann, K., Schmidt, M., Ranero, C. R., & Suess, E. (2004). Fluid expulsion related to mud extrusion off Costa Rica — A window to the subducting slab. *Geology*, *32*(3), 201–204. https://doi.org/10.1130/G20119.1

Hernandez Salazar, M. J. (2020). *Evolution of the forearc basins in Ecuador : from the accretion of oceanic allochthonous terranes to the uplift of the Andes and Coastal Cordilleras*. Sorbonne Université.

Heuret, A. (2005). *Dynamique des zones de subduction: étude statistique globale et approche analogique*. Université Montpellier II.

Hicks, S. P., Rietbrock, A., Ryder, I. M. A., Lee, C., & Miller, M. (2014). Anatomy of a megathrust: The 2010 M8.8 Maule, Chile earthquake rupture zone imaged using seismic tomography. *Earth and Planetary Science Letters*, *405*, 142–155. https://doi.org/10.1016/j.epsl.2014.08.028

Hirose, H., Kimura, H., Enescu, B., & Aoi, S. (2012). Recurrent slow slip event likely hastened by the 2011 Tohoku earthquake. *Earth, Atmospheric, and Planetary Sciences*, *109*(38), 15157–15161. https://doi.org/10.1073/pnas.1202709109

Hobbs, T. E., Kyriakopoulos, C., Newman, A. V, Protti, M., & Yao, D. (2017). Large and primarily updip afterslip following the 2012 Mw 7.6 Nicoya, Costa Rica, earthquake. *Journal of Geophysical Research: Solid Earth*, *122*, 5712–5728. https://doi.org/10.1002/2017JB014035

Hoffmann-Rothe, A., Kukowski, N., Dresen, G., Echtler, H., Oncken, O., Klotz, J., Scheuber, E., & Kellner, A. (2006). Oblique Convergence along the Chilean Margin: Partitioning, Margin-Parallel Faulting and Force Interaction at the Plate Interface. In *The Andes* (pp. 125–146).

Holtkamp, S. G., Pritchard, M. E., & Lohman, R. B. (2011). Earthquake swarms in South America. *Geophysical Journal International*, *187*, 128–146. https://doi.org/10.1111/j.1365-246X.2011.05137.x

Hoskins, M. C., Meltzer, A., Font, Y., Agurto-detzel, H., Vaca, S., Rolandone, F., Nocquet, J.-M., Soto-cordero, L., Stachnik, J. C., Beck, S. L., Lynner, C., Ruiz, M., Alvarado, A., Hernandez, S., Charvis, P., Regnier, M., León-Ríos, S., & Rietbrock, A. (2021). Triggered crustal earthquake

swarm across subduction segment boundary after the 2016 Pedernales, Ecuador megathrust earthquake. *Earth and Planetary Science Letters*, *553*(116620). https://doi.org/10.1016/j.epsl.2020.116620

Hough, S. E. (1997). Empirical Green's function analysis: Taking the next step. *Journal of Geophysical Research*, *102*, 5369–5384.

Huang, H., Xu, W., Meng, L., Bürgmann, R., Carlos Baez, J., & Baez, J. C. (2017). Early aftershocks and afterslip surrounding the 2015 Mw 8.4 Illapel rupture. *Earth and Planetary Science Letters*, *457*, 282–291. https://doi.org/10.1016/j.epsl.2016.09.055

Huang, Y., Ellsworth, W. L., & Beroza, G. C. (2017). Stress drops of induced and tectonic earthquakes in the central United States are indistinguishable. *Science Advances*, *3*.

Hughes, L. G., Chamberlain, C. J., Townend, J., & Thomas, A. (2021). A Repeating Earthquake Catalog From 2003 to 2020 for the Raukumara Peninsula, Northern Hikurangi Subduction Margin, New Zealand. *Geochemistry, Geophysics, Geosystems*, *22*. https://doi.org/10.1029/2021GC009670

Husen, S., & Kissling, E. (2001). Postseismic fluid flow after the large subduction earthquake of Antofagasta, Chile. *Geology*, *29*(9), 847–850.

Husen, S., Kissling, E., & Quintero, R. (2002). Tomographic evidence for a subducted seamount beneath the Gulf of Nicoya, Costa Rica: The cause of the 1990 Mw = 7.0 Gulf of Nicoya earthquake. *Geophysical Research Letters*, *29*(8).

Hyndman, R. D., Yamano, M., & Oleskvich, D. A. (1997). The seismogenic zone of subduction thrust faults. *The Island Arc*, *6*, 244–260.

Ide, S., Beroza, G. C., Prejean, S. G., & Ellsworth, W. L. (2003). Apparent break in earthquake scaling due to path and site effects on deep borehole recordings. *Journal of Geophysical Research*, *108*(B5). https://doi.org/10.1029/2001JB001617

Ide, S., Beroza, G. C., Shelly, D. R., & Uchide, T. (2007). A scaling law for slow earthquakes. *Nature Letters*, *447*, 76–79. https://doi.org/10.1038/nature05780

Igarashi, T. (2020). Catalog of small repeating earthquakes for the Japanese Islands. *Earth, Planets and Space*. https://doi.org/10.1186/s40623-020-01205-2

Igarashi, T., Matsuzawa, T., & Hasegawa, A. (2003). Repeating earthquakes and interplate aseismic slip in the northeastern Japan subduction zone. *Journal of Geophysical Research*, *108*(B5), 1–9. https://doi.org/10.1029/2002JB001920

Iinuma, T., Hino, R., Uchida, N., Nakamura, W., Kido, M., Osada, Y., & Miura, S. (2016). Seafloor observations indicate spatial separation of coseismic and postseismic slips in the 2011 Tohoku earthquake. *Nature Communications*, *7*. https://doi.org/10.1038/ncomms13506

Ikari, M. J., Niemeijer, A. R., Spiers, C. J., Kopf, A. J., & Saffer, D. M. (2013). Experimental evidence linking slip instability with seafloor lithology and topography at the Costa Rica convergent margin. *Geology*, *41*(8), 891–894. https://doi.org/10.1130/G33956.1

Jaillard, E., Lapierre, H., Ordoñez, M., Alava, J. T., Amortegui, A., & Vanmelle, J. (2009). Accreted oceanic terranes in Ecuador : Southern edge of the Caribbean plate ? *Geological Society Special Publication*, *328*, 469–485.

Jarrard, R. D. (1986). Relations Among Subduction Parameters. *Review of Geophysics*, *24*(2), 217–284.

Jiménez, C., Saavedra, M., & Moreno, N. (2021). Seismic source characteristics of the 2016 Pedernales-Ecuador earthquake (Mw 7.8). *Physics of the Earth and Planetary Interiors*, *312*. https://doi.org/10.1016/j.pepi.2021.106670

Kanamori, H. (2006). Lessons from the 2004 Sumatra–Andaman earthquake. *Philosophical Transactions Royal Society*, *364*, 1927–1945. https://doi.org/10.1098/rsta.2006.1806

Kanamori, H., & McNally, K. (1982). Variable rupture mode of the subduction zone along the Ecuador-

Colombia coast. *Bulletin of the Seismological Society of America*, *72*(4), 1241–1253.

Kaneko, Y., & Shearer, P. M. (2014). Seismic source spectra and estimated stress drop derived from cohesive-zone models of circular subshear rupture. *Geophysical Journal International*, *197*, 1002–1015. https://doi.org/10.1093/gji/ggu030

Kaneko, Y., & Shearer, P. M. (2015). Variability of seismic source spectra, estimated stress drop, and radiated energy, derived from cohesive-zonemodels of symmetrical and asymmetrical circular and elliptical ruptures. *Journal of Geophysical Research: Solid Earth*, *120*, 1053–1079. https://doi.org/10.1002/2014JB011642.Received

Kato, A., Fukuda, J., Kumazawa, T., & Nakagawa, S. (2016). Accelerated nucleation of the 2014 Iquique, Chile Mw 8.2 Earthquake. *Nature*, *6*. https://doi.org/10.1038/srep24792

Kato, A., & Igarashi, T. (2012). Regional extent of the large coseismic slip zone of the 2011 Mw 9.0 Tohoku-Oki earthquake delineated by on-fault aftershocks. *Geophysical Research Letters*, *39*, 2–7. https://doi.org/10.1029/2012GL052220

Kato, A., & Nakagawa, S. (2014). Multiple slow-slip events during a foreshock sequence of the 2014 Iquique, Chile Mw 8.1 earthquake. *Geophysical Research Letters*, *41*, 5420–5427. https://doi.org/10.1002/2014GL061138.Received

Kato, A., Obara, K., Igarashi, T., Tsuruoka, H., Nakagawa, S., & Hirata, N. (2012). Propagation of Slow Slip Leading Up to the 2011 Mw 9.0 Tohoku-Oki Earthquake. *Science*, *335*, 705–709.

Kawamura, M., & Chen, K. H. (2017). Influences on the location of repeating earthquakes determined from a and b value imaging. *Geophysical Research Letters*, *44*(1), 6675–6682. https://doi.org/10.1002/2017GL073335.Received

Kelleher, J. A. (1972). Rupture zones of large South American earthquakes and some predictions. *Journal of Geophysical Research*, *77*(11), 2087–2103.

Kelly, C. M., Rietbrock, A., Faulkner, D. R., & Nadeau, R. M. (2013). Temporal changes in attenuation associated with the 2004 M6.0 Parkfield earthquake. *Journal of Geophysical Research*, *118*, 630–645. https://doi.org/10.1002/jgrb.50088

Khoshmanesh, M., Shirzaei, M., & Nadeau, R. M. (2015). Time-dependent model of aseismic slip on the central San Andreas Fault from InSAR time series and repeating earthquakes. *Journal of Geophysical Research: Solid Earth*, *120*, 6658–6679. https://doi.org/10.1002/2015JB012039.Received

Kirkpatrick, J. D., Edwards, J. H., Verdecchia, A., Kluesner, J. W., Harrington, R. M., & Silver, E. A. (2020). Subduction megathrust heterogeneity characterized from 3D seismic data. *Nature Geoscience*, *13*, 369–374. https://doi.org/10.1038/s41561-020-0562-9

Koch, C. D., Lynner, C., Delph, J., Beck, S. L., Meltzer, A., Font, Y., Soto-cordero, L., Hoskins, M. C., Stachnik, J. C., Ruiz, M., Alvarado, A., Agurto-Detzel, H., Charvis, P., Regnier, M., & Rietbrock, A. (2020). Structure of the Ecuadorian forearc from the joint inversion of receiver functions and ambient noise surface waves. *Geophysical Journal International*, *222*, 1671–1685. https://doi.org/10.1093/gji/ggaa237

Lay, T., & Bilek, S. L. (2007). Anomalous Earthquake Ruptures at Shallow Depths on Subduction Zone Megathrusts. In T. H. Dixon & C. Moore (Eds.), *The Seismogenic Zone of Subduction Thrust Faults* (pp. 476–511). Columbia University Press.

Lay, T., Kanamori, H., Ammon, C. J., Koper, K. D., Hutko, A. R., Ye, L., Yue, H., & Rushing, T. M. (2012). Depth-varying rupture properties of subduction zone megathrust faults. *Journal of Geophysical Research*, *117*. https://doi.org/10.1029/2011JB009133

Lay, T., & Schwartz, S. Y. (2004). Comment on " Coupling Semantics and. *Eos*, *85*(36), 339–340. https://doi.org/10.1029/2003

Lengliné, O., Lamourette, L., Vivin, L., Cuenot, N., & Schmittbuhl, J. (2014). Fluid-induced

earthquakes with variable stress drop. *Journal of Geophysical Research : Solid Earth*, *119*, 1–14. https://doi.org/10.1002/2014JB011282.Received

Lengliné, O., & Marsan, D. (2009). Inferring the coseismic and postseismic stress changes caused by the 2004 Mw=6 Parkfield earthquake from variations of recurrence times of microearthquakes. *Journal of Geophysical Research*, *114*(10), 1–19. https://doi.org/10.1029/2008JB006118

León-Ríos, S., Agurto-Detzel, H., Rietbrock, A., Alvarado, A., Beck, S. L., Charvis, P., Edwards, B., Font, Y., Garth, T., Hoskins, M. C., Lynner, C., Meltzer, A., Matthieu, J., Régnier, M., Rolandone, F., Ruiz, M., & Soto-cordero, L. (2019). Tectonophysics 1D-velocity structure and seismotectonics of the Ecuadorian margin inferred from the 2016 Mw7 . 8 Pedernales aftershock sequence. *Tectonophysics*, *767*(July), 228165. https://doi.org/10.1016/j.tecto.2019.228165

León-ríos, S., Bie, L., Agurto-detzel, H., Rietbrock, A., Galve, A., Alvarado, A., Beck, S. L., Charvis, P., Font, Y., Hidalgo, S., Hoskins, M. C., Laigle, M., Oregioni, D., Meltzer, A., Ruiz, M., & Woollam, J. (2021). 3D Local Earthquake Tomography of the Ecuadorian Margin in the Source Area of the 2016 Mw 7.8 Pedernales Earthquake. *Journal of Geophysical Research: Solid Earth*, *126*. https://doi.org/10.1029/2020JB020701

Lin, Y., & Lapusta, N. (2018). Microseismicity Simulated on Asperity-Like Fault Patches : On Scaling of Seismic Moment With Duration and Seismological Estimates of Stress Drops. *Geophysical Research Letters*, *45*, 8145–8155. https://doi.org/10.1029/2018GL078650

Liu, Y., & Rice, J. R. (2007). Spontaneous and triggered aseismic deformation transients in a subduction fault model. *Journal of Geophysical Research*, *112*. https://doi.org/10.1029/2007JB004930

Lomax, A., Virieux, J., Volant, P., & Berge-thierry, C. (2000). *Probabilistic earthquake location in 3D and layered models*.

Lonsdale, P. (2005). Creation of the Cocos and Nazca plates by fission of the Farallon plate. *Tectonophysics*, *404*, 237–264. https://doi.org/10.1016/j.tecto.2005.05.011

Lonsdale, P., & Klitgord, K. D. (1978). Structure and tectonic history of the eastern Panama Basin. *Geological Society of America Bulletin*, *89*, 981–999.

Lowry, A. R. (2006). Resonant slow fault slip in subduction zones forced by climatic load stress. *Nature Letters*, *442*. https://doi.org/10.1038/nature05055

Luzieux, L. D. A., Heller, F., Spikings, R., Vallejo, C. F., & Winkler, W. (2006). Origin and Cretaceous tectonic history of the coastal Ecuadorian forearc between 1°N and 3°S: Paleomagnetic, radiometric and fossil evidence. *Earth and Planetary Science Letters*, *249*, 400–414. https://doi.org/10.1016/j.epsl.2006.07.008

Lynner, C., Koch, C. D., Beck, S. L., Meltzer, A., Soto-Cordero, L., Hoskins, M. C., Stachnik, J. C., Ruiz, M., Alvarado, A., Charvis, P., Font, Y., Régnier, M., Agurto-Detzel, H., Rietbrock, A., Porritt, R. W., Regnier, M., Agurto-Detzel, H., Rietbrock, A., & Porritt, R. W. (2020). Upper-plate structure in Ecuador coincident with the subduction of the Carnegie Ridge and the southern extent of large mega-thrust earthquakes. *Geophysical Journal International*, *220*, 1965–1977.

Magee, M. E., & Zoback, M. D. (1993). Evidence for a weak interplate thrust fault along the northern Japan subduction zone and implications for the mechanics of thrust faulting and fluid expulsion. *Geology*, *21*, 809–812.

Manchuel, K., Régnier, M., Béthoux, N., Font, Y., Sallarès, V., Díaz, J., & Yepes, H. (2011). New insights on the interseismic active deformation along the North Ecuadorian – South Colombian (NESC) margin. *Tectonics*, *30*. https://doi.org/10.1029/2010TC002757

Marcaillou, B., Collot, J., Ribodetti, A., D'Acremont, E., Mahamat, A., & Alvarado, A. (2016). Seamount subduction at the North-Ecuadorian convergent margin: Effects on structures, inter-seismic coupling and seismogenesis. *Earth and Planetary Science Letters*, *433*, 146–158. https://doi.org/10.1016/j.epsl.2015.10.043

Marcaillou, B., Spence, G., Collot, J., & Wang, K. (2006). Thermal regime from bottom simulating

reflectors along the north Ecuador–south Colombia margin: Relation to margin segmentation and great subduction earthquakes. *Journal of Geophysical Research*, *111*. https://doi.org/10.1029/2005JB004239

Marcaillou, B., Spence, G., Wang, K., Collot, J., & Ribodetti, A. (2008). Thermal segmentation along the N.Ecuador–S.Colombia margin (1–4°N): Prominent influence of sedimentation rate in the trench. *Earth and Planetary Science Letters*, *272*, 296–308. https://doi.org/10.1016/j.epsl.2008.04.049

Marone, C. (1998). Laboratory-Derived Friction Laws and Their Application To Seismic Faulting. *Annual Review of Earth and Planetary Sciences*, *26*(1), 643–696. https://doi.org/10.1146/annurev.earth.26.1.643

Marone, C., Vidale, J. E., & Ellsworth, W. L. (1995). Fault healing inferred from time dependent variations in source properties of repeating earthquakes. *Geophysical Research Letters*, *22*(22), 3095–3098.

Matsubara, M., Yagi, Y., & Obara, K. (2005). Plate boundary slip associated with the 2003 Off-Tokachi earthquake based on small repeating earthquake data. *Geophysical Research Letters*, *32*(8), 1–4. https://doi.org/10.1029/2004GL022310

Mavrommatis, A. P., Segall, P., Uchida, N., & Johnson, K. M. (2015). Long-term acceleration of aseismic slip preceding the Mw 9 Tohoku-oki earthquake: Constraints from repeating earthquakes. *Geophysical Research Letters*, *42*, 9717–9725. https://doi.org/10.1002/2015GL066069.1.

Meltzer, A., Beck, S. L., Ruiz, M., Soto-cordero, L., Stachnik, J. C., Lynner, C., Porritt, R. W., Portner, D., Alvarado, A., Hernandez, S., Yepes, H., Charvis, P., Font, Y., Régnier, M., Agurto-Detzel, H., Rietbrock, A., León-Ríos, S., & Mercerat, E. D. (2019). The 2016 Mw 7.8 Pedernales, Ecuador, Earthquake: Rapid Response Deployment. *Seismological Research Letters*, *90*(3). https://doi.org/10.1785/0220180364

Mendoza, C., & Dewey, J. W. (1984). Seismicity associated with the great Colombia-Ecuador earthquakes of 1942, 1958, and 1979: implications for barrier models of earthquake rupture. *Bulletin of the Earthquake Research Institute*, *74*(2), 577–593.

Meng, L., Huang, H., Bürgmann, R., Ampuero, J. P., & Strader, A. (2015). Dual megathrust slip behaviors of the 2014 Iquique earthquake sequence. *Earth and Planetary Science Letters*, *411*, 177–187. https://doi.org/10.1016/j.epsl.2014.11.041

Menke, W. (1999). Using Waveform Similarity to Constrain Earthquake Locations. *Bulletin of the Seismological Society of America*, *89*(4), 1143–1146.

Meschede, M., & Barckhausen, U. (2000). The plate tectonic evolution of the Cocos-Nazca spreading center. *Proceedings of the Ocean Drilling Program, Scientific Results*, *170*. https://doi.org/10.2973/odp.proc.sr.170.009.2000

Michaud, F., Witt, C., & Royer, J. Y. (2009). Influence of the subduction of the Carnegie volcanic ridge on Ecuadorian geology: Reality and fiction. *Geological Society of America*, *204*. https://doi.org/10.1130/2009.1204(10).

Migeon, S., Garibaldi, C., Ratzov, G., Schmidt, S., Collot, J.-Y., Zaragosi, S., & Texier, L. (2017). Earthquake-triggered deposits in the subduction trench of the north Ecuador/south Colombia margin and their implication for paleoseismology. *Marine Geology*, *384*, 47–62. https://doi.org/10.1016/j.margeo.2016.09.008

Mothes, P. A., Nocquet, J.-M., & Jarrín, P. (2013). Continuous GPS Network Operating Throughout Ecuador. *Eos*, *94*(26). https://doi.org/10.1029/2012EO090001

Nadeau, R. M., Antolik, M., Johnson, P. A., Foxall, W., & Mcevilly, T. V. (1994). Seismological Studies at Parkfield III: Microearthquake Clusters in the Study of Fault-Zone Dynamics. *Bulletin of the Seismological Society of America*, *84*(2), 247–263.

Nadeau, R. M., & Johnson, L. R. (1998). Seismological Studies at Parkfield VI: Moment Release Rates

and Estimates of Source Parameters for Small Repeating Earthquakes. *Bulletin of the Seismological Society of America*, *88*(3), 790–814.

Nadeau, R. M., & Mcevilly, T. V. (1999). Fault Slip Rates at Depth from Recurrence Intervals of Repeating Microearthquakes. *Science*, *285*, 718–721. https://doi.org/10.1126/science.285.5428.718

Nakahara, H. (2004). Correlation distance ofwaveforms for closely located events—I. Implication of the heterogeneous structure around the source region of the 1995 Hyogo-Ken Nanbu, Japan, earthquake (Mw = 6.9). *Geophysical Journal International*, *157*, 1255–1268. https://doi.org/10.1111/j.1365-246X.2004.02278.x

Nakajima, J., & Uchida, N. (2018). Repeated drainage from megathrusts during episodic slow slip. *Nature Geoscience*. https://doi.org/10.1038/s41561-018-0090-z

Nakano, M., Hori, T., Araki, E., Kodaira, S., & Ide, S. (2018). Shallow very-low-frequency earthquakes accompany slow slip events in the Nankai subduction zone. *Nature Communications*, *9*(984). https://doi.org/10.1038/s41467-018-03431-5

Nocquet, J.-M., Jarrín, P., Vallée, M., Mothes, P. A., Grandin, R., Rolandone, F., Delouis, B., Yepes, H., Font, Y., Fuentes, D., Régnier, M., Laurendeau, A., Cisneros, D., Hernandez, S., Sladen, A., Singaucho, J. C., Mora, H., Gomez, J., Montes, L., & Charvis, P. (2017). Supercycle at the Ecuadorian subduction zone revealed after the 2016 Pedernales earthquake. *Nature Geoscience*, *10*(2), 145–149. https://doi.org/10.1038/ngeo2864

Nocquet, J.-M., Mothes, P. A., & Alvarado, A. (2009). *Geodésia , geodinámica y ciclo sísmico en Ecuador*.

Nocquet, J.-M., Villegas-Lanza, J. C., Chlieh, M., Mothes, P. A., Rolandone, F., Jarrín, P., Cisneros, D., Alvarado, A., Audin, L., Bondoux, F., Martin, X., Font, Y., Régnier, M., Vallée, M., Tran, T., Beauval, C., Maguiña Mendoza, J. M., Martinez, W., Tavera, H., & Yepes, H. (2014). Motion of continental slivers and creeping subduction in the northern Andes. *Nature Geoscience*, *March*. https://doi.org/10.1038/NGEO2099

Nomura, S., Ogata, Y., Uchida, N., & Matsu'ura, M. (2017). Spatiotemporal variations of interplate slip rates in northeast Japan inverted from recurrence intervals of repeating earthquakes. *Geophysical Journal International*, *208*(1), 468–481. https://doi.org/10.1093/gji/ggw395

Obara, K., Hirose, H., Yamamizu, F., & Kasahara, K. (2004). Episodic slow slip events accompanied by non-volcanic tremors in southwest Japan subduction zone. *Geophysical Research Letters*, *31*(23), 1–4. https://doi.org/10.1029/2004GL020848

Oth, A. (2013). On the characteristics of earthquake stress release variations in Japan. *Earth and Planetary Science Letters*, *377–378*, 132–141. https://doi.org/10.1016/j.epsl.2013.06.037

Oth, A., Bindi, D., Parolai, S., & Giacomo, D. Di. (2010). Earthquake scaling characteristics and the scale-(in) dependence of seismic energy-to-moment ratio: Insights from KiK-net data in Japan. *Geophysical Research Letters*, *37*. https://doi.org/10.1029/2010GL044572

Peng, Z., & Gomberg, J. (2010). An integrated perspective of the continuum between earthquakes and slow-slip phenomena. *Nature Geoscience*, *3*(9), 599–607. https://doi.org/10.1038/ngeo940

Peng, Z., Vidale, J. E., Marone, C., & Rubin, A. M. (2005). Systematic variations in recurrence interval and moment of repeating aftershocks. *Geophysical Research Letters*, *32*(June), 3–6. https://doi.org/10.1029/2005GL022626

Perfettini, H., & Avouac, J.-P. (2004). Postseismic relaxation driven by brittle creep : A possible mechanism to reconcile geodetic measurements and the decay rate of aftershocks, application to the Chi-Chi earthquake , Taiwan. *Journal of Geophysical Research*, *109*, 1–15. https://doi.org/10.1029/2003JB002488

Prevot, R., Chatelain, J.-L., Guillier, B., & Yepes, H. (1996). Mapping of the P wave velocity structure beneath the Ecuadorian Andes. *Third ISAG, St Malo*, 103–106.

Prévot, R., Chatelain, J.-L., Guillier, B., & Yepes, H. (1996). Tomographie des Andes Equatoriennes: évidence d'une continuité des Andes Centrales. *C.R. Académie Des Sciences de Paris*, *323*, 833–840.

Prieto, G. A., Parker, R. L., Thomson, D. J., Vernon, F. L., & Graham, R. L. (2007). Reducing the bias of multitaper spectrum estimates. *Geophysical Journal International*. https://doi.org/10.1111/j.1365-246X.2007.03592.x

Prieto, G. A., Parker, R. L., & Vernon, F. L. (2009). A Fortran 90 library for multitaper spectrum analysis. *Computers and Geosciences*, *35*, 1701–1710. https://doi.org/10.1016/j.cageo.2008.06.007

Ranero, C. R., Phipps Morgan, J., Mcintosh, K., & Reichert, C. (2003). Bending-related faulting and mantle serpentinization at the Middle America trench. *Nature*, *425*, 367–373.

Reyners, M., & Bannister, S. (2007). Earthquakes triggered by slow slip at the plate interface in the Hikurangi subduction zone, New Zealand. *Geophysical Research Letters*, *34*. https://doi.org/10.1029/2007GL030511

Rice, J. R. (1993). Spatio-temporal Complexity of Slip on a Fault. *Journal of Geophysical Research*, *98*, 9885–9907.

Rogers, G., & Dragbert, H. (2003). Episodic Tremor and Slip on the Cascadia Subduction Zone: The Chatter of Silent Slip. *Sciencexpress*. https://doi.org/10.1126/science.1084783

Rolandone, F., Nocquet, J.-M., Mothes, P. A., Jarrín, P., Vallée, M., Cubas, N., Hernandez, S., Plain, M., Vaca, S., & Font, Y. (2018). Areas prone to slow slip events impede earthquake rupture propagation and promote afterslip. *Science Advances*, *4*(January), 2–10. https://doi.org/10.1126/sciadv.aao6596

Rolandone, F., Nocquet, J.-M., Mothes, P. A., Jarrín, P., & Vergnolle, M. (2020). Afterslip and slow slip events in the postseismic deformation of the 2016 Pedernales earthquake, Ecuador. *EGU*.

Rubin, A. M., Gillard, D., & Got, J. L. (1999). Streaks of microearthquakes along creeping faults. *Nature*, *400*(6745), 635–641. https://doi.org/10.1038/23196

Ruhl, C. J., Abercrombie, R. E., & Smith, K. D. (2017). Spatiotemporal Variation of Stress Drop During the 2008 Mogul, Nevada, Earthquake Swarm. *Journal of Geophysical Research: Solid Earth*, *122*, 8163–8180. https://doi.org/10.1002/2017JB014601

Rüpke, L. H., Phipps Morgan, J., Hort, M., & Connolly, J. A. D. (2004). Serpentine and the subduction zone water cycle. *Earth and Planetary Science Letters*, *223*, 17–34. https://doi.org/10.1016/j.epsl.2004.04.018

Ryder, I. M. A., & Bürgmann, R. (2008). Spatial variations in slip deficit on the central San Andreas Fault from InSAR. *Geophysical Journal International*, *175*, 837–852. https://doi.org/10.1111/j.1365-246X.2008.03938.x

Saffer, D. M., & Tobin, H. J. (2011). Hydrogeology and Mechanics of Subduction Zone Forearcs: Fluid Flow and Pore Pressure. *Annual Review of Earth and Planetary Sciences*, *39*, 157–186. https://doi.org/10.1146/annurev-earth-040610-133408

Saffer, D. M., & Wallace, L. M. (2015). The frictional, hydrologic, metamorphic and thermal habitat of shallow slow earthquakes. *Nature Geoscience*, *8*, 594–600. https://doi.org/10.1038/ngeo2490

Sage, F., Collot, J.-Y., & Ranero, C. R. (2006). Interplate patchiness and subduction-erosion mechanisms: Evidence from depth-migrated seismic images at the central Ecuador convergent margin. *Geological Society of America*, *34*(12), 997–1000. https://doi.org/10.1130/G22790A.1

Sallarès, V., & Charvis, P. (2003). Crustal thickness constraints on the geodynamic evolution of the Galapagos Volcanic Province. *Earth and Planetary Science Letters*, *214*, 545–559. https://doi.org/10.1016/S0012-821X(03)00373-X

Sallarès, V., Charvis, P., Flueh, E. R., & Bialas, J. (2003). Seismic structure of Cocos and Malpelo

Volcanic Ridges and implications for hot spot-ridge interaction. *Journal of Geophysical Research*, *108*(B12). https://doi.org/10.1029/2003JB002431

Sallarès, V., Charvis, P., Flueh, E. R., & Bialas, J. (2005). Seismic structure of the Carnegie ridge and the nature of the Galapagos hotspot. *Geophysical Journal International*, *161*, 763–788. https://doi.org/10.1111/j.1365-246X.2005.02592.x

Sammis, C. G., & Rice, J. R. (2001). Repeating Earthquakes as Low-Stress-Drop Events at a Border between Locked and Creeping Fault Patches. *Bulletin of the Seismological Society of America*, *91*(3), 532–537.

Schaff, D. P., Beroza, G. C., & Shaw, B. E. (1998). Postseismic response of repeating aftershocks. *Geophysical Research Letters*, *25*(24), 4549–4552.

Scholz, C. H. (1998). Earthquakes and friction laws. *Nature*, *391*, 37–42.

Scholz, C. H. (2019). *The mechanics of earthquakes and faulting* (3rd ed.). Cambridge University Press. https://doi.org/https://doi.org/10.1017/9781316681473

Segall, P., Desmarais, E. K., Shelly, D. R., Miklius, A., & Cervelli, P. (2006). Earthquakes triggered by silent slip events on Kilauea volcano, Hawaii. *Nature*, *442*(July), 71–74. https://doi.org/10.1038/nature04938

Segovia, M. (2001). *El sismo de Bahia del 4 de agosto de 1998: caracterizacion del mecanismo de ruptura y analisis de la sismicidad en la zona costera*. Escuela Politecnica Nacional, Quito, Ecuador.

Segovia, M. (2016). *Microseismicity around an asperity in the Ecuadorian subduction zone*. Université Côte d'Azur.

Segovia, M., Font, Y., Régnier, M., Charvis, P., Galve, A., Nocquet, J.-M., Jarrín, P., Hello, Y., Ruiz, M., & Pazmiño, A. (2018). Seismicity Distribution Near a Subducting Seamount in the Central Ecuadorian Subduction Zone, Space-Time Relation to a Slow-Slip Event. *Tectonics*, *37*. https://doi.org/10.1029/2017TC004771

Shaddox, H. R., & Schwartz, S. Y. (2019). Subducted seamount diverts shallow slow slip to the forearc of the northern Hikurangi subduction zone, New Zealand. *Geology*, *47*(5), 415–418.

Shearer, P. M. (2009). *Introduction to Seismology* (2nd ed.). Cambridge University Press.

Shearer, P. M., Abercrombie, R. E., Trugman, D. T., & Wang, W. (2019). Comparing EGF Methods for Estimating Corner Frequency and Stress Drop From P Wave Spectra. *Journal of Geophysical Research: Solid Earth*, *124*, 3966–3986. https://doi.org/10.1029/2018JB016957

Shearer, P. M., Prieto, G. A., & Hauksson, E. (2006). Comprehensive analysis of earthquake source spectra in southern California. *Journal of Geophysical Research*, *111*. https://doi.org/10.1029/2005JB003979

Shelly, D. R., Beroza, G. C., Ide, S., & Nakamula, S. (2006). Low-frequency earthquakes in Shikoku, Japan, and their relationship to episodic tremor and slip. *Nature*, *442*(7099), 188–191. https://doi.org/10.1038/nature04931

Shelly, D. R., Ellsworth, W. L., & Hill, D. P. (2016). Fluid-faulting evolution in high definition: Connecting fault structure and frequency-magnitude variations during the 2014 Long Valley Caldera, California, earthquake swarm. *Journal of Geophysical Research : Solid Earth*, 1776–1795. https://doi.org/10.1002/2015JB012719.Received

Shrivastava, M. N., González, G., Moreno, M., Chlieh, M., Salazar, P., Reddy, C. D., Báez, J. C., Yáñez, G., González, J., & Llera, J. C. (2016). Coseismic slip and afterslip of the 2015 Mw 8.3 Illapel (Chile) earthquake determined from continuous GPS data. *Geophysical Research Letters*, *43*, 10710–10719. https://doi.org/10.1002/2016GL070684.Received

Sibson, R. H. (1990). Conditions for fault-valve behaviour. *Geological Society Special Publication*, *54*, 15–28.

Silverii, F., Cheloni, D., D'Agostino, N., Selvaggi, G., Boschi, E., Agostino, N. D., Selvaggi, G., & Boschi, E. (2014). Post-seismic slip of the 2011 Tohoku-Oki earthquake from GPS observations: implications for depth-dependent properties of subduction megathrusts. *Geophysical Journal International*, *198*, 580–596. https://doi.org/10.1093/gji/ggu149

Skarbek, R. M., Rempel, A. W., & Schmidt, D. A. (2012). Geologic heterogeneity can produce aseismic slip transients. *Geophysical Research Letters*, *39*. https://doi.org/10.1029/2012GL053762

Socquet, A., Piña Valdes, J., Jara, J., Cotton, F., Walpersdorf, A., Cotte, N., Specht, S., Ortega-Culaciati, F. H., Carrizo, D., & Norabuena, E. (2017). An 8 month slow slip event triggers progressive nucleation of the 2014 Chile megathrust. *Geophysical Research Letters*, *44*, 4046–4053. https://doi.org/10.1002/2017GL073023

Song, T. A., Helmberger, D. V, Brudzinski, M. R., Clayton, R. W., Davis, P., Pérez-Campos, X., & Singh, S. K. (2009). Subducting Slab Ultra-Slow Velocity Layer Coincident with Silent Earthquakes in Southern Mexico. *Science*, *324*. https://doi.org/10.1126/science.1167595

Soto-Cordero, L., Meltzer, A., Bergman, E., Hoskins, M. C., Stachnik, J. C., Agurto-Detzel, H., Alvarado, A., Beck, S. L., Charvis, P., Font, Y., Hayes, G. P., Hernandez, S., Lynner, C., León-Ríos, S., Nocquet, J.-M., Regnier, M., Rietbrock, A., Rolandone, F., Ruiz, M., … Ruiz, M. (2020). Structural Control on Megathrust Rupture and Slip Behavior: Insights From the 2016 Mw 7.8 Pedernales Ecuador Earthquake. *Journal of Geophysical Research: Solid Earth*, *125*, 1–28. https://doi.org/10.1029/2019JB018001

Staszek, M., Orlecka-Sikora, B., Leptokaropoulos, K., Kwiatek, G., & Martinez-Garzon, P. (2017). Temporal static stress drop variations due to injection activity at The Geysers geothermal field, California. *Geophysical Research Letters*, *44*, 7168–7176. https://doi.org/10.1002/2017GL073929

Stein, C. A., & Stein, S. (1994). Constraints on hydrothermal heat flux through the oceanic lithosphere from global heat flow. *Journal of Geophysical Research*, *99*(B2), 3081–3095.

Stern, R. J. (2002). Subduction zones. *Review of Geophysics*, *40*(4). https://doi.org/10.1029/2001RG000108

Sun, T., Saffer, D. M., & Ellis, S. (2020). Mechanical and hydrological effects of seamount subduction on megathrust stress and slip. *Nature Geoscience*, *13*(March), 249–255. https://doi.org/10.1038/s41561-020-0542-0

Swenson, J. L., & Beck, S. L. (1996). Historical 1942 Ecuador and 1942 Peru Subduction Earthquakes, and Earthquake Cycles along Colombia-Ecuador and Peru Subduction Segments. *Pure and Applied Geophysics*, *146*(1), 67–101.

Taira, T., Silver, P. G., Niu, F., & Nadeau, R. M. (2009). Remote triggering of fault-strength changes on the San Andreas fault at Parkfield. *Nature Letters*, *461*(October), 636–639. https://doi.org/10.1038/nature08395

Templeton, D. C., Nadeau, R. M., & Bürgmann, R. (2009). Distribution of postseismic slip on the Calaveras fault, California, following the 1984 M6.2 Morgan Hill earthquake. *Earth and Planetary Science Letters*, *277*. https://doi.org/10.1016/j.epsl.2008.09.024

Tolga Şen, A., Cesca, S., Lange, D., Dahm, T., Tilmann, F., & Heimann, S. (2015). Systematic Changes of Earthquake Rupture with Depth: A Case Study from the 2010 Mw 8.8 Maule, Chile, Earthquake Aftershock Sequence. *Bulletin of the Seismological Society of America*, *105*(5), 2468–2479. https://doi.org/10.1785/0120140123

Tsang, L. L. H., Vergnolle, M., Twardzik, C., Sladen, A., Nocquet, J.-M., Rolandone, F., Agurto-detzel, H., Cavalié, O., Jarrín, P., & Mothes, P. A. (2019). Imaging rapid early afterslip of the 2016 Pedernales earthquake , Ecuador. *Earth and Planetary Science Letters*, *524*, 115724. https://doi.org/10.1016/j.epsl.2019.115724

Uchida, N. (2019). Detection of repeating earthquakes and their application in characterizing slow fault slip. *Progress in Earth and Planetary Science*.

Uchida, N., & Bürgmann, R. (2019). Repeating Earthquakes. *Annual Review of Earth and Planetary Sciences*, 305–332.

Uchida, N., Iinuma, T., Nadeau, R. M., Bürgmann, R., & Hino, R. (2016). Periodic slow slip triggers megathrust zone earthquakes in northeastern Japan. *Science*, *351*(6272), 488–492. https://doi.org/10.1126/science.aad3108

Uchida, N., & Matsuzawa, T. (2011). Coupling coefficient, hierarchical structure, and earthquake cycle for the source area of the 2011 off the Pacific coast of Tohoku earthquake inferred from small repeating earthquake data. *Earth, Planets and Space*, *63*(7), 675–679. https://doi.org/10.5047/eps.2011.07.006

Uchida, N., & Matsuzawa, T. (2013). Pre-and postseismic slow slip surrounding the 2011 Tohoku-oki earthquake rupture. *Earth and Planetary Science Letters*, *374*, 81–91. https://doi.org/10.1016/j.epsl.2013.05.021

Uchida, N., Matsuzawa, T., Hasegawa, A., & Igarashi, T. (2003). Interplate quasi-static slip off Sanriku, NE Japan, estimated from repeating earthquakes. *Geophysical Research Letters*, *30*(15), 1–4. https://doi.org/10.1029/2003GL017452

Uchida, N., Nakajima, J., Hasegawa, A., & Matsuzawa, T. (2009). What controls interplate coupling?: Evidence for abrupt change in coupling across a border between two overlying plates in the NE Japan subduction zone. *Earth and Planetary Science Letters*, *283*, 111–121. https://doi.org/10.1016/j.epsl.2009.04.003

Uchida, N., Shimamura, K., Matsuzawa, T., & Okada, T. (2015). Postseismic response of repeating earthquakes around the 2011 Tohoku-oki earthquake: Moment increases due to the fast loading rate. *Journal of Geophysical Research: Solid Earth*, *120*, 259–274. https://doi.org/10.1002/2013JB010933.Received

Uchida, N., Yui, S., Miura, S., Matsuzawa, T., Hasegawa, A., Motoya, Y., & Kasahara, M. (2009). Quasi-static slip on the plate boundary associated with the 2003 M8.0 Tokachi-oki and 2004 M7.1 off-Kushiro earthquakes, Japan. *Gondwana Research*, *16*, 527–533. https://doi.org/10.1016/j.gr.2009.04.002

Uchide, T., Shearer, P. M., & Imanishi, K. (2014). Stress drop variations among small earthquakes before the 2011 Tohoku-oki, Japan, earthquake and implications for the main shock. *Journal of Geophysical Research: Solid Earth*, *119*, 7164–7174. https://doi.org/10.1002/2014JB010943.Received

Vaca, S., Vallée, M., Nocquet, J.-M., Battaglia, J., & Régnier, M. (2018). Recurrent slow slip events as a barrier to the northward rupture propagation of the 2016 Pedernales earthquake (Central Ecuador). *Tectonophysics*, *724–725*, 80–92. https://doi.org/10.1016/j.tecto.2017.12.012

Vallée, M., Nocquet, J., Battaglia, J., Font, Y., Segovia, M., Régnier, M., Mothes, P. A., Jarrín, P., Cisneros, D., Vaca, S., Yepes, H., Martin, X., Béthoux, N., & Chlieh, M. (2013). Intense interface seismicity triggered by a shallow slow slip event in the Central Ecuador subduction zone. *Journal of Geophysical Research: Solid Earth*, *118*, 2965–2981. https://doi.org/10.1002/jgrb.50216

Vidale, J. E., Ellsworth, W. L., Cole, A., & Marone, C. (1994). Variations in rupture process with recurrence interval in a repeated small earthquake. *Nature Letters*, *368*, 624–626.

Viegas, G., Abercrombie, R. E., & Kim, W. Y. (2010). The 2002 M5 Au Sable Forks, NY, earthquake sequence: Source scaling relationships and energy budget. *Journal of Geophysical Research*, *115*. https://doi.org/10.1029/2009JB006799

Waldhauser, F., & Ellsworth, W. L. (2000). A Double-Difference Earthquake Location Algorithm: Method and Application to the Northern Hayward Fault , California. *Bulletin of the Seismological Society of America*, *90*(6), 1353–1368.

Waldhauser, F., & Schaff, D. P. (2008). Large-scale relocation of two decades of Northern California seismicity using cross-correlation and double-difference methods. *Journal of Geophysical*

Research, *113*. https://doi.org/10.1029/2007JB005479

Wallace, L. M., Kaneko, Y., Hreinsdóttir, S., Hamling, I., Peng, Z., Bartlow, N. M., Anastasio, E. D., & Fry, B. (2017). Large-scale dynamic triggering of shallow slow slip enhanced by overlying sedimentary wedge. *Nature Geoscience*. https://doi.org/10.1038/NGEO3021

Wallace, L. M., Webb, S. C., Ito, Y., Mochizuki, K., Hino, R., Henrys, S., Schwartz, S. Y., & Sheehan, A. F. (2016). Slow slip near the trench at the Hikurangi subduction zone, New Zealand. *Science*, *352*(6286), 701–704.

Walter, J. I., Dotray, P. J., Frohlich, C., & Gale, J. F. W. (2016). Earthquakes in Northwest Louisiana and the Texas – Louisiana Border Possibly Induced by Energy Resource Activities within the Haynesville Shale Play. *Seismological Research Letters*, *87*, 285–294. https://doi.org/10.1785/0220150193

Wang, K., & Bilek, S. L. (2014). Invited review paper: Fault creep caused by subduction of rough seafloor relief. *Tectonophysics*, *610*, 1–24. https://doi.org/10.1016/j.tecto.2013.11.024

Wang, K., & Tréhu, A. M. (2016). Invited review paper : Some outstanding issues in the study of great megathrust earthquakes — The Cascadia example. *Journal of Geodynamics*, *98*, 1–18.

Warren-Smith, E., Fry, B., Wallace, L. M., Chon, E., Henrys, S., Sheehan, A. F., Mochizuki, K., Schwartz, S. Y., Webb, S. C., & Lebedev, S. (2019). Episodic stress and fluid pressure cycling in subducting oceanic crust during slow slip. *Nature Geoscience*, *12*(June), 475–482. https://doi.org/10.1038/s41561-019-0367-x

Williams, J. R., Hawthorne, J. C., & Lengliné, O. (2019). The Long Recurrence Intervals of Small Repeating Earthquakes May Be Due to the Slow Slip Rates of Small Fault Strands. *Geophysical Research Letters*, *46*, 12823–12832. https://doi.org/10.1029/2019GL084778

Witt, C., Bourgois, J., Michaud, F., Ordonez, M., Jimenez, N., & Sosson, M. (2006). Development of the Gulf of Guayaquil (Ecuador) during the Quaternary as an effect of the North Andean block tectonic escape. *Tectonics*, *25*(TC3017). https://doi.org/10.1029/2004TC001723

Wu, Jianchao, Cai, Y., Li, W., & Feng, Q. (2017). Strong Aftershock Study Based on Coulomb Stress Triggering — A Case Study on the 2016 Ecuador Mw 7.8 earthquake. *Applied Sciences*, *7*(88). https://doi.org/10.3390/app7010088

Wu, Jing, Yao, D., Meng, X., Peng, Z., Su, J., & Long, F. (2017). Spatial-temporal evolutions of early aftershocks following the 2013 Mw 6.6 Lushan earthquake in Sichuan, China. *Journal of Geophysical Research: Solid Earth*, 2873–2889. https://doi.org/10.1002/2016JB013706

Wynants-Morel, N., Cappa, F., De Barros, L., & Ampuero, J. P. (2020). Stress Perturbation From Aseismic Slip Drives the Seismic Front During Fluid Injection in a Permeable Fault. *Journal of Geophysical Research: Solid Earth*, *125*. https://doi.org/10.1029/2019JB019179

Yamada, T., Duan, M., & Kawahara, J. (2021). Spatio-temporal characteristics of frictional properties on the subducting Pacific Plate off the east of Tohoku district, Japan estimated from stress drops of small earthquakes. *Earth, Planets and Space*, *73*(18). https://doi.org/10.1186/s40623-020-01326-8

Yang, H., Liu, Y., & Lin, J. (2012). Effects of subducted seamounts on megathrust earthquake nucleation and rupture propagation. *Geophysical Research Letters*, *39*. https://doi.org/10.1029/2012GL053892

Yao, D., Walter, J. I., Meng, X., Hobbs, T. E., Peng, Z., Newman, A. V, Schwartz, S. Y., & Protti, M. (2017). Detailed spatiotemporal evolution of microseismicity and repeating earthquakes following the 2012 Mw 7.6 Nicoya earthquake. *Journal of Geophysical Research: Solid Earth*, *122*, 524–542. https://doi.org/10.1002/2016JB013632.Received

Ye, L., Kanamori, H., Avouac, J.-P., Li, L., Cheung, K. F., & Lay, T. (2016). The 16 April 2016, Mw 7.8 (Ms 7.5) Ecuador earthquake: A quasi-repeat of the 1942 Ms7.5 earthquake and partial re-rupture of the 1906 Ms8.6 Colombia–Ecuador earthquake. *Earth and Planetary Science Letters*,

454(April), 248–258. https://doi.org/10.1016/j.epsl.2016.09.006

Yepes, H., Audin, L., Alvarado, A., Beauval, C., Aguilar, J., Font, Y., & Cotton, F. (2016). A new view for the geodynamics of Ecuador: Implication in seismogenic source definition and seismic hazard assessment. *Tectonics*, *35*, 1249–1279. https://doi.org/10.1002/2015TC003941.Received

Yoshida, K., Saito, T., Urata, Y., Asano, Y., & Hasegawa, A. (2017). Temporal Changes in Stress Drop, Frictional Strength, and Earthquake Size Distribution in the 2011 Yamagata-Fukushima, NE Japan, Earthquake Swarm, Caused by Fluid Migration. *Journal of Geophysical Research: Solid Earth*, *122*, 10379–10397. https://doi.org/10.1002/2017JB014334

Yoshimoto, M., Kumagai, H., Acero, W., Ponce, G., Vásconez, F., Arrais, S., Ruiz, M., Alvarado, A., Pedraza Garcia, P., Dionicio, V., Chamorro, O., Maeda, Y., & Nakano, M. (2017). Depth-dependent rupture mode along the Ecuador-Colombia subduction zone. *Geophysical Research Letters*, *44*, 2203–2210. https://doi.org/10.1002/2016GL071929.Received

Zheng, Y., Chen, R., XU, Z., & Zhang, S. (2016). The transport of water in subduction zones. *Science China Earth Sciences*, *59*, 651–682. https://doi.org/10.1007/s11430-015-5258-4

Appendix A: Table of Figures

Appendix B: Supplementary materials for Chapter 3

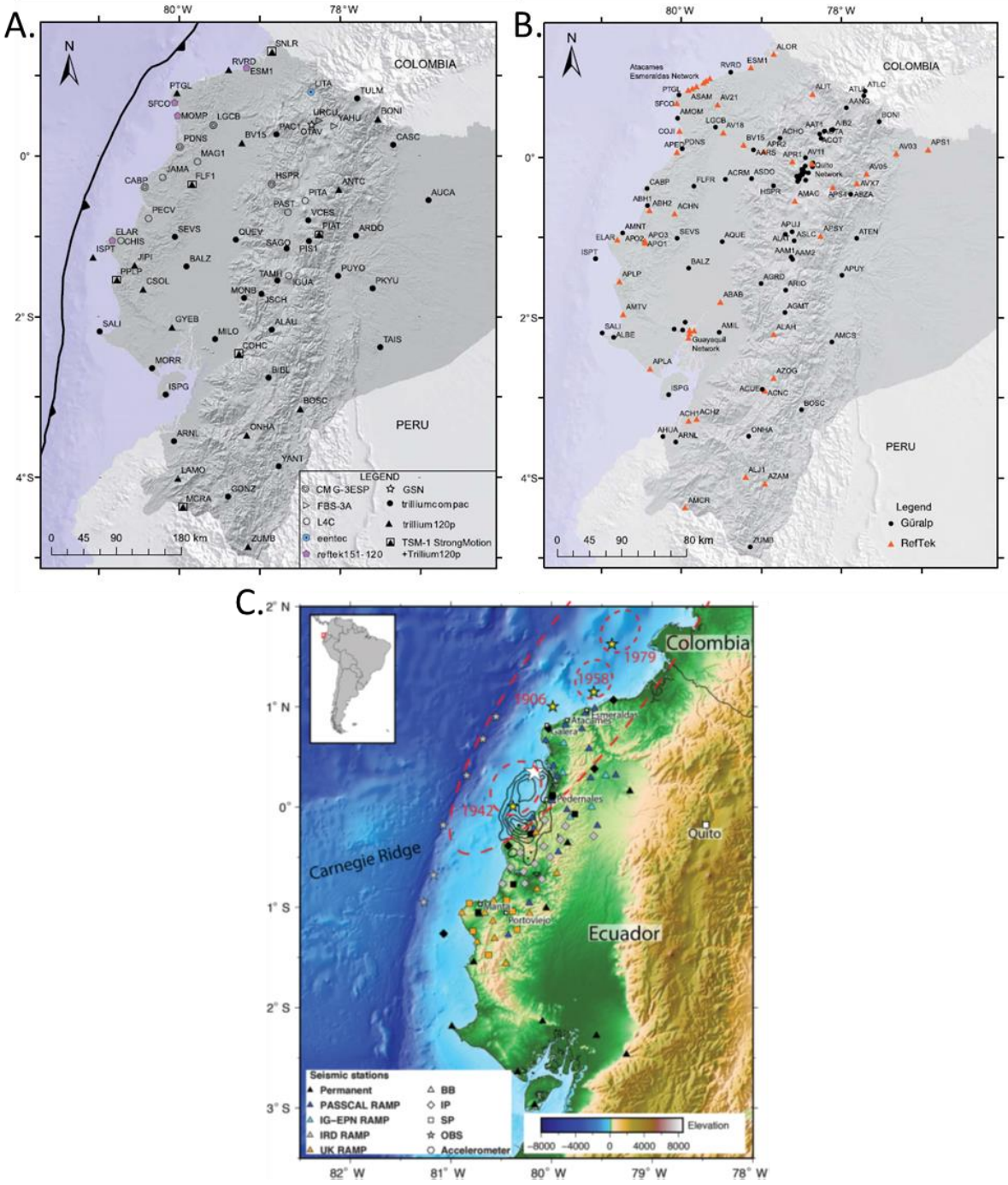

Figure SB.1 : Maps of all network stations by Alvarado et al. (2018) (A-B, permanent networks) and Meltzer et al. (2019) (C, temporary networks)

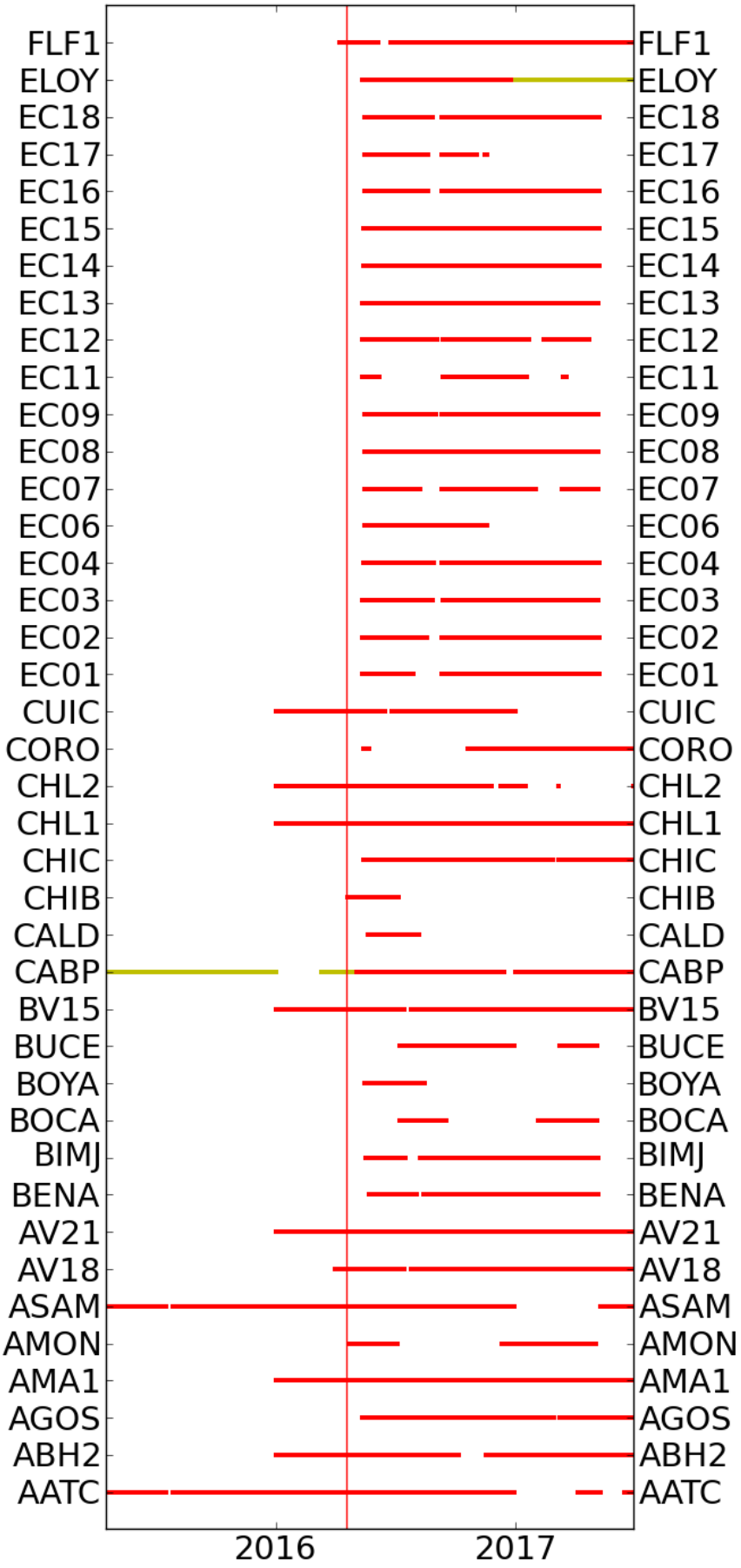
FLF1
ELOY
EC18
EC17
EC16
EC15
EC14
EC13
EC12
EC11
EC09
EC08
EC07
EC06
EC04
EC03
EC02
EC01
CUIC
CORO
CHL2
CHL1
CHIC
CHIB
CALD
CABP
BV15
BUCE
BOYA
BOCA
BIMJ
BENA
AV21
AV18
ASAM
AMON
AMA1
AGOS
ABH2
AATC
2016
2017

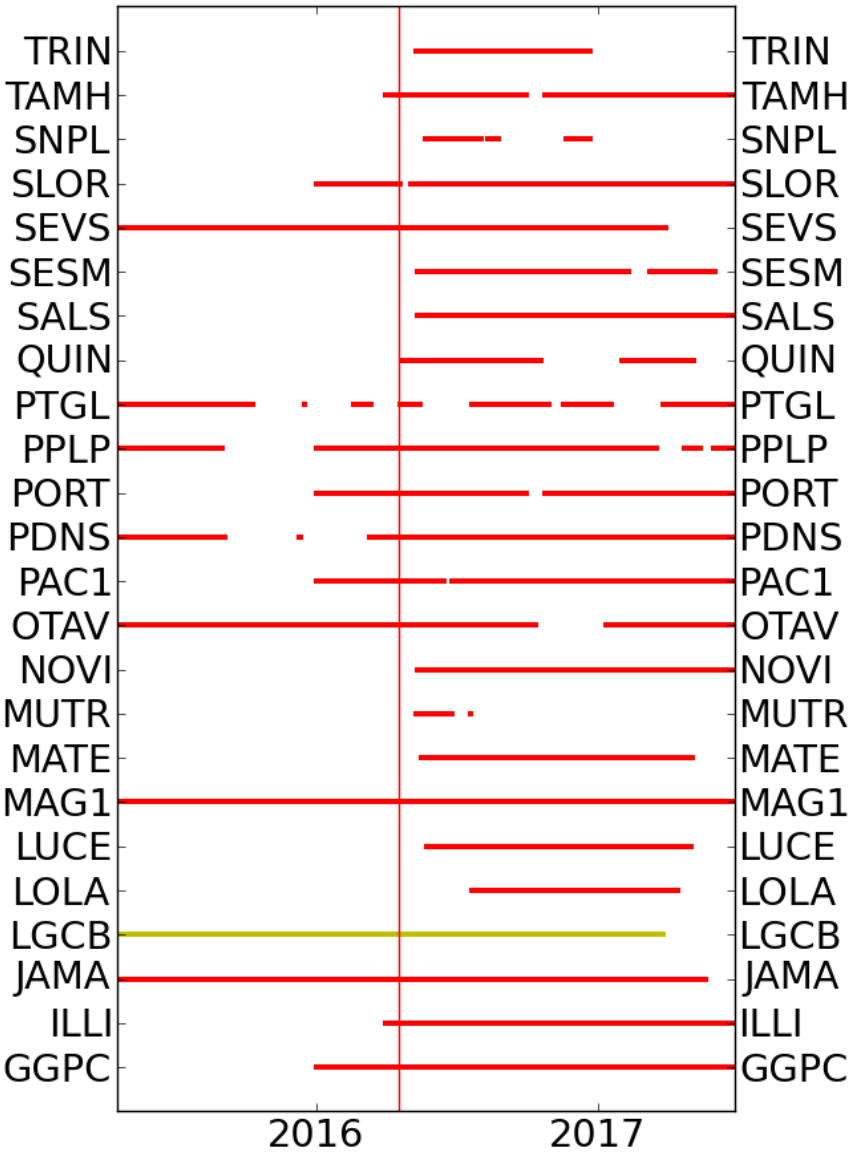

Figure SB.2 : Availability of stations used in this study as a function of time (red). Green bars show stations which are available with notable issues: ELOY has a clock issue in 2017, CABP has no signal on its Z component in its early period, and LGCB has frequent spikes on its N component.

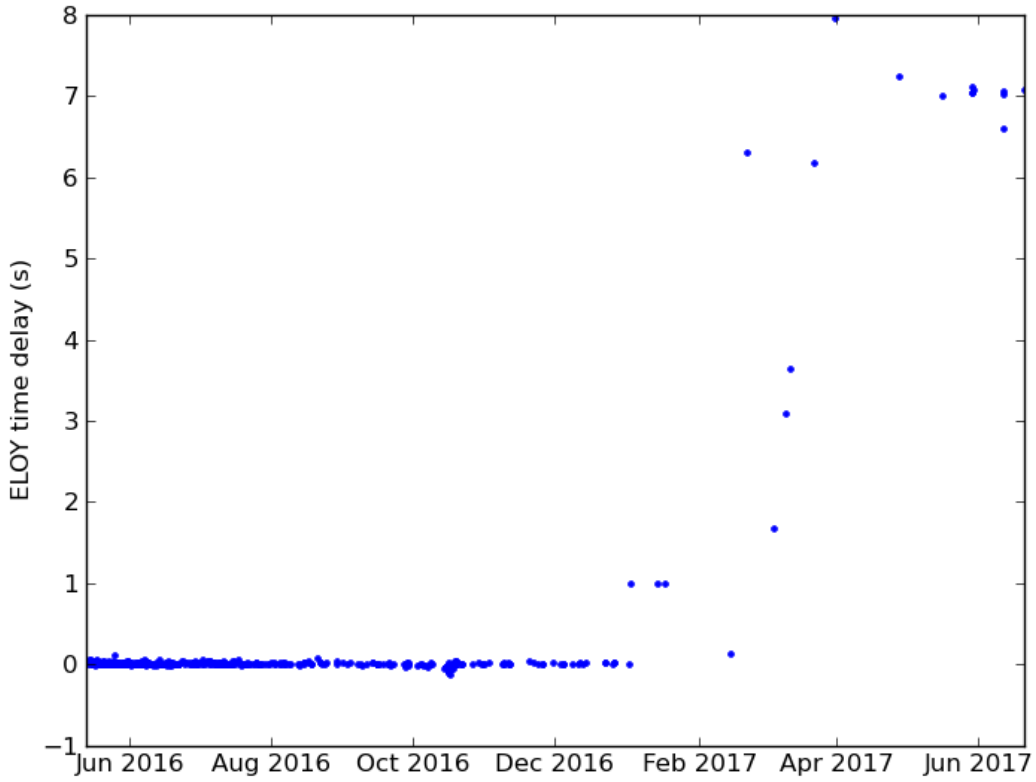

Figure SB.3 : Delay times between template matching detections made by ELOY and detections made by all other stations. This shows the drift of the ELOY clock starting in January 2017.

Tableau SB.1: Correlation coefficient computation stations

Station	Channel	Sampling rate (Hz)	Frequency band (Hz)	Used in North classification	Used in South classification	Used in whole region classification
AGOS	EHZ	200	2 to 9		x	x
BENA	HHZ	100	1,5 to 9		x	
CABP	HHZ	125	2,5 to 10			x
CHIB	HHZ	200	1,5 to 9	x		
EC03	HHZ	100	3 to 10	x		x
EC12	HHZ	100	2 to 9	x		x
EC14	HHZ	100	2 to 9	x		x
EC15	HHZ	100	1,5 to 9	x		x
EC16	HHZ	100	2,5 to 10		x	x
EC18	HHZ	100	1,5 to 9		x	x
ELOY	EHZ	200	1,5 to 9		x	x
FLF1	HHZ	100	3,5 to 10		x	x
LGCB	HHZ	125	1,5 to 9	x	x	x

LOLA	HHZ	100	2,5 to 10	x		
LUCE	HHZ	100	1,5 to 9			x
NOVI	EHZ	200	2 to 9		x	x
OTAV	HHZ	100	1,5 to 9	x		x
PDNS	ENZ	125	2,5 to 10	x	x	x
PTGL	HHZ	125	2,5 to 10	x		x
SEVS	HHZ	100	1,5 to 9		x	x

Tableau SB.2: HypoDD stations used in the north

Station	T before P arrival (s)	T after P arrival (s)	T before S arrival (s)	T after S arrival (s)	F1 (Hz)	F2 (Hz)	Activity after mainshock (% days)	Active before mainshock	Active first month
AATC	2	2	2,5	2,5	3	10	41	0,34	1
AGOS	3	2	3	3	2	10	92	0	0
AMA1	2	2	2,5	2,5	3	9	97	0,29	1
ASAM	3	2	2	3	4	11	19	0,37	1
AV18	2,5	2,5	3	3	3	8	97	0,05	1
AV21	3	2	2	3	3	9	93	0,05	1
BOCA	3	2	3	3	1,5	9	38	0	0
BUCE	3	2	2	3	2	10	54	0	0
BV15	2,5	2,5	2,5	2,5	1,5	8	97	0,05	1
CHL1	3	3	3	3	1,5	8	100	0,29	1
CHL2	3	3	3	3	1,5	8	61	0,29	1
CUIC	3	3	3	3	1,5	8	58	0,29	1
EC01	3	2	2	3	2	9,5	74	0	0
EC02	3	2	2	3	3	9	79	0	0
EC03	2,25	2	2	3	2	10	80	0	0
EC04	3	2	3	3	1,5	8	81	0	0
EC06	2,5	2	3	3	2	8	44	0	0
EC08	3	3	3	3	1,5	8	82	0	0
EC11	3	2	2	3	2	8	38	0	0
EC12	2,5	2	2	3	2	10	73	0	0
EC13	2,5	2	2	3	2	9	83	0	0
EC14	2,5	2	2	3	1,5	9	84	0	0
EC15	2,5	2,25	2,25	2,5	1,5	9	84	0	0
EC16	3	2	3	3	3	10	79	0	0
EC17	2,5	2,5	3	3	2	10	36	0	0
EC18	3	2	3	3	2	8	80	0	0
ELOY	3	3	3	3	2	8	94	0	0
FLF1	2,5	2,5	3	3	3	10	94	0,02	1
GGPC	3	3	3	3	2	10	99	0,02	1

ILLI	3	3	3	3	2	7	100	0,05	1
LGCB	2,5	2	3	3	2	8	80	1	1
LOLA	2	2	2	3	2,5	10	63	0	0
NOVI	3	2	3	3	2	10	94	0	0
OTAV	3	3	3	3	1	9	79	1	1
PAC1	2,5	2,5	3	3	1,5	8	98	0,05	1
PDNS	1,75	2,5	3	3	2,5	10	99	0,49	1
PTGL	2,25	2	2	3	2,5	10	62	0,54	1
QUIN	2,5	2,5	3	3	1,5	7	63	0	1
SLOR	3	3	3	3	2	9	97	0,29	1
TRIN	3	2	3	3	1,5	8	53	0	0
WILF	3	3	3	3	1	6	89	0	0

Tableau SB.3: HypoDD stations used in the south

Station	T before P arrival (s)	T after P arrival (s)	T before S arrival (s)	T after S arrival (s)	F1 (Hz)	F2 (Hz)	Activity after mainshock (% days)	Active before mainshock	Active first month
AGOS	3	2	2	3	2	9	92	no	no
BENA	3	2	2	3	1,5	9	80	no	no
EC16	3	2	2	3	2,5	10	79	no	no
EC18	3	2	2	3	1,5	9	80	no	no
ELOY	3	2	2	3	1	9	94	no	no
FLF1	3	2	2	3	3,5	10	94	yes	yes
LGCB	3	3	3	3	1,5	9	80	yes	yes
NOVI	3	2	2	3	1,5	9	94	no	no
PDNS	3	2	2	3	2,5	10	99	yes	yes
SEVS	3	3	3	3	1,5	9	58	yes	yes
ABH2	3	2	2	3	3	10	18	yes	yes
AMON	3	3	3	3	2	9,5	51	no	yes
BIMJ	3	3	3	3	2,5	10	78	no	no
BV15	3	3	3	3	1,5	8	97	yes	yes
CABP	3	2	2	3	2,5	10	95	yes	yes
CHIB	3	2	2	3	1,5	8,5	58	no	yes
CHIC	3	2	2	3	2	9	90	no	no
CHL1	3	3	3	3	1,5	7	100	yes	yes
CHL2	3	3	3	3	1,5	9	61	yes	yes
CORO	3	2	2	3	3	8	57	no	no
EC04	3	2,5	2,5	3	1,5	9	81	no	no
EC08	3	2	2	3	1	9	82	no	no
EC12	3	2	2	3	2	9	73	no	no

EC14	3	3	3	3	1,5	8,5	84	no	no
EC15	3	3	3	3	1,5	9	84	no	no
EC17	3	2	2	3	2	10	36	no	no
GGPC	3	3	3	3	3,5	11	99	yes	yes
ILLI	3	3	3	3	1,5	9	100	yes	yes
JAMA	3	2	2	3	3,5	8	100	yes	yes
LUCE	3	2,5	2,5	3	1,5	8	80	no	no
OTAV	3	3	3	3	1,5	9	79	yes	yes
PORT	3	3	3	3	2	10	94	yes	yes
PPLP	3	3	3	3	2	9,5	80	yes	yes
PTGL	3	3	3	3	2,5	10	62	yes	yes
SESM	3	2	2	3	1,5	8	84	no	no
TAMH	3	3	3	3	2	9	94	yes	yes
TRIN	3	2	2	3	1,5	9	53	no	no
WILF	3	3	3	3	1	7	89	no	no
MAG1	3	2	2	3	2	8	100	yes	yes
BUCE	3	2	2	3	2	10	54	no	no
BOCA	3	2	2	3	1,5	8	38	no	no
BOYA	3	2	2	3	1,5	8	22	no	no
CALD	3	3	3	3	2	10	18	no	no
EC03	3	2	2	3	3	10	80	no	no
EC06	3	2	2	3	2	8	44	no	no
EC07	3	3	3	3	1	6,5	67	no	no
EC09	3	3	3	3	1,5	8	81	no	no
EC11	3	3	3	3	2	10	38	no	no
EC13	3	2	2	3	2,5	8	83	no	no
LOLA	3	2	2	3	2	10	63	no	no
MUTR	3	2	2	3	1,5	8	11	no	no
SNPL	3	3	3	3	1,5	8	28	no	no

Tableau SB.4: HypoDD iteration parameters

HypoDD iteration parameters North										
Iteration group	Number of iterations in group	CC P pick weight	CC S pick weight	Cutoff residual for CC pairs (std)	Max distance between CC pairs (km)	CT P pick weight	CT S pick weight	Cutoff residual for CT pairs (std)	Max distance between CT pairs (km)	Damping
1	5	0,2	0,15	-9	-9	1	0,8	-9	6	10
2	5	0,2	0,15	-9	-9	1	0,8	4	6	10
3	5	1	0,8	-9	-9	0,25	0,2	4	6	10
4	15	1	0,8	6	6	0,25	0,2	4	6	20
5	5	1	0,8	6	6	0,1	0,06	3	6	30
HypoDD iteration parameters South										

Iteration group	Number of iterations in group	CC P pick weight	CC S pick weight	Cutoff residual for CC pairs (std)	Max distance between CC pairs (km)	CT P pick weight	CT S pick weight	Cutoff residual for CT pairs (std)	Max distance between CT pairs (km)	Damping
1	5	0,2	0,15	5	20	1	0,8	5	6	10
2	10	0,2	0,15	5	20	1	0,8	4	6	10
3	10	1	0,8	5	20	0,25	0,2	4	6	10
4	15	1	0,8	4	6	0,25	0,2	4	6	20
5	5	1	0,8	4	6	0,1	0,06	3	6	30

Appendix C: Supplementary materials for Chapter 4

Supporting Information for:

Repeating earthquakes at the edge of the afterslip of the 2016 Ecuadorian M7.8 Pedernales earthquake

Caroline Chalumeau[1], Hans Agurto-Detzel[1], Louis De Barros[1], Philippe Charvis[1], Audrey Galve[1], Andreas Rietbrock[2], Alexandra Alvarado[3], Stephen Hernandez[3], Susan Beck[4], Yvonne Font[1], Mariah C. Hoskins[5], Sergio Leon-Rios[2], Anne Meltzer[5], Colton Lynner[4], Frederique Rolandone[6], Jean-Mathieu Nocquet[1], Marc Regnier[1], Mario Ruiz[3], Lillian Soto-Cordero[5], Sandro Vaca[3], Monica Segovia[3]

Contents of this file:

Text S1.: Magnitude calculations:

Local magnitudes (M_L) for all earthquakes are calculated from their maximum amplitudes on the vertical component of 31 stations to get homogenized values for the whole catalogue. The relationship used is the one used by SeisComP3, on which the initial aftershock catalogue was picked:

$$M_L = log_{10}(A) - log_{10}(A_0) + C_1$$

Where A is the amplitude in mm, C_1 is an empirical constant determined for each station, and $log_{10}(A_0)$ is interpolated from:

$$\begin{cases} log_{10}(A_0) = -1.3 \; when \; d = 0 \; km \\ log_{10}(A_0) = -2.8 \; when \; d = 60 \; km \\ log_{10}(A_0) = -4.5 \; when \; d = 400 \; km \end{cases}$$

The total catalogue has local magnitudes ranging from 0.9 to 7.3, with a median magnitude of 2.4 (Figure S2a). The average error in magnitude is 0.3 ± 0.08. Meanwhile, repeaters' local magnitudes range between 1.5 and 4.6, with a median of 2.7. We use the relationship developed

by Agurto-detzel *et al.* (2019) for this aftershock sequence to calculate moment magnitudes from local magnitudes:

$$M_W = 1.46 \times M_L - 2.59$$

We then calculate seismic moment (in N.m) using the relationship from Hanks and Kanamori (1979) :

$$M_0 = 10^{1.5 \times M_W + 9.1}$$

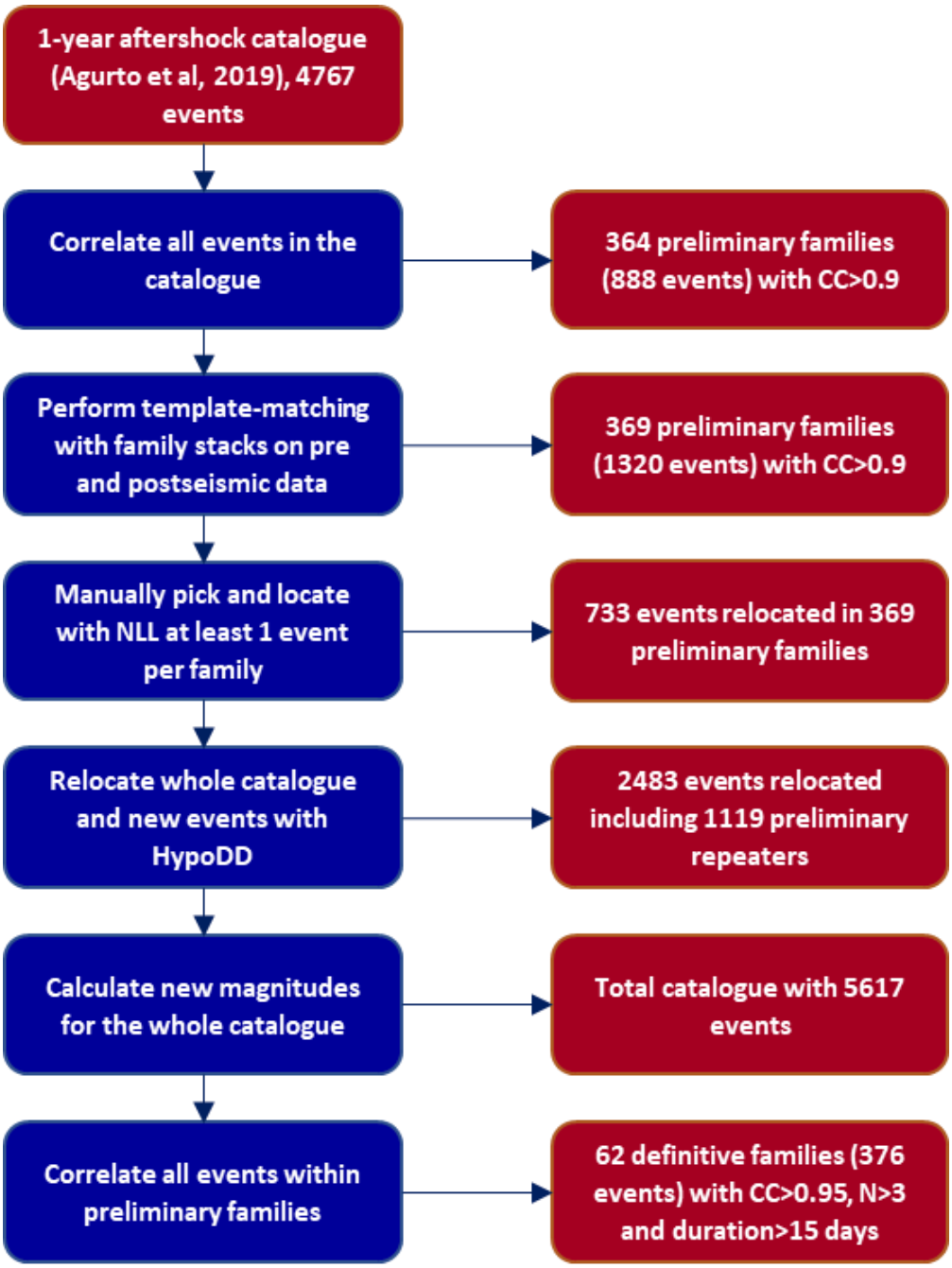

Figure SC.1: Flowchart summarizing the different processing steps used to obtain relocated families of repeating earthquakes.

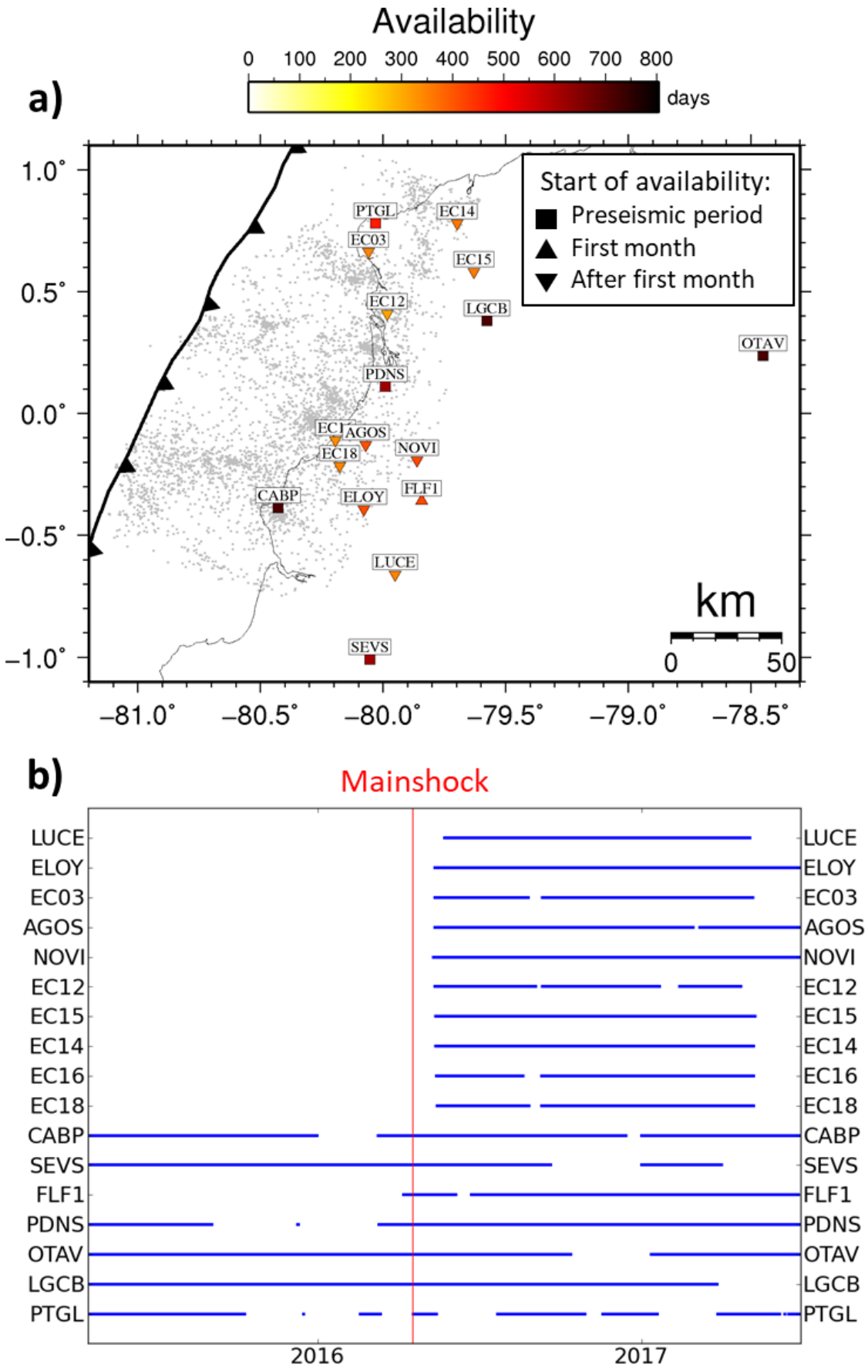

Figure SC.2: Stations used. ***a)*** *Distribution of stations used for repeating earthquake classification. Gray dots are the total aftershock catalogue. Color of the station denotes the number of days they are active within the study period. Shape of the*

station denotes the earliest time they become active during the study period. ***b)*** *Availability of stations used for repeating earthquake classification. Red vertical line shows the occurrence of the mainshock (April 16th, 2016)*

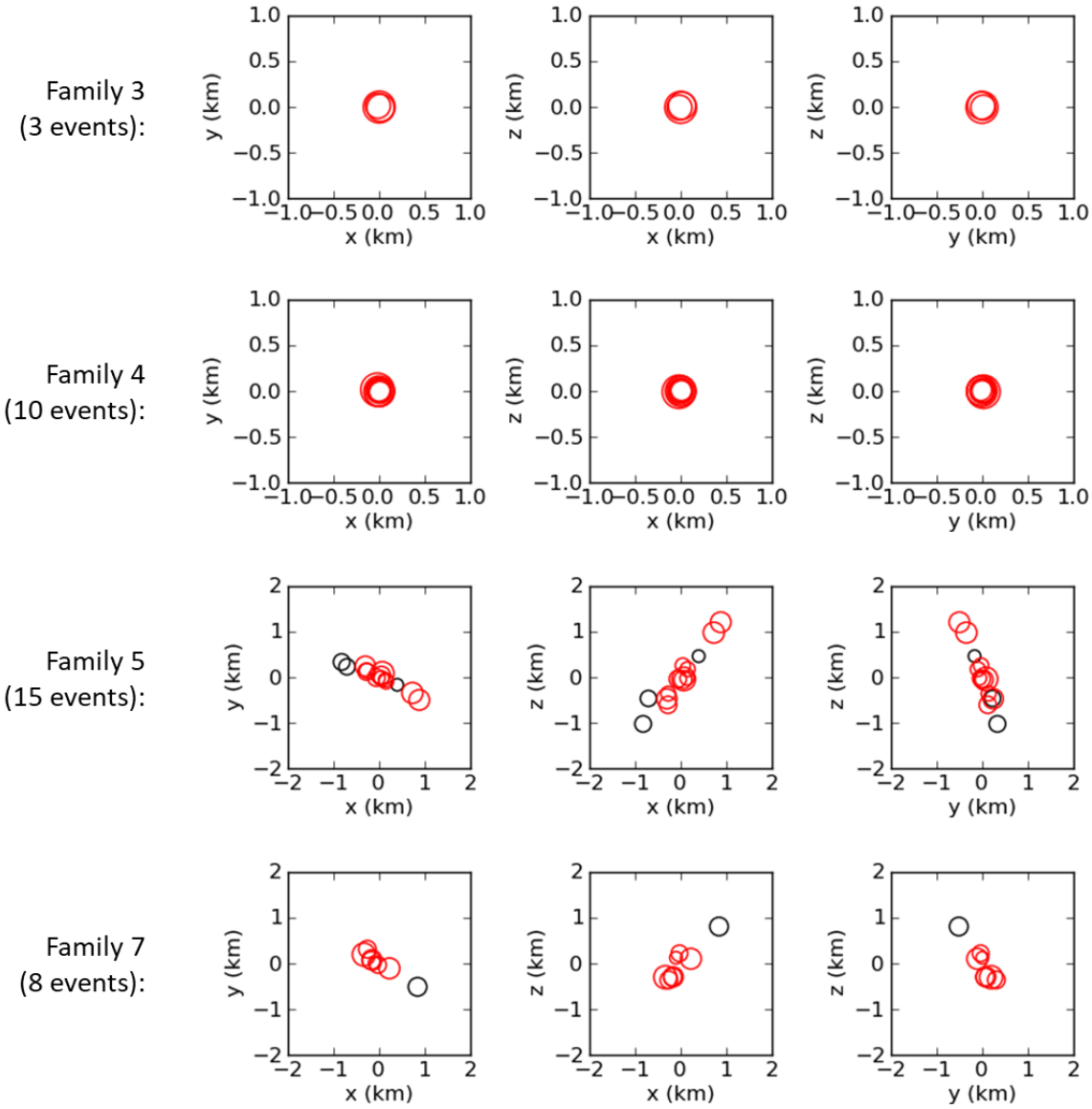

Figure SC.3: Relative relocation of events in 4 families, using HypoDD. Red circles represent events with overlapping rupture zones and black circles are isolated events.

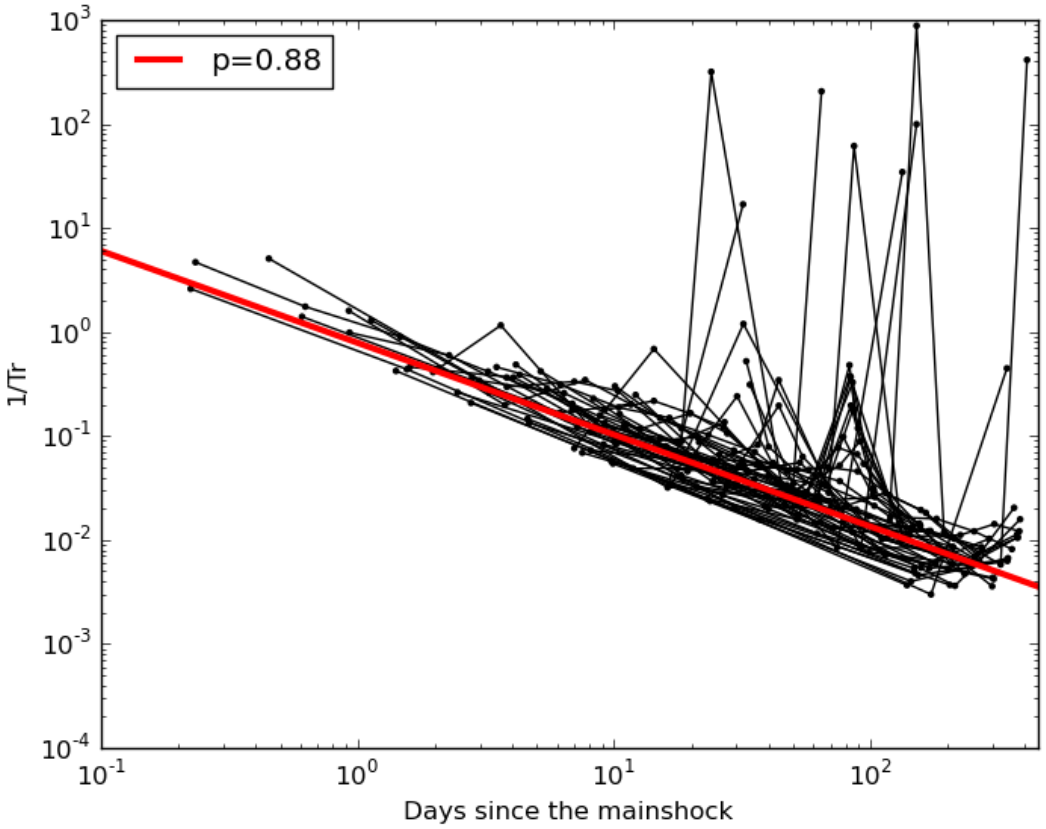

Figure SC.4: Evolution of recurrence time (Tr) with time after the mainshock. The families' average recurrence time decay is shown as a red line with a slope of p=-0.88.

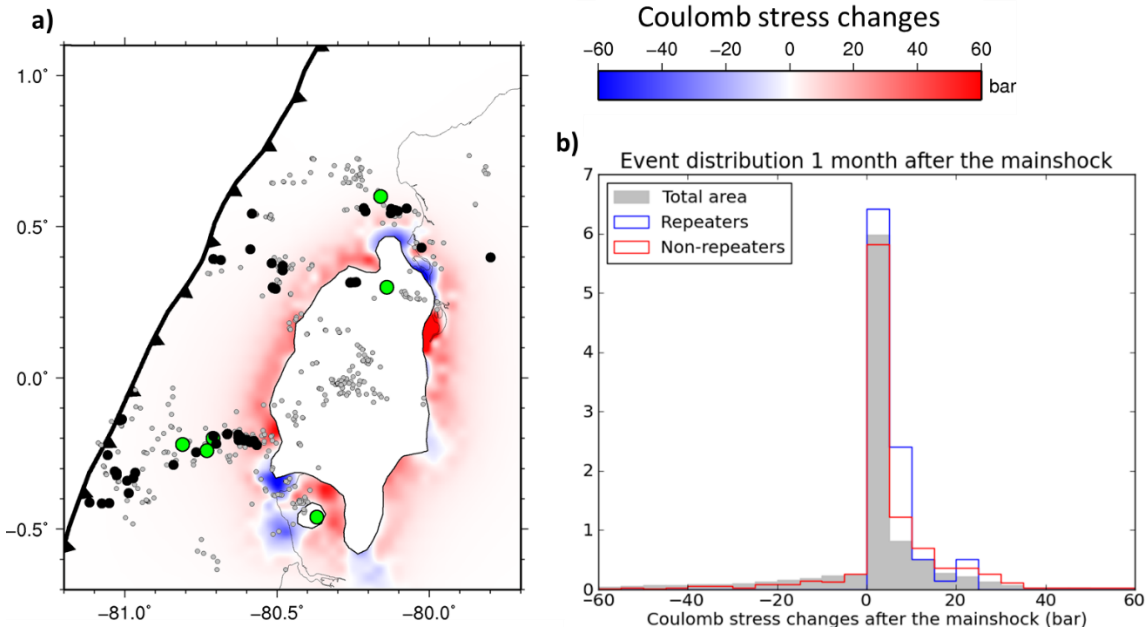

Figure SC.5: Coseismic Coulomb failure stress changes induced by the mainshock at the subduction interface, from Rolandone et al. (2018). ***a)*** *Map of repeating families started within the first month (in black) and relocated non-repeaters*

(in grey). The area within the rupture is masked and outlined in black. Large green circles are aftershocks with local magnitudes above 6. ***b)*** *Distribution of first month events with regards to the coseismic stress changes induced by the mainshock. Only events outside of the mainshock rupture zone are used.*

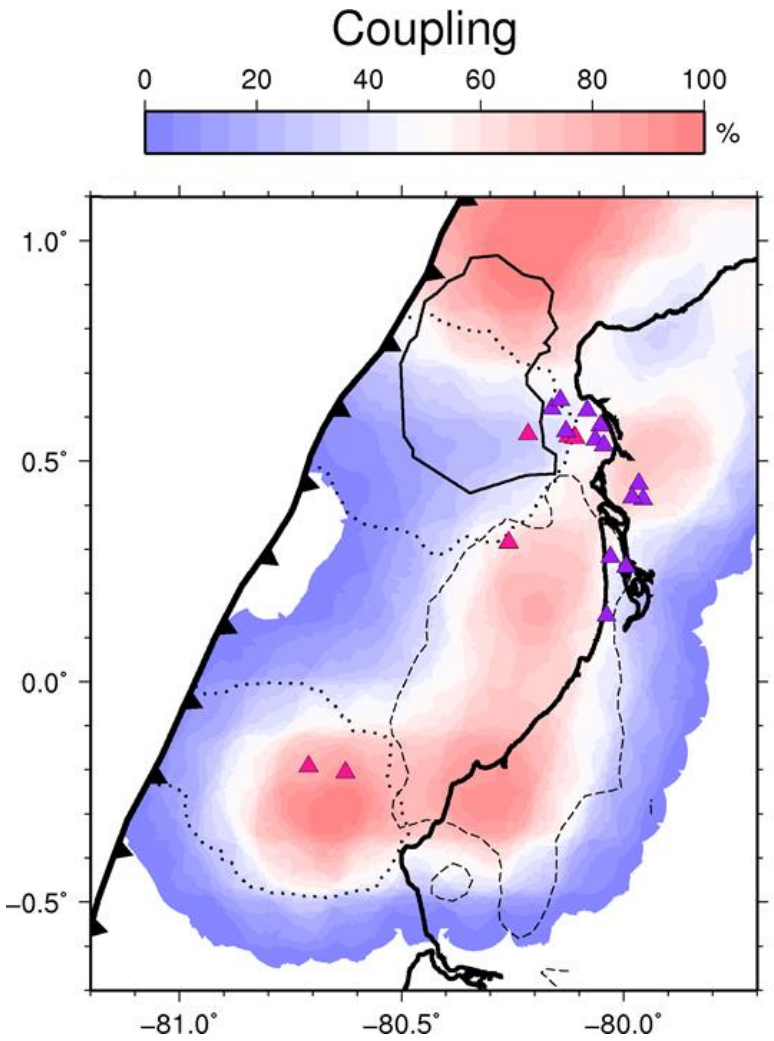

Figure SC.6: Interseismic repeating earthquakes detected in this study (pink triangles), and possible repeaters (purple triangles) detected by Vaca et al., (2018) in 2013. The 20 mm contour of the 2013 slow slip event (Vaca et al., 2018) is shown as a full black line. Interseismic coupling from Nocquet et al., (2014) is shown in red and blue. The 1 m contour of the Pedernales rupture, and the 200 mm contours of the afterslip, are shown as dashed and dotted lines respectively.

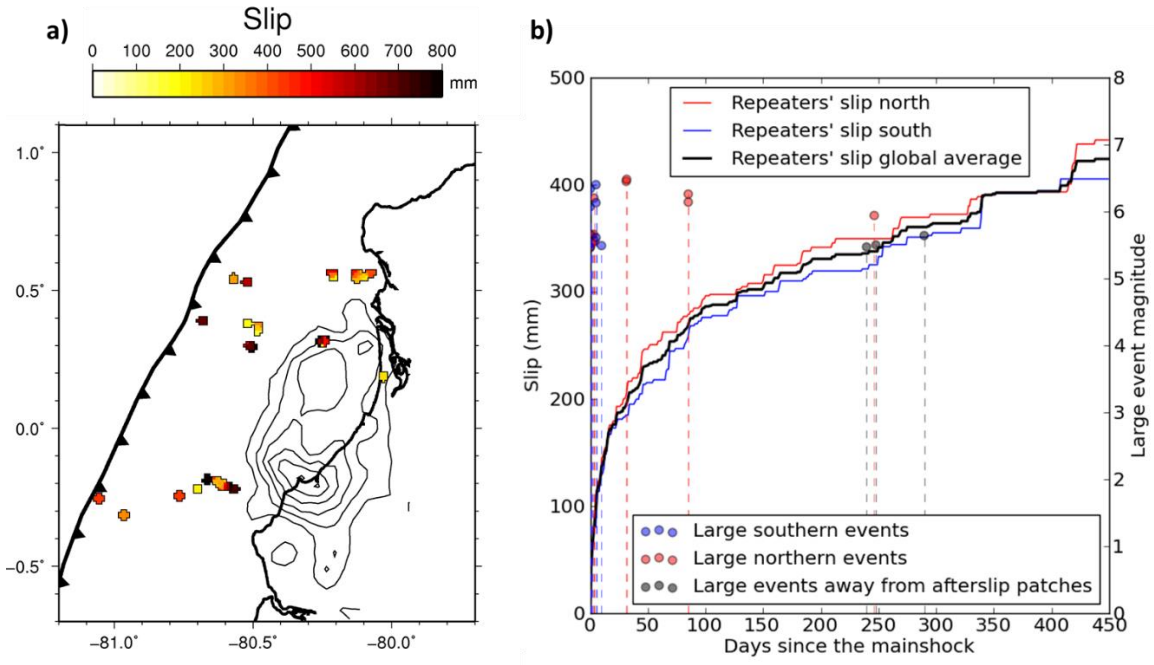

Figure SC.7: One-year slip calculated from repeaters. Only families that were active for 7 months or more are used here. ***a)*** *Map showing the slip calculated from repeaters in the 14 months after the mainshock (outlined areas).* ***b)*** *Average cumulative afterslip experienced in 14 months by repeating families within 50 km of the northern (red) and southern (blue) patch, and over the whole area (black). Red and blue circles represent earthquakes with Ml>5.5 occurring in the north and south respectively.*

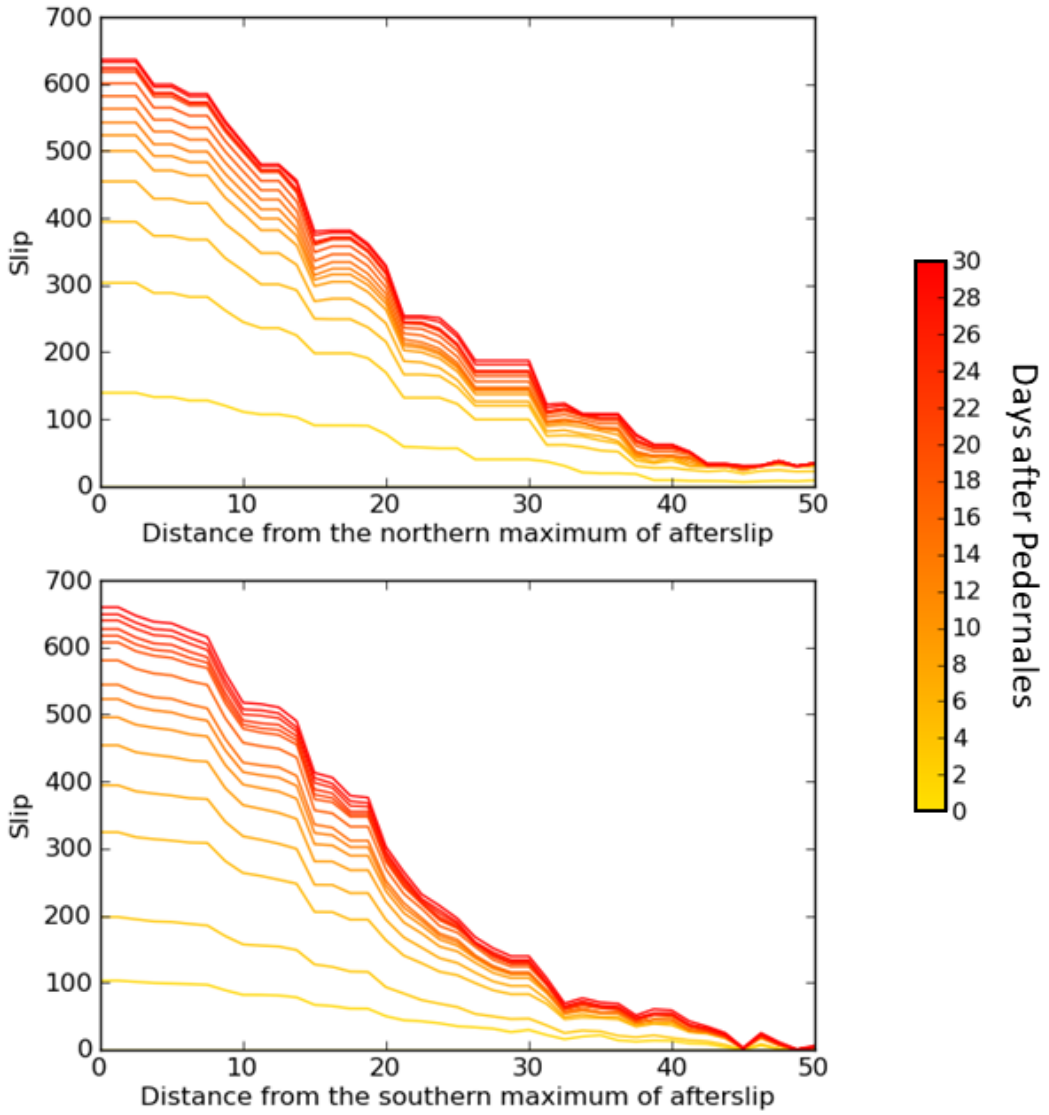

Figure SC.8: Daily average slip as a function of distance from the center of the afterslip. One month afterslip by Rolandone et al. (2018).

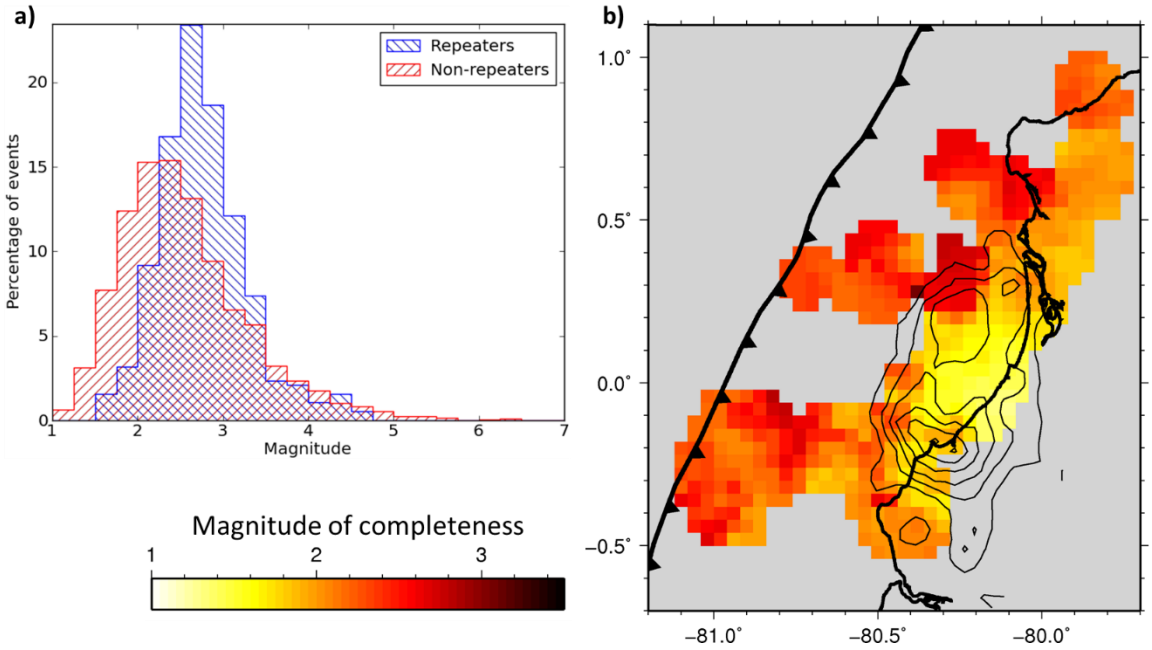

Figure SC.9: Catalogue magnitudes. ***a)*** *Frequency distribution of aftershock (red) and repeater (blue) magnitudes.* ***b)*** *Map showing the magnitude of completeness of the whole catalogue over the whole time period, including the new repeaters found through template-matching.*

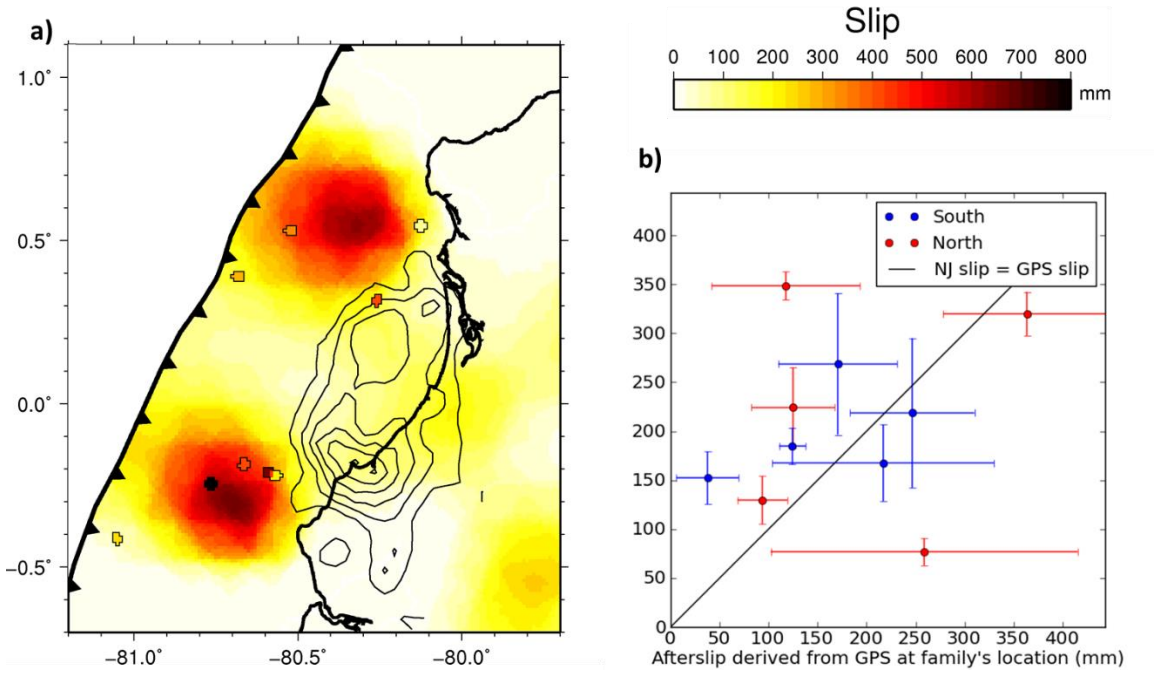

Figure SC.10: GPS-derived slip compared to slip from families with median magnitudes above 3 and minimum magnitudes above 2.7. ***a)*** *Total aseismic slip after 1 month (Rolandone et al., 2018). Outlined patches represent slip calculated from repeating families with 2 or more events in the first month, using the NJ equation. For easier comparison both among families and with the geodetic model, NJ slip from each family was extrapolated to one month, using the ratio of slip calculated using the NJ equation to slip modeled by GPS between the first and last repeater of the month. Each cell averages slip from families within a 2 km radius.* ***b)*** *Aseismic slip experienced by a family between the first and the last repeater of the first month, estimated from the geodetic model versus estimated using the NJ equation. Only families with 2 or more events*

in the first month, and more than a day between the first and the last event of the month, are used. Families within 50 km of the northern and southern afterslip patch are shown in red and blue respectively.

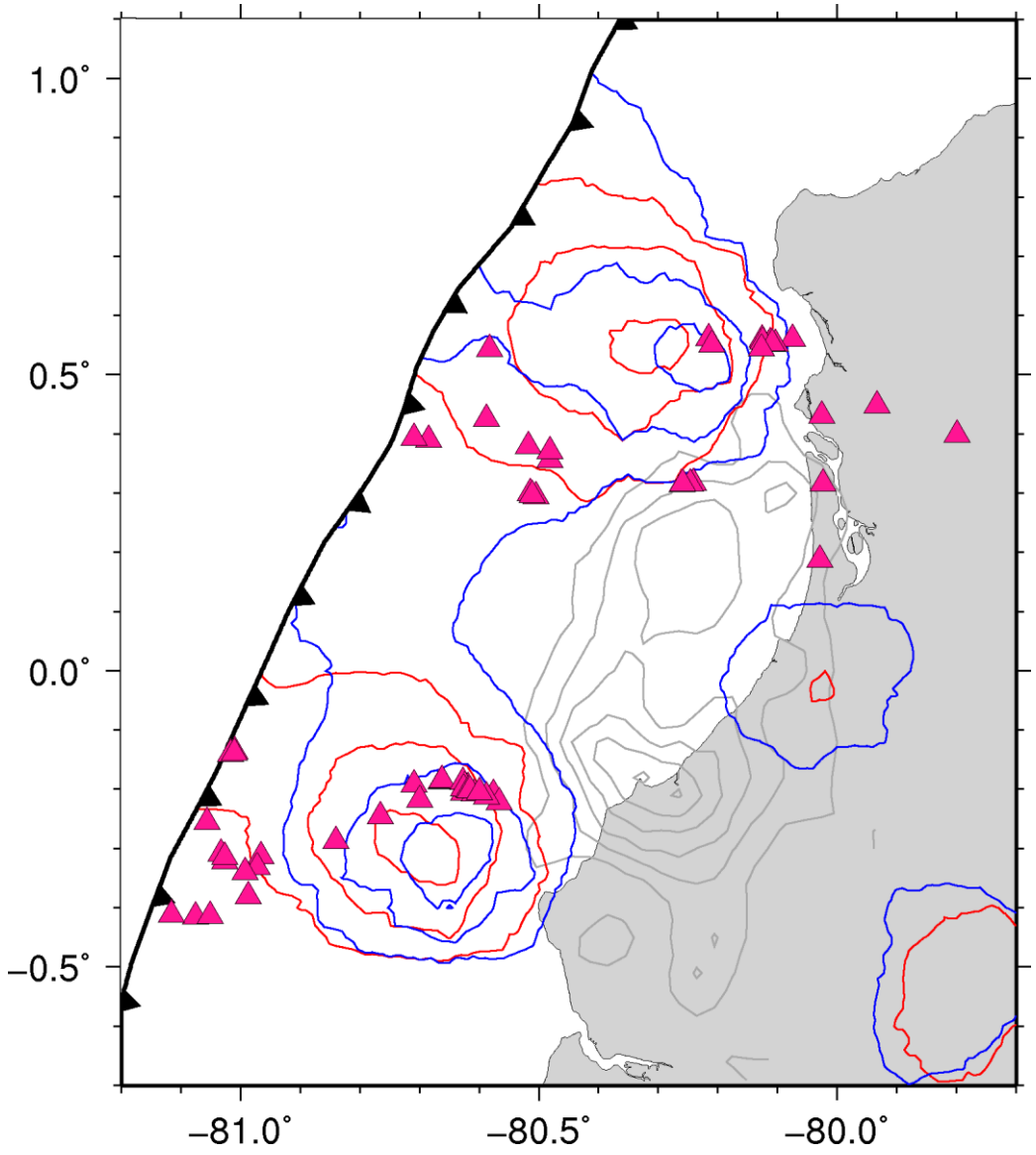

Figure SC.11: Comparison of two one-month afterslip models: the Rolandone et al. (2018) afterslip model in red and the Tsang et al., (2019) afterslip model in blue. Contour lines are every 200 mm. The coseismic rupture is shown in grey. Pink triangles are repeating families.

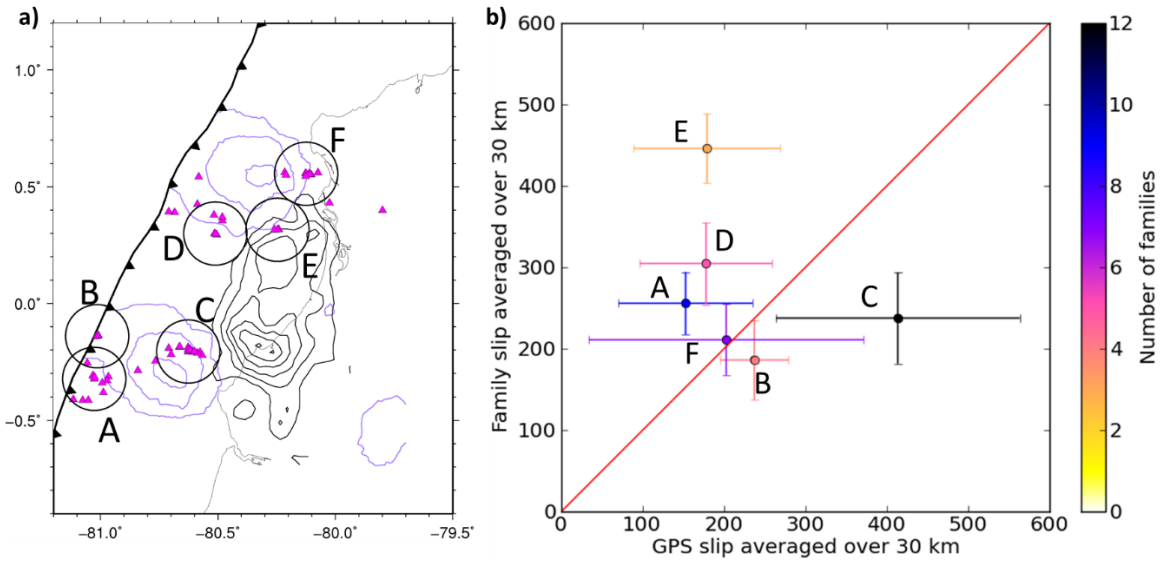

*Figure SC.12: Regional comparisons of GPS-derived and repeaters-derived slip **a)** Map of first month families (pink triangles) with the 20 cm afterslip contours (purple lines). The six regions shown all have a 30 km diameter and contain 3 or more families with 2 or more events in the first month. **b)** Comparison of aseismic slip experienced in first month by the six regions shown in a), estimated from the geodetic model Vs estimated using the Nadeau and Johnson equation. Only families with 2 or more events in the first month, and more than a day between the first and the last event of the month, are used. Colors show the number of families used for the average per region.*

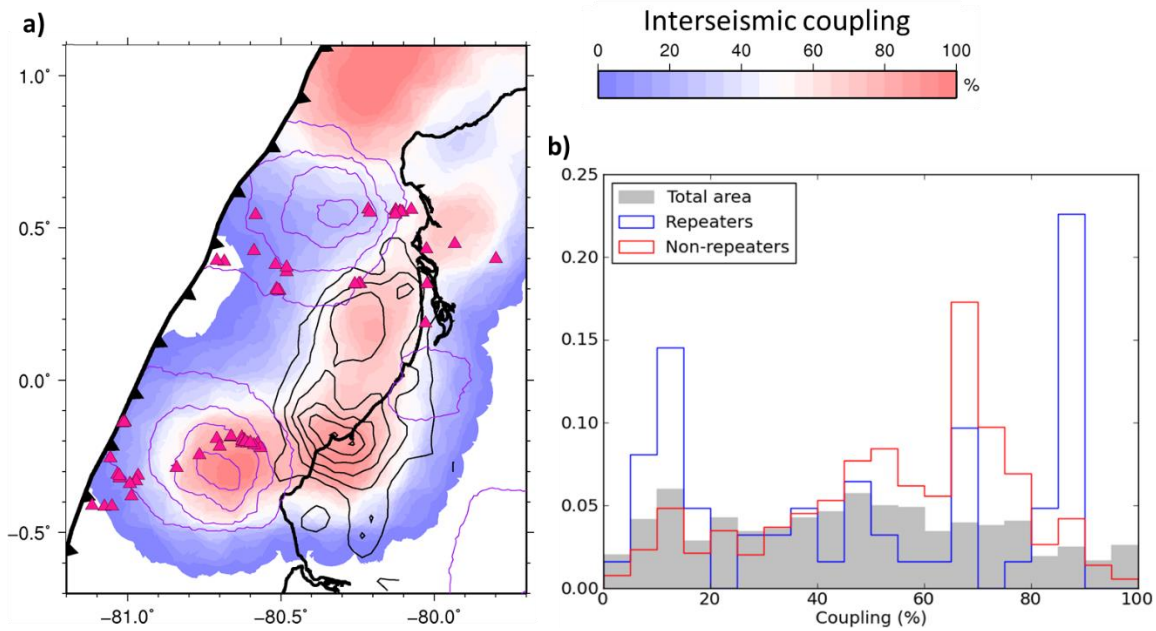

*Figure SC.13: Location of repeaters and interseismic coupling **a)** Map of repeating families (pink triangles) overlaying the interseismic coupling model (Nocquet et al., 2014). In purple are the 150 mm contours of the one-month afterslip model (Rolandone et al., 2018). The coseismic rupture is shown in black. **b)** Percentage of events in areas experiencing a given amount of interseismic coupling. Non-repeating earthquakes are shown in red and repeating earthquakes are shown in blue. In grey is the percentage of the study area experiencing a given amount of interseismic coupling.*

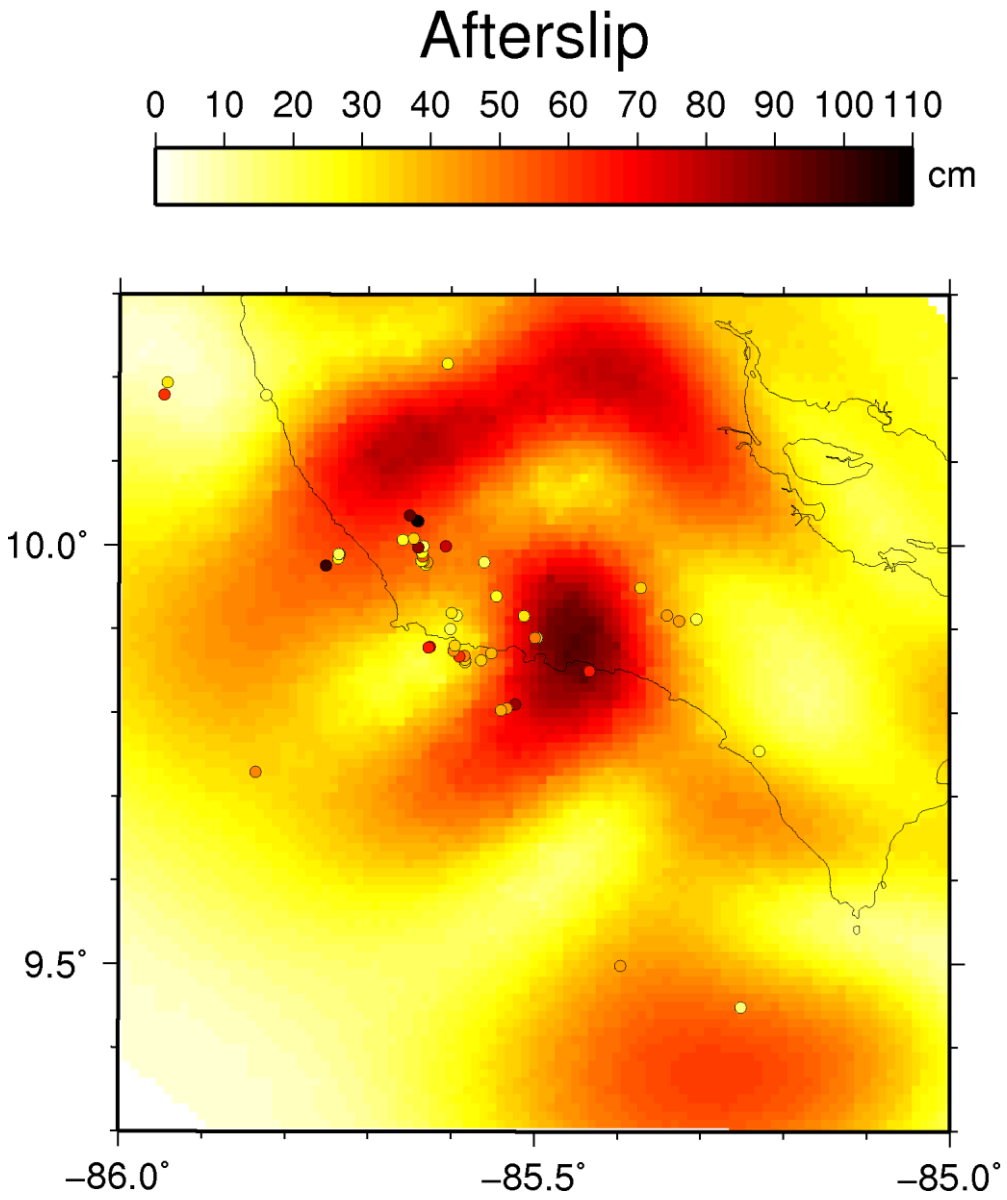

Figure SC.14: Repeating earthquakes from Costa rica after the 2012 Nicoya earthquake (Yao et al., 2017), along with the 3-month afterslip model (Yao et al., 2017). Families are colored by slip calculated with the NJ equation, experienced between September 5th and December 31st 2012.

Tableau SC.1: Correlation coefficient computation parameters, used to sort repeaters into families

Station	Time before P arrival (s)	Time after P arrival (s)	Frequency band (Hz)	Maximum distance from station (km)
AGOS	2	28	2 to 9	140
CABP	2	28	2,5 to 10	140
EC03	2	28	3 to 10	140
EC12	2	28	2 to 9	140
EC14	2	28	2 to 9	140
EC15	2	28	1,5 to 9	140

EC16	2	28	2,5 to 10	140
EC18	2	28	1,5 to 9	140
ELOY	2	28	1,5 to 9	140
FLF1	2	28	3,5 to 10	140
LGCB	2	28	1,5 to 9	140
LUCE	2	28	1,5 to 9	140
NOVI	2	28	2 to 9	140
OTAV	2	55	1,5 to 9	280
PDNS	2	28	2,5 to 10	140
PTGL	2	28	2,5 to 10	140
SEVS	2	28	1,5 to 9	140

Appendix D:Supplementary materials for Chapter 5

Text S1: Maximum resolvable corner frequency:

Corner frequencies can be underestimated when the bandwidth is limited and the maximum frequency is too low. Previous studies have estimated that corner frequencies could not be resolved if they exceeded a limit ranging from one third (Abercrombie, 2015) to two thirds (Ruhl et al., 2017) of the high frequency bandwidth limit. Here we calculate the maximum resolvable corner frequency for our dataset and workflow. At each station individually, we use well-recorded events whose corner frequency is estimated to be lower than a third of the high frequency bandwidth limit. We then calculate a new corner frequency with the maximum high frequency bandwidth limit being fixed at 10 Hz (Figure SD.5). Above 5 Hz, over 10 % of corner frequencies are underestimated by at least 25 %, while the median deviation goes from less than 2% to more than 5 %. We therefore estimate the maximum resolvable corner frequency to be half of the upper frequency limit of the data.

Text S2: Stability of the method in the postseismic period:

The goal of the spectral ratio method is to remove the effect of attenuation by comparing events that, due to their proximity, should experience the same path and site effects. However, this relies on the assumption that attenuation changes through time can be neglected, which isn't necessarily true after a large earthquake. Before proceeding to further discussions, we therefore want to ensure that our results are comparable when using earthquakes occurring at different times during the postseismic period.

We test this assumption by separating all earthquakes between early events (before July 1st 2016) and late events (after July 1st 2016). At a given station, for every reference event, we calculate 2 values of fc and M0: one using spectral ratios of other events only from the early period, and the other using spectral ratios of other events only from the late period. To ensure stability, we only use events that were paired with at least 4 other events in both time periods. In our initial methodology, the absolute value of M0 was calibrated by averaging all the starting values of M0 within the cluster, and setting it to remain constant during the inversion. However, if we do the same here for the early and late groups, then the final difference in M0 for the reference event will reflect errors in the starting values of M0 for the early events and the late events. Therefore, we instead decided to calibrate seismic moments by keeping constant one

event M0 among early events and one among late events, and by separately obtaining the magnitude difference between these two events using their ratio, in order to correct the reference event magnitude difference.

We find that there are no systematic differences between the values of fc and Mw calculated using only early events, and the values of fc and M0 calculated using only late events (Figure SD.12). We do see some scatter for corner frequencies, as expected given the low number of pairs available, but no bias. We conclude that, if there are attenuation changes, they do not invalidate the use of spectral ratios in our case, as results remain consistent whether we use early or late aftershocks.

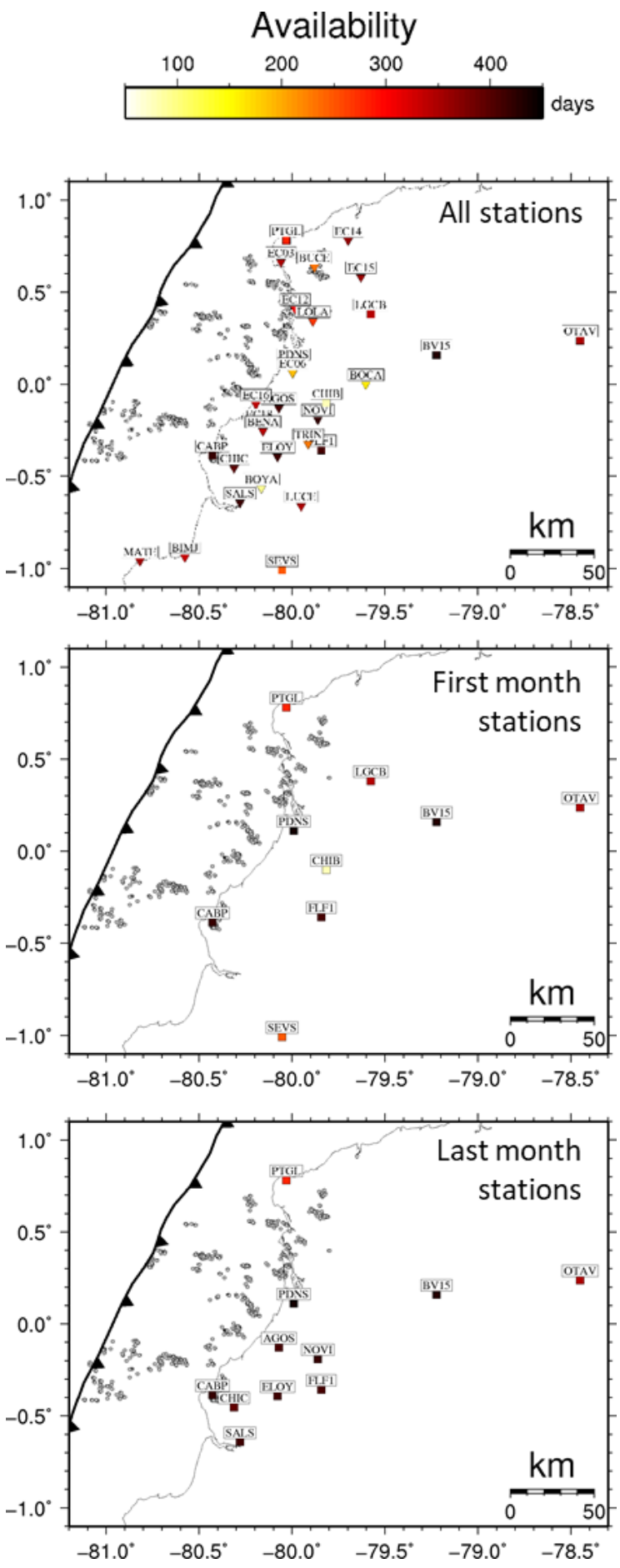
Availability
100
200
300
400
days
All stations
First month stations
Last month stations
km
0
50
1.0°
0.5°
0.0°
−0.5°
−1.0°
−81.0°
−80.5°
−80.0°
−79.5°
−79.0°
−78.5°
PTGL
EC14
EC03
BUCE
EC15
EC12
LOLA
LGCB
OTAV
BV15
PDNS
EC06
BOCA
EC16
AGOS
CHIB
NOVI
BENA
TRIN
FLF1
CABP
ELOY
CHIC
BOYA
SALS
LUCC
MATI
BIMJ
SEVS

Figure SD.1: Map of stations used. The top panel shows all stations used to calculate source properties, with color showing the number of days they were available. The middle panel shows the stations that were available at any point during the first month. The bottom panel shows the stations that were available at any point during the last month.

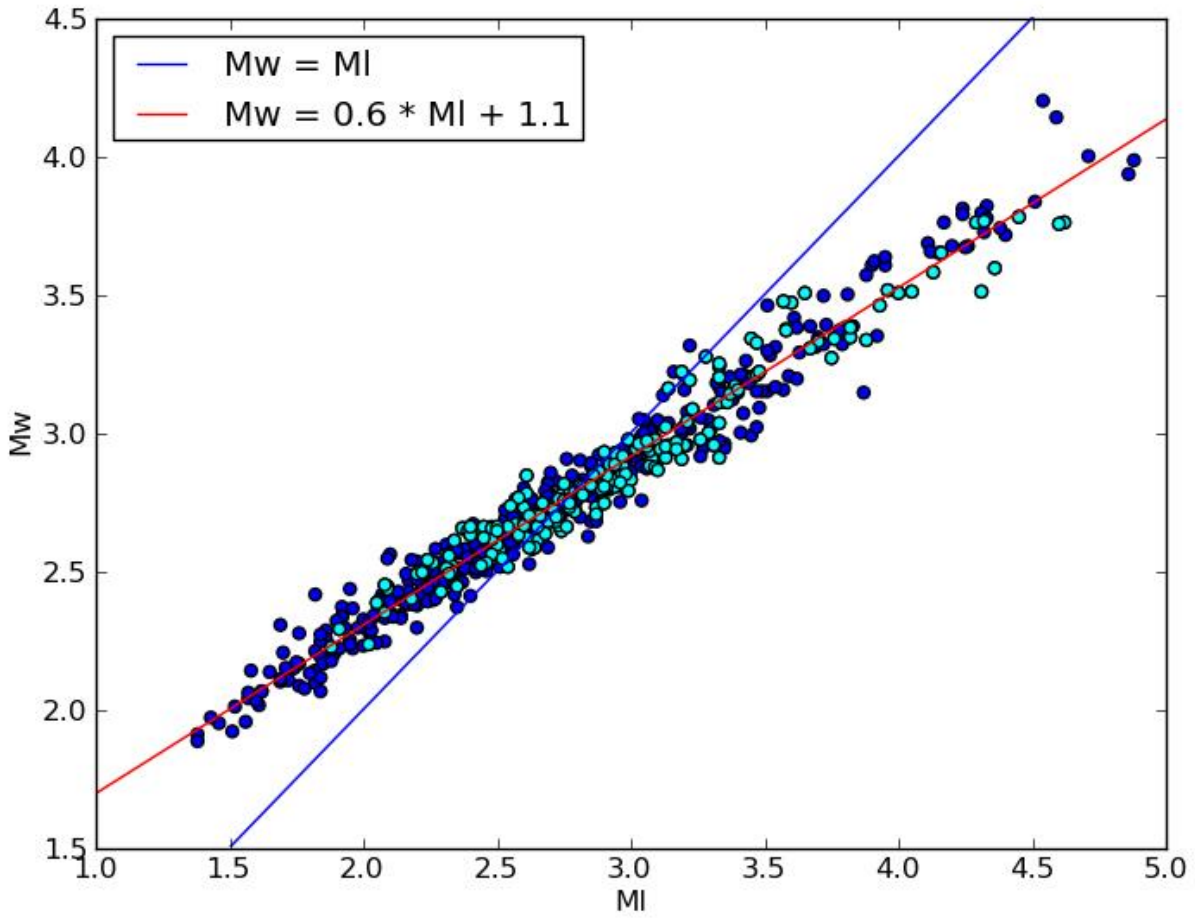

Figure SD.2: Relationship of local magnitude to moment magnitude for all earthquakes. The red line is the least squares fit to the data. Light blue dots are repeaters and dark blue dots are non-repeaters.

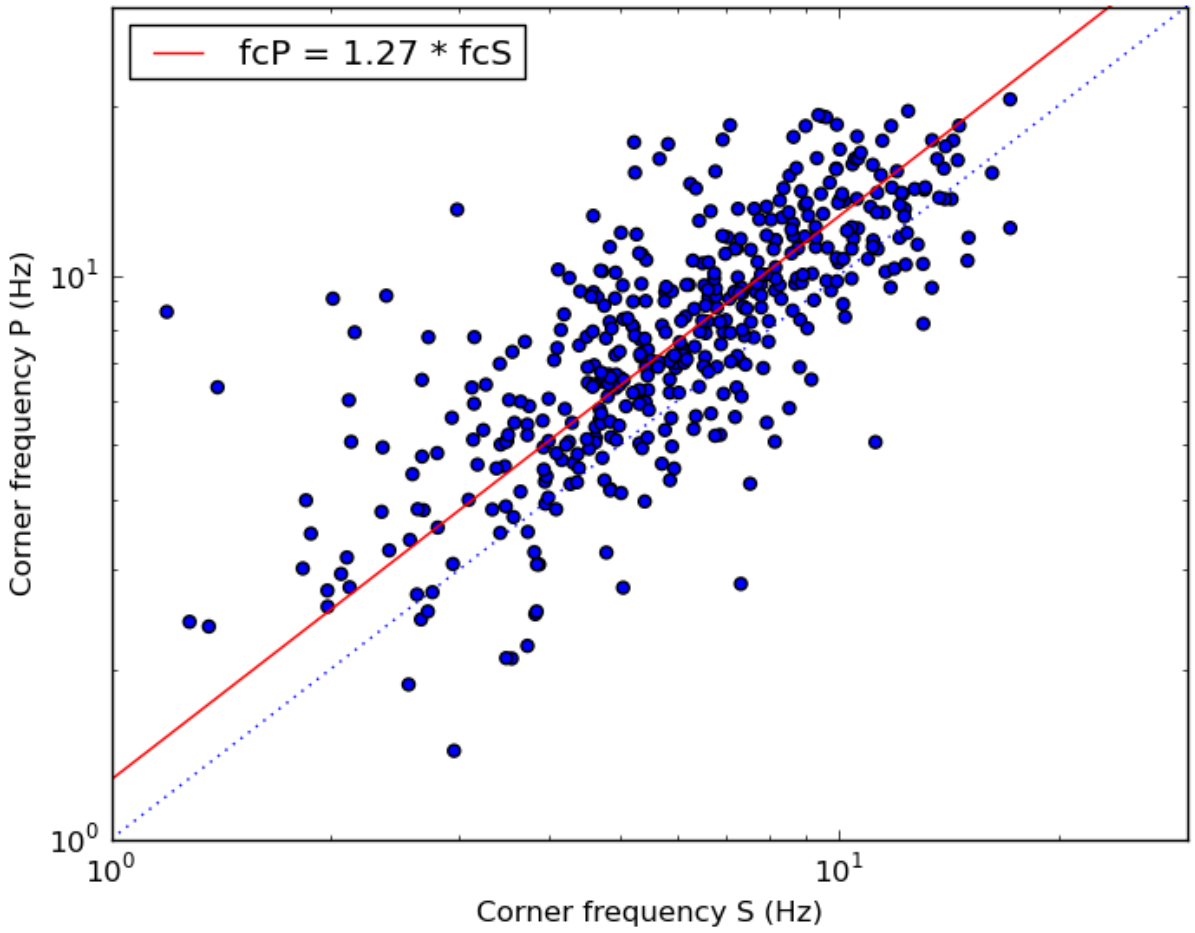

Figure SD.3: P Vs S corner frequencies averaged at the same stations. The red line represents the median P/S corner frequency ratio.

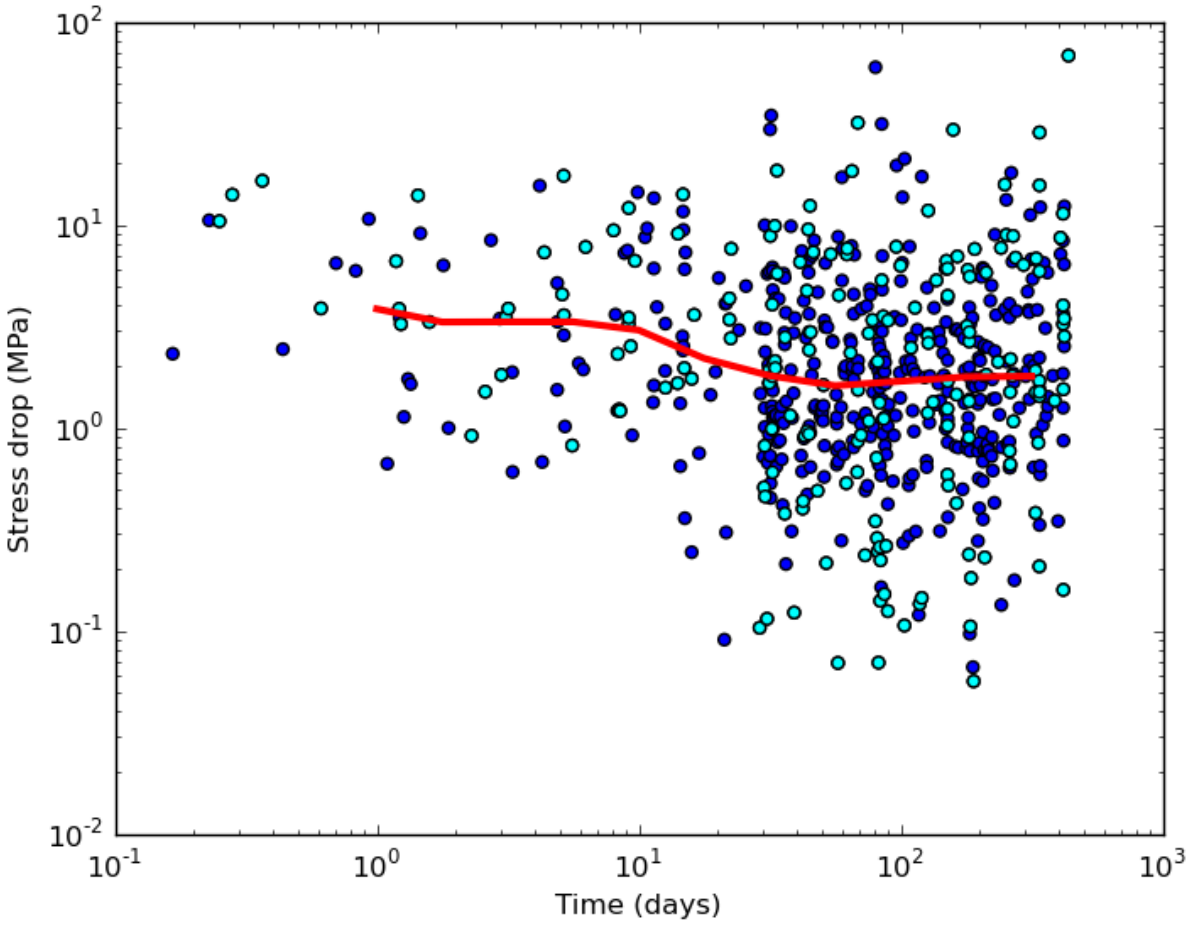

Figure SD.4: Stress drop calculated as a function of time. The red line is the median stress drop. Light blue dots are repeaters and dark blue dots are non-repeaters.

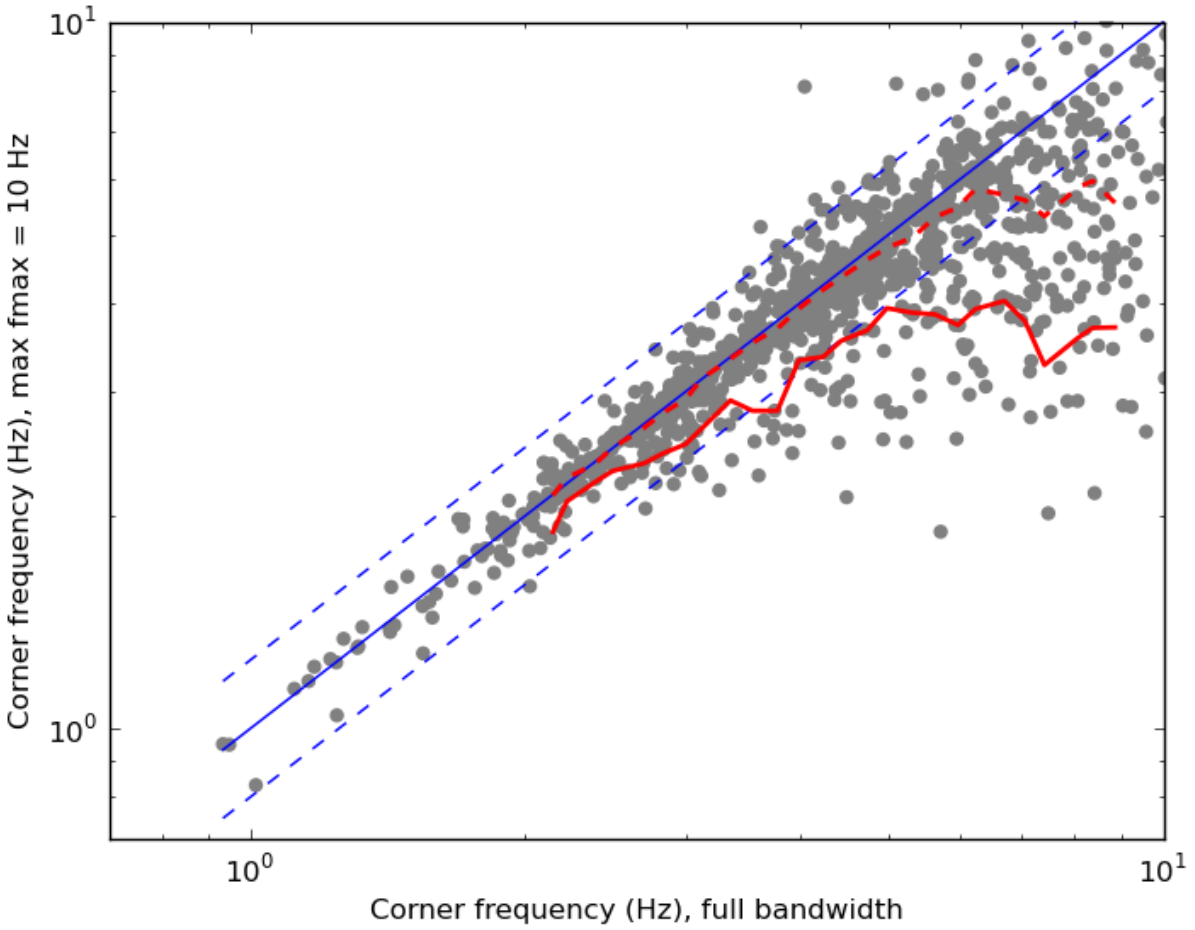

Figure SD.5: Comparison of corner frequencies calculated using the full available bandwidth Vs corner frequencies calculated using a limited bandwidth with a maximum possible frequency of 10 Hz. The dotted red line is the median restricted corner frequency as a function of the full corner frequency, and the full red line is the 10th percentile. The full blue line is the 1:1 line and the dotted lines represent plus or minus 25%. All corner frequencies are compared at a single station. All earthquakes used in this calculation had a full corner frequency lower than 50% of their upper frequency limit.

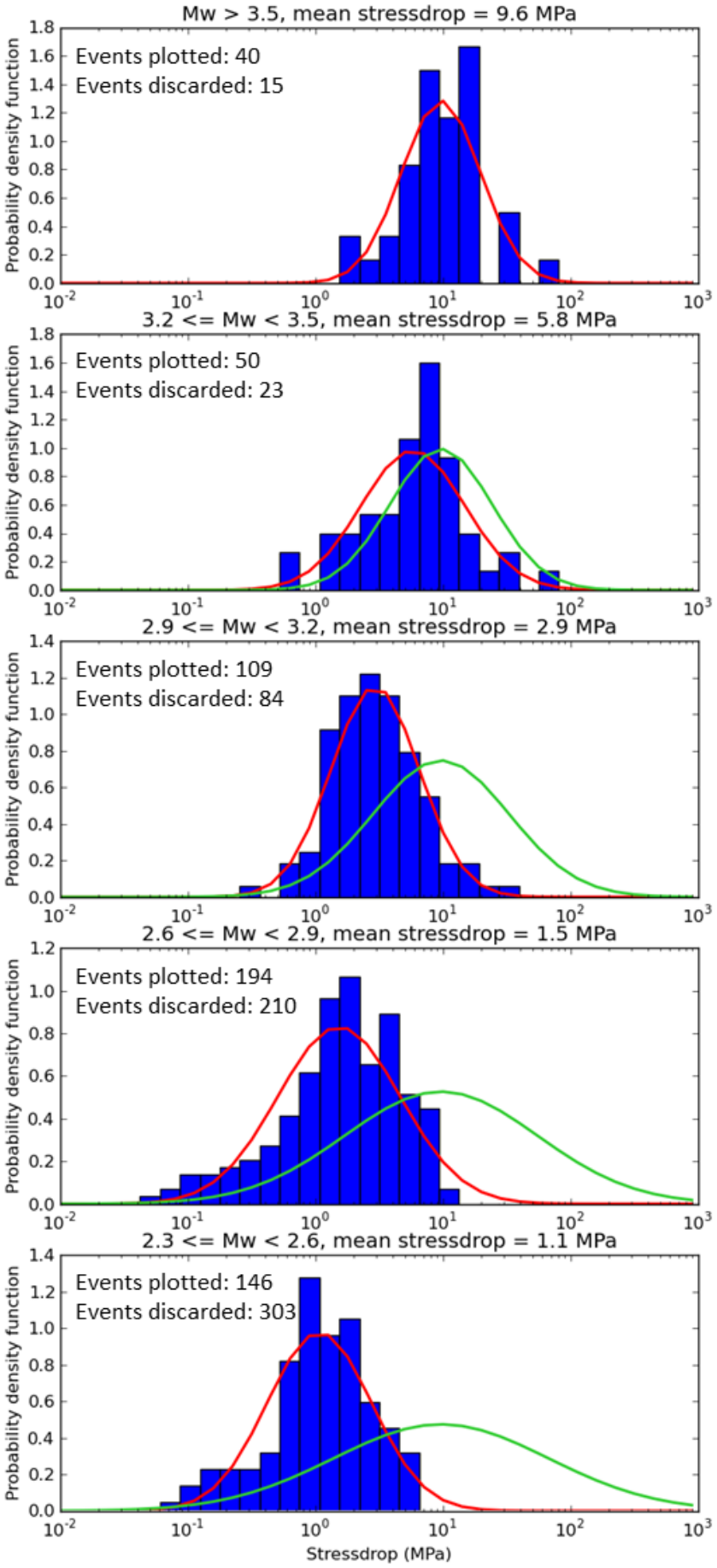
Mw > 3.5, mean stressdrop = 9.6 MPa
Events plotted: 40
Events discarded: 15
3.2 <= Mw < 3.5, mean stressdrop = 5.8 MPa
Events plotted: 50
Events discarded: 23
2.9 <= Mw < 3.2, mean stressdrop = 2.9 MPa
Events plotted: 109
Events discarded: 84
2.6 <= Mw < 2.9, mean stressdrop = 1.5 MPa
Events plotted: 194
Events discarded: 210
2.3 <= Mw < 2.6, mean stressdrop = 1.1 MPa
Events plotted: 146
Events discarded: 303
Probability density function
Stressdrop (MPa)

Figure SD.6: Distribution of stress drops at different magnitudes. We display the number of stress drops recovered within the magnitude range, as well as the number of stress drops that could not be recovered during the inversion. The red lines show the best fit for a normal distribution for each magnitude range. Green lines are normal distributions centered on 9.6 MPa with a standard deviation calculated around 9.6 MPa using all stress drops from earthquakes with magnitudes within or above the observed magnitude range. If the stress drops were constant with magnitude, and the apparent trend a result of missing high stress drop events, then the number of missing events should be able to complement the current plotted events to make the distributions of stress drops at all magnitude ranges approximate the green line. We show that, for low magnitude ranges, there are too few discarded events to account for the difference between the real distribution of stress drops, and a normal distribution centered on 9.6 MPa, represented by the green line.

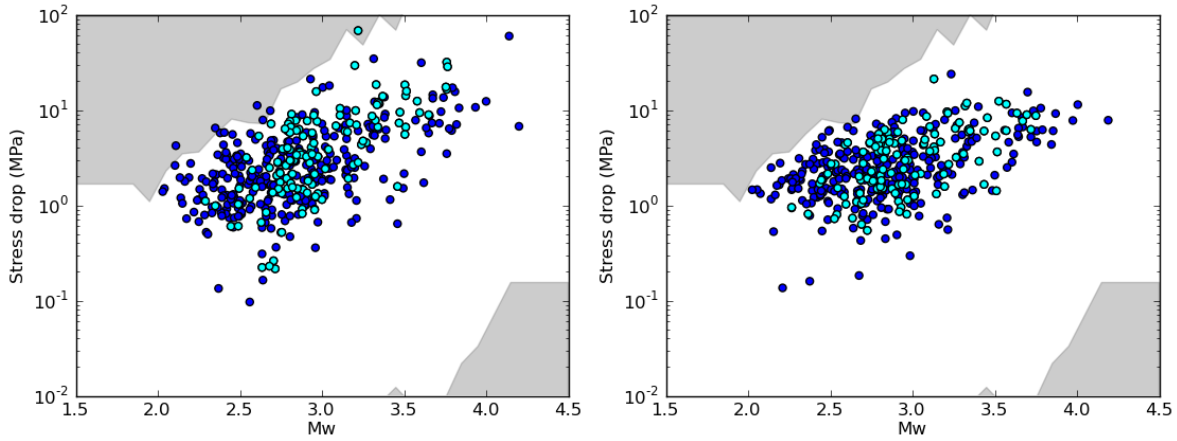

Figure SD.7: Comparison between two inversions showing the potential bias introduced by allowing all corner frequencies, even poorly resolved ones, to be free parameters when modelling spectral ratios. On the left, the normal inversion, with all corner frequencies allowed to change freely. On the right, corner frequencies outside the resolvable range for a given cluster are fixed with the assumption that the associated stress drop is 2 MPa. We apply this condition to events which either have a previously calculated corner frequency above half of the maximum frequency, or which, assuming a stress drop of 2 MPa, would have a corner frequency above half of the maximum frequency given their magnitude. We only show stress drops from lower corner frequency events.

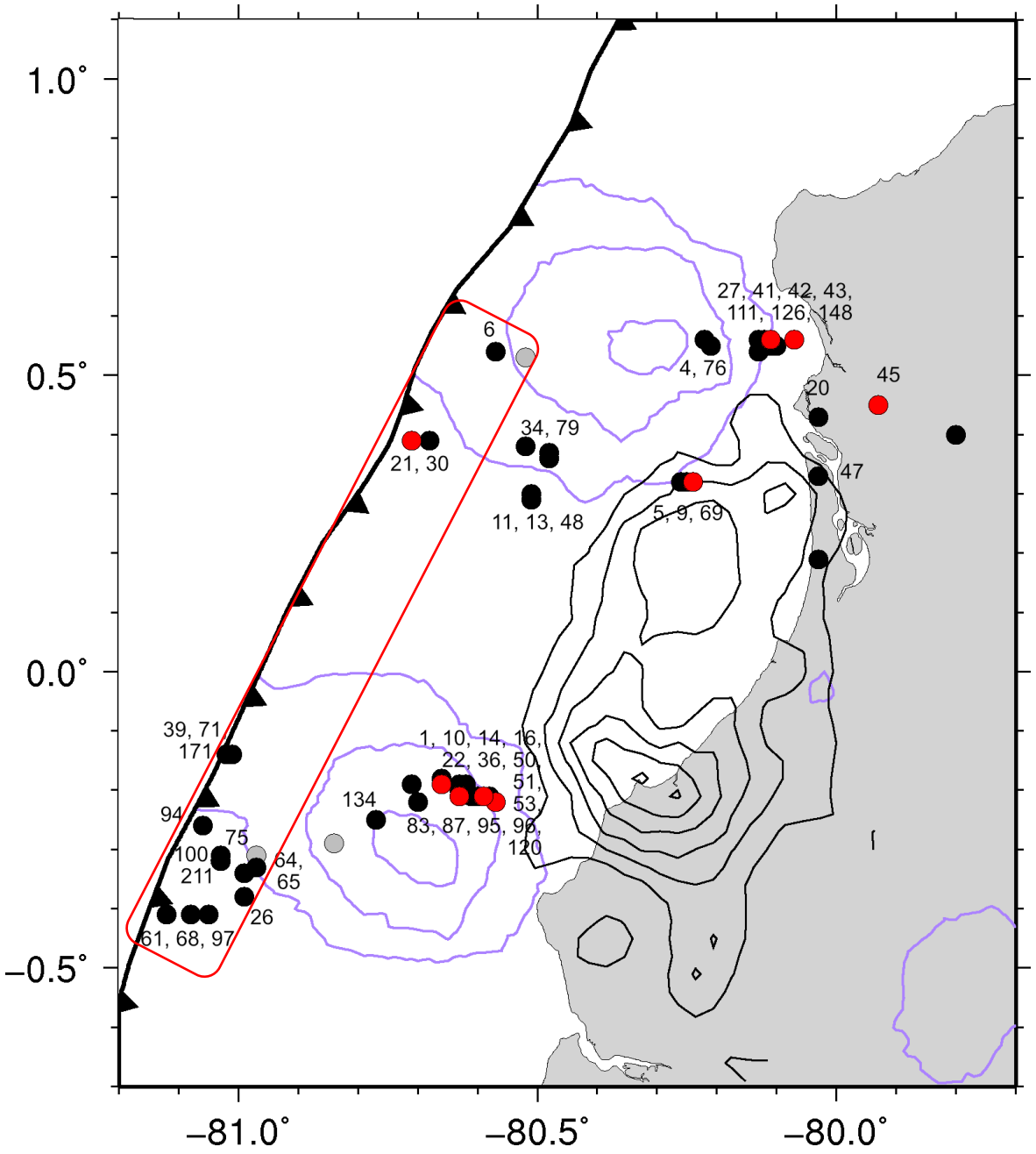

Figure SD.8: Map of all repeating earthquake families. Red circles are families where every events' source properties are recovered. Black circles are families where only some source properties are recovered. Grey circles are families where no source properties are recovered. Numbers are the names of families presented in Figure SD.9. The red box shows families near the trench with similarities in behavior.

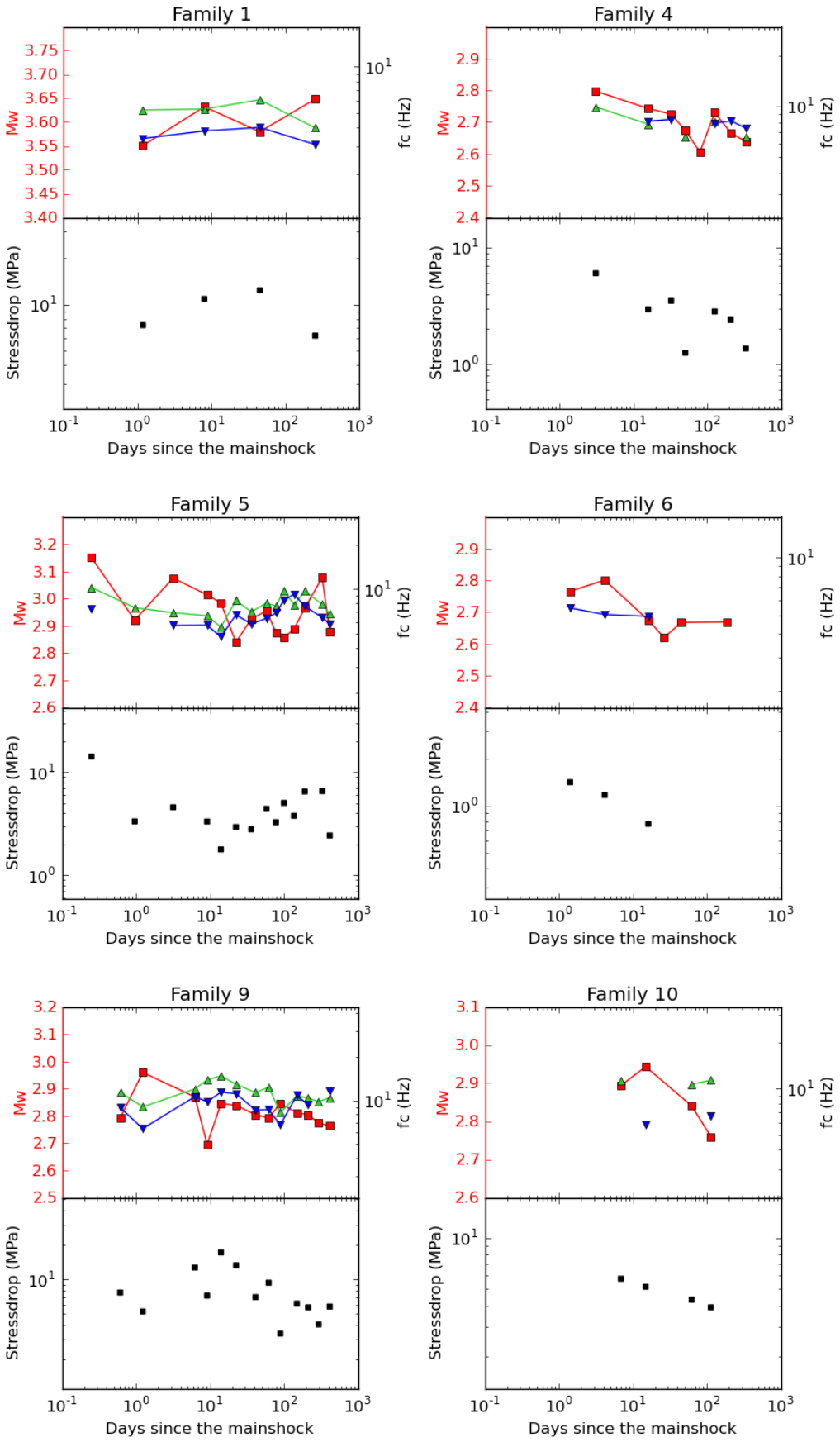
Family 1
Family 4
Family 5
Family 6
Family 9
Family 10
Mw
fc (Hz)
Stressdrop (MPa)
Days since the mainshock

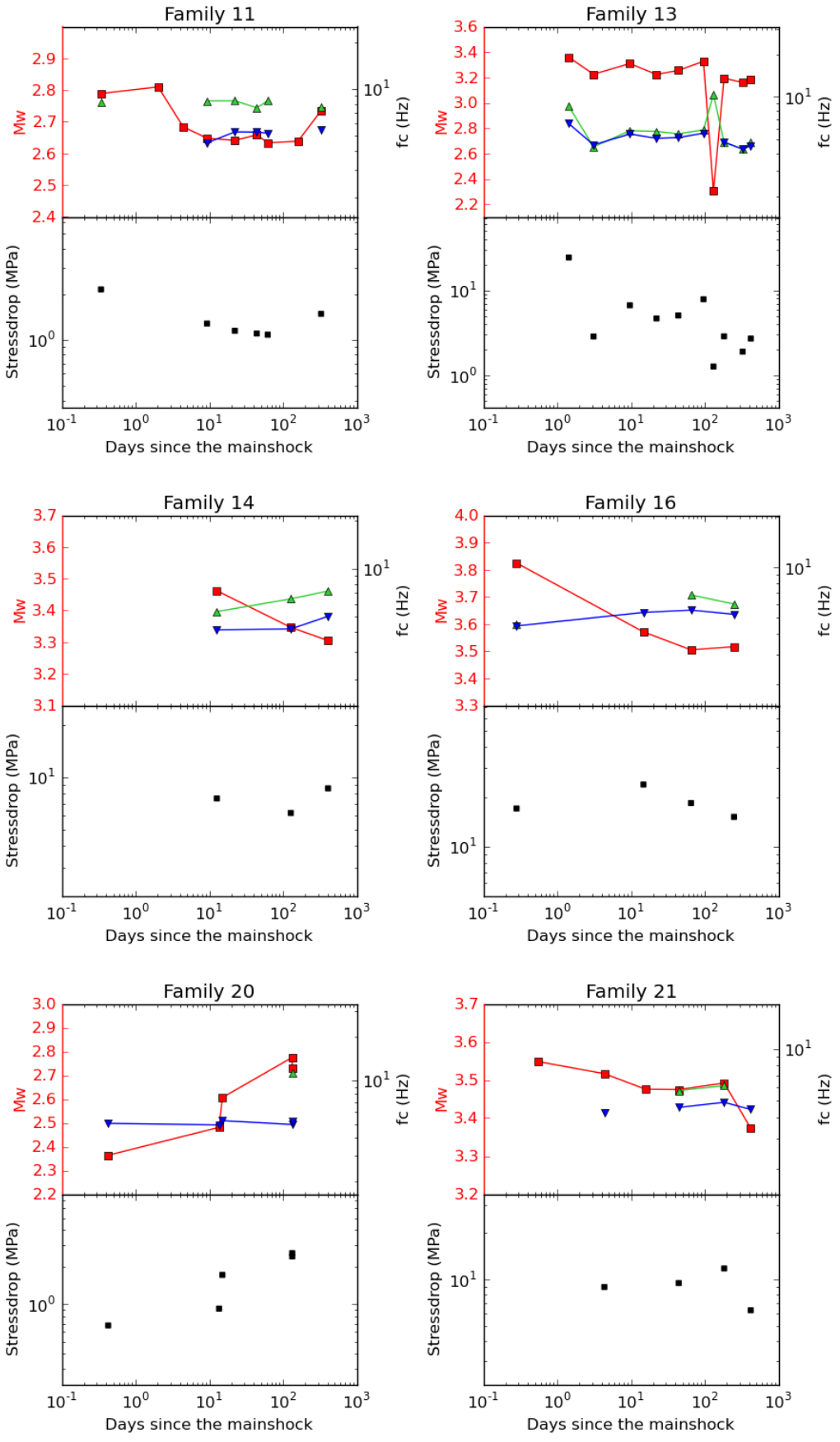
Family 11
Family 13
Family 14
Family 16
Family 20
Family 21
Mw
fc (Hz)
Stressdrop (MPa)
Days since the mainshock

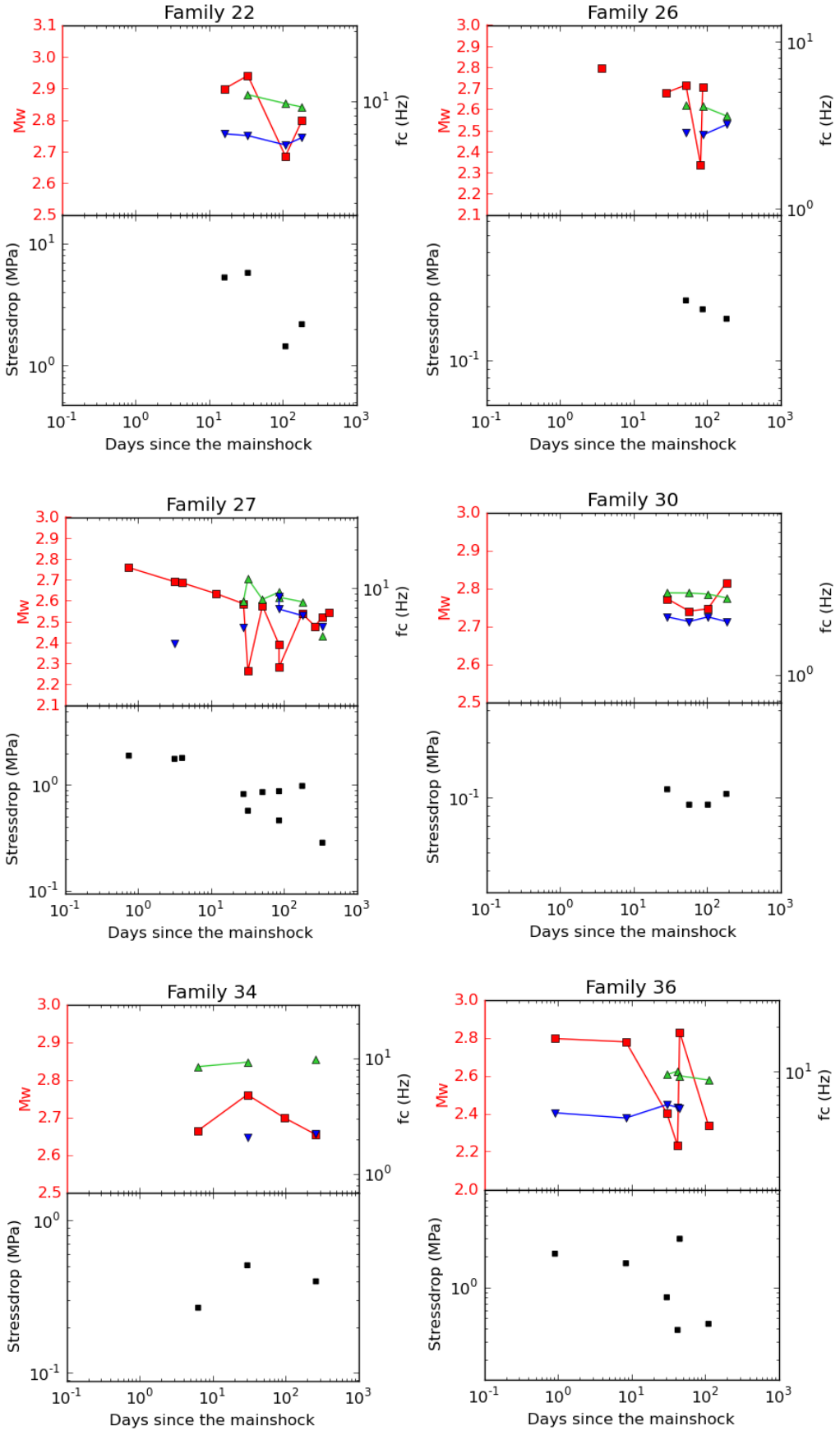
Family 22
Family 26
Family 27
Family 30
Family 34
Family 36
Mw
fc (Hz)
Stressdrop (MPa)
Days since the mainshock

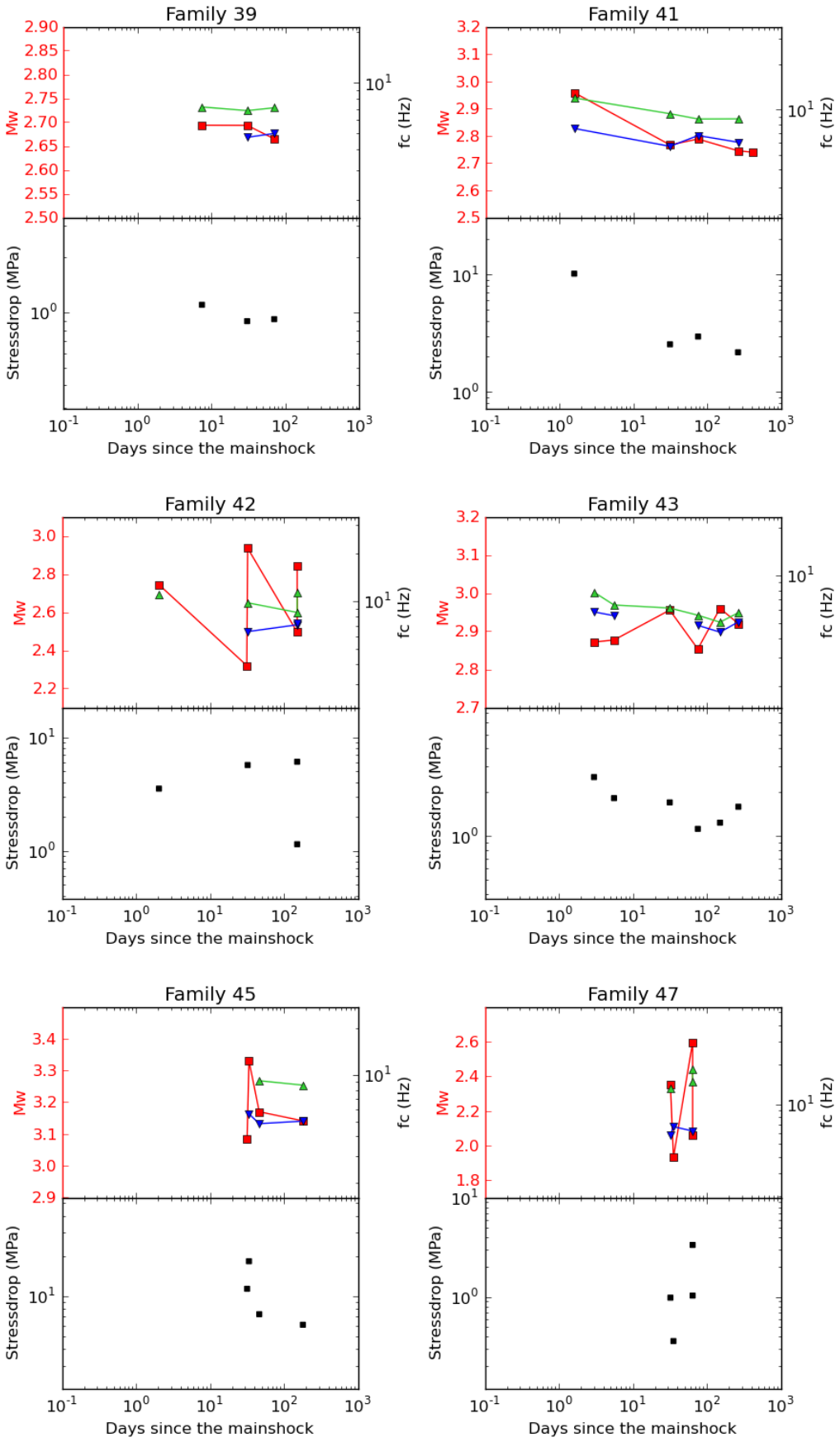
Family 39
Family 41
Family 42
Family 43
Family 45
Family 47
Mw
fc (Hz)
Stressdrop (MPa)
Days since the mainshock

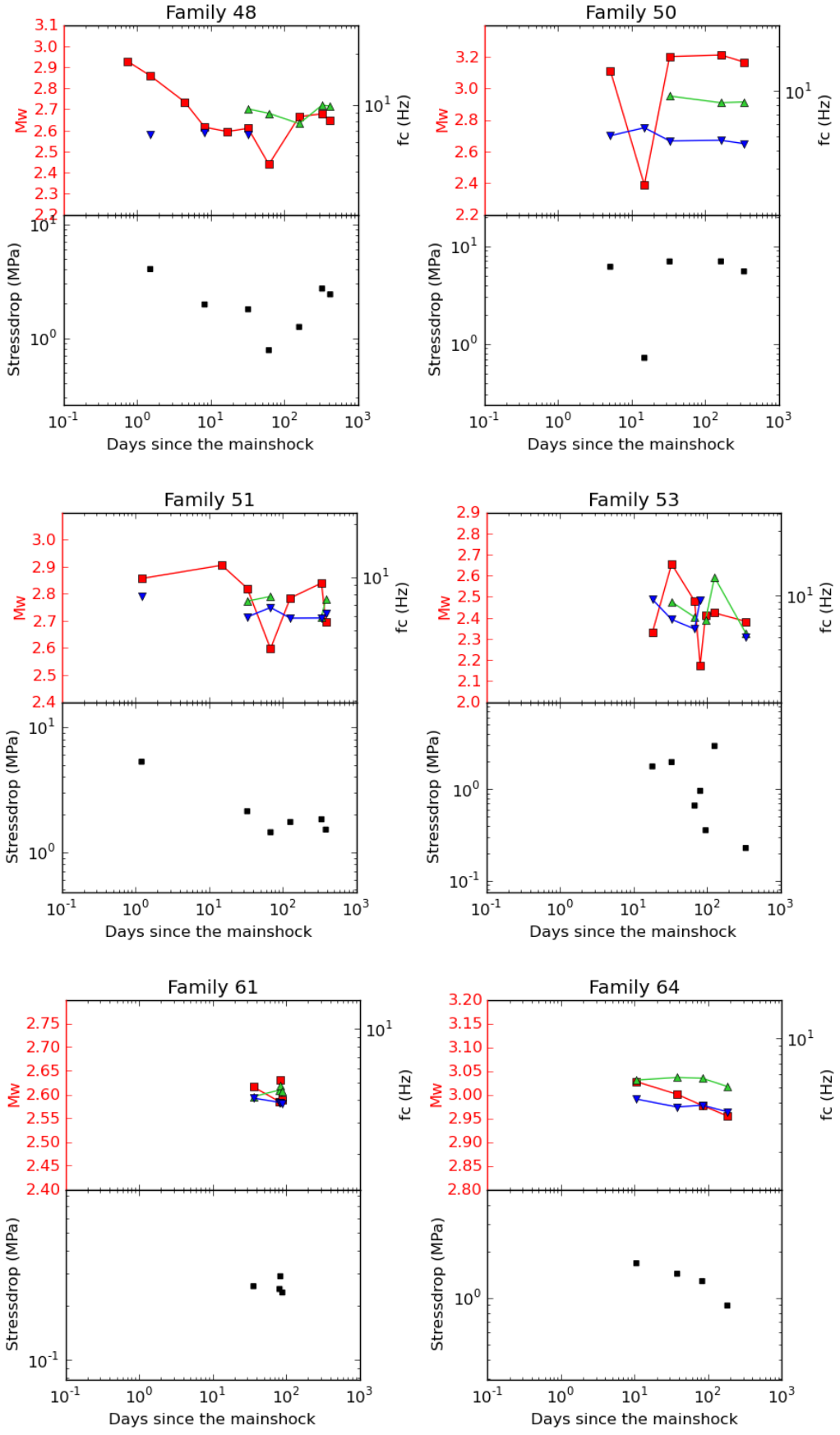
Family 48
Family 50
Family 51
Family 53
Family 61
Family 64
Mw
fc (Hz)
Stressdrop (MPa)
Days since the mainshock

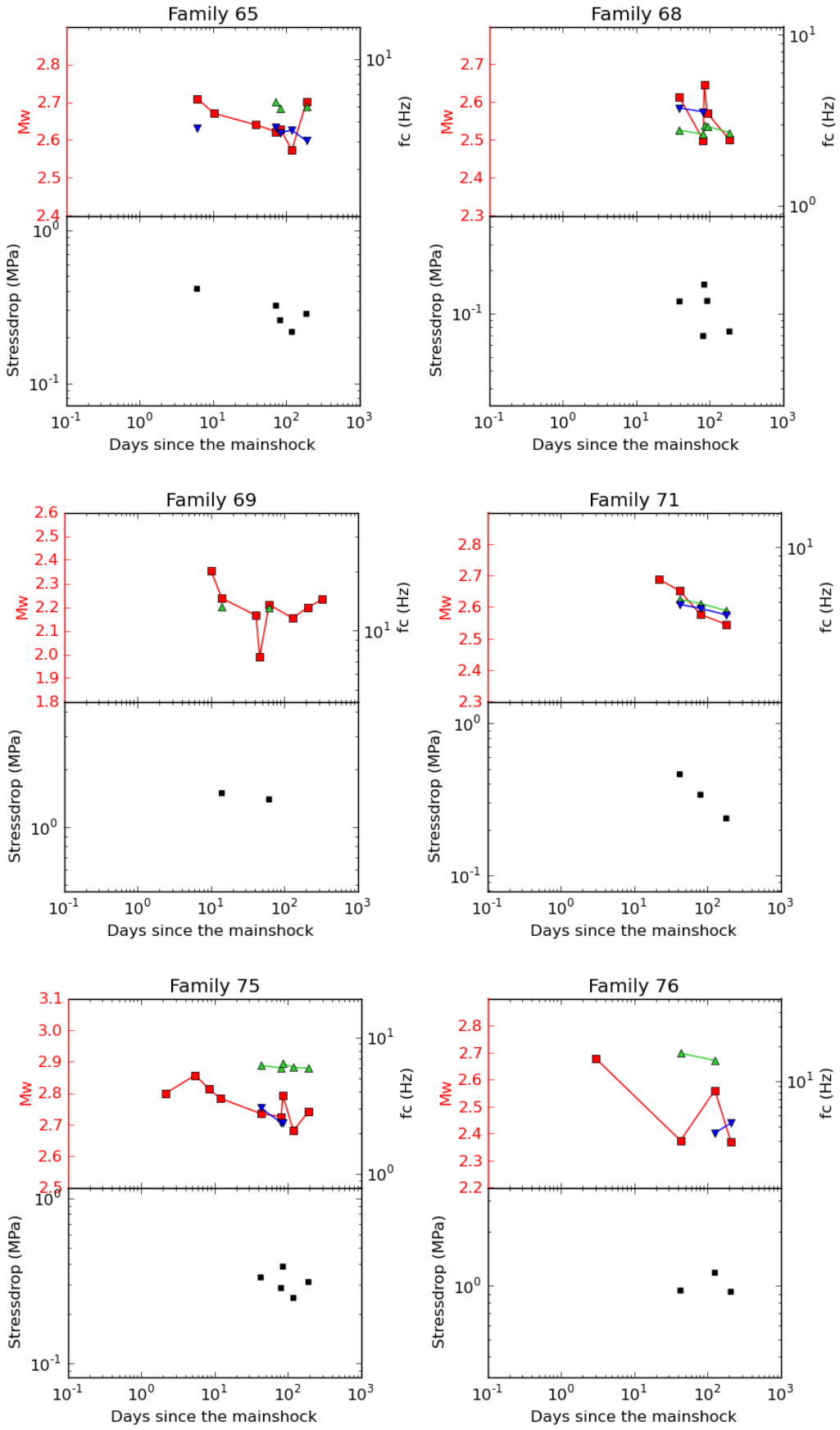
Family 65
Family 68
Family 69
Family 71
Family 75
Family 76
Mw
fc (Hz)
Stressdrop (MPa)
Days since the mainshock

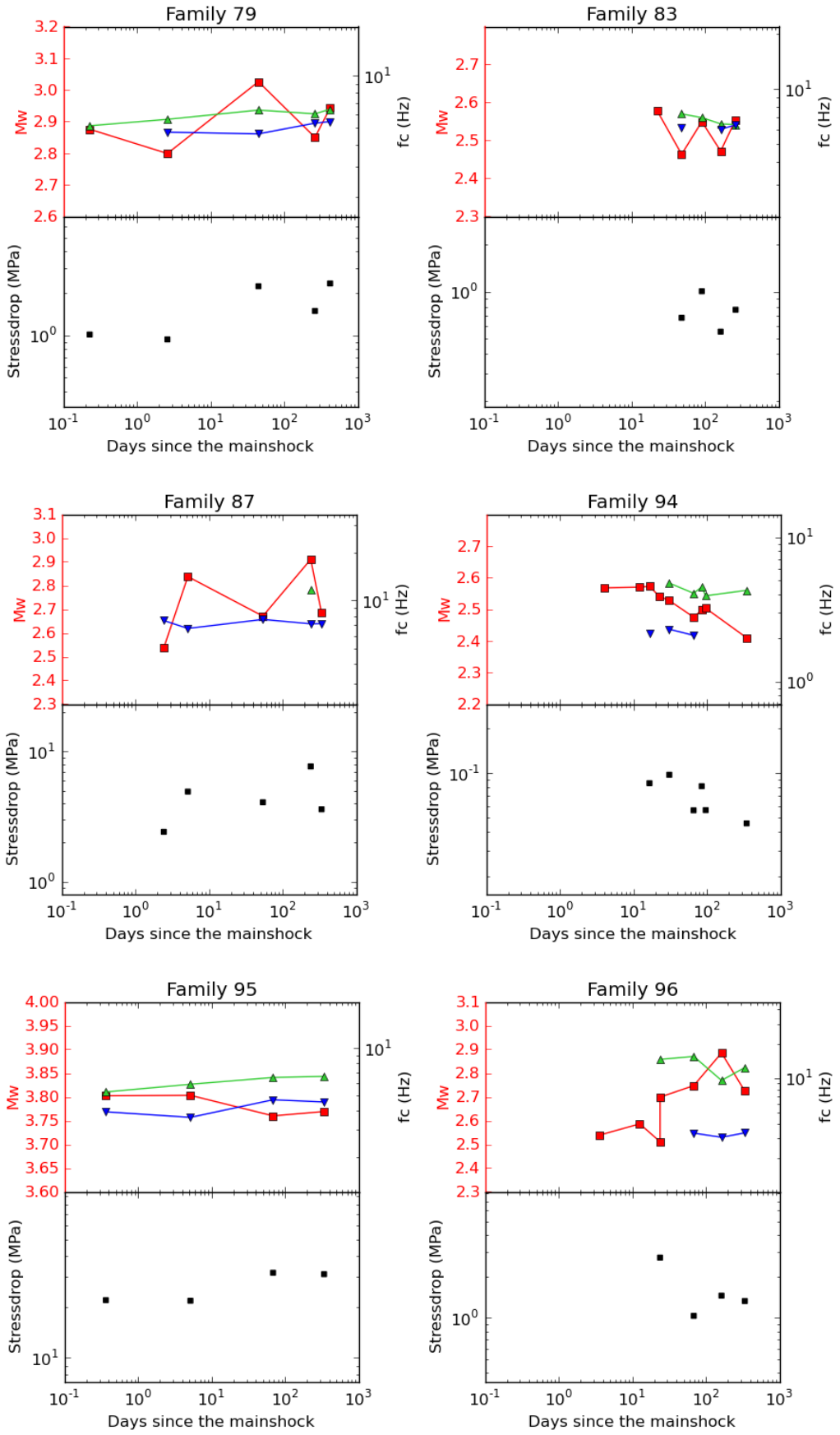
Family 79
Family 83
Family 87
Family 94
Family 95
Family 96
Mw
fc (Hz)
Stressdrop (MPa)
Days since the mainshock

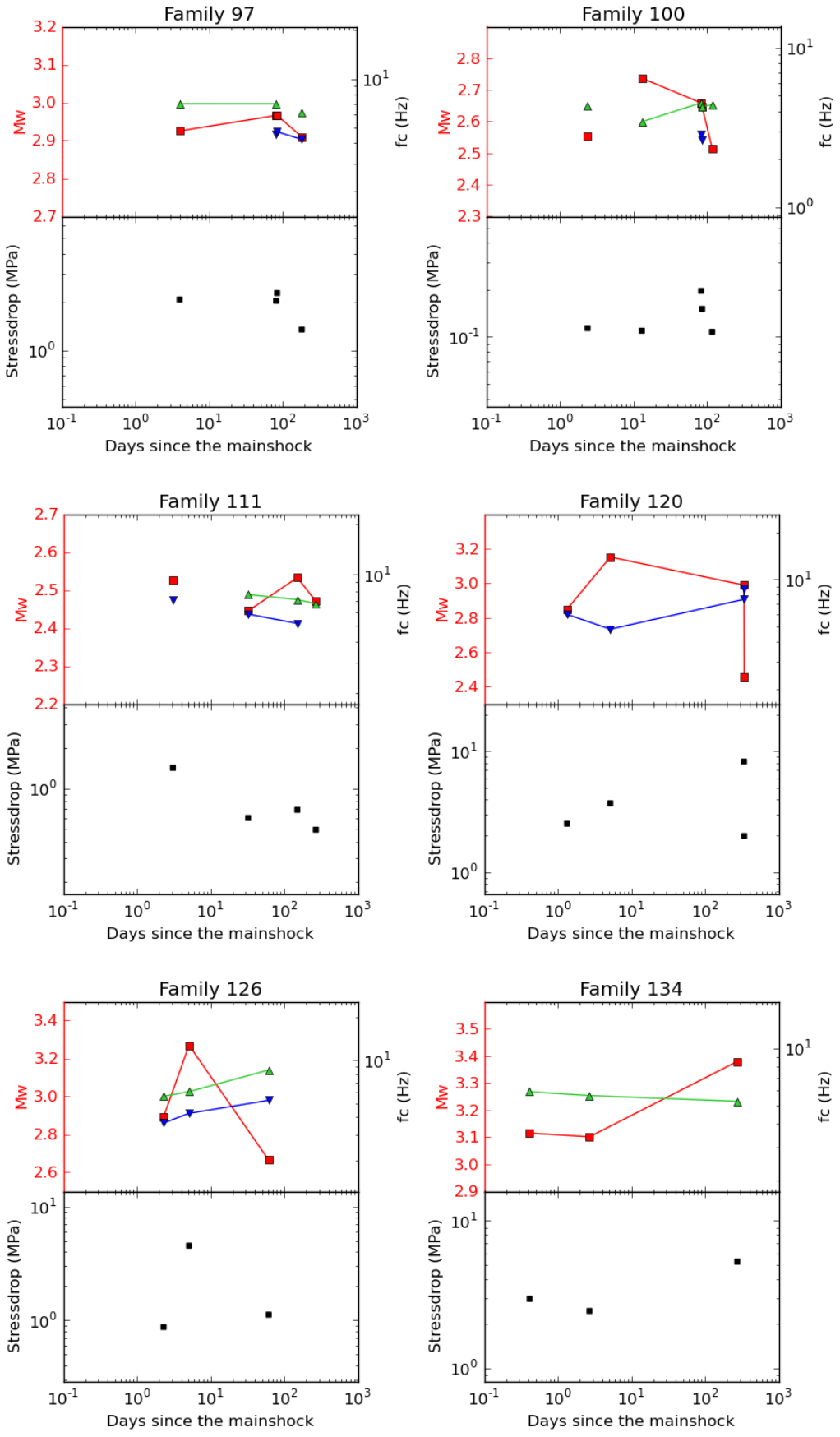
Family 97
Family 100
Family 111
Family 120
Family 126
Family 134
Mw
fc (Hz)
Stressdrop (MPa)
Days since the mainshock

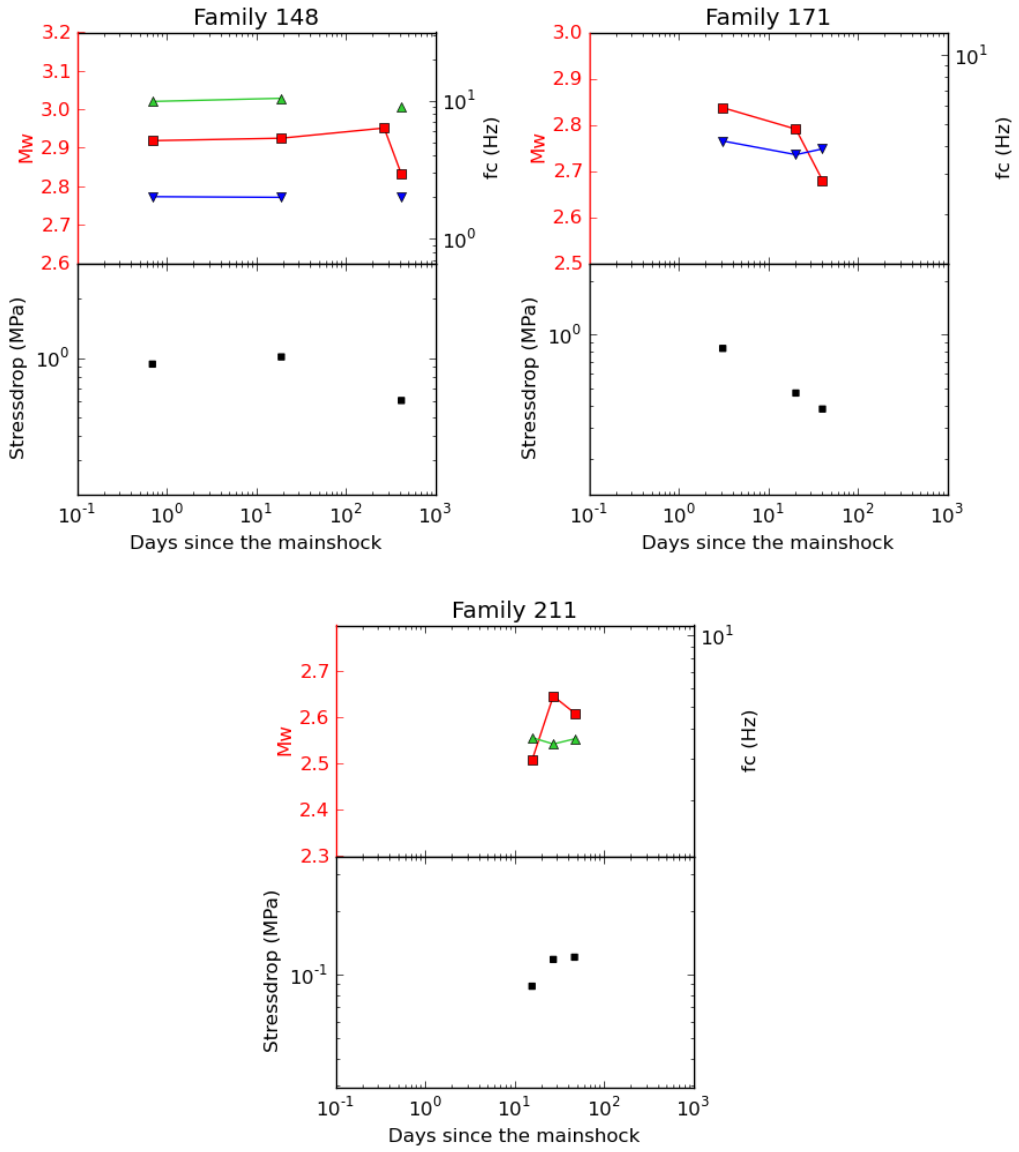

Figure SD.9: Evolution of source properties in families. Moment magnitudes are red squares, P corner frequencies are green triangles, S corner frequencies are blue upside down triangles, and stress drops are black squares. Magnitudes and corner frequencies are connected by a line if they are consecutive, and are separated if an event is missing between them.

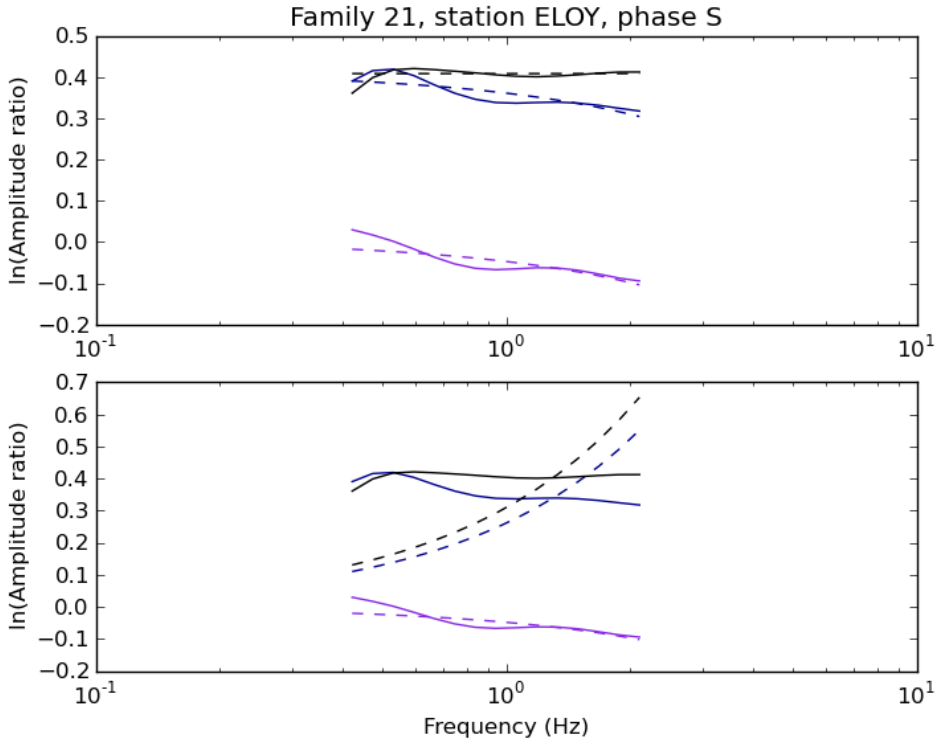
Family 21, station ELOY, phase S
ln(Amplitude ratio)
ln(Amplitude ratio)
Frequency (Hz)

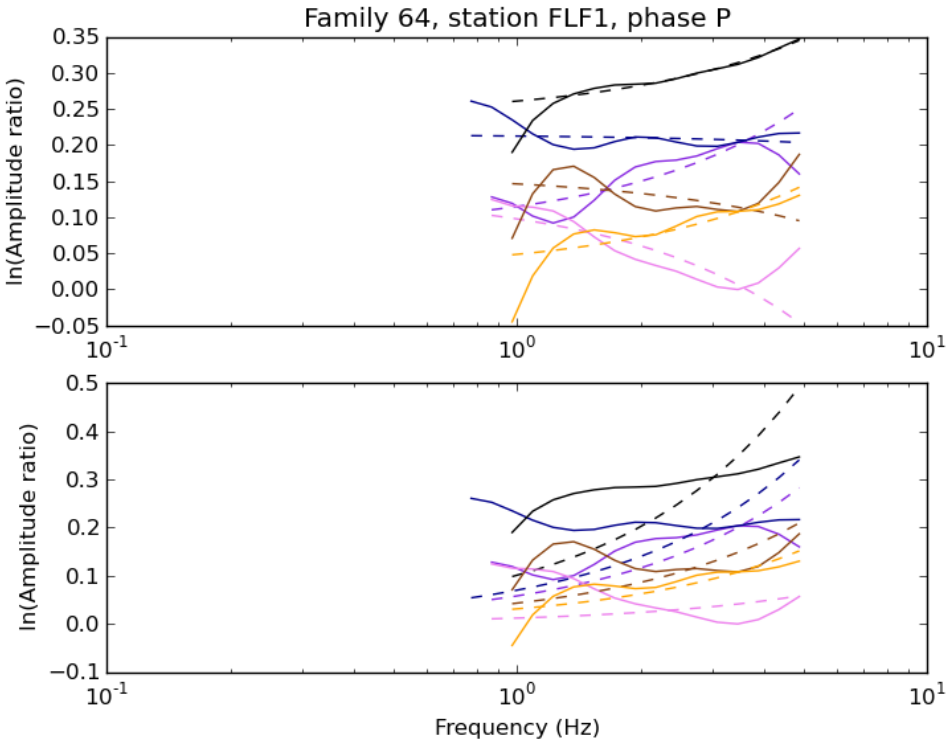
Family 64, station FLF1, phase P
ln(Amplitude ratio)
ln(Amplitude ratio)
Frequency (Hz)

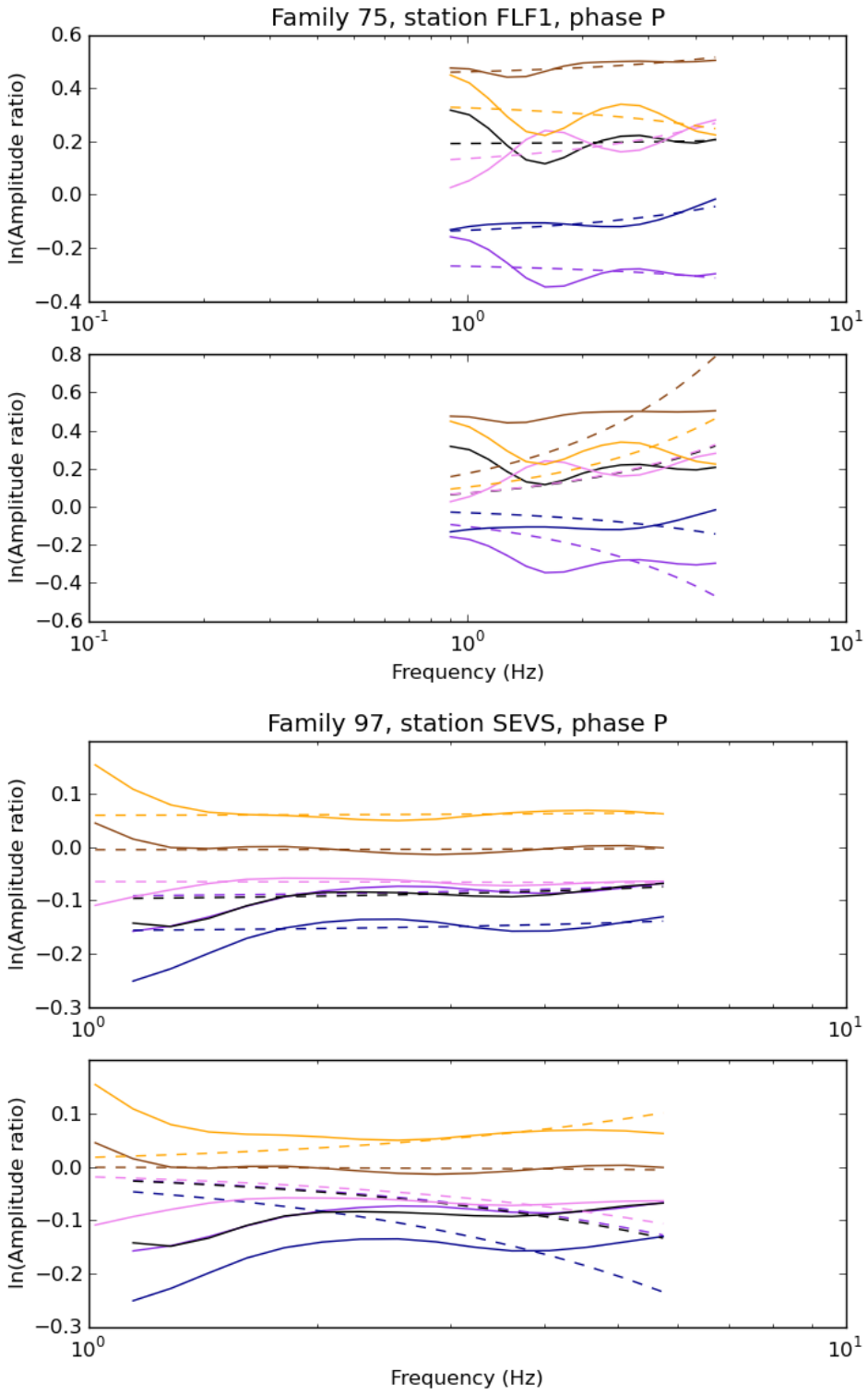

Figure SD.10: Attenuation modeling for 4 different families of repeating earthquake. For each family, the top panel shows the spectral ratios of earthquakes within the families under the minimum calculated corner frequency (full line), and the modelled spectral ratios assuming a constant corner frequency (dashed line). The bottom panel shows the spectral ratios again (full line), and the modelled spectral ratios assuming a constant corner frequency and a constant seismic moment (dashed line).

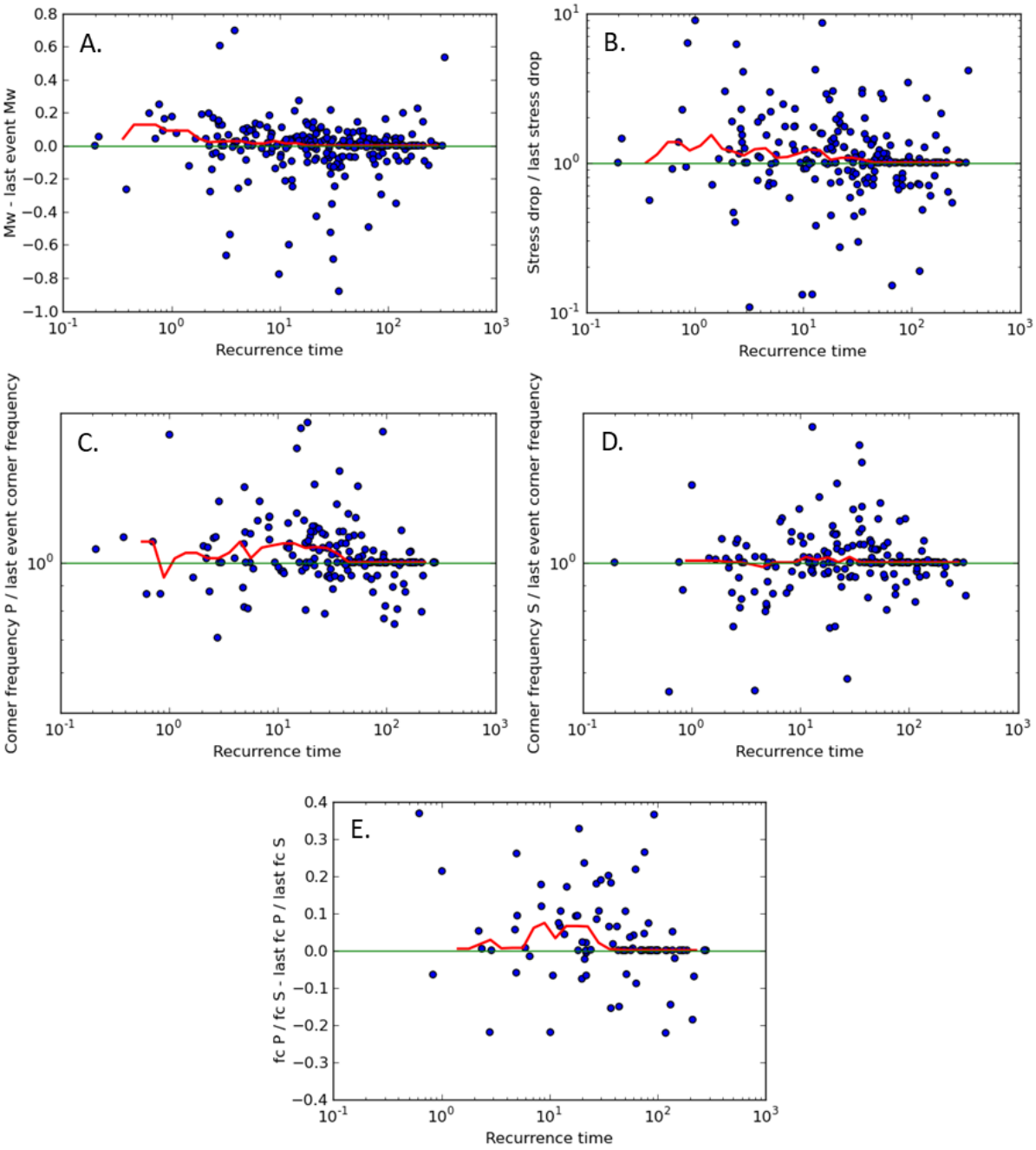

Figure SD.11: Normalized source properties within families as a function of recurrence time. Each event within a family is normalized by the last event of that family with all source properties determined. The red line is the median computed using a sliding window 0.6 in log space. The recurrence time of first events within a family is considered to be the time from the mainshock.

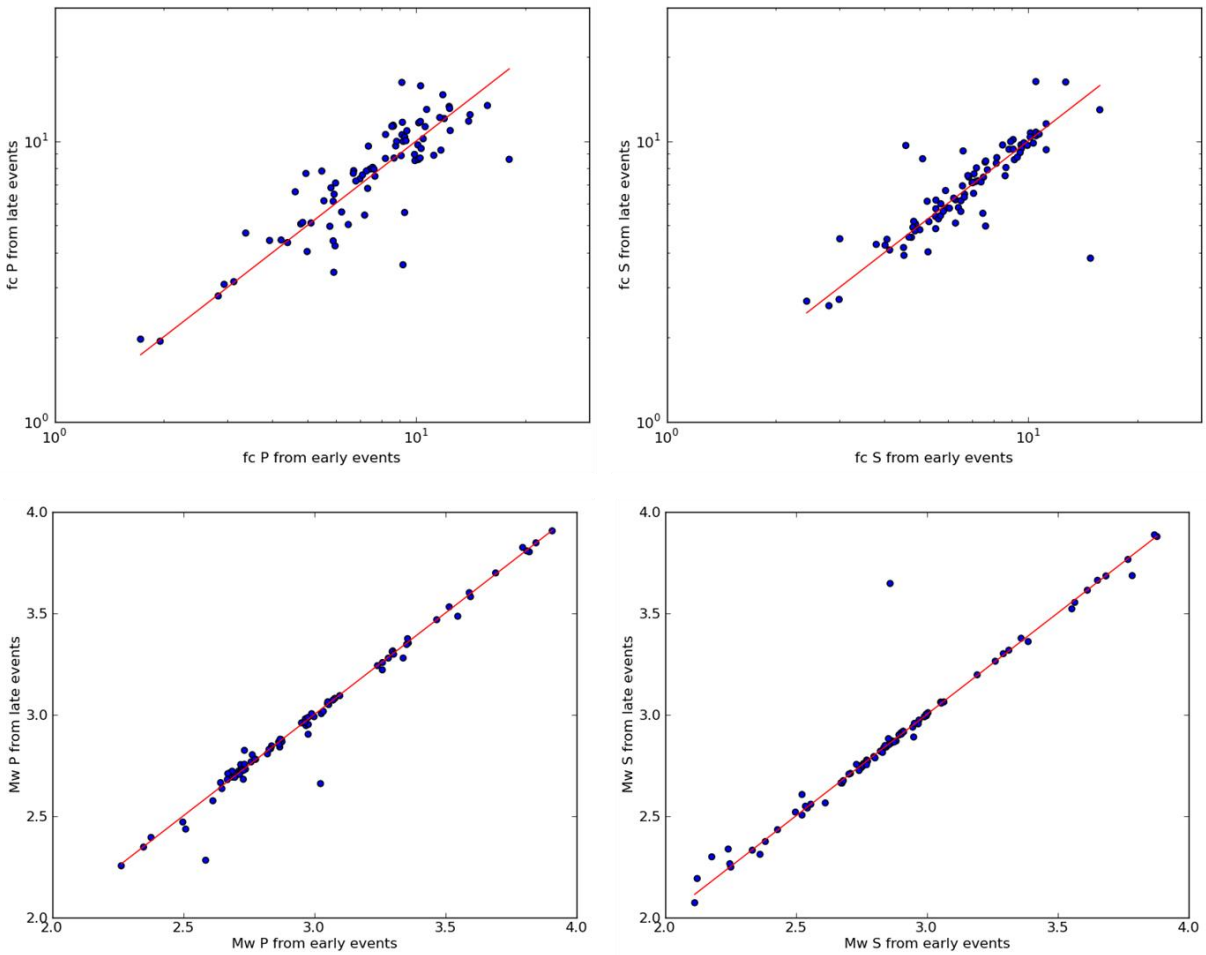

Figure SD.12: Comparison of source properties of a single event at a single station obtained only using ratios of early events (x axis) Vs late events (y axis).

Appendix E: List of scientific publications and communications

Articles published:

- *Repeating Earthquakes at the Edge of the Afterslip of the 2016 Ecuadorian MW 7.8 Pedernales Earthquake*
  Chalumeau C., Agurto-Detzel H., De Barros L., Charvis P., Galve A., Rietbrock A., Alvarado A., Hernandez S., Beck S., Font Y., Hoskins M., León-Ríos S., Meltzer A., Lynner C., Rolandone F., Nocquet J-M., Régnier M., Ruiz M., Soto-Cordero L., Vaca S., Segovia M.
  2021, Journal of Geophysical Research: Solid Earth, 126(5), pp.e2021JB021746.
- *Seismic Exploration of the Deep Structure and Seismogenic Faults in the Ligurian Sea by Joint Multi Channel and Ocean Bottom Seismic Acquisitions: Preliminary Results of the SEFASILS Cruise*
  Dessa J.X., Beslier M.O., Schenini L., Chamot-Rooke N., Corradi N., Delescluse M., Déverchère J., Larroque C, Sambolian S., Canva A., Operto S., Ribodetti A., Agurto-Detzel H., Bulois C., **Chalumeau C.**, Combe L.
  2020, Geosciences, 10 (3), pp.108

Oral presentations:

- *Repeating earthquakes cluster at the edge of the afterslip following the 2016 Pedernales earthquake (Ecuador)*
  Chalumeau C., Agurto-Detzel H., De Barros L., Charvis P., Galve A., Rietbrock A., Alvarado A., Hernandez S., Beck S., Font Y., Hoskins M., León-Ríos S., Meltzer A., Lynner C., Rolandone F., Nocquet J-M., Régnier M., Ruiz M., Soto-Cordero L., Vaca S., Segovia M.
  2021, AGU Fall Meeting
- *Repeating earthquakes line the edge of the afterslip in the aftermath of the 2016 Pedernales earthquake*
  Chalumeau C., Agurto-Detzel H., De Barros L., Charvis P., Galve A., Rietbrock A., Alvarado A., Hernandez S., Beck S., Font Y., Hoskins M., León-Ríos S., Meltzer A., Lynner C., Rolandone F., Nocquet J-M., Régnier M., Ruiz M., Soto-Cordero L., Vaca S., Segovia M.
  2021, SSA Annual Meeting
- *Repeating Aftershocks of the 16th April 2016 Mw 7.8 Pedernales (Ecuador) Earthquake Underline the Interplay Between Afterslip and Seismicity*
  Chalumeau C., Agurto-Detzel H., De Barros L., Charvis P., Galve A., Rietbrock A., Alvarado A., Hernandez S., Beck S., Font Y., Hoskins M., León-Ríos S., Meltzer A., Lynner C., Rolandone F., Nocquet J-M., Régnier M., Ruiz M., Soto-Cordero L., Vaca

S., Segovia M.
2019, AGU Fall Meeting

- *Repeating aftershocks of the 2016 Pedernales earthquake highlight interactions between afterslip and seismicity*
  Chalumeau C., Agurto-Detzel H., De Barros L., Charvis P., Galve A., Rietbrock A., Alvarado A., Hernandez S., Beck S., Font Y., Hoskins M., León-Ríos S., Meltzer A., Lynner C., Rolandone F., Nocquet J-M., Régnier M., Ruiz M., Soto-Cordero L., Vaca S., Segovia M.
  2019, 8th International Symposium on Andean Geodynamics (ISAG)

Poster and e-lightning presentations:

- *The August 14, 2021 Nippes, Haiti Earthquake Mainshock and Aftershock Sequence Recorded by The Ayiti-seismes Citizen Network*
  Monfret T., Lomax A., Paul S., Delouis B., Courboulex F., Chaize J., Deschamps A., Calais E., Symithe S., St Fleur S., Agurto-Detzel H., **Chalumeau C**., Clouard V., Duval A.M., Ende M.
  2021, AGU Fall Meeting
- *Repeaters cluster around the afterslip after the 16/04/2016 M7.8 Pedernales earthquake (Ecuador)*
  Chalumeau C., Agurto-Detzel H., De Barros L., Charvis P., Galve A., Rietbrock A., Alvarado A., Hernandez S., Beck S., Font Y., Hoskins M., León-Ríos S., Meltzer A., Lynner C., Rolandone F., Nocquet J-M., Régnier M., Ruiz M., Soto-Cordero L., Vaca S., Segovia M.
  2021, Cargèse summer school on Earthquakes: nucleation, triggering, rupture, and relationships with aseismic processes
- *Repeating earthquakes follow afterslip gradient in the aftermath of the 16th April 2016 M7.8 Pedernales earthquake in Ecuador*
  Chalumeau C., Agurto-Detzel H., De Barros L., Charvis P., Galve A., Rietbrock A., Alvarado A., Hernandez S., Beck S., Font Y., Hoskins M., León-Ríos S., Meltzer A., Lynner C., Rolandone F., Nocquet J-M., Régnier M., Ruiz M., Soto-Cordero L., Vaca S., Segovia M.
  2021, EGU General Assembly Conference
- *Imaging the megathrust in subduction zones: lessons from Greece, Ecuador and the Lesser Antilles*
  Laigle M., Agurto-Detzel H., Bécel A., Boucard M., **Chalumeau C**., Charvis P., Dessa J.X., Galve A., Hernandez M.J., Hussni S., Klingelhoefer F., Kopp H., Laurencin M., Lebrun J.F., Marcaillou B., Michaud F., Paulatto M., Ribodetti A., Sachpazi M., Schenini L.
  2020, EGU General Assembly Conference